

Max-Planck-Institut für Kolloid- und Grenzflächenforschung

Carbon Nitride Incorporation in Polymer Networks

Light-driven integration and utilization of graphitic carbon nitride
into macroscale polymeric networks

Dissertation

zur Erlangung des akademischen Grades

Doktor der Naturwissenschaften (Dr. rer. nat.)

In der Wissenschaftsdisziplin „Polymerchemie“

eingereicht an der

Mathematisch-Naturwissenschaftlichen Fakultät

der Universität Potsdam

von

Cansu Esen

Geboren am 01.07.1991 in Istanbul

Potsdam-Golm, im August 2022

Unless otherwise indicated, this work is licensed under a Creative Commons License Attribution 4.0 International.

This does not apply to quoted content and works based on other permissions.

To view a copy of this licence visit:

<https://creativecommons.org/licenses/by/4.0>

Published online on the

Publication Server of the University of Potsdam:

<https://doi.org/10.25932/publishup-57625>

<https://nbn-resolving.org/urn:nbn:de:kobv:517-opus4-576253>

Foreword

First of all, I would like to express my special thanks to Prof. Markus Antonietti, who is not only remarkable scientist and pioneer in chemistry but also a visionary free-spirit, tremendously inspiring Professor who has widen my academic perception as well as world by giving me the chance to pursue my PhD at MPIKG. It has been a great honor to work with, immense motivation for future and unique opportunity to come across with his constructive supervision

There are thousands of words to describe my deepest appreciations for my wonderful group leader, Assist. Prof. Dr. Baris Kumru, a bright-minded person who has amazed me from the moment I started to work with him and motivated me throughout this journey with his constructive discussions and sincere guidance. Thank you for immense patience, support and trust that encouraged me always to do my best. I could never ask for a better group leader, a mentor, a friend than you.

I would like to thank Prof. Dr. Helmut Schlaad for providing me teaching opportunity and his valuable help with thesis reviewing.

My sincere gratitude to Dr. Paolo Gusto for his great support, ultimate kindness and delightful guidance I always receive with my all pleasure, many thanks to Dr. Majd Al-Naji for all the amazing and fruitful discussions on very late nights at Institute, my full respect and sympathy for Dr. habil. Nadja and Dr. Nieves Lopez as such successful role models for many female researchers.

I sincerely appreciate every technician whom I received help from, but exclusively from Ursula Lubahn and Marlis Gräwert, it was amazing working with both of you. Also many thanks to Antje Völkel, Heike Runge, Bolortuya Badamdorj and Irina Shekova.

I would like to express my all gratitude to the amazing people of colloids department. My journey started and went through with covid however, this only strengthen our relations so that now I have wonderful people in my life, people I will always remember and can recall them as family. Diana and Janina, my dearest babes, I cannot imagine this journey without you (it would be such a boring, dull, and not precise ‘in timing’ that could kill us

‘softly’ PhD period). Agata, the ray of sunshine at our institute, thank you for being amazing and all the sincere love you have always given me.

Julya & Ivan, the best couple ever I have met in here, I will always remember how deeply you welcomed and helped me always with your unlimited kindness during tough times as well as joyful days we spent together. Enrico, Stefano and Francesco; my dearest Italian community, I will always appreciate your warm welcoming and splendid taste of joy in life that you shared with me (home-made pizzas, introducing me to Negroni, wonderful lake times and many more memories together). Enis, the rockstar, the coolest chez briel master ever, thank you for being a wonderful office mate that I could have ever asked and a close friend that I could always count on. Evgeny, amazing cheerful spirit, such a lovely colleague you have been to me, thank you for being a part of this journey. Begum, my kumbi, spreading your amazing joy to your surroundings and I am so grateful that you shared a bit of it with me during this period. Bradley, thank you so much for the warmest welcome of my PhD and all the memories we had together. And the rest of people: Mina, Qian, Esther, Naresh, Hannes, Zhenia, Jing, Zihan, Yen-Han, Katja, Melis, sending my all love and gratitude you all. Lastly, “Life is a ‘highway’ with full of surprises” once was said by a young teacher, Jan F., whom I accidentally met, yet, much grateful to know.

I am immensely grateful to my family, whom are always supported me in every step of my life. My sweet mom (Canan), having an angel’s soul, a kindest persona on earth. My sister (Ceylan), always showing me the right way to be a better person in all circumstances. My brother in law (Alper), supporting relentlessly no matter how far I have been. My little niece (Alin), sending me thousands of kisses tirelessly. And, my father, who did not live long enough to see these days, I thank you for giving me the chance to be a person who I become, and proudly am now.

Thank you all by heart,
Cansu Esen

Dedicated to whom taught me

Nothing is *late* in life

“Nothing in life is to be feared, it is only to be understood.
Now is the time to understand more, so that we may fear less”

Marie Skłodowska Curie

“Without data, you're just another person with an opinion”

W. Edwards Deming

Abstract

The urge of light utilization in materials fabrication is as encouraging as challenging. Steadily increasing energy consumption in accordance with rapid population growth requires a corresponding solution within the same rate of occurrence speed.¹ Demographics exhibited an approximate timeline for the end of population growth, in 2100 at about 11 billion people, which means the population will grow by approx. forty percent of the current state.² First industrial revolution which triggered coal demand and led to escalate coal mining in accordance with the advancing coal-powered steam engines thereafter electrification (second industrial revolution), undoubtedly endowed us with tremendous practicality and advantages in our lives. If we consider the time all before this, human history was initially manipulated by two crucial cycles relies upon ‘plants’ and ‘solar radiation’.³ As human beings, we are only capable of converting energy as we started accessing heat by burning woods or mobilizing overseas by harnessing the wind. Nevertheless, given the rise to particular energy sources that we majorly use like petroleum, coal, or natural gas have been dropping the contribution in long-term environment viability just to fulfill the high demand of society. Annually calculated energy consumption per capita results have clearly shown the emergence of immediate action that we have been underestimating for so long. In one article, the sun was described as ‘nuclear fusion reactor’ along with pointing out the economic challenges of building renewable energy facilities, especially nuclear power plants.⁴ Solar energy, compared to nuclear power, besides an ultimate quantity of energy that it possesses, also provides zero carbon emission with no posing any danger in nature like waste products, and codependency against foreign assets.⁵ Therefore, creating, designing, and manufacturing materials that can interact with light and in further be applicable as well as disposable in photo-based applications are very much under the attention of researchers, with an ever-increasing effort. Insights of light-driven processes revealed day by day, also revived the complexity in the creation of photo-active materials. In most cases, having only the photo-responsive compound was insufficient to apply or function properly in some particular

systems. It is therefore essential to explore and bring more effort into integration processes of materials for desired purposes.

Materials that span from natural to synthetic in hybrid or composite forms, have been in use ever since the dawn of civilization. Not only did they meet our needs since then, but also their advanced feature to progress enabled them simultaneously to develop in many disciplines. From a broader spectrum, materials that we can identify in four main titles; metals, nonmetal inorganics (ceramics), polymers, and composites (intersection set) have served society in various ways at every stage of the hominin timeline.⁶ Polymers has surged in production of numerous materials ever since the first invention of bioplastic, semi-synthetic cellulose acetate in 1830, followed by sulfur addition into natural rubber and its further vulcanization process achieved by Charles Goodyear, thereafter invention of artificial silk (rayon or viscose) and first synthetic thermoset resin invented by Leo Baekeland in 1907 (bakelite). These multi-taking artificial materials with high strength, flexibility, and resistivity created a global impact in many sectors ranging from packing, coating, automotive, and construction since the beginning of the 20th century. However, due to escalated demand for products with higher performances, researchers have upgraded the synthetic polymers by fabricating hybrid or/and composite components. These advanced materials paved the way for further innovative technological achievements only when sustainable.

In the era of sustainability and renewable energy systems, semiconductor-based photoactive materials have received great attention not only based on solar and/or hydrocarbon fuels generation from solar energy, but also successful stimulation of photocatalytic reactions such as water splitting, pollutant degradation and organic molecule synthesis. First usage of ‘semiconducting’ term by A. Volta in 1792,⁷ followed by ‘semiconductor effect’ from M. Faraday in 1833, ‘photovoltaic effect’ by A. E. Becquerel in 1839, ‘rectification’ observation by K. F. Braun in 1874, led all the way of discovery in experimental confirmation of barrier in metal-semiconductor junction from W. Schottky and N. Francis Mott (1929).⁸ The turning point had been reached for water splitting with an electrochemical cell consisting of TiO₂-Pt electrode illuminated by UV

light as energy source rather than an external voltage, that successfully pursued water photolysis by Fujishima and Honda in 1972.⁹ Ever since, there has been a great deal of interest in research of semiconductors (e.g. metal oxide, metal-free organic, noble-metal complex) exhibiting effective band gap for photochemical reactions. Most common processes to modify semiconductors include surface modification of metal nanoparticles, doping with non-metals, and photosensitization via dyes.¹⁰ To date, some common inorganic ones might be sorted as follows TiO₂, Fe₂O₃, CdS, ZnO, WO₃, SnO₂, CdSe, CuO and conjugated polymer-based hybrids such as poly(3-hexylthiophene)/CdS, polypyrrole/Fe₂O₃, polyaniline/TiO₂, and poly(3,4-ethylenedioxythiophene)/Au NPs.¹¹ In the case of environmental friendliness, toxicity of metal-based semiconductors brings some restrictions in possible applications. Regarding this, a very robust and ‘earth-abundant’ organic semiconductor, graphitic carbon nitride, has been synthesized and successfully applied in photoinduced applications as novel photocatalyst.¹² Properties such as suitable band gap, low charge carrier recombination and feasibility for scaling up paved the way of advance combination with other catalysts to gather higher photoactivity based on compatible heterojunction. Besides, synergistic effect based on organic character that increases the possibilities of integration with polymeric materials, widens the viability and profitability of both fields. It certainly leads the way to design multifunctional hybrid and composite materials that seem more realistic in the sense of meeting future expectations.

This dissertation aims to demonstrate a series of combinations between the organic semiconductor g-CN and polymer materials that are forged through photochemistry, either in synthesis or application. Fabrication and design processes, as well as applications performed in accordance to the scope of thesis will be elucidated in detail. In addition to UV light, more attention is placed on visible light as energy source with a vision of more sustainability and better scalability in creation of novel materials and solar energy-based applications.

Kurzfassung

Die Nutzung von Licht für die Herstellung von Materialien ist ebenso vielversprechend wie herausfordernd. Der stetig steigende Energieverbrauch in Übereinstimmung mit dem rasanten Bevölkerungswachstum erfordert eine entsprechende Lösung in der gleichen Geschwindigkeit.¹ Die Bevölkerungsstatistik deutet einen Zeitpunkt für das Ende des Bevölkerungswachstums im Jahr 2100 mit etwa 11 Milliarden Menschen an, was bedeutet, dass die Bevölkerung um weitere vierzig Prozent des heutigen Standes wachsen wird.² Die erste industrielle Revolution, die die Nachfrage nach Kohle auslöste und zu einem drastischen Anstieg des Kohleabbaus für die fortschreitenden kohlebetriebenen Dampfmaschinen führte und schließlich der Elektrifizierung den Weg ebnete (zweite industrielle Revolution), hat uns zweifellos enorme praktische Vorteile für unser Leben beschert. Betrachtet man die Zeit davor, so wurde die menschliche Geschichte zunächst von zwei entscheidenden Kreisläufen beeinflusst, die sich auf Pflanzen und Sonneneinstrahlung stützten.³ Als Menschen waren wir lediglich in der Lage, Energie umzuwandeln, indem wir Holz für die Gewinnung von Wärme verbrannten oder indem wir den Wind nutzten, z. B. auf Segelschiffen in den Weltmeeren. Heutzutage haben bestimmte Energiequellen, wie Erdöl, Kohle oder Erdgas die wir inzwischen hauptsächlich nutzen um den hohen Energiebedarf der Gesellschaft zu decken, ihren Beitrag zur langfristigen Umweltverträglichkeit verloren. Jährlich berechnete Pro-Kopf-Energieverbräuche haben deutlich gezeigt, dass wir den sofortigen Handlungsbedarf, den wir so lange unterschätzt haben, immer noch nicht erkannt haben. In einem Artikel wurde die Sonne als ‘Kernfusionsreaktor’ bezeichnet und auf die wirtschaftlichen Herausforderungen beim Bau von Anlagen für erneuerbare Energien, insbesondere von Kernkraftwerken, hingewiesen.⁴ Im Vergleich zur Kernenergie bietet die Solarenergie neben der ultimativen Energiemenge, die sie besitzt, auch keine Kohlenstoffemissionen und stellt keine Gefahr für die Natur dar, wie z. B. Abfallprodukte und die Abhängigkeit von ausländischen Ressourcen.⁵ Aus diesem Grund widmen Forscher der Entwicklung, dem Design und der Herstellung von Materialien, die mit Licht interagieren können und darüber hinaus in fotobasierten Anwendungen einsetzbar sind, große Aufmerksamkeit

und unternehmen immer größere Anstrengungen. Die Erkenntnisse aus lichtgesteuerten Prozessen, die fortlaufend gemacht werden, haben auch die Komplexität bei der Herstellung fotoaktiver Materialien erhöht. In den meisten Fällen reichte es nicht aus, nur eine lichtsensitive Verbindung zu haben, um in bestimmten Systemen effektiv eingesetzt zu werden oder zu funktionieren. Es ist daher unerlässlich, die Integrationsprozesse von Materialien für die gewünschten Zwecke zu erforschen und zu verbessern.

Materialien, die von natürlichen bis hin zu synthetischen reichen und in Hybrid- oder Verbundformen vorliegen, werden seit Anbeginn der Zivilisation verwendet. Seitdem haben sie nicht nur unsere Ansprüche befriedigt, sondern sich aufgrund ihrer fortschreitenden Eigenschaften auch in viele Fachrichtungen weiterentwickelt. Das breite Spektrum von Materialien können wir in vier Hauptkategorien einteilen: Metalle, anorganische Nichtmetalle (Keramik), Polymere und Verbundwerkstoffe. Diese Materialien haben der Gesellschaft in jeder Phase der menschlichen Zeitrechnung auf unterschiedliche Weise gedient.⁶ Seit der Erfindung des ersten Biokunststoffs, des halbsynthetischen Celluloseacetats im Jahr 1830, gefolgt von der Zugabe von Schwefel zu Naturkautschuk und dessen weiterer Vulkanisierung durch Charles Goodyear, der Erfindung von Kunstseide (Rayon oder Viskose) und des ersten synthetischen, duroplastischen Harzes, das Leo Baekeland 1907 erfand (Bakelit), hat die Produktion von Polymeren stark zugenommen. Diese vielseitigen künstlichen Materialien mit hoher Festigkeit, Flexibilität und Widerstandsfähigkeit haben seit Anfang des 20. Jahrhunderts weltweite Auswirkungen auf viele Bereiche wie Verpackung, Beschichtung, Automobile und Bauwesen. Aufgrund der gestiegenen Nachfrage nach Produkten mit höherer Leistung, haben Forscher die Verwendung synthetischer Polymere durch die Herstellung von Hybrid- und/oder Verbundwerkstoffkomponenten verbessert. Diese fortschrittlichen Materialien ebneten den Weg für weitere innovative technologische Errungenschaften.

Im Zeitalter der Nachhaltigkeit und erneuerbarer Energiesysteme haben photoaktive Materialien auf Halbleiterbasis nicht nur aufgrund der Erzeugung von Solarenergie oder der Herstellung von Brennstoffen aus Sonnenenergie große Beachtung gefunden. Auch für den erfolgreichen Einsatz in photokatalytischen Reaktionen wie der Wasserspaltung,

Schadstoffabbau und Synthese organischer Moleküle sind diese Materialien von großer Bedeutung. Die erste Verwendung des Begriffs "halbleitend" durch A. Volta im Jahr 1792,⁷ gefolgt vom "Halbleitereffekt" von M. Faraday im Jahr 1833, dem "photovoltaischen Effekt" von A. E. Becquerel im Jahr 1839 und der Beobachtung des "Gleichrichtereffektes" durch K. F. Braun im Jahr 1874 führte zur experimentellen Bestätigung der Barriere im Metall-Halbleiter-Übergang von W. Schottky und N. Francis Mott (1929).⁸ Der Wendepunkt für die Wasserspaltung wurde mit einer elektrochemischen Zelle erreicht, die aus einer TiO₂-Pt-Elektrode besteht, die mit UV-Licht als Energiequelle anstelle einer externen Spannung beleuchtet wird, und mit der Fujishima und Honda 1972 erfolgreich die Wasserphotolyse betrieben.⁹ Seitdem besteht ein großes Interesse an der Erforschung von Halbleitern (z. B. Metalloxide, metallfreies organisches Material, Edelmetallkomplexe), die eine effektive Bandlücke für photochemische Reaktionen aufweisen. Zu den gängigsten Verfahren zur Modifizierung von Halbleitern gehören die Oberflächenmodifizierung von Metallnanopartikeln, die Dotierung mit Nichtmetallen und die Photosensibilisierung durch Farbstoffe.¹⁰ Zu den bisher bekannten anorganischen Nanopartikeln gehören TiO₂, Fe₂O₃, CdS, ZnO, WO₃, SnO₂, CdSe, CuO und Hybride auf der Basis konjugierter Polymere wie Poly(3-Hexylthiophen)/CdS, Polypyrrol/Fe₂O₃, Polyanilin/TiO₂ und Poly(3,4-Ethylendioxythiophen)/Au NPs.¹¹ Was die Umweltfreundlichkeit anbelangt, so bringt die Toxizität von Halbleitern auf Metallbasis einige Einschränkungen bei den möglichen Anwendungen mit sich. Diesbezüglich wurde der sehr robuste und bezüglich seiner Ausgangsstoffe häufig vorkommende organische Halbleiter Graphitkohlenstoffnitrid synthetisiert und erfolgreich in photoinduzierten Anwendungen als neuartiger Photokatalysator eingesetzt.¹² Eigenschaften wie eine geeignete Bandlücke, geringe Ladungsträgerrekombination und die Möglichkeit der Skalierung ebnet den Weg für eine fortschrittliche Kombination mit anderen Katalysatoren, um eine höhere Photoaktivität auf der Grundlage eines kompatiblen Heteroübergangs zu erzielen. Außerdem erhöht der Synergieeffekt aufgrund des organischen Charakters, der die Möglichkeiten der Integration mit polymeren Materialien erhöht, die Lebensfähigkeit und Rentabilität beider

Bereiche. Dies ebnet den Weg für die Entwicklung multifunktionaler Hybrid- und Verbundwerkstoffe, die im Hinblick auf künftige Erwartungen realistischer erscheinen.

Diese Dissertation zielt darauf ab, eine Reihe von Kombinationen zwischen organischen g-CN-Halbleitern und Polymermaterialien zu demonstrieren, die durch Photochemie entweder in der Synthese oder in der Anwendung hergestellt wurden. Die Herstellungs- und Designprozesse sowie die Anwendungen, die im Rahmen dieser Arbeit durchgeführt wurden, werden im Detail erläutert. Neben UV-Licht wird auch dem sichtbarem Licht als Energiequelle mehr Aufmerksamkeit gewidmet. Das ermöglicht eine höhere Nachhaltigkeit und bessere Skalierbarkeit bei der Entwicklung neuartiger Materialien und Anwendungen auf der Grundlage von Solarenergie.

Notation

AAM – Acrylamide

AIBN – 2,2'-Azobis(2-methylpropionitrile)

ATRP – Atom transfer radical polymerization

CB – Conduction band

CM – Carbon nitride (made by Cyanuric acid - melamine complex)

CMB – Carbon nitride (made by Cyanuric acid - melamine-barbituric acid complex)

CMB-vTA – Vinylthiazole modified carbon nitride

CMp – Carbon nitride (made by Cyanuric acid-2,4-diamino-6-phenyl-1,3,5-triazine complex)

CMp-vTA or vTA-CMp – Vinylthiazole modified organodispersible graphitic carbon nitride

CN – Carbon Nitride

DMA – *N,N*-Dimethylacrylamide

DMSO – Dimethyl sulfoxide

DN – Double network

DVB – Divinyl benzene

EDOT – 3,4-ethylenedioxythiophene

EDX – Energy dispersive x-ray spectroscopy

g-CN – Graphitic Carbon Nitride

HEMA-hydroxyethyl methacrylate

IPN – Interpenetrating network

KPS – Potassium persulfate

MA – Methyl acrylate

MB – Methylene blue dye

MBA – *N,N'*-methylenebis(acrylamide)

MMA – Methyl methacrylate

PAMPS – Poly(2-acrylamido-2-methyl-1-propane sulfonic acid)

PANI – Polyaniline

PDMAEMA – Poly(2-(dimethylamino)ethyl methacrylate)
PEDOT – Poly-3,4-ethylenedioxythiophene
PEG – Poly(ethyleneglycol)
PEGDMA – Poly(ethylene glycol) dimethacrylate 750
PEGMEMA – Poly(ethylene glycol) methyl ether methacrylate 300
PEO – Poly(ethylene oxide)
PET – Photoinduced electron/energy transfer
PPy – Polypyrrole
PS – Polystyrene
QD – Quantum dot
RAFT – Reversible addition fragmentation transfer
RhB – Rhodamine B dye
St – Styrene
TEOA – Triethanolamine
THF – Tetrahydrofuran
UV – Ultraviolet
VB – Valence band
vTA – 4-methyl 5-vinyl thiazole
XRD – X-ray diffraction

Contents

FOREWORD	I
ABSTRACT	V
NOTATION	XIII
CHAPTER 1	1
MOTIVATION, OBJECTIVES AND OUTLINE OF THESIS	1
CHAPTER 2	5
TECHNICAL BACKGROUND	5
2.1 METAL-FREE ORGANIC SEMICONDUCTOR: GRAPHITIC CARBON NITRIDE	5
2.2 PHOTOPOLYMERIZATION: PHOTOCHEMICAL PRINCIPLES & POLYMERIZATION MECHANISM	15
2.3 EXAMPLES OF PHOTOCATALYST INCORPORATED MACROSCALE POLYMER NETWORKS	23
CHAPTER 3	47
UPGRADING POLY(STYRENE-CO-DIVINYLBENZENE) BEADS: INCORPORATION OF ORGANOMODIFIED METAL-FREE SEMICONDUCTOR GRAPHITIC CARBON NITRIDE THROUGH SUSPENSION PHOTOPOLYMERIZATION TO GENERATE PHOTOACTIVE RESIN	47
3.1. OVERVIEW	47
3.2. RESULTS AND DISCUSSION	51
3.3. CONCLUSIONS	67
CHAPTER 4	69
THIOL-ENE POLYMER BEADS VIA LIQUID-LIQUID PRINTING: ARMORED INTERFACES AND PHOTOPOLYMERIZATION VIA GRAPHITIC CARBON NITRIDE	69
4.1. OVERVIEW	69
4.2. RESULTS AND DISCUSSION	71
4.3. CONCLUSIONS	78
CHAPTER 5	79
PHOTOINDUCED POST-MODIFICATION OF GRAPHITIC CARBON NITRIDE EMBEDDED HYDROGELS: SYNTHESIS OF 'HYDROPHOBIC HYDROGELS' AND PORE SUBSTRUCTURING	79
5.1. OVERVIEW	79

5.2.	RESULTS AND DISCUSSION	81
5.3.	CONCLUSIONS	94
CHAPTER 6	95
	OXIDATIVE PHOTOPOLYMERIZATION OF 3,4-ETHYLENEDIOXYTHIOPHENE (EDOT) VIA GRAPHITIC CARBON NITRIDE: A MODULAR TOOLBOX FOR ATTAINING PEDOT.....	95
6.1.	OVERVIEW	95
6.2.	RESULTS AND DISCUSSION	98
6.3.	CONCLUSIONS	106
CHAPTER 7	107
	CONCLUSIONS	107
8. APPENDIX	111
8.1.	MATERIALS	111
8.2.	SYNTHETIC PROCEDURES.....	112
8.3.	CHARACTERIZATION METHODS	122
8.4.	SUPPLEMENTARY FIGURES AND TABLES	125
8.5.	LIST OF FIGURES.....	153
8.6.	LIST OF TABLES	156
8.7.	LIST OF SCHEMES	156
9. REFERENCES	159
10. LIST OF PUBLICATIONS	173
11. DECLARATION	175

Chapter 1

Motivation, Objectives and Outline of Thesis

Motivation: Making a small contribution, let alone making a major impact on environmental sustainability, is a difficult task in its own right. Every step taken to shift through renewable energy resources (solar, wind, hydroelectric, biomass), reduction /degradation of pollutants, and recycling of materials must be developed as collectively most effective long-term solution strategies. In terms of polymeric materials, the tremendous work that has been built on since H. Staudinger¹³ has evolved polymeric materials in many ways from the views of synthesis, characterization, and utilization. In the course of time, materials and techniques established so far, are nowadays expected to serve to society in ways that they clean up the initial damage that has been brought to the environment. Regarding this, to establish sustainability in our society, we need to utilize our renewable sources in all aspects. Especially sunlight, which is convertible into electrical energy that can be stored in batteries, via photovoltaic panels or concentrated mirrors. This process has been shaped by the materials which are exhibiting ‘photovoltaic effect’, in other words, ‘semiconducting materials’. From general view, these advanced materials not only contributing in generation of solar and hydrocarbon fuels, but also stimulating photocatalytic reactions such as hydrogen evolution, pollutant degradation,

organic compound reactions. Utilizing a semiconductor that can be synthesized from abundant precursors that neither possess nor necessarily require metal ions, e.g. graphitic carbon nitride, is a quite accurate response from a sustainability perspective. Regarding this, integration of g-CN as heterogeneous photocatalyst or/and initiator in photo-based applications has been under further attention, extending its utilization and processability by combining it with polymer science, revealed a brand new way of constructing innovative hybrid or/and composite light harvesting materials. Either by endowing its photoactivity on dormant surfaces or dressing materials with g-CN that can subsequently harvest light directly addresses this thesis's motivation. Regarding this, two chapters of this dissertation will demonstrate carbon nitride utilization in organic media by synthesizing g-CN integrated PS-DVB resin beads via suspension photopolymerization and thiol-ene/g-CN beads by liquid-liquid printing technique. These will be followed by the example of carbon nitride in aqueous media, demonstrated with the fabrication of g-CN embedded hydrogel and its further photoinduced modifications leading to 'hydrophobic hydrogel' formation and secondary network introduction. In the last chapter, an example of g-CN utilization as a heterogeneous photocatalyst that successfully initiates photooxidative polymerization of EDOT forming non-doped and processable oligoEDOT under visible light irradiation will be covered. Overall, three different g-CN utilization processes will illustrate versatile opportunities based on a simple yet powerful combination of semiconductor in polymeric networks.

Objectives: The aim of this thesis is to demonstrate light-driven utilization of graphitic carbon nitride into various polymeric networks span from PS-DVB based resin to soft matter like hydrogel or conjugated system, e.g., PEDOT to thiol-ene beads. Regarding this, the presented study follows two approaches: photoactivity of graphitic carbon nitride is introduced either via light illumination (visible or UV) in fabrication of novel structures or utilizing photoactive composites possessing g-CN as light harvesters. The resourcefulness of g-CN despite some colloidal drawbacks like poor dispersibility and stability (based on strong π - π stacking of nanosheets), will address a variety of media and emerging photocatalytic applications as well as offering novel polymerization routes.

Outline: The scope of the thesis underlines utilization of g-CN with polymer networks through photochemistry. Two types of g-CN (CM, CMp-vTA) are associated with various monomers are integrated either in dispersed (CMp-vTA for organic and CM for aqueous and) or bulk form (CM, mixed with reaction mixture as heterogeneous photocatalyst). Photoactivity of g-CN is utilized either by conducting it as heterogeneous photoinitiator in photopolymerizations or integrating first through embedding or physical adsorption to furtherly process photo-based applications (dye photo-degradation or in-situ photo grafting on g-CN).

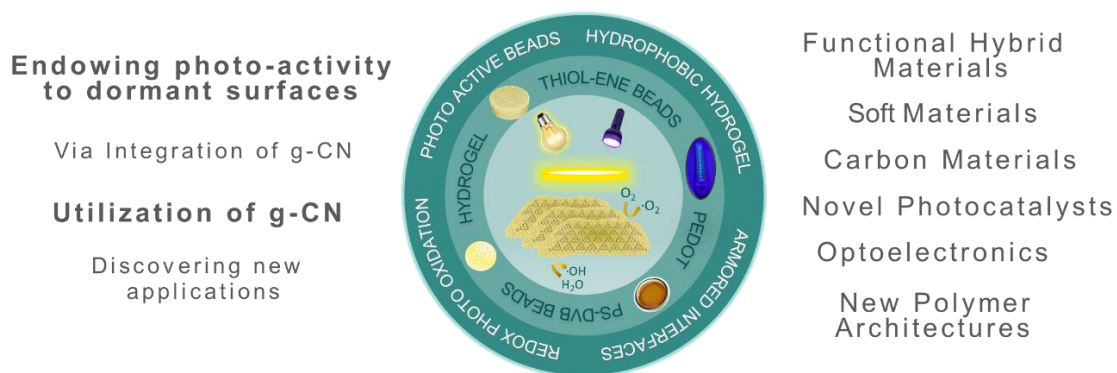
In order to understand the fundamentals of g-CN and its relation with photopolymerization, I will initially describe background of g-CN from synthesis to characterization followed by general photopolymerization principles in **Chapter 2**. Then, a few examples (mainly based on macro-scale porous polymeric matrices covering resins, hydrogels, aero-organogels to sponge type structures with commonly used semiconductors incorporated) will be presented to give an insight of integration techniques of popular semiconductors in various polymer networks to fabricate advanced materials.

In **Chapter 3**, I will continue by description of the light-driven synthesis of porous resin called poly(styrene-co-divinylbenzene) via suspension photopolymerization to generate recyclable photocatalyst beads via g-CN. In addition, photo-based applications such as dye degradation and in-situ surface modification of g-CN integrated beads will be evaluated.

Chapter 4, will demonstrate g-CN incorporation into macro-scale thiol-ene beads via a liquid-liquid printing technique. g-CN dispersed in organic media and acts as a photoinitiator in the fabrication of thiol-ene beads where it also serves as an interfacial stabilizer which sustains the as-formed spherical shape of drop-wise formed beads (in aqueous media). Besides, the opportunity to obtain S, N codoped carbonaceous materials through carbonization of as-synthesized beads will be reported.

In **chapter 5**, aqueous dispersion of g-CN will be employed for embedding g-CN nanosheets in aqueous hydrogel materials. Transforming a hydrogel into a ‘hydrophobic hydrogel’ and subsequent network formation which leads to ‘pore substructuring’ under light irradiation will be elucidated in this chapter.

Finally, in **Chapter 6**, I will present visible light induced oxidative photopolymerization via g-CN to attain non-doped oligoEDOT material from 3,4-ethylenedioxythiophene (EDOT). Two reaction pathways based on photocatalyst amount are presented, both leading to a great difference of the resulting materials. g-CN can be separated after reaction and oligoEDOT can be processed and post-doped, alternatively, oligoEDOT is doped with g-CN nanosheets and g-CN nanosheets are coated with oligoEDOT by charge complexation. Furthermore, carbonization of doped oligoEDOT material is performed and evaluated as high sulfur content carbon material.



Scheme 1.1 Versatility of g-CN into various polymer materials that are presented in this thesis.

Chapter 2

Technical Background

This thesis combines two main subjects: organic semiconductor g-CN and polymeric networks. Regarding this, in the present chapter, the fundamentals of g-CN and its possible connections with polymeric materials based on photochemistry will be briefly introduced. It will start with summarizing background of g-CN and continues with general photopolymerization principles followed by recent development of semiconductor integration in polymeric materials.

2.1 Metal-Free Organic Semiconductor: *Graphitic Carbon Nitride*

Graphitic carbon nitride is a member of carbon nitride ‘family (C_xN_y), that is fundamentally set-up by nitrogen and carbon atoms.^{12c} Since the initial discovery by Berzelius in 1830 and later contributions from Liebig in 1834 that eventually led to the first composition and properties of carbon nitride that has attracted great interest from researchers based on its remarkable electronic and mechanical properties.¹⁴ It was defined as high-temperature species, based on formerly occurring intermediates ‘melam’ and ‘melem’ and in further ‘melon’ named according to

deammoniation degrees at different temperatures which leads to the formation of triazine and heptazine(tri-s-triazine) tectonic units-based compounds, respectively (**figure 2.1**).¹⁵ The insoluble yellowish powder product, melon, did not eventuate as the final member of the g-CN family according to extensive research made after the discovery, starting from the early 1920s.^{12c}

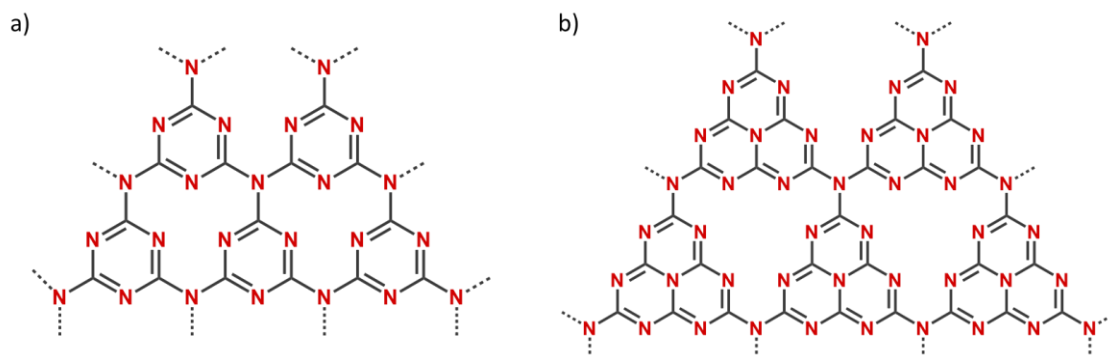


Figure 2.1. Triazine (a) and tri-s-triazine (heptazine) units of g-C₃N₄.

By further thermal treatment, the resulting material called carbonic carbon nitride (C₃N₄)_χ was proposed as the possible final product. Prior to this, a first crystal structure was reported in 1982 by Leonard¹⁶ which laid the foundation for the studies made during the 1990s that successfully revealed a possible single phase of sp³-hybridized C₃N₄ (expressed as β-C₃N₄ which is isostructural with β-Si₃N₄) presumed that exhibiting higher Young's modulus than diamond, conferring high bulk hardness, referred to as even 'tougher than diamond'. Researchers reported seven crystal phases of C₃N₄, including α-C₃N₄, β-C₃N₄, cubic C₃N₄, pseudocubic C₃N₄, g-h-triazine, g-o-triazine, and g-h-heptazine and among all the phases, the most stable solid-state allotrope found as graphitic C₃N₄ (g-C₃N₄) at ambient pressure, derives its name according to the similarity of 2D bond arrangement along with stacking in 3D of graphite.¹⁷ Regarding the applied ambient temperature for synthesis, tri-s-triazine/heptazine tectonic units were deemed to be thermodynamically more stable than triazine units in as-formed g-C₃N₄.^{12a}

The ideal composition is interpreted as carbon and nitrogen atom ratio of 3:4, indicating the stoichiometric composition with no other elements present.¹⁸ This approach asserted

mainly based on conducted nitrogen-rich precursors condensing at elevated temperatures under an inert atmosphere. If the preparative process can be briefly simplified, nitrogen-rich monomer or a mixture of supramolecular form of precursor are placed in a capped crucible for heating.¹⁹ Condensation of precursor of elevated temperature proceeds over recondensation of decomposed gas molecules, which form thermodynamically stable solid substances. By this reason, during the synthesis, the crucible must be capped and kept under the inert gas atmosphere otherwise oxidation and low conversion take place. However, incomplete condensation that leaves small amount of primary or secondary amino groups, so-called 'surface defects', incorporate hydrogen atoms in structure (1-2 wt.%) accordingly. On later researches, other element's presence (i.e., oxygen) originating from employed precursors can be also included. Hydrogen presence directly influenced the crystal structure of g-CN by low crystallinity, thus a relatively high degree of disorder.^{12c, 20} This also stood for high functionality, in other words, rich surface properties in a manner of promoting surface activities as well as increased interaction possibilities with other reactants. Researchers focused heavily on this with the aim of creating more opportunities for photocatalytic applications. So that various fabrication methods to synthesize g-CN with desired structures have established variety of geometries such as nanosheets, 2D films, quantum dots, nano-tubes/spheres/rods and more.²¹

Commonly used nitrogen-rich and earth-abundant precursors such as urea,²² melamine,^{12b} cyanamide,²³ dicyandiamide,²⁴ thiourea,²⁵ guanidinium chloride, and guanidine thiocyanate²⁶ are thermally condensed at different temperatures and various ratios to synthesize g-C₃N₄ (**Figure 2.2**). Considering this, selected precursor/s and the ratio along with corresponding thermal treatment had a distinct influence on such physicochemical properties like porosity, surface area, C/N ratio, absorption edge, and photoluminescence. g-C₃N₄ exhibits thermal stability up to 630 °C then the entire decomposition occurs until 750 °C with zero residues.¹⁸

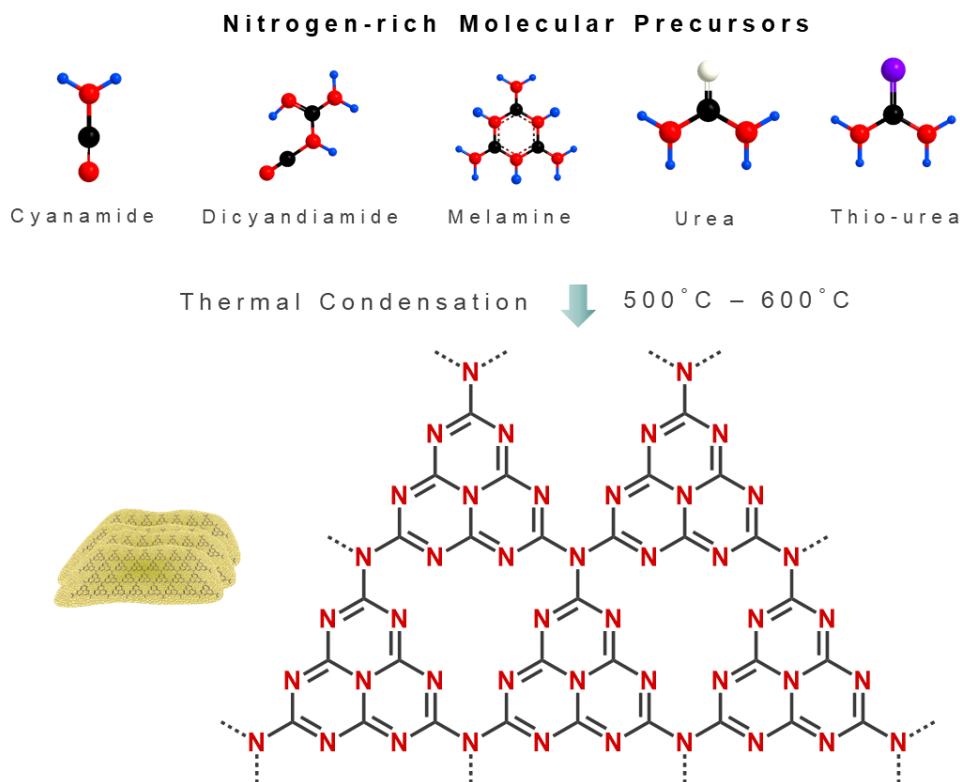


Figure 2.2. Schematic overview of g-CN synthesis via nitrogen-rich precursors.

The ideal composition, so-called ‘defect-free’ g-C₃N₄, is considered to be quite challenging to obtain regarding to expected C/N ratio of 0.75.²⁷ Nevertheless, the closest C/N ratios ranged from 0.721 to 0.742 obtained starting from 500 °C to 580 °C, in which can be considered as another opportunity to tailor the structure.^{12b} Since the synthesis method is a thermal condensation polymerization, it can be described as in the above-mentioned temperature range, polymerization (resulting with the formation of solid g-CN species) occurs over depolymerization via simultaneously formed precursor-derived oligomers.^{19a} Regarding that, condensation or, in other words, polymerization degree, is directly related to applied temperature so that one can synthesize g-CN according to the desired structure such like low molecular weight that can be obtained at low temperatures (e.g. 450 °C).²⁸ Low condensation degree comes with high edge functionality (non-condensed amino groups) and narrow surface area that influence positively hydrophilic and photoluminescence properties unlike photocatalytic efficiency which is lowered by high degree of structural defects.²⁹ As a result of possessing conjugated aromatic

repeating units, g-CN exhibits strong π - π interaction between as-formed nanosheets, which consequently causes insolubility yet low processability in many solvents, like graphite.¹⁸ According to this, the X-ray diffraction (XRD) pattern exhibits two characteristic peaks around 13° and 27° due to intraplanar distance of holes and interplanar stacking that shows non-centered organization with an offset of as-formed heptazine units.³⁰ From this point of view, having abundant edge functionalities such as hydrophilic amino groups, which are prone to give post functionalization, can be advantageous in preparation of aqueous g-CN dispersions.

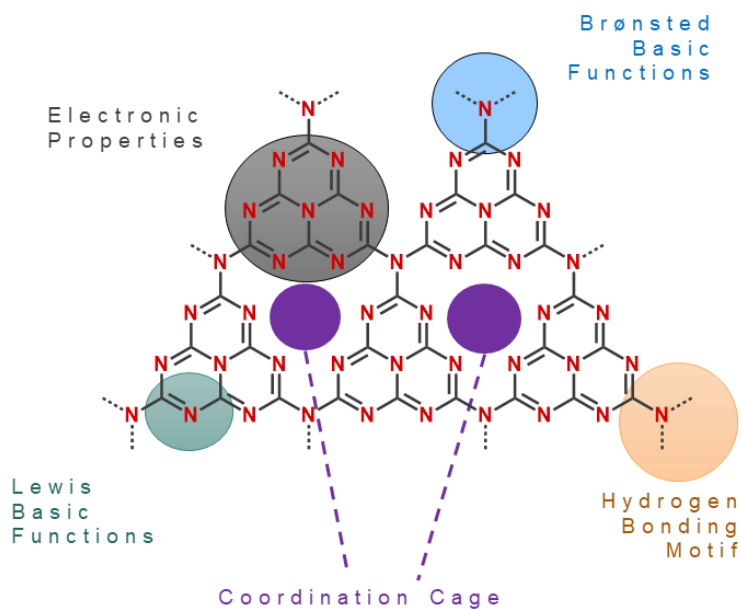


Figure 2.3. Tunable properties of g-CN.

Simply decorating g-CN from edge to edge can also create the possibility of tuning the overall negative surface charge that may help solvent-media based preparative challenges (**Figure 2.3**).³¹ The other main consequence of highly defectuous structure is low surface area, as mentioned above. In this context, using various templating methods that can expand g-CN surface area proved to be quite efficient.³² Especially, hard template method (nanocasting) that allows the growth of g-CN over inert support (hard template, i.e., silica, alumina oxide, carbon NPs) during thermal condensation and further removal of the support to obtain high surface area g-CN replicas, has been established as one of the

compelling method in this regard. Besides hard templating, soft templating technique is also quite effective in increasing surface area.²⁰ In general, block copolymers, ionic liquids and amphiphilic surfactants are considered as soft templates based on the “self-assembly” property occurring between g-CN precursor and soft template. In this way, the process does not lead to g-CN result in certain type of soft template replica, unlike the hard templating method.³³ Despite the fact that of disadvantages regarding template separation in the as-formed structure that also restricts upscaling, hard templates are still commonly applied materials in obtaining high surface area.³⁴

It is widely reported that by manipulating the condensation temperature and synthesis duration, various forms of g-CN can be readily obtained.^{12b, 12c} For instance, as calcination temperature increases in the range of 450 °C-650 °C with melamine as precursors, the resulting pore structure at elevated temperatures became finer and thinner.³⁵ In the case of urea-derived g-C₃N₄, high degree of porosity is obtained in comparison to thiourea and dicyandiamide-derived g-C₃N₄ under the same synthesis conditions, which is further enhanced the resulting photocatalytic efficiency.³⁶

Post and pre-modification techniques are the advanced strategies in synthesizing desired g-CN's. Besides various physicochemical features that can be varied e.g., surface area/charge, porosity, crystallinity, and element ratio, photophysical properties like absorption, quantum yields and fluorescence lifetimes can be tuned based on performed pre- or post modifications. In this regard, grinding g-CN precursors with eutectic salts thereafter thermally condensing the as-prepared mixture (ionothermal process) can result in altered physical (high ordered) as well as enhanced photophysical properties (reduced band gap) such as in K or Na-PHI (potassium or sodium -poly(heptazine imide)) synthesis.³⁷ Utilized salts that are melting during g-CN synthesis brings solvent like environment, whereas metal ion are placed in the pores of as-formed g-CN repeating heptazine imide units. Performing this technique with other eutectic salt mixtures such as LiCl/KCl, LiBr/KCl, and NaCl/KCl also succeeded in advanced charge separation and transformation.³⁸

An alternative way of introducing metal ions to achieve enhanced charge separation through better electrical conductivity was achieved via the ‘doping’ technique.³⁹ Depending on the purpose of application (photo-organic or -electro catalysis), various organometallic complexes and metal-nitrogen-carbon (M–N/C) materials were synthesized by annealing broad range of metals. Especially noble metals were stabilized over g-CN framework quite efficiently in a single atom state, which paved the way for further utilization as single atom catalysts. Most common and successfully conducted metals into g-CN framework are Pt, Au, Ag, Fe, Mn, Ni, Co (either at single-atom/state or coordinated with co-metals). Non-metal doping by initially employing proper elemental sources (elemental sulfur (S₈), citric acid, H₂O₂, H₃PO₄, B₂O₃ or NaB(C₆H₅)₄ corresponding to non-metals S, C, O, P, B, respectively) was associating with various thermal condensation ramps and succeeded in obtaining altered structures compared to conventionally synthesized g-CN frameworks.^{38a, 40}

Another yet highly performed pre-modification technique is acid treatment of traditional nitrogen rich precursors before the thermal calcination. Strong acids like H₂SO₄, HCl or HNO₃ are commonly employed under varied synthesis conditions, resulting in enhanced charge separation and surface areas.⁴¹

Supramolecular assembly is another fabrication methodology to foster advanced g-CNs (**Figure 2.4**).⁴² It relies on intermolecular interactions through hydrogen/halogen bonding or acid-base complexes under equilibrium conditions of the employed monomers and comonomers prepared as mixture in a proper solvent, thereafter dried and then calcined.⁴³ Combination of electron-rich monomers and comonomers giving spontaneous molecular self-assembly is the key factor in obtaining enhanced electronical and optical properties along with higher surface area.^{21g, 44} Employment of diverse monomer increases the possibilities of multi-functional edges that can be further utilized in forming advance g-CN derivatives via post-modification techniques. Most common examples are cyanuric acid/melamine (CM), cyanuric acid/melamine/barbituric acid (CMB) or cyanuric acid/melamine/3-amino-1,2,4-triazole followed by cyanuric acid/melamine/2,4-diamino-

6-phenyl-1,3,5-triazine represents phenyl decoration (more aromatic properties) supramolecular complex assemblies in the literature.⁴⁵

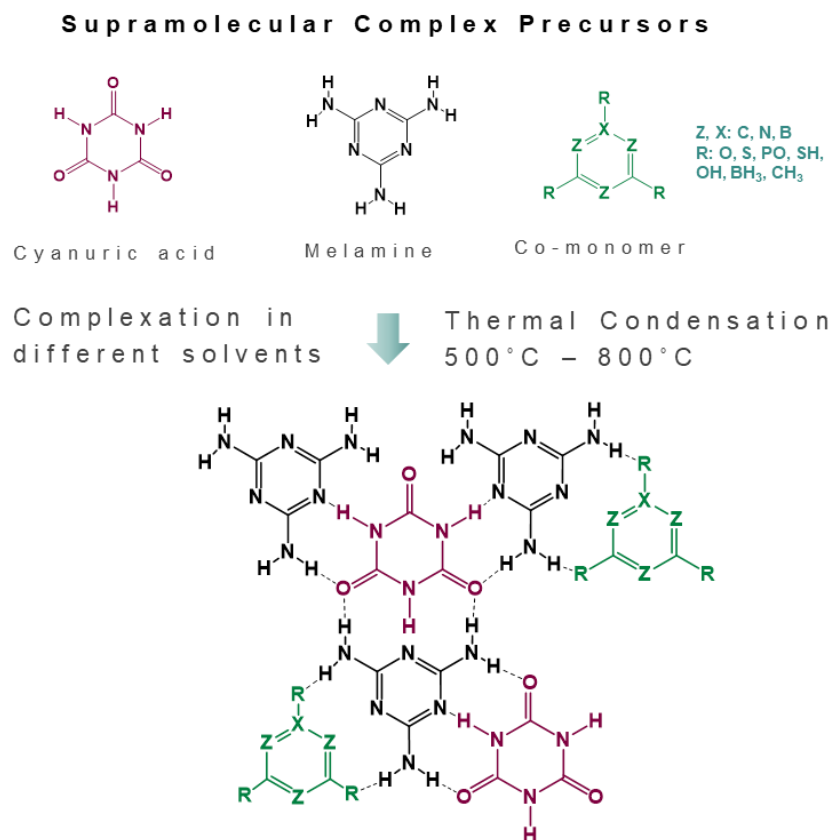


Figure 2.4. Representative scheme of supramolecular structure formation via supramolecular complexation.

All the above-mentioned post or pre-modification techniques are designed to upgrade physicochemical properties and photophysical features. Especially to broaden light absorption range of g-CN through controlling electronic band structure is vital for many photo-based applications. g-CN as semiconductor, forms band gap based on electron transfer from conduction band (CB) to valence band (VB) under proper light irradiation.^{12a, 46} Excited electrons (e^-) occupying CB leave holes (h^+) over VB proceeds in further reduction and oxidation pathways depending on accurate charge separation and hindered recombination.⁴⁷ Photo formed e-h pairs are in charge of further reduction and oxidation pathways. This key feature of g-CN marked its milestone application in water

splitting under visible light illumination by producing gaseous hydrogen and oxygen molecules for the first time.^{12a} In the case of organic molecule interaction (pollutant degradation or organic molecule reaction), excited electrons at CB reducing oxygen molecules (O_2) to superoxide anion radicals ($\bullet O_2^-$) meanwhile photoformed holes producing $\bullet OH$ radicals and H^+ via oxidation of water molecules. These will furtherly contribute to various reactions, that means they also can possibly degrade organic molecules in diverse media. Removal of organic pollutants (organic dyes e.g. RhB, MB, MO or pharmaceutical active compounds e.g. tetracycline hydrochloride-based antibiotics) from wastewaters via adsorption-photo degradation performance of g-CN under accurate light irradiation were successfully achieved based on photo-formed radicals along the paths.⁴⁸ Besides, solar-driven CO_2 reduction via proton coupled electron transfer (PCET) through g-CN also resulted with high efficiency in renewable fuels production (carbon monoxide, methane and methanol).⁴⁹

Photo-formed radicals also could be used for radical photo polymerizations, which means g-CN was utilized as photoinitiator/catalyst in this manner. The first report exhibited methyl methacrylate (MMA) free-radical photopolymerization over mesoporous g-CN via visible light irradiation, then a couple of years later, photochemically controlled atom transfer radical polymerization (ATRP) followed by photoinduced azide-alkyne cycloaddition reaction and photo induced electron/energy transfer (PET) reversible addition-fragmentation chain transfer (RAFT) polymerization were described.⁵⁰ g-CN utilized as heterogeneous photoinitiator together with tertiary amines (triethylamine or/and triethanolamine) that are acting as sacrificial co-initiators by being oxidized via the holes and producing radical cations that initiate polymerization in most of the radical polymerization cases. Copper mediated radical photopolymerizations began with the reduction of copper (II) to copper (I) via excited electrons at CB of g-CN, and the system followed the controlled polymerization steps under accurate light illumination. In a more controlled way of synthesizing polymers via g-CN, certain RAFT agents were associated with excited electrons provided by g-CN, which further led to successful initiation of polymerization, resulting in narrower molecular weight

distributions compared to ATRP. Besides, oxygen tolerance in reaction media came as a beneficial side effect owing to the photo-oxidative properties of g-CN (reduction of dissolved O₂ via electrons).⁵¹

Combining aqueous dispersion of g-CN with water-soluble vinyl monomers and crosslinker, succeeded in the fabrication of various types of hydrogels. As g-CN acts as photoinitiator in the reaction system, it is also further reported that it can act like crosslinker due to charge carrier migration through g-CN nanosheets surfaces. Hence offers covalent bonding with employed vinyl monomers.⁵² Considering this, in-situ photomodification of g-CN nanosheets with various vinyl monomers possessing diverse functionalities (hydroxyl, carboxylic acid, amine, alkyl chain or aromatic) was reported in detail, and the modification process was described as ‘grafting from’ regarding the way of covalent attachment.⁵² Afterwards, bringing g-CN aqueous dispersions into several polymerization techniques such as emulsion and inverse suspension paved the way for creating hybrid g-CN materials.⁵³ Amongst in-situ modified g-CN examples, the most significant one can be considered as the one which is photo-modified with the vinyl thiazole molecule, that inherently endowed organodispersibility to g-CN. This solved the long-term organic media association challenge of g-CN.⁵⁴ This success was followed by the study which showed interfacial stability arising from g-CN nanosheets in a biphasic system that eventuated in the creation of g-CN decorated droplets via liquid-liquid printing technique.⁵⁵

g-CN materials can be synthesized in film form as well, mainly employing CVD to polymerize g-CN precursors on glass surfaces that form high optical quality thin films used for photocatalysis, photografting and photopolymerization.⁵⁶ Moreover, such fabricated uniform thin films took place in solar energy production and energy storage devices such as photovoltaics, light emitting diodes (LED), fuel/solar cells and batteries based on efficient electrochemical (chemical bond energies and extended proton accepting sites) and photochemical properties.^{57 58}

Many substantial photo-based applications have been successfully achieved over g-CN so far (**Figure 2.5**).^{48b, 49a, 59} Ever-growing intention to design new g-CN family members from a multi-disciplinary perspective, will undoubtedly bring many more opportunities to expand their application range and efficiencies in the future.

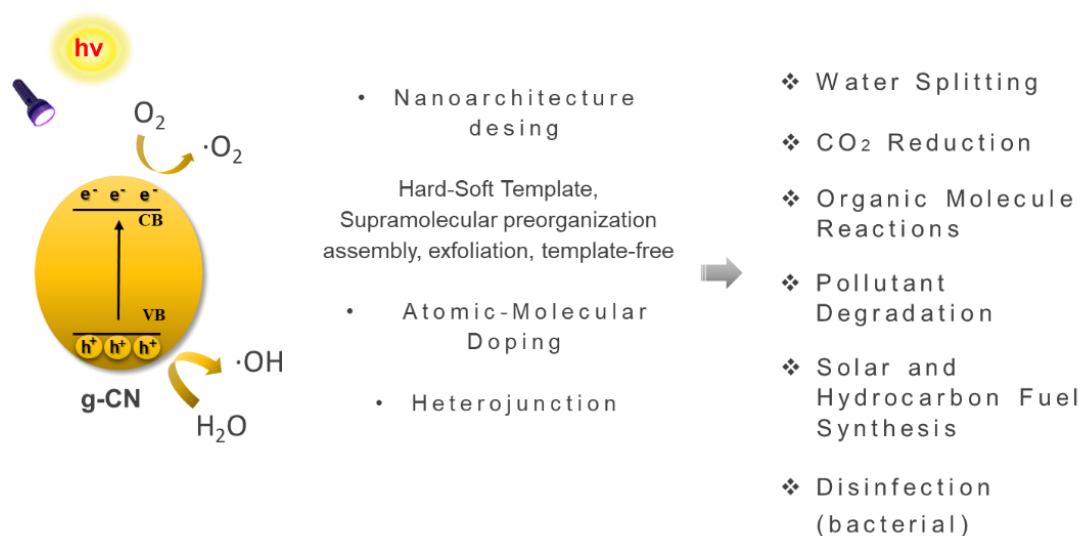


Figure 2.5. Utilization of g-CN in various photo-based applications.

2.2 Photopolymerization: *Photochemical Principles & Polymerization Mechanism*

Photopolymerization consists of the fact that various photochemical reactions take place. Photochemical reaction is a chemical reaction initiated by adsorption of light as a form of energy. In Nature, photoinduced reactions constantly occur in numerous organisms (e.g. plants, algae, cyanobacterias, helicobacterias) that can harvest light and convert it into biomass energy. In the case of learning and simulating from nature to conducting photosynthetic routes such as performing chemical reactions with light or storing chemical energy are worth beyond simple expectations.

Principles

In any chemical reaction, a certain amount of activation energy has to be provided. Considering this, in the range of electromagnetic radiations e.g. infrared radiation (750-2500 nm), visible light (400-750 nm) or ultraviolet (100-400 nm), light would be the source of activation energy in photochemical reactions.⁶⁰ As long as the accurate energy is provided (corresponding of the light wavelength according to Stark-Einstein law, equation 1.1), the absorption of photons by photo-active substance will give a response in the form of altered electronic and vibrational states according to Franck-Condon principle (expresses also Kasha's rule: degree of overlap between their vibrational wavefunctions.) (Figure 2.6).^{60a, 61}

$$\Delta E = E_{\text{excited state}} - E_{\text{ground state}} = h\nu \quad (1.1)$$

h : Planck's constant, ν : light frequency

Absorption of photons by molecule is given by Beer-Lambert law, which describes the relationship between concentration of molecule, distance of light and how strongly the molecule absorbs the light at given wavelength (equation 1.2).⁶²

$$A = \epsilon c l \quad (1.2)$$

A= absorbance, c= concentration (M), l = path length (cm), ϵ = molar extinction coefficient ($\text{L mol}^{-1} \text{cm}^{-1}$)

Gained energy will be promoting ground state (denoted S_0) electrons to higher vibrational energy states (e.g. denoted S_n , where $n>0$) on extremely fast time scales ($\sim 10^{-15}$ s, faster than molecular vibration ($\sim 10^{-12}$ s)). Electronically higher excited level reached by electrons changes chemical and physical properties as a result of altered electron distribution of nuclei in the molecule (e.g. photoacids). After the excitation, a series of cases may occur *i*) vibrational relaxation leading the molecule to a new energy minimum of the excited state *ii*) reaching triplet state by intersystem crossing via spin inversion *iii*) returning to ground state by emitting light (e.g., fluorescence, phosphorescence) *iv*) quenching at the excited state that transfers the energy to another molecule *vi*) the occurrence of a non-radiative transition that brings back the molecule to ground state with no light emission.^{61c, 63}

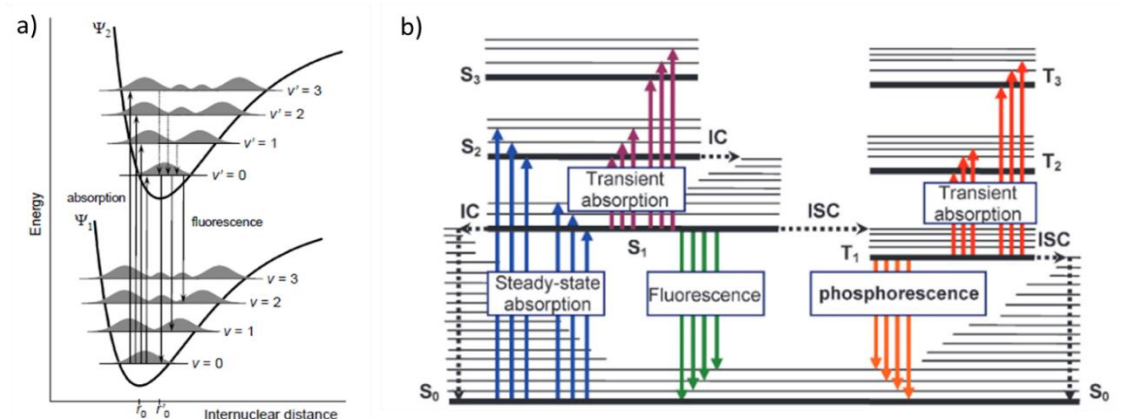


Figure 2.6. Franck-Condon energy diagram (a) ⁶⁴, extended Jablonski diagram with transient absorption displays the time-independent energies for the electronic states of a molecule (b). ⁶⁵

Electronic transitions can be variously employed in special situations, for instance, quenching (-inter/intra) of molecule/s for some photosensitization cases or long-lived singlet state that is beneficial for photoinitiation mechanism in photopolymerizations. There are several types of quenching e.g. physical (energy loss in the form of heat), energy or/and electron transfer (to the introduced second molecule or so-called quencher). The kinetics of quenching in the presence of a quencher can be investigated via Stern-Volmer plot ($1/\text{quantum yield}$ vs concentration of quencher) based on the following equation (equation 1.3).⁶³

$$\frac{I_f^0}{I_f} = 1 + kq \tau_0 [Q] \quad (1.3)$$

I_f^0 : Intensity (without quencher), I_f : intensity (with quencher), kq : quencher rate coefficient
 τ_0 : lifetime of emissive excited state of matter (without quencher), Q : concentration of quencher.

Considering the possibilities of losing or transferring the absorbed energy after excitation, it is advised to evaluate the efficiency of the desired process by the adsorbed photons through *quantum yield* (QY). It simply defines the rate of a particular process as a fraction of all the abovementioned possible pathways of energy loss. In the range of 0-1, the corresponding number indicates certain processes that undergoes whereas the other possibilities are reduced to sum up the total possibility to 1 (quantum efficiency is at

100%) (equation 1.4). In the case of some radiation-induced reactions, quantum yield can be also higher than 1 (hydrogen reaction with chlorine, QY:10⁶).^{63, 66}

$$\Phi = \text{number of events} / \text{number of photons absorbed} \quad (1.4)$$

There are also some cases where the activation energy is not necessarily expected to be overcome to proceed with a photochemical reaction, as long as photosensitization changes the symmetry of the applied molecule and its electronic configuration. This may lead to a further reaction that has been restricted before (e.g., pericyclic 2+2 cycloaddition according to Woodward–Hoffmann selection rules).⁶⁷

There are two main basic laws of photochemistry; *i*) Grotthuss–Draper law, refers that photochemical reaction only occurs when a system is capable of absorbing light, *ii*) Stark–Einstein law (equation 1.5), which indicates the energy absorbed by one mole of reactant to induce the reaction must be higher than the missing energy. Considering this, resulting radicals or free atoms will be responsible of photochemical reactions, and the related photopolymerization techniques which will be discussed in the following section.^{60b, 61c}

$$\Delta E = N h \nu \quad (1.5)$$

h: Planck's constant, *ν*: frequency, *N*: Avogadro's constant

Radical Polymerization Mechanisms

Radical polymerization (mainly 'chain-growth' through free radicals as active centers) is one of the most applied technique in the field of photopolymerization. According to radical polymerization mechanism, initiator induces the reaction in the form of radical, and the following steps such as propagation/chain transfer/termination vary depending on the performed radical system e.g. atom transfer radical (ATRP), nitroxide-mediated radical (NMP), single electron transfer living radical (SET-LRP) and reversible addition–fragmentation chain-transfer (RAFT) polymerizations besides to other controlled radical polymerization (CRP) classes (metal-catalyzed/mediated, trace metal containing and metal-free photo-CRP reaction systems).⁶⁸ Free radical system differs from the rest of the given examples based on continuous propagation initiated radical species that are not

immediately and reversibility consumed in reaction media. So unlike the others, it can not be considered as a “living-controlled” process. In all photo-based polymerization techniques, it is crucial to produce radicals through photoinitiator. For this, abovementioned photochemical principles are applied to design effective photoinitiators. Since radical photopolymerization is already a well-established and highly applied technology in many fields (e.g. curing-coating processes of construction, textile, automotive sectors as well as in creation of 3D printed systems and biomaterial applications), high-performance photoinitiators are synthesized with and successfully applied in many ways.⁶⁹ There are 3 types of photoinitiators well reported so far according to the way of photo-formed radical species over photoinitiators under sufficient light illumination: Norrish type I (homolytic α -cleave leading to two radical fragments of original initiator that contributes to polymerization), Norrish type II (H-abstraction from a synergist, e.g., amines, only the synergist-derived radical contributes in polymerization).⁷⁰ Type II initiators are more favorable in terms of energy consumption due to being active with a broader spectral range (visible light vs. UV light irradiation) however, they exhibit intermolecular radical formation that slows down the reaction which, reduces the efficiency, compared to type I initiators, which are mostly applied in industry. To conclude, photoinitiators are simply the first species expected, which under accurate light irradiation, generate reactive radical species. Thereafter, single-state photoinitiator reacts properly with monomer to induce polymerization, unless instant recombination or non-radiative transition occurs.^{61c, 70a} After the photo-induced initiation producing primary radical species, the following steps that are depicted in **figure 2.7** occur in radical photopolymerization.⁷¹ Chain initiation exhibits an

Chapter 2

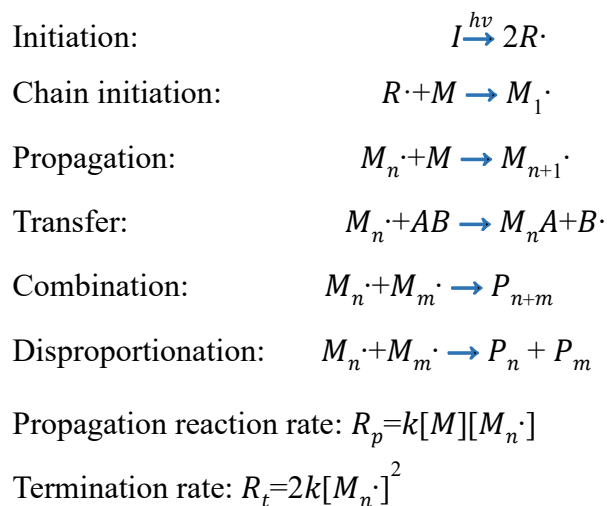


Figure 2.7. Radical photopolymerization mechanism.

attack from spin-paired primary radical to the pi bond of the alkene monomer simultaneously forming a stable bond with one of the pi electrons, whereas the other electron remains loose and turns into a radical. The moment the chain has initiated, it propagates until there are no accessible monomer in reaction media, and radical formation takes places at the end of polymer chain. Propagation consists of chain transfer in parallel as well, where the radical is transferred to another species, which is still considered 'active', meanwhile terminating the initial radical source. The rate of propagation for an idealized case kinetically depends on the formation of radical species over monomers as depicted in **figure 2.7**. Termination also occurs in several ways like combination or disproportionation of as-formed radical species, and the termination rate can be kinetically described as in **figure 2.7** if the molecular weight dependence, polymer uniformity and radical trapping are neglected. As a result of increased chain lengths, eventually increased viscosity influences the radical-monomer interactions, i.e. mass transfer and diffusion of molecules in a restricted environment. By this reason, termination rate can be kinetically depending on growth of chains for some certain systems where the crosslinking ratio is relatively high. Another case that can influence the overall reaction rate, yet monomer conversion too, is the light attenuation on polymerization. If the thickness of ongoing pre-polymer restricts the incident light penetrating through the polymerization media, the propagation rate is directly affected,

as-formed radicals may cause undesired side reactions by attacking to the closest possible functionalities.^{71a, 72} A very wide range of monomers can be utilized in radical photopolymerization, vinyl monomers such as styrene, acrylic acid, (meth) acrylates and acrylamides are most applied ones to fabricate polymers in various compositions (e.g. homo, block, alternating) as well as advanced polymer architectures (e.g. hyperbranched, brushes, stars, cyclic).⁷³

Innovation of photoinitiators can be described as high sensitivity at longer wavelength. Less energy consumption together with longer lifetime at single-state radical are most wanted. In this regard, besides low molecular weight organic photoinitiators that are commonly applied, there are also photoredox catalysts in the form of transition-metal complexes, organic dyes or semiconductors working through the single-electron-transfer (SET) process.⁷² Simply, two types of primary processes describe the pathway of radical photopolymerization: intermolecular photochemical and photoredox processes (**Figure 2.8**). In the former process, fragmentation of initiator based on bond cleavage or energy transfer are the primary steps. In addition, photoredox catalysts are generally considered to be of greater interest to researchers as they are more stable and less toxic, such as a metal-free organic semiconductor g-CN, which is used as a heterogeneous photoredox catalyst based on its effective photoredox potential in many processes.^{74, 75}

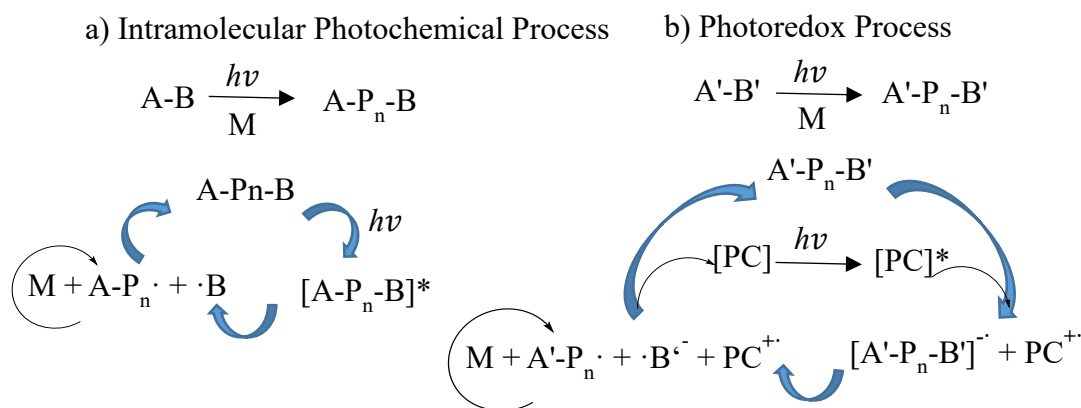


Figure 2.8. Overview of intermolecular photochemical and photoredox mechanisms through photo-radical polymerization.

Chapter 2

Radical photopolymerization became widely applied technique in many fields e.g., in adhesives, coatings, lithography, printing, biomaterials, nanoparticles modification, gel formation, and in advanced high-technology purposes e.g. microelectronics and optoelectronics, holographic data storage, micro/nano stereolithography, and so on.^{72, 76}

Photo-induced radical polymers have been serving the purpose of diverse applications in various complex systems as briefly mentioned in this chapter. Light stimulation has always been quite attractive based on light's abundance, availability, low cost and mild nature.

2.3 Examples of Photocatalyst Incorporated Macroscale Polymer Networks*

In this section, the synthesis and application perspective of various semiconductor incorporated crosslinked macroscale polymer networks will be presented.

Utilization of sunlight to conduct chemistry has been on a stark rise in the era of sustainability. A similar trend is observed in polymer science mainly to initiate polymerization and modify polymer materials, however, mostly relying on the utilization of soluble initiator/activator molecules. Semiconductors, on the other hand, grant a platform for ‘photoredox’ induced chemical initiations so that reductive and oxidative reactions (as well as radical formation) can be tailored according to band positions as discussed in detail in the previous chapter. Despite their utilization as dispersed or dissolved phases, a potential immobilization of semiconductors on macroscale solid surfaces is attractive to entail scale-up options.

Despite the discovery of crosslinked polymer networks and their large-scale utilization long ago, crosslinked polymers keep receiving attention.^{77,78} These materials possess stability against solvents and environmental effects, as well as they exhibit dimensional stability.⁷⁹ A majority of crosslinked polymers can be considered as thermosets. Vulcanization of rubber is a benchmark example for such systems,⁸⁰ or epoxy thermosets that serve as a matrix for aviation composites. From a synthetic point of view, crosslinking can be achieved via covalent and non-covalent crosslinks, and aims to form a linkage between independent polymer chains. Some synthetic examples of covalent crosslinking are i) Carbon-carbon bond formation,⁸¹ ii) carbon-heteroatom bond formation⁸² and iii) various other approaches such as S-S bond⁸³ formation and tertiary amine-halogen quaternization.⁸⁴ It is important to note that some covalent crosslinking can possess dynamic reversibility, as in the case of S-S bonds. Non-covalent crosslinking is in general a ‘reversible’ property, in a way that supramolecular forces-interactions building the network can be influenced.

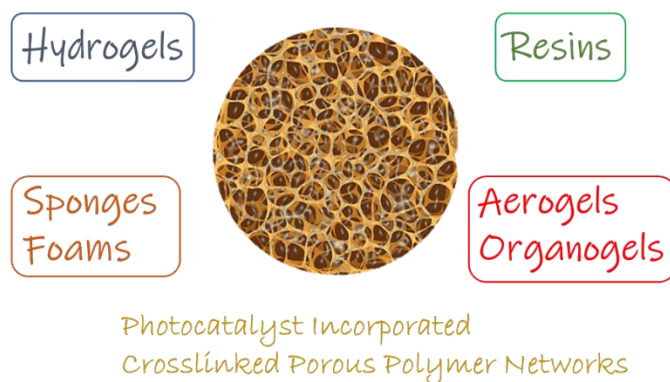
The most prevailing choices to generate supramolecular crosslinking are hydrogen bonding,⁸⁵ electrostatic interactions,⁸⁶ π interactions⁸⁷, and host-guest mechanisms.⁸⁸

Macroscale crosslinked porous polymer networks can be classified by the nature of polymer chains in a way that a library of materials based on aqueous-air nature (i.e. hydrogels,⁸⁹ aerogels⁹⁰), organic nature (i.e. resins,⁹¹ organogels⁹²) and silicon-based nature (i.e. (polydimethylsiloxane)s⁹³) exist. The porosity of aforementioned networks is identified via ‘swelling’ and ‘uptake’ parameters. When utilized for catalytic purposes, accessible porosity and an interlinked channel formation in these networks is a key issue. Potential application of crosslinked porous polymers relies on the nature of the polymer, thermal-mechanical properties and its affinity for solvents. While hydrogels are attractive for tissue engineering⁹⁴ and wound dressing,⁹⁵ organic resins are employed as column fillers⁹⁶ and catalyst supports.⁹⁷ Aerogels and PDMS sponge materials are preferred based on their superior structural and thermal stability.⁹⁸

Natural photosynthesis has been an inspiration to scientists to develop light-driven reactions. Billions of years of evolution optimized working system with active centers, enzymes and membranes to reach unprecedented performances based on converting CO₂ into hydrocarbons and oxygen.⁹⁹ The natural process starts with complicated visible light induced water oxidation to O₂ and 4 electrons-4 protons that are guided by natural membranes for optimized charge separation,¹⁰⁰ which then are consumed in Calvin cycle with CO₂ to form oxygen and hydrocarbons.¹⁰¹ Abovementioned references exceptionally summarize natural photocatalytic reactions in detail. Photocatalytic reactions such as water splitting aim to perform such processes similarly. Semiconductors possess prime importance in daily life as they are mainly employed in electronic devices.¹⁰² On an electron conductivity scale, they lie between conductors and insulators hence their fundamental properties arise from there.¹⁰³ Since the discovery of photoactivity of TiO₂ for water photolysis via photoredox reactions in 1972, the impact of semiconductors in photocatalysis flourished.⁹ Photoredox chemistry in semiconductors differs from other mechanisms (radical initiators etc.) as more complex chemical routes can generate a broad range of possible reactions.^{75a} One of the key parameters for photoactivity is the charge

separation, as e^- and h^+ must be separated to retain activity. There are several well-established strategies to enhance charge separation so far.^{104, 105} Semiconductors can be classified as elements (Si, Ge), inorganic materials (i.e., TiO_2 , CdS, perovskites, InP, ZnO, ZnS, Cu_2O , SnO_2 , $BaTiO_3$), organic material, (i.e., polymeric carbon nitrides, soluble dyes, xanthenes) and precious metal complexes (Ir complexes etc.). When one designs a semiconductor, it is very crucial to elucidate its properties. The synthesis and characterization of semiconductors require a joint input from chemistry and physics. While element and metal-based systems are restricted by means of tunability (one can tune grain size, crystallinity, surface etc.), polymeric carbon nitride stands out as it represents a family of materials.⁴³ Hence, by rational design approach it is possible to tune many parameters such as conductivity, charge separation, crystallinity, porosity, absorption, dispersibility and sheet size.^{44, 106} Some of the most popularized photoredox based applications of semiconductors include water splitting,¹⁰⁷ organic synthesis,¹⁰⁸ photovoltaics,¹⁰⁹ environmental remediation,¹¹⁰ CO_2 photoreduction,¹¹¹ polymer synthesis,^{51, 112} and photoelectrochemical transformations.¹¹³

The potential impact of semiconductors can be addressed via their utilized form, such as being homogeneous or heterogeneous. At a simple glance, heterogeneous catalysis provides the ease of removal and recyclability when compared to homogenous catalysis.¹¹⁴ Furthermore, employing semiconductors in their dispersed (colloidal) state offers novel applications.^{19b} Due to the fact that the previously described semiconductors mainly consist of inorganic crystal and conjugated polymer structures, their utilization lies in the colloidal state. However, on a large scale, using nano or micron-sized powder photocatalysts can bear significant disadvantages, especially in purification that can become energy and time consuming. To tame their colloidal properties, semiconductors have been incorporated into polymer materials to form macroscale photoactive hybrids. In this chapter, I would like to introduce some examples of semiconductors on macroscale crosslinked porous polymer networks span from hydrogels, aerogels-organogels, sponges-foams, and resins (additionally photocatalyst coated glasses,¹¹⁵ clays¹¹⁶, and silica gel beads¹¹⁷).



Scheme 2.1. A sketch of crosslinked polymer network and subjects under the scope of the thesis.

Hydrogels

Hydrogels possess a 3D macroporous structure with a high affinity to water. Polymer chains are hydrophilic; thus, it is possible to afford functional soft materials in the presence of water. Many traditional covalent hydrogels can be prepared via free radical polymerization using the big existing library of hydrophilic vinyl-based monomers and crosslinkers, hence simplicity offers attractive subject to be studied. Despite their massive popularity in tissue engineering or adsorption on an industrial scale, macroscale hydrogels can also be ideal hosts to accommodate photoactive materials to access novel applications. Owing to their hydrophilic nature, hydrogel-based photoactive composites can exhibit unprecedented activities in aqueous applications.¹¹⁸

A representative example for supramolecular hydrogel (SMH) based photocatalyst elucidates fabrication of Ag₂O/Alginate (ALG) SMH films via solution casting process. In this method, Na⁺ in alginate was replaced with Ag⁺ which led to interwoven network formation followed by in-situ transformation of Ag⁺ into Ag₂O after irradiation in water. By this way, Ag₂O is successfully maintained in as-prepared composite films thanks to both ALG, which accommodates photo-formed holes, and O₂ that captures photo-formed electrons generated via Ag₂O under light irradiation. Regarding this, photoactivity of Ag₂O/ALG SMH composite films were investigated by methylene blue (MB) and

malachite green (MG) dyes photodegradation experiments, and in conclusion all results showed quite high activities (above 93% for both dyes under either UV or visible light irradiation).¹¹⁹

TiO₂/agarose hybrid gel photocatalyst was prepared via simple gelation of an agarose gel with uniformly dispersed TiO₂ NPs in hot water. This thermal construction method is followed by a cooling step and fractionation of hybrid gel in capsule form as a final step. The overall process has shown very effective encapsulation of TiO₂ NPs as well as recovery via simple separation from the matrix. Excellent recovery of TiO₂ NPs in monolithic hybrid gel resulted in enhanced photodegradation of MB dye and its degradation rate was investigated by varied concentration, size, and uniformity of the hybrid gel.¹²⁰ An alternative to immobilization of TiO₂ NPs in the hydrogel network was also achieved via embedding technique. Two hydrogel supports based on poly (methyl acrylate) (PMA) and succinamic acid (SAA) combined with TiO₂ NPs during the gelation step and resulting composite hydrogel-TiO₂ samples exhibited preferable photodegradation for four organic dyes (MO, methylene blue, RhB, and bright green) under UV light irradiation, in addition to promising H₂ generation that can be improved by optimizing sample transparency in order to harvest more incident light (**Figure 2.9a**).¹²¹ Design strategy by using nanoparticles highly rely on colloidal dispersions and colloidal stabilities, as sedimentation of particles cause lowered photoactivities despite having high solid contents.

Metal-free semiconductor graphitic carbon nitride has recently been a popular choice for hydrogel matrices. As g-CN is a conjugated sheet-like semiconductor; mechanical reinforcements in hybrid hydrogels compared to pristine ones were the focus of some studies however, we will stress photoactive hydrogel composites here. In one study, three-dimensional g-CN based self-standing hydrogels were fabricated via photopolymerization in plastic syringes, where g-CN can be employed as a colloidal photoinitiator. The as-obtained hybrid hydrogel photocatalysts were immersed in a mixture of various cationic and ionic dyes to prove the selective adsorption properties of as-synthesized hybrid hydrogels over counter-ion attraction (best result was obtained via methylene blue, and

the rest of employed dyes were congo red, crystal violet, methyl orange, rhodamine B). In further, a set of dye-absorbed hydrogels exhibited enhanced dye photodegradation under visible light illumination. Furthermore, the authors demonstrated the potential of photocatalytic hydrogen generation from water under visible light by designing a tube-like model hydrogel in order to tackle thickness issues (**Figure 2.9b**).¹²² Photoactivity of hydrogel can also be harnessed to form a double network-like system. The stability of g-CN in monomer-crosslinker aqueous dispersion systems diminishes upon the addition of charged monomers, thus restricting admission to functional systems. To overcome this, g-CN based prepolymer was synthesized (g-CN dispersion in water; ethylene glycol: monomer followed by irradiation under continuous stirring), which possesses high viscosity yet improved colloidal stability against charged molecules. For the formation of a secondary network, g-CN based prepolymer was mixed with an anionic monomer (3-sulfopropyl methacrylate potassium salt) in the presence of water and crosslinker, and visible light irradiation creates a double interpenetrating network-like polymer that has cartilage-like toughness and lubricity.¹²³ In these studies, once again stable colloidal dispersions are key enablers for successful immobilization of semiconductors, additionally photoactivity of semiconductor was harnessed to form hydrogel network in initial stage.

To switch from bulk systems to heterophase polymerization, g-CN incorporated macrohydrogel beads were synthesized via inverse suspension photopolymerization technique, in which water dispersible g-CN was employed in aqueous phase with ethylene glycol and water-soluble acrylamide monomer in continuous oil phase prepared by cyclohexane and various amount of crosslinkers (acrylamide based). In this heterophase polymerization, g-CN was utilized as photoinitiator in fabricating hybrid macrogels in various sizes (from 30 μm to 4 mm) that can be tuned via parameters such as crosslinker ratio and agitation speed. The photoactivity of hybrid hydrogel beads were elucidated via RhB photodegradation as well as hydrogen generation under visible light, with good recyclability and reliability, unlike powder g-CN (**Figure 2.9c**).⁵³ However, obtaining a

perfect bead shape was not possible as structural deformations took place during polymerization.

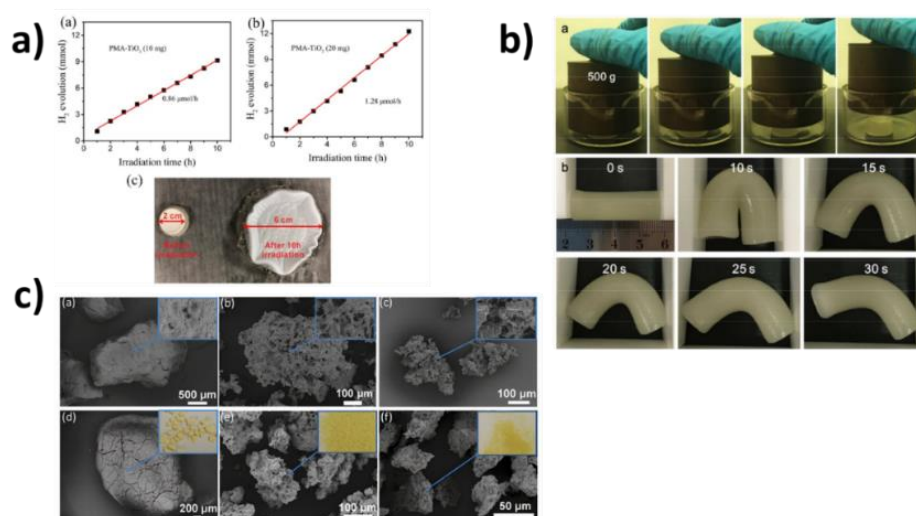


Figure 2.9. a) Photocatalytic hydrogen production from water using TiO₂ containing hydrogels with varied TiO₂ amounts (TiO₂ amount doubled on right curve) and the digital image of photoactive hydrogel before and after photocatalytic reaction,¹²¹ b) Digital images of photoactive hydrogel cylinder against 500 g load (top) and tubular photoactive hydrogel against compression and its recovery (bottom),¹²² c) SEM images of photoactive porous hydrogel beads (with varied g-CN content and crosslinker amount) obtained via inverse suspension polymerization.⁵³

Synthetic conditions might be altered by embedding g-CN nanosheets during hydrogelation, and in further can lead to create ‘hydrophobic hydrogel’ as well as allow to modify morphology via ‘pore substructuring’, as explained in the 5th chapter of this thesis.¹²⁴

CO₂ can help forming porosity on the macroscale, as shown in the fabrication of g-CN-immobilized alginate porous gel beads. Aqueous dispersions of g-CN nanosheets (CNNSs) were mixed with sodium alginate (NaAlg) solution containing sodium dodecyl sulfate (SDS) and sodium bicarbonate (NaHCO₃) under agitation until a foamy solution was obtained. Thereafter, the as-prepared solution was treated with calcium chloride/acetic acid (CaCl₂/CH₃COOH) solution by dripping via an automated syringe. This process solidifies droplets on the interface and builds interconnected porosity inside (CO₂ released from the reaction between CH₃COOH and NaHCO₃) (**Figure 2.10a**).

Interconnected macroporosity with accessible semiconductor sides enabled RhB photodegradation activities.¹²⁵

The heterojunction of g-CN with silver halide in a water-permeable cross-linked CMC (carboxy methyl cellulose) matrix showed remarkable photocatalytic performance in regards to RhB dye photodegradation (60 min, 74% efficiency). Photoactive CMC based hydrogels prepared by addition of AlCl_3 or FeCl_3 ($\text{Ag}/\text{AgCl}@/\text{Al}-\text{CMC}$ and $\text{AgCl}@/\text{Fe}-\text{CMC}$, respectively) to entrap AgCl formation during interconnected cross-linking. The overall benefit of silver species in photocatalytic applications, especially zero-valent silver that significantly reduces electron-hole recombination rate, worked quite effectively after a successful combination with Fe^{3+} that acts as electron trapping sites in the CMC network. As a result, both $\text{Ag}/\text{AgCl}@/\text{Al}-\text{CMC}$ and $\text{AgCl}@/\text{Fe}-\text{CMC}$ hybrid samples exhibited remarkable photocatalytic performance under visible light irradiation (98% and 87% of RhB dye removal efficiency in 60 min, respectively).¹²⁶

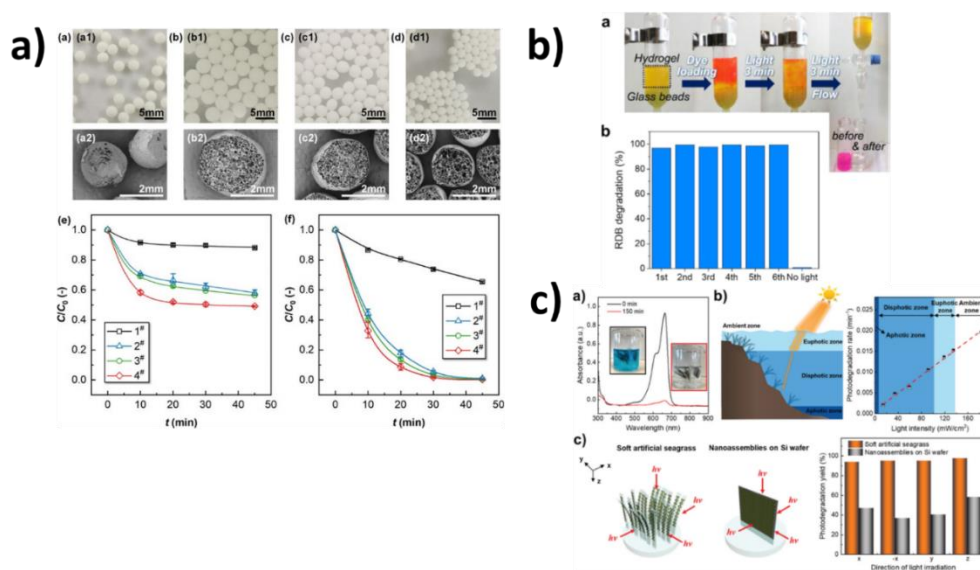


Figure 2.10. a) Digital images and SEM images of g-CN based photoactive CO_2 -induced porous hydrogels synthesized via tunable parameters and their influence on photocatalytic RhB degradation,¹²⁵ b) Digital images of photoactive hydrogel beads in the column for RhB photodegradation as well as recyclability data,¹²⁹ c) Photoactive hydrogel composite in dye removal and the influence of light intensity and direction on photocatalytic reaction inspired by natural seagrass.¹³⁶

Sulfide-based semiconductors are often employed in hydrogel systems as well. In the first example, hydrogel matrix was produced by Co- γ radiation-induced copolymerization, and CuS loading was performed via an in-situ precipitation method which successfully gave a hybrid hydrogel photocatalyst (p(HEA/NMMA)-CuS). In the following, the resulting novel photocatalyst was used in adsorption and degradation of Sulfamethoxazole (SMX) in aqueous solution. Briefly, sulfonamide antibiotics (SAs) are commonly known for their difficult degradation, and these aqueous micropollutants pose a danger to society by causing resistivity against drugs. SMX is a compound that is often found in water resources and therefore was chosen to be employed as a model compound in photocatalytic investigations. Regarding the photocatalytic degradation process, the hybrid hydrogel adsorbed SMX molecules which enhanced physical contact with CuS under visible light irradiation. Total photodegradation of SMX molecules down to water and CO₂ was based on photogenerated electrons and holes formed after exciting CuS nanoparticles (OH⁻ and the H₂O molecules generated hydroxyl radicals via oxidation thereafter holes and •OH radicals attack SMX molecules). According to the results, p(HEA/NMMA)-CuS photocatalyst hydrogel degraded SMX in an aqueous solution under visible light within 24 h at 95.91% removal as well as reaching 43.56% of mineralized SMX. Theoretical calculations of frontier electron densities (FEDs) regarding possible degradation routes of SMX intermediates were also presented and discussed.¹²⁷

In the second example, almost the same preparation route was followed to synthesize hydrogel via Co- γ radiation-induced copolymerization then in-situ precipitation method for loading CdS nanoparticles, resulted as photoactive composite named P(HEA-co-HAM)-CdS. This was employed for the removal of bisphenol A (BPA). Results of BPA adsorption from aqueous solution and in-situ photocatalytic degradation under visible light irradiation were successful as the adsorption capacity of P(HEA-co-HAM)-CdS hydrogel was higher than the similar base of adsorbents (11.26 mg/g), and BPA degradation and mineralization rates reaching 92% and 47% within 3 h, respectively. Degradation pathways were discussed both theoretically and experimentally.¹²⁸

It is crucial to retain hydrophilicity in order to maximize semiconductor contact in aqueous media. Considering this, a translucent conjugated polymer hydrogel photocatalyst (P-BT-GX), possessing anionic as well as cationic sides (therefore also named as conjugated polyelectrolyte) prepared by a successful complexation of a photoactive polycation and various amounts of polyacrylic acid (polyanion). This voluminous water-compatible photocatalyst (deionized water absorption up to 470 times of its weight) exhibited enhanced RhB dye degradation and formation of the enzyme cofactor nicotinamide adenine dinucleotide (NAD^+) via photo-oxidation in water, under adequate visible light irradiation (**Figure 2.10b**). NADH photo-oxidation was described in detail by starting with cationic radical ($\text{NADH}^{\bullet+}$) formation via photogenerated holes from P-BT-GX, which further transformed into NAD^+ via superoxide radical (formed from molecular oxygen quenched with photogenerated electrons). Accumulation of perhydroxyl radicals as side products led to the generation of peroxide molecules that can form hydroxyl radicals, and those hydroxyl radicals captured a proton from $\text{NADH}^{\bullet+}$ that of involved oxidation of NAD^+ . In addition, a facile solvent exchange method was presented that exhibited profitable regeneration of as-prepared hydrogel photocatalyst.¹²⁹

In another example with a polyelectrolyte (PE) hydrogel as photocatalyst matrix, chromophore amphiphile (CA) photocatalyst was integrated via self-assembly based on both electrostatic interactions and physical entrapment. The pre-synthesized PE covalent hydrogel (via free radical polymerization) as host platform, combined with monomeric perylene monoimide (PMI) CA, led to their successful self-assembly via solvent exchange method from organic to water. Obtained hybrid hydrogels demonstrated noticeable photocatalytic hydrogen production, good reusability with enhanced mechanical strength and partial retention of CA assemblies (ribbon-like nanostructures obtained via Coarse-grain molecular dynamics simulations) even after thorough washing process (retention was expected from a system where the assemblies are not covalently attached to hydrogel network).¹³⁰

As we have briefly referred the importance of light accessibility in photo-based applications, a recent study showed the remarkable impact of highly transparent matrix

obtained via DMAA based hydrogel which is further cross-linked with benzothiadiazole and employed in photo-oxidation of glyphosate (N-(phosphonomethyl)glycine), RhB dye, organic sulfurs and the photoreduction of Cr^{VI}. The overall results were all successful, clearly highlighting the importance of light penetration into the hydrogel matrix to maximize light-semiconductor contact.¹³¹

Hydrophobic association hydrogels (HyA) are the type of hydrogel that are built on hydrophobic interactions. This physical crosslinking intrinsically endowed high mechanical as well as effective self-healing properties to the final material. In this particular study, TiO₂ nanoparticles associated as both photo-initiator and physical cross-linking points in fabrication of TiO₂/HyA-n hydrogels through in-situ radical polymerization. By this strategy, remarkable mechanical behavior (tensile strength of 306 kPa, compressive strength of 2.17 MPa) as well as advantageous anti-fatigue property and excellent photocatalytic activity (MB photodegradation rate 96.63%) were obtained from a tough hybrid photoactive hydrogel.

Microporous polymers with a highly crosslinked 3D network are promising candidates as reinforcing agents in a certain types of wastewater treatments. They simply provide high surface area along with low density by tunable chemical feature relying on employed monomer type that creates the skeleton of the polymeric structure. Regarding this, photoactive conjugated microporous polymer (CMP)-hydrogel composites possessing benzothiadiazole (as photoactive species) were synthesized via chemical modification of CMP particles (via acrylic groups) followed by crosslinking that forms polyacrylamide network as hydrogel which simultaneously incorporates CMP particles to the hydrogel covalently. Results exhibited enhanced elasticity by means of mechanical performance, and methylene blue dye removal from aqueous solution by photodegradation under UV irradiation (2.6 times higher than polyacrylamide hydrogel with no photocatalyst incorporation).¹³²

Removal of organic contaminants from wastewaters is a complex task when powderous photocatalysts are used, mainly due to separation problems. Hydrophilic hydrogels

endowed with photoactivity can offer improved performances and stability. Two significant examples combined microfluidics technique to form photocatalyst encapsulated polymer particles as alternative to slurries or fixed batch reactors. Furthermore, reliable high throughput production technologies were demonstrated. In the first example, a mixture of acrylate-derived monomers (HEMA, AA, EGDMA), crosslinker (DMPA), and dispersion of TiO₂ nanoparticles (5–15 nm anatase) were prepared in aqueous media. After radical initiator addition, a hydrogel–TiO₂ composite was obtained via photopolymerization in a PDMS mold designed in the size and shape of a micro reactor (via a 2-step soft lithography process). The resulting hydrogel scaffolds were tunable despite ionic strength (AA volume fraction) and pore size, and were capable of transmitting incident visible as well as ultraviolet (UV) light. They showed remarkable permeability of MB and its further photodegradation under UV light irradiation. Additionally, photocatalytic hydrogel reactor was examined in norfloxacin (type of pharmaceutical that can be detected in wastewaters and has a similar photodegradation behavior with MB) removal, in a channel with a continuous flow of water. Related results exhibited that the despite of the lower photodegradation rate of norfloxacin compared to MB, the composite hydrogel shows promising data as photoactive microreactor, e.g., it possessed better transport.¹³³ In the second example, TiO₂ and ZnO nanoparticles encapsulated in poly(methacrylic acid) based hydrogel, termed as photocatalyst-in-capsule (PIC), via complex water-in-oil-in-water double emulsions produced by glass capillary microfluidic device. The fabrication starts with photopolymerization of methacrylic anhydride (MAN) and ethylene glycol dimethacrylate (EGDMA) that results in poly(anhydride) structure in the shell, whereas aqueous dispersion of photocatalyst is located at the core. Photopolymerization and further hydrolysis yield poly(methacrylic acid) hydrogel photoactive microcapsules, successfully. According to the results, photocatalytic nanoparticles in a thin shell hydrogel microcapsule photodegraded MB dye quite effectively based on adsorption–oxidation mechanism that is comparable to powder photocatalysis. The flow reactor filled with hydrogel microcapsule showed effective water purification performance as well.¹³⁴

Reduced graphene hydrogels (rGH) were demonstrated to be a suitable platform for quantum dots (QDs) decoration. In this study, QDs self-decorated BiVO₄ NPs structure were coupled to rGH hydrogel by an in situ growth method. The obtained highly porous rGH network showed well distributed of BiVO₄ NPs yet QDs on both sides of the rGH sheets. The fabricated composite succeeded tetracycline hydrochloride (TC.HCl) photodegradation via visible light irradiation, thanks to the highly effective photoinduced charge carrier separation achieved by rapid migration of electrons to the rGH surface. The composite also exhibited significant stability and reusability up to 4 cycles with no structural change. In conclusion, this quantum dots self-decoration over graphene hydrogel network approach has proven once again the advantage of hydrogel structure as a support platform to enhance photocatalytic efficiency.¹³⁵ Despite the benefits of having graphene as electron acceptor in hydrogel systems, increased graphene amount would significantly lower light absorption of the photoactive moieties.

Being inspired by the nature, especially on the subject of photo-based applications referred in this thesis, can pave the way of novel material design (**Figure 2.10c**) Sea-grass-like structures were fabricated firstly by constructing monodisperse Au–Pd–CdS multifunctional nanohexagons (mNHs) (via seed-mediated method using gold nanohexagons (Au NHs) as seeds), followed by polyvinylpyrrolidone (PVP) modification and casting on aluminum for nanoassembly. Drop-casting 1% agarose aqueous solution and heating leads to gelation after removal of the aluminum foil which gives a free-standing nanoassembly-based photoactive composite. Regarding the concept, plasmonic nanoparticles (gold nanohexagons (NHs)) possessed corner-specific deposition of Pd nanoparticles meanwhile, semiconductor (CdS nanoparticles) integration takes place over the surfaces. Hydrogel hybrids showed high photocatalytic performance on methylene blue (MB) photodegradation by omnidirectional light-harvesting under low-intensity sunlight irradiation as it was aimed to mimic natural sea grasses. In the study, it was stressed that fabricated sea-grass-like material had superior recycling and flexibility and did not require photocatalyst regeneration which means it is fully capable to be run in continuous photocatalytic operations.¹³⁶

Another example for the solvothermal method shows the combination of carboxymethyl cellulose & poly(β -cyclodextrin) hydrogel support with photoactive metal organic frameworks (MIL-101(Fe)) (CMC/MIL-101(Fe)/ β -CDP). β -CDP as a host material features a hydrophilic surface with hydrophobic cavities where in MIL-101(Fe) is accommodated, and the final composite with CMC significantly enhanced the selective oxidation of tetracycline under visible light illumination due to lower electron/hole recombination supported by β -CDP as promoter matrix.¹³⁷

Aerogels-Organogels

Thermal insulation and mechanical features primarily define aerogel materials. In general, aerogels are fabricated via solvent removal process from hydro/organogel networks. Organogel formation is a supramolecular process that relies on convenient gelator agents in organic solvents. These networks as host materials for semiconductors can offer many features such as interconnected large surface areas, ease of recyclability and mechanical stability.¹³⁸ A self-supported macroscopic carbon nitride (CN) aerogel was fabricated via aqueous sol-gel technique which requires neither external cross-linking agent nor strong acid treatment unlike traditional methods. Principles of colloid chemistry were entailed in this approach, so that self-assembly of low-density CN nanoparticles (LD CN NPs) in aqueous media first formed a hydrogel, that was subsequently transformed into a pure CN aerogel by freeze drying (**Figure 2.11a**). The resulting photoactive three-dimensional monolithic aerogel network exhibited enhanced hydrogen evolution and H₂O₂ production under visible light comparable to bulk CN, mainly due to introduced functional groups, high internal surface area, increased carrier conduction, as well as improved physical properties.¹³⁹ However, structural stability is low. In another study, a polysulfone-alginate matrix (PSF 10:6 Alg) was converted into visible light responsive composite beads (PATAg, o.d.~3 mm) via successful immobilization of TiO₂/Ag₃PO₄ (10:1, 12 wt.%) semiconductor nanocomposite via assembly. The resulting PATAg beads possessing interconnected macrovoids (more dominant) led by PSF at the backbone and micropores via Alg have shown unique adhesion of catalyst in addition to high adsorption capacity and buoyancy-suspension interconversion. As a proof of concept,

photodegradation of waste-water pollutants (methylene blue) and pharmaceutical contaminants (diclofenac and triclosan) in suspended form, as well as water disinfection (bacterial inactivation) and biofilm retardation (decomposition of acyl-homoserine lactones) under visible light irradiation, noted the photocatalytic activity of hybrid PATAg beads.¹⁴⁰ Alternatively, upgrading mechanical properties of nanoparticle-based aerogels via introducing 3D printed polymeric scaffolds for gas phase reactions is a further example that reveals aerogels versatility. A 3D printed resin scaffold was treated with TiO₂-Pd dispersion followed by solvent exchange and supercritical drying to obtain the final photoactive aerogel.

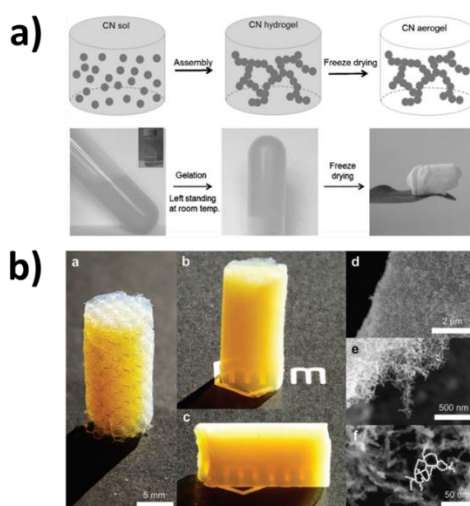


Figure 2.11. a) Schematic description and digital images of g-CN based aerogel synthesis,¹³⁸ b) Digital images and SEM images of 3D-printed photocatalytic aerogels.¹⁴¹

3D printing allows precise control on channel structure to optimize gas flow-photocatalyst contact to boost the photocatalytic activity while minimizing waste (**Figure 2.11b**). Consolidating the hierarchical architecture of aerogel with tunable polymeric scaffolds allowed TiO₂-Pd based photocatalytic aerogels to be highly efficient in reforming methanol for H₂ production through a gas flow reactor under UV light illumination.¹⁴¹ However, transparency is hindered, which restricts light penetration and prevents the full potential of the 3D printed photoactive aerogel. On macro or/and larger scales, supramolecular gels combined with semiconductors have shown immense impact on photo-based applications. Their reversible nature based on assembly-disassembly

equilibria via non-covalent interactions (hydrogen bonding, a pi–pi stacking, donor–acceptor interactions, metal coordination, hydrophobic forces, van der Waals interactions) allows further reactions in confined spaces which plays a key role in tuning photocatalytic activity of the desired materials.¹⁴² Low molecular weight compounds (LMWCs) formed through self-aggregation of small gelator molecules result in entangled Self-Assembled Fibrillar Networks (SAFINs) and photon upconversion based on triplet-triplet annihilation (TTA-UC) technique was observed once they are successfully integrated with semiconductors. A good example is prepared from transparent bile-organogelator (derived from dimeric urea) integrated with luminescent CdSe quantum dots (QDs), showing well-defined QD array in resulting hybrid-SAFIN network formed via supramolecular assembly.¹⁴³ Moreover, QD doped SAFIN exhibited thermoreversible luminescence based on enhanced rigidification of QD over the network, however, the authors did not perform photocatalysis in this project.

Sponges-Foams

When 'sponge' or 'sponge-like' materials are mentioned in materials science, polydimethylsiloxane (PDMS) based ones are by far one of the most studied. Different than foams (fabricated by blowing agents leading to generation of gaseous molecules creating bubbles), silicone-based sponges are mainly synthesized via two techniques; the 'open-cell method', which leads to interconnected porosity or 'closed-cell method' that creates isolated cells throughout the structure. Either way, the obtained 3D stochastic cellular scaffolds exhibiting hierarchical porosity withdrew attention in photocatalysis, especially given the fact that of enhanced binding-sites for an efficient mass transfer throughout the sponge channels. Various methods in fabrication of PDMS-photocatalysts have been reported so far, and in a recently published review three most common techniques were briefly summarized as; i) incorporation of photocatalysts into liquid PDMS monomer before curing, ii) depositing photocatalyst particles onto cured PDMS thermoset support, iii) coating photocatalysts with PDMS. Besides providing the opportunity to be fabricated in various ways, PDMS sponge as host material inherently brings some relevant advantages in photocatalytic applications, e.g., I) super hydrophobic

properties, which are quite substantial in attracting organic pollutants that can support photocatalytic efficiency, II) transparency that facilitates accessibility of light, III) robustness and chemical resistivity which in return boosts photocatalyst recyclability, IV) facile preparation methods at low cost.¹⁴⁴

A prominent example of PDMS supported photocatalyst, $\text{TiO}_2\text{-SiO}_2\text{@PDMS}$ hybrid prepared via sol-gel process (silica&titanium gel first functionalized with hexamethyldisilazane then dispersed in PDMS/ CHCl_3 followed by curing), has shown efficient photocatalytic activity for methylene blue photodegradation performed in both aqueous dye solution and MB dyed films. Besides, hybrid photocatalytic powder exhibited superhydrophobicity (water contact angle (WCA) $<5^\circ$) and good thermal stability (470 °C).¹⁴⁵ In another work, a PDMS sponge (prepared via conventional sugar template method) was dipped into hydrocarbon/ TiO_2 nanoparticle solution (prepared in isopropyl alcohol), sonicated and dried for successful coating, hence resulting nano-sponge/porous polydimethylsiloxane (NS/p-PDMS) composite exhibiting UV-induced wetting transitions. The superhydrophobic nature arise from hydrocarbon functionalities on NS/p-PDMS as well as PDMS structure itself and leads to selective oil absorption in aqueous media. This also showed remarkable air bubble-driven desorption mechanism under UV light irradiation. This photo-responsive behavior over oil absorption/desorption proves the versatility of fabricated NS/p-PDMS hybrid photocatalyst.¹⁴⁶ Another article features a composite $\text{TiO}_2\text{-PDMS}$ sponge fabricated via hexamethyldisilazane (HMDS) functionalized TiO_2 NPs insertion on as-prepared PDMS sponge (sugar templating method) at various ratios and demonstrated not only high adsorption against Rhodamine B dye ($\text{TiO}_2\text{-PDMS}$ sponge is embedded in dye solution) but also exhibited high efficiency in photo degradation of adsorbed dye molecules via solar light irradiation. Embodying hydrophobic $-\text{CH}_3$ groups over TiO_2 NPs clearly enhanced the interaction between PDMS matrix as well as increased the attraction of organic dye molecules for a higher photodegradation rate.¹⁴⁷

For an improved photocatalytic activity, the PDMS- TiO_2 sponge is treated with Au NPs solution ($\text{HAuCl}_4 \cdot 3\text{H}_2\text{O}$ in anhydrous EtOH) by insertion followed by a drying process

(60°C-6h) to obtain PDMS–TiO₂–Au composite sponge. Host PDMS-TiO₂ network was obtained via slightly modified sugar cube templating to allow maximized access of Au NPs on TiO₂ rich interface. This strategy led to create a highly effective, porous plasmonic, flow photocatalyst thanks to localized surface plasmon resonance (LSPR) effect arising from Au NPs under visible light irradiation (red shifted in comparison to PDMS–Au sponge).¹⁴⁸ In another example, referring surfactant wrapping sol–gel method for the fabrication of multiple-walled carbon nanotubes/titanium dioxide (MWCNTs/TiO₂) nanocomposite on PDMS via needle-based micro-fluidic device was reported. The resulting PDMS–MWCNTs/TiO₂ micro droplets (oil-in-water single emulsion template method) transformed into microparticles after thermal curing and showed strong synergetic effect for azo-type dye sorption and degradation under UV light illumination. In this way, the advantage of immobilized TiO₂ NPs over CNTs substrate that acts as electron acceptor paved the way to a higher photocatalytic activity compared to solo performance of TiO₂ NPs. In addition, the microfluidic system inherently provides more control over droplet formations and a lower consumption of reactants.¹⁴⁹

The benefits of TiO₂ NPs in photo-based applications certainly set forward the design of photo active hybrid and composite materials. However, when TiO₂ abundancy and toxicity is considered, various semiconductors can substitute in, such as ZnO. As an example, PDMS/ZnO composite sponge synthesized via sugar templating method (kneaded sugar particles mixed with different concentration of ZnO, immersed in PDMS prepolymer, cured and purified from sugar, respectively) resulted in 3D interconnected photoactive macroporous network. ZnO particles on PDMS matrix demonstrated excellent MB dye photo degradation under various light sources (UV, visible and UV-visible). Strong adhesion of incorporated ZnO particles on the PDMS substrate was cross-checked via a filtration method to prosecute leached amount of ZnO after the sugar dissolution step.¹⁵⁰ As an alternative to ZnO, ultrathin carbon nitride nanosheets (prepared via thermal condensation of melamine) decorated on PDMS sponge via injection also showed high photo catalytic activity according to the performed RhB dye photodegradation results (PDMS sponge synthesized via sugar template method, injected

with CN nanosheets dispersion, as-prepared composite annealed at 200 °C for 2 h). Moreover, the photocatalyst composite exhibited selective absorption against various oils, self-cleaning (**Figure 2.12a**), separation of oil-in-water emulsion in bi-phasic systems, and facile recyclability.¹⁵¹ However, there was no investigation on the stability and leaching of CN nanosheets. Overall, for embedding photocatalysts in PDMS matrix, the main consideration should be the accessibility of semiconductor particles. Even though porous structures are obtained, location of semiconductors at the interface plays a key role in photocatalytic performances.

Surface modification of PDMS can bring photoactivity as well. Therefore, it is certainly worth to mention a surface post-modified PDMS photocatalysts showing unique performance in cross-dehydrogenative coupling (CDC) reactions via visible light. For example, rose bengal (RB) is immobilized on plasma-oxidized PDMS surface rich in hydroxyl groups (**Figure 2.12b**). Vinyltrimethoxysilane (VTMS) is used for silanization of hydroxyl groups and resulting brushes polymerized via free radical polymerization with METAC (2-(methacryloyloxy)ethyl-trimethylammonium-chloride), and then mixed with rose bengal disodium salt for ion exchange. The obtained PDMS-RB photocatalyst was examined in CDC reaction (N-phenyl tetrahydroisoquinoline-nitromethane) under visible light illumination and results revealed its high efficiency which is almost comparable to the Iridium (Ir)-based catalysts that are common for CDC reactions. Moreover, an easy-to-build continuous flow reactor was set up to demonstrate the industrial potential of PDMS-RB sponge catalyst, and results clearly pointed out that gram scale reaction of CDC could be performed in flow reactor too (isolated yield 88% after 48 h).¹⁵² CDC of tertiary amines with ketones succeeded via the organic photoactive PDMS material. A plasma treated hydroxy rich PDMS sponge was modified with 3-aminopropyl trimethoxysilane and resulting amino groups were coupled with Fmoc-Glu(OtBu)-OH resulting in Glu-functionalized PDMS sponge. PDMS based photocatalyst offers a profitable solid-phase peptide synthesis (SPPS) which in further functions quite well for CDC reactions.¹⁵³ These methods are constructed on covalent attachment of photoactive moieties, which is reported to result in enhanced photocatalytic

performances. Yet, the active sides are restricted to modified surfaces rather than porous interfaces.

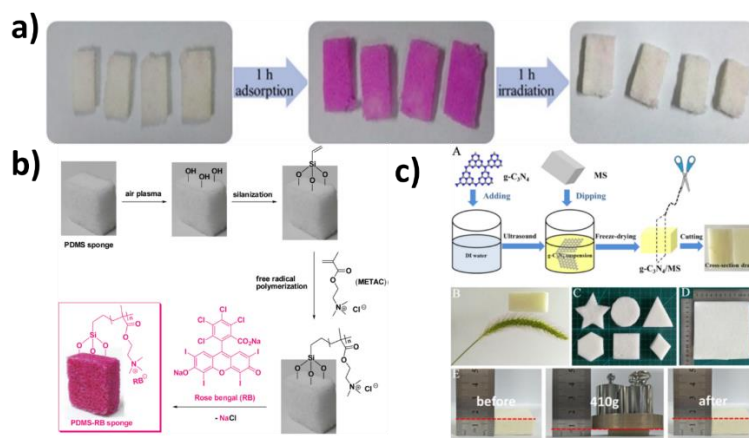


Figure 2.12. a) Visible light induced self-cleaning activity of g-CN based PDMS sponge visualized via photocatalytic RhB degradation,¹⁵¹ b) Formation of rose Bengal grafted photocatalytic PDMS sponge,¹⁵² c) Schematic description for fabrication of g-CN based photoactive melamine sponge, as well as digital images of various samples and a preliminary compression strength demonstration.¹⁵⁴

In addition to PDMS as a host network, melamine sponge (MS) is also an attractive choice as it has high porosity, low density, good elasticity, amphiphilicity, cheap price and industrial availability. For instance, MS was dipped into graphitic carbon nitride (g-C₃N₄) suspension, then squeezed and re-immersed until adequate amount of g-C₃N₄ over MS network were obtained, then freeze-dried to gain monolithic g-C₃N₄/MS (**Figure 2.12c**). This novel photoactive composite has shown decent photooxidation ability according to NO photo-removal experiment (optimum activity 78.6%) besides effective CO₂ photoreduction in comparison to powder g-C₃N₄.¹⁵⁴

In another study, significant photodegradation activity as well as excellent recyclability towards RhB dye under visible light irradiation was achieved by a carbon nitride foam (CNF) supported hybrid photocatalyst (CNB). MS was initially carbonized in a tube furnace, and the resulting CNF was dipped into BiOBr solution (Bi(NO₃)₃·5H₂O-CTAB in 40 ml ethylene glycol) of different concentrations then placed in autoclave (160°C-16h) in order to obtain the hybrid CNF supported BiOBr (CNB). This solvo-thermal photocatalyst fabrication method is a significant example for effective heterojunction

between well distributed BiOBr microspheres over fibrillar g-C₃N₄ scaffolds. In addition, resulting low-density open macroporous structure granted floatability.¹⁵⁵

Considering sponge-like features, a biomass source called ‘Loofah’ and its as-prepared sponge (derived from loofah plants) revealed unique property to be applied as bio-carrier for an intimately coupled photocatalysis and biodegradation (ICPB) system. This natural macroporous structure is quite similar to synthetic sponges thus can highlight the potential of biobased resources as porous networks. Combination of bio sourced sponge with Bi₂₄O₃₁Br₁₀ photocatalyst that was spray-coated showed better performance than polyurethane based competitive carriers (after being immersed in sludge) in removal and mineralization of tetracycline hydrochloride (TCH) under visible light. ICPB system works via combination of photocatalysis and bacterial enzymatic degradation, so diffusion-based accessibility has a prime importance. Under light irradiation, photo formed products (reactive oxygen species, ROS) successfully accessed the interior of carrier and were biodegraded by loaded amount of bacteria.¹⁵⁶

In a more sophisticated way of utilizing sponge-like carrier, carbonized charred wood slices resulting in wood/photocatalyst (wood/CoO) architectures exhibited high hydrogen production rate (up to 220.74 $\mu\text{mol h}^{-1} \text{cm}^{-2}$) under solar light. Photothermal–photocatalytic biphasic system prepared via spin-coating of various photocatalyst dispersions (MoS₂, C₃N₄, TiO₂) homogeneously on the surface of carbonized wood slices pointed out that carbonization of biobased resources as sponge-like host materials for photocatalysts can convert liquid water to water steam under solar light.¹⁵⁷

Resins

Resins are naturally occurring (plant based) or industrially produced (synthetic) robust organic matters. Their transformation to light-responsive structures after suitable combination with photoactive substances paves the way for highly effective hybrid materials for photo-based applications. As a good example for this, Novolac type resins (PR, formaldehyde:phenol <1) after surface complexation with TiO₂ particles result in PR–complexed-TiO₂ composite, which shows very efficient photocatalytic H₂ evolution

along with adequate photocurrent generation and favorable degradation of organic pollutants under visible light irradiation.¹⁵⁸ In this case, photoactivity relied on ligand-to-metal charge transfer (LMCT) sensitization, which occurred between adsorbate and TiO₂ particles through electron transfer process. The most favorable PR-TiO₂ composite was obtained via optimizing TiO₂ ratio. In another study with phenolic-type resin, photosensitization was achieved via chlorophyll incorporation through Fisher esterification.¹⁵⁹ The chlorophyll-sensitized resin demonstrated a favorable photoreduction mechanism via trapping charge carriers over chlorophyll (based on centered magnesium ions) followed by electron flux throughout the phenolic resin based on its electron de-localization. In this way of integration, immobilization of chlorophyll on phenolic resin matrix provided higher photocatalytic activity besides superior chemical resistivity both in acidic and alkaline media, as exemplified for photodegradation of blue dye waste & methylene blue. The starting point for these systems is the synthesis of phenolic resin matrix (i.e., phenol-formaldehyde) via polycondensation. Styrene-based resin matrices are popular choices as well. Copolymerization of styrene with a photoactive 2,1,3-benzothiadiazole based custom-made divinyl crosslinker via free radical polymerization resulted in various heterogeneous photosensitizers in different forms (bead, monolith).¹⁶⁰ Resulting photoactive resin materials could form singlet oxygen species under visible light irradiation that can be exploited for organic oxidation reactions. Furthermore, the variety of obtained forms showed different photocatalytic activities in batch and flow conditions thanks to structural variations of resin matrix. Utilization of a side-chain conjugated polystyrene-based macroporous resin (tailor-made sulfamide-PS resin synthesized from chlorosulfonated PS resin) that is grafted with silver nanoparticles (Ag NPs) via sulfamide bonds successfully prevented common Ag NPs aggregation, thus the hybrid material exhibited excellent photocatalytic activity according to photoreduction reaction under visible light (from 4-nitrophenol (4-NP) to 4-aminophenol (4-AP)).¹⁶¹

Chapter 2

Alternatively, semiconductors can be integrated into resins during the heterophase polymerization stage via dispersing semiconductors in the organic monomer phase, as will be demonstrated in Chapter 3 and 4 of this thesis.^{162, 163}

In conclusion, crosslinked polymer networks can offer a broad range of properties from mechanical to optical material perspectives. Bringing the opportunity of fabrication advance hybrid/composite systems by accommodating photocatalysts in their structure, can pave the way to reduce high amount photocatalyst consumption meanwhile increasing recyclability.

Chapter 2

Chapter 3

Upgrading poly(styrene-co-divinylbenzene) Beads: Incorporation of Organomodified Metal-Free Semiconductor Graphitic Carbon Nitride Through Suspension Photopolymerization to Generate Photoactive Resin*

Carbon Nitride in Organic Media

3.1. Overview

The inclusion of the metal free semiconductor graphitic carbon nitride (g-CN) into polymer systems brings a variety of new options, for instance as a heterogeneous photoredox polymer initiator. In this chapter, we present here the decoration of the inner surface of poly(styrene-co-divinylbenzene) beads with organomodified g-CN via one pot suspension photopolymerization. The resulting beads are varied by changing reaction parameters such as crosslinking ratio, presence of porogens and mechanical agitation. The photocatalytic activity of so-formed beads was tested by aqueous rhodamine B dye photodegradation experiments. Additionally, dye adsorption/desorption properties were examined in aqueous as well as in organic solvents. Photoinduced surface modification with vinylsulfonic acid and 4-vinyl pyridine is introduced. Overall, metal-free semiconductor g-CN donates photoactivity to polymer networks that can be employed for dye photodegradation and acid-base catalyst transformation through facile photoinduced surface modifications.

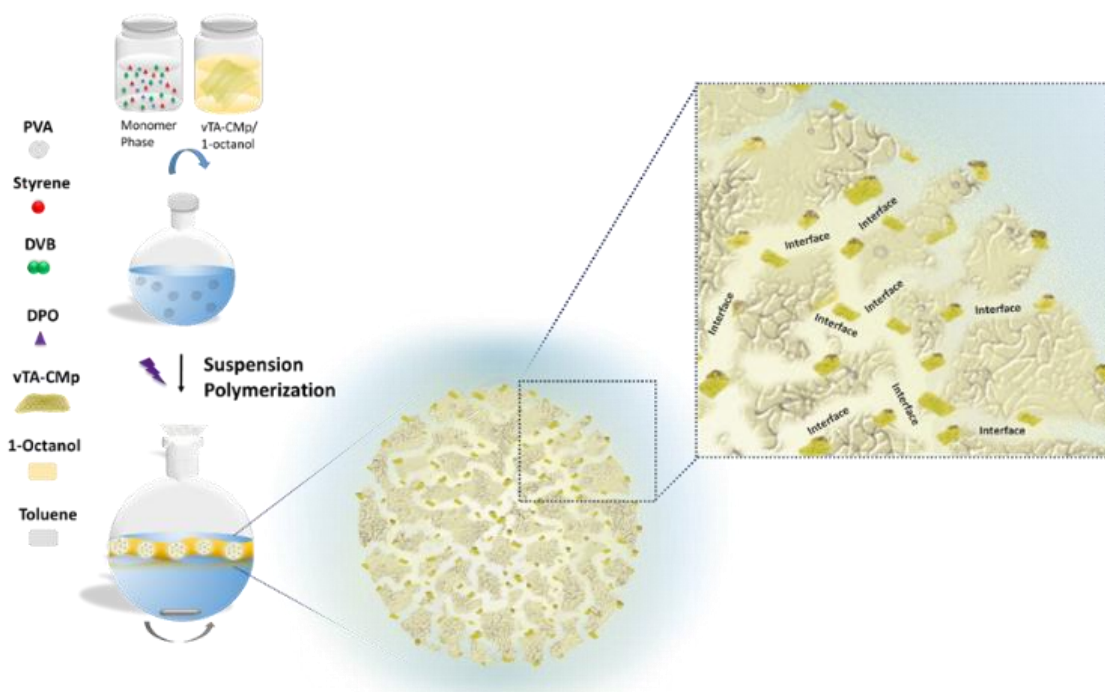
Semiconductors for photochemical purposes, e.g. for energy harvesting, water treatment and pollution degradation, usually suffer from sustainability and toxicity issues, taking lead or cadmium derivatives as an example. Considering this, graphitic carbon nitride (g-CN) as a metal-free semiconductor is an alternative to be investigated, bringing advantages such as ease of handling, low cost and low toxicity as well as showing a sufficient photocatalytic activity under visible light.¹⁶⁴ As a heterogeneous photocatalyst, it has been used in many applications such as water splitting, hydrogen evolution, CO₂ reduction and degradation of aqueous contaminants.^{12c, 164c, 165} Moreover, tunable morphology and composition along with the facile functionalization brings a rich chemical diversity.^{19b, 166} Very recent review by Zhang and colleagues nicely describes the synthesis of diverse carbon nitride materials and their corresponding electronic properties and applications, thus underlining the emergent interest on g-CN family.¹⁶⁷ For instance, tailored g-CN nanosheets from 2D layers to 3D network by reversible assembly resulted in a functional hydrogel network exhibiting high selectivity for dye extraction.¹⁶⁸ g-CN was also described as a radical photoinitiator for radical polymerization reactions by a photoredox initiation mechanism.^{50d, 169} Hydrogels made as such proved that the (left-in) carbon nitride not only acted as a photoinitiator, but also mechanically reinforced the resulting hybrid gels.¹⁷⁰ In emulsion polymerization, g-CN could act as a photoinitiator and a Pickering stabilizer.¹⁷¹ Lately, g-CN was employed in an inverse suspension photopolymerization as a water dispersible photoinitiator to obtain recollectable macrohydrogel beads with the purpose of wastewater treatment under visible light.¹⁷² When the dispersibility of g-CN was altered in a solid-state matrix, high-performance PL sensor was fabricated in a cost and time efficient way.¹⁷³ In organic media, the poor organic dispersibility of g-CN (which is due to the strong aggregation of the 2d-sheets by stacking interactions) was the main challenge to overcome. This problem could be efficiently solved by functionalizing phenyl-doped g-CN with vinyl-thiazole under visible light irradiation. The as-made vinyl thiazole grafted g-CN (vTA-CMp) demonstrated excellent organodispersibility based on organo-electrostatic stabilization via edge-induced surface modification.⁵⁴ Since then, surface modified vTA-CMp has been applied in organic media.¹⁷⁴

For the present subject of making porous polymer beads as supports for adsorption and catalysis, suspension polymerization is the industrial method of choice. In a typical suspension polymerization; the organic phase (initiator, monomer and solvent/nonsolvent as porogen) is dispersed in aqueous media with a stabilizer, and proper shear or mechanical agitation is applied in order to result in uniform, stable droplets which are then later converted into the corresponding polymer beads. Reaction conditions include physical parameters, such as stirring speed, temperature, time, or equipment dimensions, and chemical parameters as monomer, initiator, cross-linker and diluent can be altered.¹⁷⁵ Standard recipes operated on industrial scale include styrene mixed with different cross-linkers such as divinylbenzene (DVB), ethylene glycol dimethylacrylate (EGDMA) and triethylene glycol dimethylacrylate (TEGMA),¹⁷⁶ resulting for instance in polystyrene–divinylbenzene (PS-co-DVB) resins. Since its first availability as a sulfonated PS-co-DVB resin by D'Alenio in 1944,¹⁷⁷ its high potential as a heterogeneous catalyst has been explored, and possible advantages over homogeneous acid catalysts i.e. recyclability, clean-processes, matrix selectivity, by-product elimination and long-term storage, were described.¹⁷⁸ Over the years, numerous structural variations from microreticular to macroporous and hyperbranched structures were accomplished, and all served well in many different applications¹⁷⁹ such as water treatment,¹⁸⁰ catalyst support,¹⁸¹ immobilization of enzymes¹⁸² and templates for nanoparticle growth.¹⁸³ Novel functionalities that would extend the viability of PS-co-DVB are still strived.

Furthermore, the covalent modification of chemically inactive PS-DVB beads¹⁸⁴ is problematic which hinders the integration of further surface functionalities. Common functionalities involve a cross-linked bead copolymer modified by sulfonation,^{81b, 185} chloromethylation¹⁸⁶ and amination.¹⁸⁷ Other derivatization techniques include Friedel-Crafts alkylation and acylation and introduction of complex ligands.¹⁸⁸ Indeed, most of these techniques require corrosive and toxic chemicals which limits the feasibility and sustainability of final production, i.e. to PS-DVB matrix is boiled by mixture of acetic anhydride and concentrated sulfuric acid to attain sulfonation.¹⁸⁹ Another method to access surface modification requires the addition of a third monomer, such as 4-chloro

styrene and vinyl methyl ketone, both that are more prone to modification compared to PS and DVB, or an addition of a monomer which possesses an acidic or basic functionality.^{91, 190} This is why we intended to develop a remarkably simplified and more sustainable synthesis process, based on hybrids with carbon nitride.

For that, organodispersible vTA-CMp nanosheets will be added to the oil phase composed of styrene, divinylbenzene, and an organic porogen, and further photopolymerization will be performed to integrate the carbon nitride nanosheets into the polymer structure located at the interface as a cross-linking, multifunctional initiator (**Scheme 3.1**). The stability of the recipe will be examined by varying the amount of cross-linker and bead sizes, and corresponding characterizations will be enclosed. Furthermore, photoactivity of the final beads will be confirmed by aqueous RhB photodegradation and organic character of the beads will be addressed via organic dye adsorption experiments. A brief insights into the possibility of a photoinduced surface modification will be exhibited.



Scheme 3.1. Schematic overview of organomodified g-CN (vTA-CMp) incorporation into PS-DVB beads via suspension photopolymerization

3.2. Results and discussion

3.2.1 Bead Synthesis

The organic phase consisting of St, DVB, toluene and a photoinitiator was prepared by varying conditions and ratios as indicated in **Table 3.1**. Considering suspension polymerization, controlling bead size by agitation speed is a standard practice. Moreover, as the amount of cross-linker is affecting both surface morphology and porosity, its amount was varied 25 wt.%, 35 wt.%, and 50 wt.%. Furthermore, presence and absence of solvent during polymerization is also investigated in order to examine its role onto final bead size.

Meanwhile, the vTA-CMp/1-octanol dispersion is prepared in another vial, then together with monomer phase they are injected in 25 mL round bottom flask containing 15 mL PVA/water (1 wt.%) solution. The flask is capped, and polymerization is initiated via UV light. Efficient reaction time is determined to be 8 hours along with the constant adequate agitation for all beads except for CBT5m, which is the one with vTA-CMp as photoinitiator and requires 10 hours under UV light irradiation.

Table 3.1. Preparation parameters of PS-co-DVB beads with vTA-CMp.

Beads	Crosslinker (DVB %) ^a			Solvent (Toluene)		Photoinitiator		Stirring rate (rpm)	
	25	35	50	Incl.	Excl.	DPO	vTA-CMp	400	700
BT5m	x			x		x			x
BT7m		x		x		x			x
BT10m			x	x		x			x
B5m	x				x	x			x
BT5s	x			x		x		x	
CBT5m	x						x		x
REF ^b	x			x		x			x

^a) DVB ratios are in relation to Styrene, ^b) Reference beads were prepared without vTA-CMp.

In order to investigate the integration of vTA-CMp, the resulting BT5m, CBT5m and reference beads were characterized via XRD (**Figure 3.1a**). Diffraction between 17° and 20° can be attributed to the layer-layer stacking of aromatics and patterns show similar profile arising from PS-DVB nature. The peak located at 27.6° that is observed for carbon nitride containing samples BT5m and CBT5m can be assigned to carbon nitride 002 plane diffraction. Following that, FT-IR spectra (**Figure 3.1b**) were also examined as well. Firstly, as a general peak assignment regarding the copolymer formation, from 3106 to 3030 cm^{-1} indicates C-H aromatic stretching, from 2365 to 2330 cm^{-1} shows aromatic overtones, the region in between $1600 - 1400\text{ cm}^{-1}$ corresponds to C-C aromatic stretching, at fingerprint region from 1080 to 985 in-plane C-H bending and lower fingerprint region shows out-of-plane C-H bending. All spectra display similar characteristic peaks that might be associated with low amount of vTA-CMp into the beads (around 4 wt.%).

Moreover, solid UV-Vis spectra comparison between reference bead, model bead and vTA-CMp powder shows the specific broadening of BT5m from 209 - 334 nm which is significantly different than a reference bead spectrum (no photoactivity is expected from the reference bead) and can be assigned to the presence of vTA-CMp as it matches with the pure vTA-CMp spectrum (**Figure 3.1c**). Furthermore, TGA measurement (**Figure 3.1d**) demonstrated that the vTA-CMp incorporation enhances thermal resistance of the beads (on 85 % weight loss point, reference bead at 378°C and model bead at 404°C) therefore vTA-CMp acts a filler as well. Moreover, photoluminescence spectroscopy was employed in order to gain more insight into optical properties of synthesized beads (**Figure 3.1e**). Considering the previous work of our group, 380 nm excitation wavelength was reported as optimum for PL study, so the same excitation wavelength was chosen to investigate polymer beads. As expected, almost no signal was received from reference bead, and strong spectra were recorded for vTA-CMp containing beads that possess a similar profile to pure vTA-CMp.⁵⁴ An interesting phenomenon is observed when vTA-CMp is employed as a photoinitiator, meaning that when it has covalent interaction with the polymer network, then the intensity of the spectra decreases compared to its embedded

analogue. This leads to a conclusion that contrary to a common belief, an insulator aromatic polymer has an influence on the photodynamics of an excited semiconductor (partial hole transfer) once attached covalently, which was observed very recently in PS grafted g-CN thin films as well.¹⁹¹

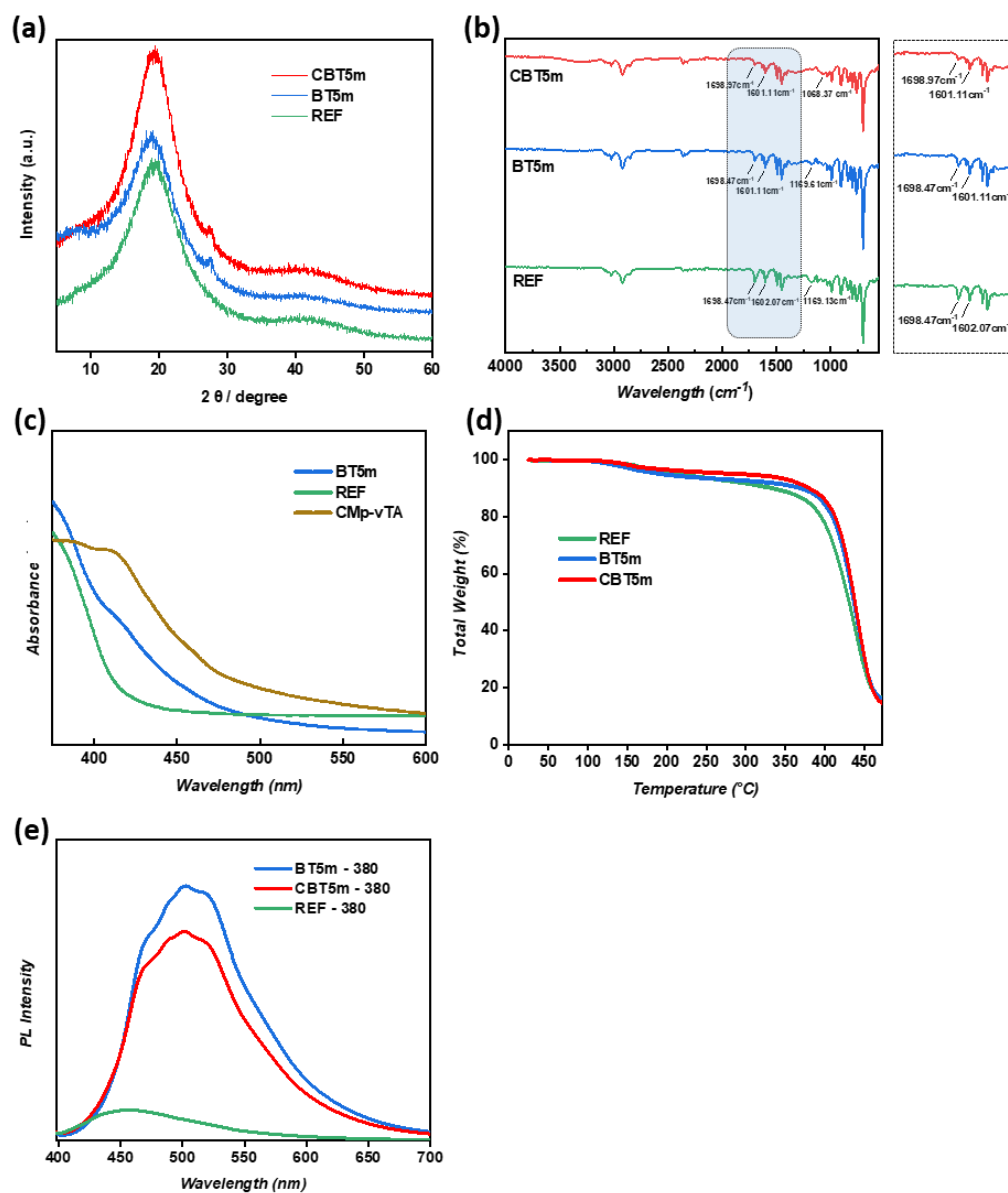


Figure 3.1. a) XRD profiles and b) FT-IR spectra of the CBT5m, BT5m (model), and reference beads. c) Solid UV-Vis spectra of BT5m (model), reference beads and pure vTA-Cmp powder. d) TGA measurement of the CBT5m, BT5m (model), and reference beads. e) Photoluminescence spectra of CBT5m, BT5m and reference beads at 380 nm excitation wavelength.

In order to examine the morphology of the model (BT5m), scanning electron microscopy is performed and shown in combination with the optical microscope images in **Figure 3.2**. All images exhibit the acquired pore structure and surface roughness based upon formed holes and cavities leading to visually observable internal and external porosity for model bead (**Figure 3.2a**). The presence of 1-octanol played a significant role in producing relatively porous PS-DVB-vTA-CMp beads via both enabling an integration of vTA-CMp into the organic media and acting as a porogen by exhibiting a template effect to the network. In addition, we have not attempted to increase the vTA-CMp content in an organic phase at this stage. It is highly important to note that the reaction with non-modified g-CNs does not take place as g-CN does not remain in organic phase in a heterophase system. Despite the commercial porogens in an industry are long chain alkanes such as dodecane, it can not be integrated into vTA-CMp system as it prevents dispersibility, however 1-octanol works successfully in our system.

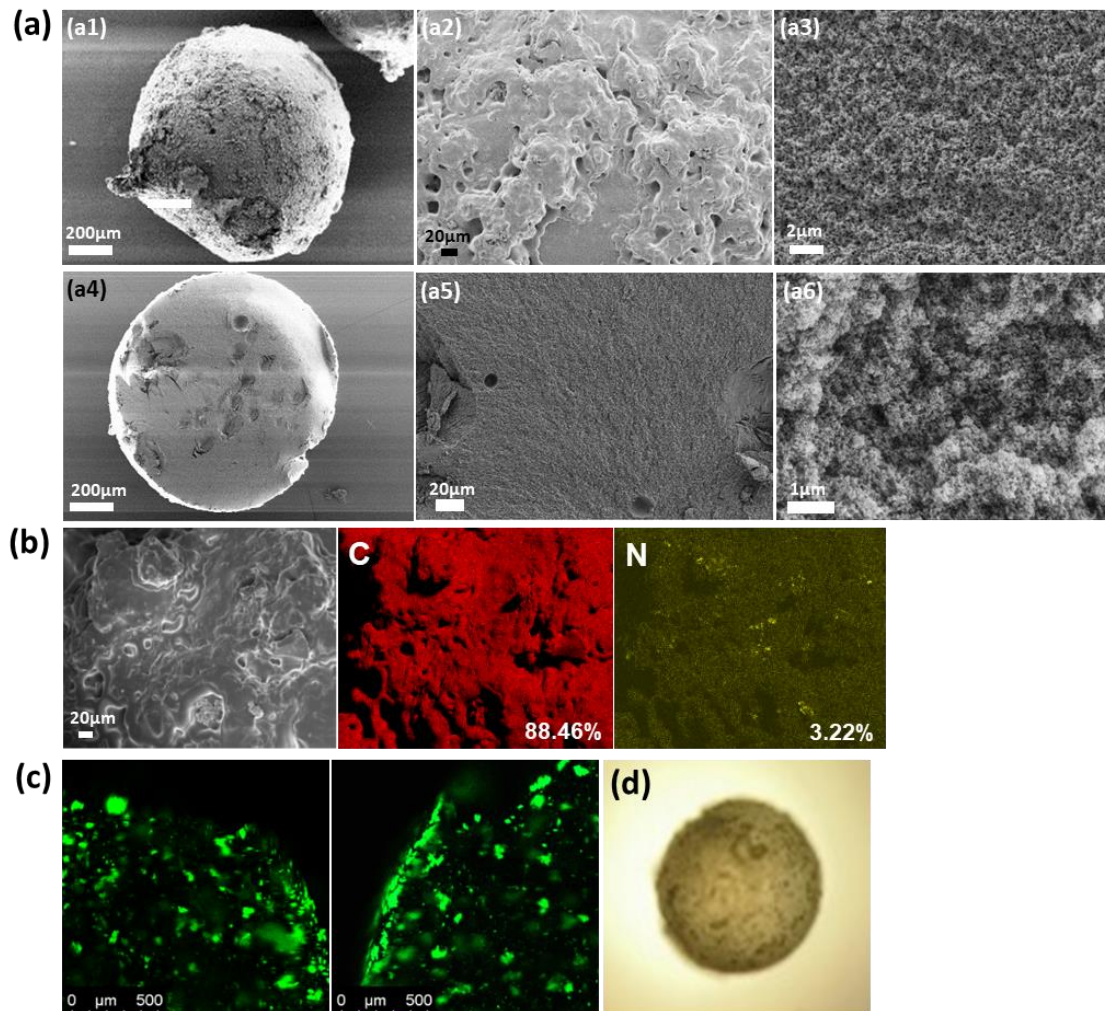


Figure 3.2. Scanning electron microscopy (SEM) images of a1-a3) Model bead and a4-a6) its cross-section. b) Elemental mapping of Model bead via EDX, c) Confocal laser scanning microscopy images of toluene immersed Model bead from the right and left side, d) optical microscope image of Model bead taken after immersing in toluene.

The reference bead is not expected to bear any nitrogen groups (neither from monomers-photoinitiator nor solvent), while the model sample exhibits homogeneously distributed nitrogen atoms as indicated via elemental mapping (with a mass of 3.2 % on the investigated area) which highlights the presence of vTA-CMp particles (**Figure 3.2b**). Based on the homogeneous distribution of nitrogen atoms over the investigated area, one can conclude that the vTA-CMp is fairly distributed in the polymer network. In addition, a major carbon content was monitored as well (with a 88.4% on the investigated area). Another distinct advantage of vTA-CMp that can be useful for applications (here as

characterization) is its emissive property (**Figure S3.1**). As expected, confocal laser scanning microscopy images clearly present emissive sections on the bead via an intense green luminescence around 540 nm which arises from vTA-CMp, once again indicating a successful incorporation and a fair distribution (**Figure 3.2c**).

It is well known that a stabilizer is to be added to the continuous phase to perform a successful suspension polymerization. PVA is one of the most established stabilizer in aqueous phase, which allows a distinct separation of organic spheres and leading to a bead formation of organic phase upon agitation. It is important to underline that our attempts with 31 kDa PVA did not result in well-defined bead formation, while 145 kDa PVA was the optimum for the presented reaction systems. In order to take a step closer to industrial processes, we have attempted suspension polymerization by thermal initiator, namely AIBN. For this purpose, a reference bead and a model bead including vTA-CMp-1-octanol dispersion were synthesized. As a result, successful incorporation of vTA-CMp was confirmed via elemental mapping result exhibiting homogeneously distributed nitrogen atoms for Model-I bead (**Figure S3.2**). Furthermore, based on SEM images, 1-octanol was able to generate porous structures by acting as an anti-solvent in a suspension media during polymerization for both cases (**Figure S3.3**), which is a very vital factor as 1-octanol is required to address vTA-CMp in organic phase. The major unconformity which was confronted in terms of reaction parameters was that the miscibility of 1-octanol in water enhances at 70°C which can disrupt the stability of pre-formed suspension droplets leading to undesired clustering, at least in a flask in a lab scale. We have attempted to overcome this problem by temperature settings, and it worths mentioning that the industrial scale integration of vTA-CMp into PS-co-DVB by the help of chemical engineering and parameter-tuning would be highly promising in near future.

The solvent uptake properties of all beads were characterized by immersing the dry beads in water, toluene and 1-octanol over 24 hours, and their solvent uptake or water uptake results for all media were calculated by using a mass difference of dry and swollen forms (**Figure 3.3**). It is a general knowledge that higher crosslinking leads to a tighter network formation thus less solvent uptake behavior, which was observed in our case studies as

well. Considering agitation effect upon solvent uptake property, lowered stirring speed leads to a bigger particle size and resulted in lower solvent uptake performance compared to a sample synthesized via medium stirring speed.

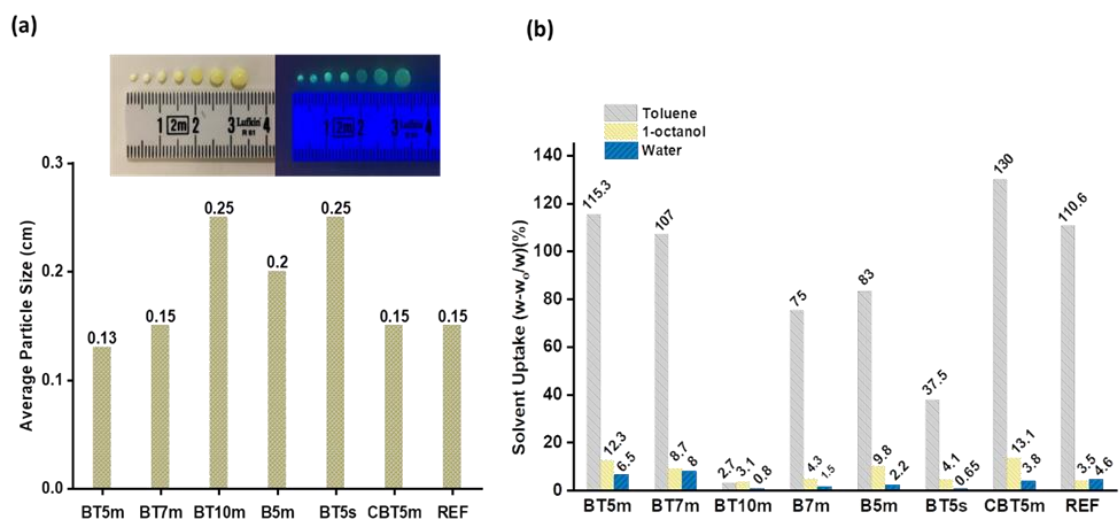
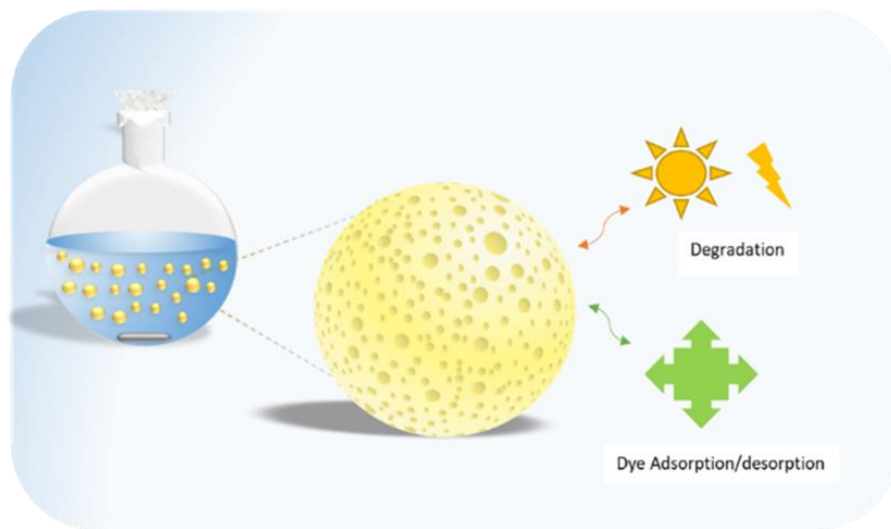


Figure 3.3 a) Average bead size of PS-co-DVB derived beads along with the size range (measured manually) and corresponding digital images of the tunable bead sizes, b) solvent uptake ratio measurements performed by 0.020g beads in 1 mL solvent for 24 hours.

CBT5m interestingly has a slightly higher solvent uptake result than a model bead, this can be correlated synergetic effect since CBT5m is photoinitiated via vTA-CMp, thus a sheet-like vTA-CMp provides a polymerization loci.¹⁷¹ Water uptake ratios are explicitly lower in comparison with toluene uptake ratios. As expected, based on the organic nature of PS-co-DVB network, there is almost no tendency for water uptake. As a conclusion, most of the vTA-CMp incorporated beads have exhibited significant solvent uptake behavior in toluene.

3.2.2 Photocatalytic Properties

vTA-CMp incorporation has a distinct advantage regarding photoactivity and such property will be harnessed in the current section (**Scheme 3.2**). We have chosen aqueous Rhodamine B (RhB) photodegradation as a model example, which would restrict the photoactivity of the beads solely on the surface as the beads have almost no (to minor) tendency for water uptake.



Scheme 3.2. The application spectra of vTA-CMp incorporated PS-co-DVB beads.

Herein, photocatalytic dye degradation performances of PS-DVB derived beads were recorded via UV-vis spectroscopy. Pure RhB dye solution is included in every experiments as a reference. All prepared samples are irradiated via visible light illumination for 5 hours and resulting conclusions were made accordingly (**Figure 3.4**).

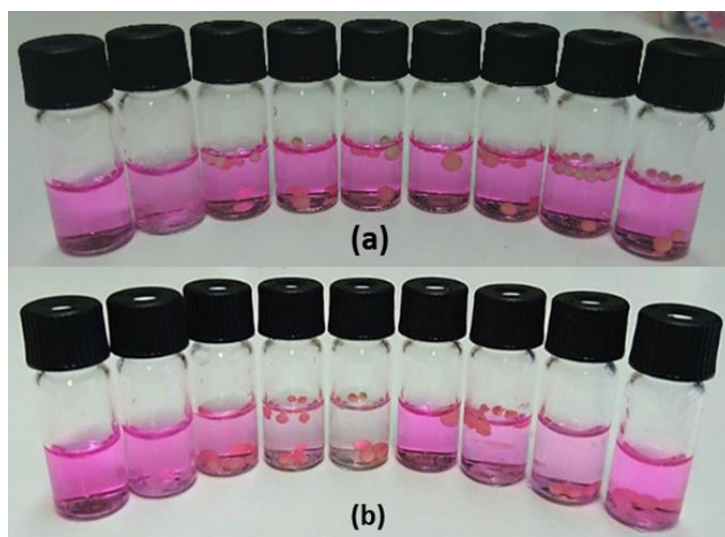


Figure 3.4. Digital images of PS-co-DVB derived beads in RhB solution, from left to right: RhB Dye, REF, B5m, BT5m, CBT5m, BT5s, B7m, BT7m, BT10m a) before visible light irradiation, b) after 5 hours visible light irradiation.

In terms of reaction condition parameter, the first focus can be put on the model bead analogues (**Figure S3.4a**). For the same series, smaller particle size (agitation effect) exhibits an enhanced RhB dye photodegradation activity under visible light irradiation. During the visible light illumination, absorption of photons by the photocatalyst containing beads leads to a electron-hole pair formation. Subsequently, photo-generated electrons and holes are linked to the formation of active radical species ($\text{HO}\cdot$, $\text{O}_2\cdot^-$, $\text{HO}_2\cdot$), which in turn degrade RhB dye molecules in aqueous solution.^{172, 192} Considering the experimental results and degradation mechanism, photodegradation activity can be influenced by the characteristic bead properties such as particle size and porous structure since these vital properties are influencing the interaction between dye molecules and catalytically active surface sites. It has also been noticed that CBT5m which was initiated via vTA-CMp instead of DPO, has performed highest photodegradation activity towards RhB dye. This result is also in a deal with the PL spectra results of CBT5m, BT5m and reference beads, which hint towards a possible interaction of vTA-CMp with covalently bound aromatic polymer upon illumination. Following that, increasing crosslinker ratio has decreased the photodegradation activity (**Figure S3.4b**), as well as beads synthesized in the absence of toluene (B5m) showed lower photoactivity than the beads synthesized with toluene (BT5m, **Figure S3.4c**). The effect of particle size by the means of agitation speed exhibited that the smaller particle size indeed serves an enhanced photoactivity due to more exposed surface (**Figure S3.4d**).

Simultaneously, a second sample series including reference bead, BT5m and CBT5m were left under the dark with the aim of clarifying a potential physical dye adsorption during photodegradation interval (5 hours), which can cause a dubious situation over dye degradation by decreasing RhB concentration in water. Apparently, the physical dye adsorption in 5 hours is not as active as photodegradation according to the UV-vis absorption spectra (**Figure 3.5a, Figure S3.5**). Reference bead (without vTA-CMp) both at the dark and under visible light show quite similar photodegradation activity with pure RhB solution. Therefore one can strongly conclude that in 5 hours, the decreased RhB concentration is solely arising from the photodegradation which is due to vTA-CMp

incorporation. As recycling is an essential parameter for photocatalysts, CBT5m was introduced to recycling test owing to its highest photodegradation performance based on previously evaluated RhB photodegradation results. (**Figure 3.5b**, **Figure S3.6**). In addition to the depicted dye degradation procedure, employed beads were left in distilled water overnight for the next run after each completed cycle. As shown in **Figure 3.5b**, degradation efficiencies exhibited slight retardation starting from 89% to 76.5% until the 4th cycle followed by a significant decrease resulting in 55.6% at 7th cycle. Observed downtrend is quite reasonable if surface-attached non-degraded RhB dye molecules are taken into consideration since they are occupying the pores and quantitatively increasing within every run cycle meanwhile not being ultimately released during desorption period. This situation was also observed in adsorption/desorption rate experiment, which will be discussed later on in the following section. Corresponding to the best photoactive performance in which obtained via CBT5m beads, its photodegradation rate constant for RhB dye degradation was examined accordingly. (**Figure 3.5c**). Regarding the kinetic experiment of the first cycle, samples were collected every one hour and RhB concentration was monitored by UV-vis spectrum. The adsorption kinetics of CBT5m were fitted to pseudo-first-order rate based on the Langmuir-Hinshelwood model considering reported studies of parental carbon nitride in literature. Regarding that, collected results were calculated according to the integral equation shown here:

$$\ln(Q_e - Qt) = \ln Q_e - k_1 t$$

Q_e is the quantity of dye adsorbed at equilibrium (mg.g^{-1}), Qt is equilibrium concentration at various times t (mg.L^{-1}), and k_1 is the rate constant of adsorption (min^{-1}). As shown in **Figure 3.5c**, the rate constant was determined by the plot of $\ln(Q_e - Qt)$ versus time. According to pseudo-first-order principle, adsorption rate is proportional to the difference between saturated concentration and adsorption amount of adsorbent thus adsorption is under the control of proceeding diffusion steps. Resulting R^2 value (0.971) of CBT5m beads is quite reasonable yet efficient when free radical polymerization nature in terms of controllability and adjustability to batch to batch in lab-scale fabrication was considered. On the other hand, the investigation on the photodegradation activity of the pristine vTA-

CMp (10 mg/0.01 L) in RhB (4mg.L⁻¹) solution resulted in 97% degradation in 150 minutes (**Figure S3.7**). Reaction rate constant k of RhB photodegradation is 0.0226 min⁻¹ for pristine vTA-CMp and 0.0063 min⁻¹ (0.38 h⁻¹) for CBT5m bead. One can not compare the photoactivity of pristine g-CNs with the presented vTA-CMp incorporated polymer network, however the synthesized beads are performing well in comparison to g-CN embedded polymer networks. It should be noted that integration of vTA-CMp in a polymeric network directly influences the primal photodegradation rate constant for RhB. Despite the limitation of vTA-CMp/1-octanol dispersion at higher concentration which undermines the final integration, CBT5M beads (55 mg/0.015 L) resulted in 89% efficiency in 5 hours with 3 times recyclability regardless of significant activity loss for RhB photodegradation.

In order to evaluate the pH effect on the photodegradation performance of photoactive beads, CBT5m beads were subjected to RhB solutions in acidic, neutral and alkaline conditions. (**Figure 3.5d**). As shown in **Figure S3.8**, overall photodegradation efficiencies are 82.8%, 77%, 77.8% at pH2, pH7 and pH13, respectively. Generation of photoactive species to perform dye degradation were not influenced by the pH of the media significantly. It is also worth mentioning that CBT5m beads showed very decent physical as well as chemical stability towards strong acidic (pH2) and basic conditions (pH13), so that no host degradation products were observed.

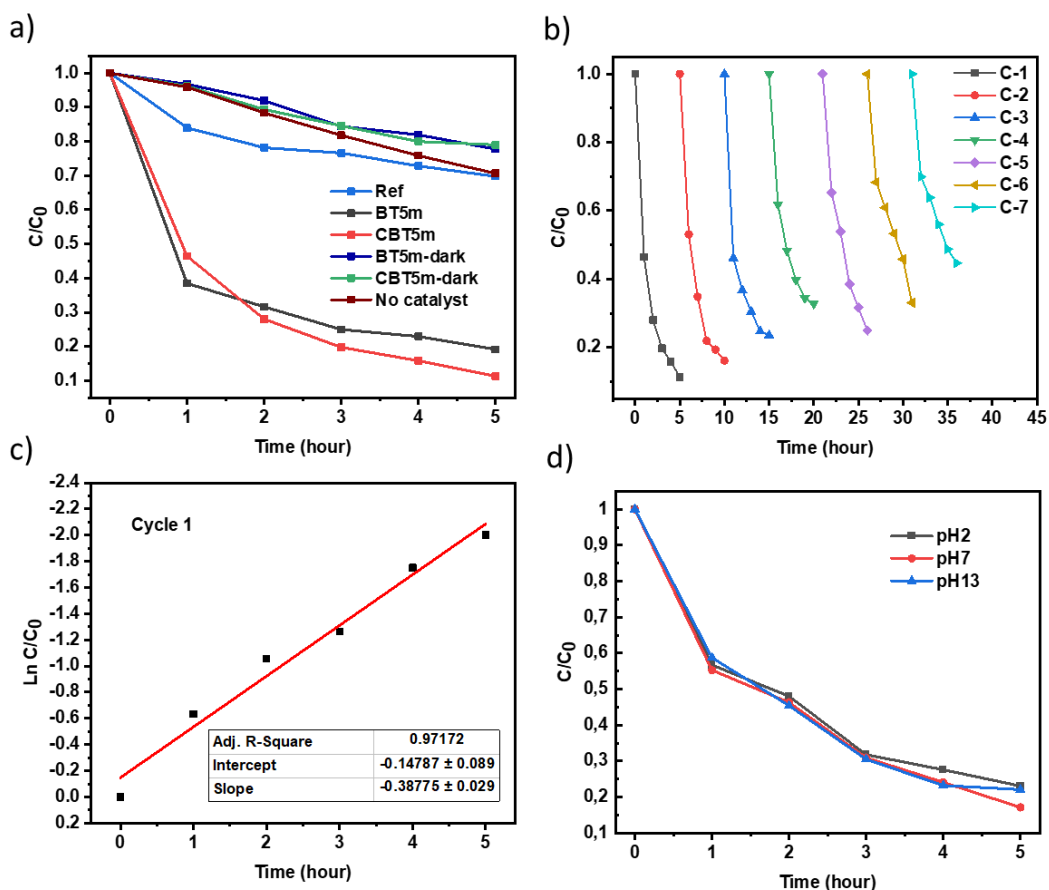


Figure 3.5. a) RhB dye degradation of BT5M, CBT5m, reference and RhB dye solution (no catalyst) under visible light irradiation (BT5m-dark and CBT5m-dark were not exposed to visible light). b) Cyclic photocatalytic RhB dye degradation with several run cycles in the presence of CBT5m under visible light irradiation. c) Pseudo-first order kinetic fitting data of cycle 1 (pH:6.3, $T=25^\circ\text{C}$, bead/RhB:0.055/0.0015 $\text{g}\cdot\text{L}^{-1}$) d) pH effect on photodegradation of CBT5m under visible light irradiation.

3.2.3 Dye Adsorption and Desorption

In addition to photodegradation, the removal of dyes from aqueous systems can be achieved by an adsorption via utilizing an adsorbent by heterogeneous means. Our target in this section is to investigate the synthesized beads for adsorption-desorption performance that relies on physical interactions. For this purpose, model beads were employed into both water-soluble (RhB dye solution) and organo-soluble (Sudan Red 7B and Perylene dye solution, 200 ppm in toluene) dye containing solutions. Regarding RhB aqueous dye solution, model beads were immersed for 24 hours for adsorption, then the desorption in clean water was monitored for another 24 hours. During the experiment,

dye adsorption results were followed via UV-vis spectroscopy (**Figure S3.9**). Additionally, reference bead was also included in RhB dye adsorption experiment as a comparison. Referring the absorption spectra results of model and reference beads (**Figure S3.9b**), strong adsorption on vTA-CMp containing PS-co-DVB beads compared to a reference was noted. Despite organic character of the beads that prevents water uptake, charged vTA-CMp particles on PS-co-DVB surface can interact with the oppositely charged RhB in solution thus leading to a strong adsorption. Furthermore, dye adsorpt beads were immersed in water for 24 hours to investigate the dye desorption (**Figure S3.9d**). As expected, model beads released higher dye concentration than reference beads as they have already adsorpt significantly higher amount of dye at the adsorption process. It is worth to mention that this effect is monitored over 24 hours and does not have a significant effect during photocalysis experiments which are conducted for 5 hours. Negatively charged vTA-CMp particles render PS-co-DVB beads with a negative charge as well, which is highly promising to be employed as ion exchange resins without further modifications.

In addition, model beads were subjected to adsorption/desorption cycle to evaluate their reusability by first immersing in RhB dye solution then after in distilled water for 24 hours for seven times (**Figure 3.6a**). Until the third run cycle, both adsorption and desorption rates have been quite efficient and satisfactory, but the last two cycles exhibited significant desorption activity loss. The reason for the weakened desorption rate over time can be caused by strong electrostatic and hydrophobic interactions between bead surface and dye molecules based on largely diffused dye molecules in each absorption cycle. Besides, limited water access throughout the bead surface based on strong organic nature of PS-DVB beads, which was supported in previous section by water-uptake results, is not providing a favorable condition to similar dye desorption performance thus affecting the next absorption cycle performance. Moreover, pH effect on adsorption/desorption rates of RhB dye were performed by employing model beads at various pH values (**Figure 6b, Figure S3.10**). The most efficient dye uptake performances were obtained both in neutral media (with 63% efficiency) and in basic media (performing 60% efficiency).

Adsorption in acidic media has decreased significantly, thus the potential of the beads as adsorption materials should be monitored from neutral to basic media. The most importantly, physical and chemical stability of the beads were confirmed over wide pH range which offers a potential for chromatographic applications.

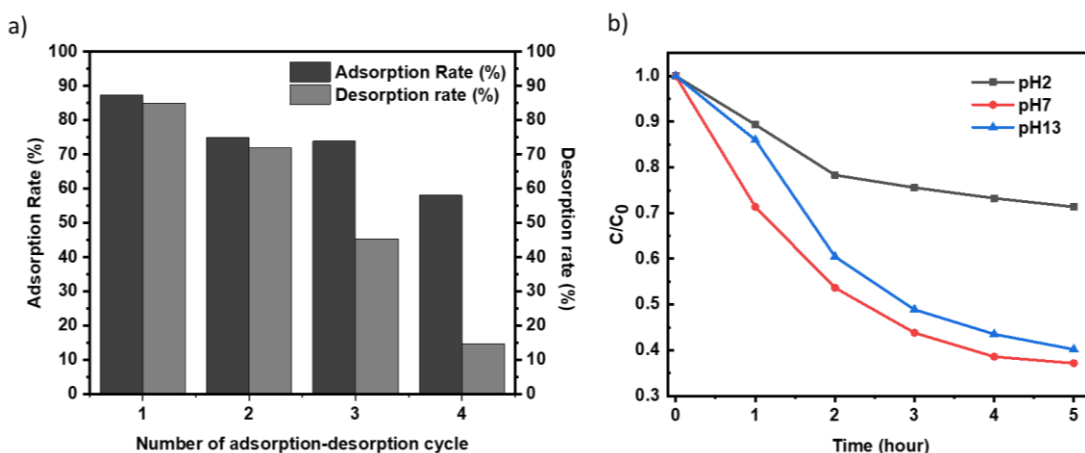
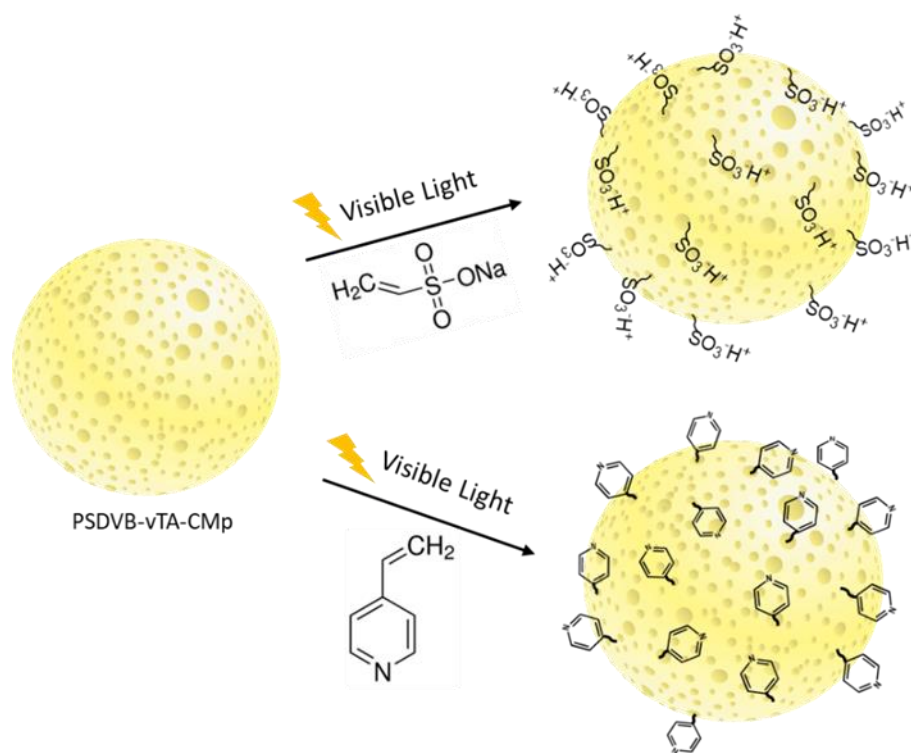


Figure 3.6. a) Adsorption/desorption rate versus number cycles plot of model bead (24h time interval). b) pH effect on adsorption rate of model bead.

Meanwhile, for organosoluble dye system, model beads were employed in two different dye solutions prepared in toluene, and a very fast dye adsorption was visually observed at frequent time intervals (**Figure S3.11**). This quick adsorption property can be remarkably useful in organic pollution treatment in aqueous media. As a simulation of recyclability, organic dye immersed beads were placed in toluene and desorption progress was followed (**Figure S3.12**). Dye releasing duration was not as fast as adsorption but even after 3 hours, toluene had to be replaced to complete a desorption. At the end of the 24 hours, a fair amount of adsorbed organic dyes were released from the beads. This simple but considerably useful dye adsorption/desorption experiment indicates that vTA-CMp incorporated PS-co-DVB beads have a high capacity towards two different dyes, even though organosoluble dye concentration in this experiment was set to be much higher than a regular pollution concentrations in an environment.

3.2.4 Surface Modification of PS-co-DVB-vTA-CMp Beads via Visible Light Irradiation

Surface modification of inactive PS-co-DVB resin beads is enabled via introduction of photoactive species, such as vTA-CMp in this case. It is important to reside surface functional groups at the accessible sites, and as vTA-CMp has dispersibility in 1-octanol and no dispersibility in toluene phase, they are ideally located at the interface. To perform post-modification, CBT5m beads were chosen as a model sample due to the highest photoactivity according to the RhB dye degradation results, and vinylic compounds such as vinylsulfonic acid (VSA) and 4-vinylpyridine (VP) were employed as reactive monomers (**Scheme 3.3**).



Scheme 3.3. Schematic overview of photo-induced surface modification of PS-co-DVB-vTA-CMp beads via visible light irradiation.

As depicted in the preparation section, CBT5m beads were separately immersed in VSA monomer solution prepared with water:DMF mixture and in pure VP. DMF was added in addition to water for VSA modification because of inherent organic character of CBT5m beads which might obstruct water-soluble monomer accessibility throughout the pores.

Immersed beads were placed in front of a visible light and left for overnight (~12 h) under medium agitation to complete the modification. After the purification step, VSA and VP functionalizations were investigated by elemental mapping via EDX, combustive elemental analysis and FT-IR.

Regarding VSA grafting, CBT5m-VSA is exhibiting sulfur and oxygen signals which align with the nitrogen atoms as expected, since nitrogen signifies catalytically active sites where VSA monomers are grafted on the surface (**Figure 3.7**).

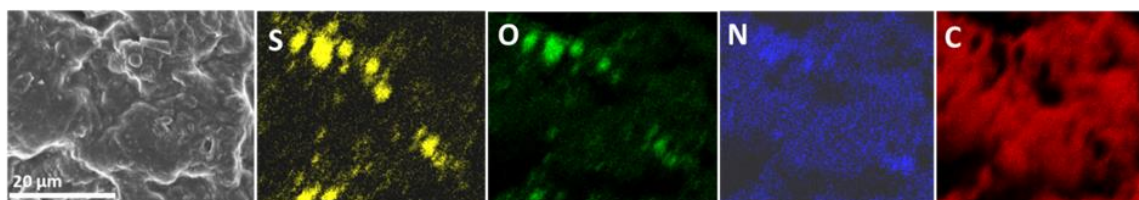


Figure 3.7. Elemental mapping results of CBT5m-VSA via EDX.

Furthermore, sulfur content was supported also via combustive elemental analysis up to 1.44 wt.% (**Table 3.2**). However, VSA modification was not detected via FT-IR analysis even though increased reaction time and DMF ratio. This might be explained with low monomer grafting or short propagation.

On the other hand, VP functionalization can be confirmed via combustive elemental analysis based upon increased nitrogen and carbon content (**Table 3.2**) along with FT-IR spectrum result which displays introduced C=C aromatic stretching vibration at 1597 cm^{-1} and C=N double bond stretching at 1416 cm^{-1} (**Figure S3.13**). In addition, CBT5m-VP shows altered luminescence under UV light irradiation (**Figure S3.14**).

Table 3.2. Combustive elemental analysis results before and after surface modification of CBT5m via VSA and VP.

<i>Name</i>	<i>N (%)</i>	<i>C (%)</i>	<i>H (%)</i>	<i>S (%)</i>	<i>C/N</i>
<i>CBT5m</i>	0.96	82.22	8.14	0.08	85.51
<i>CBT5m-VSA</i>	1.05	80.91	8.72	1.44	77.06
<i>CBT5m-VP</i>	1.08	89.52	8.17	0.3	82.91

Preliminary results on visible light induced surface modification are highly intriguing, however in near future extending the vTA-CMp amount in the beads thus improving the amount of photoinduced functionalities and their corresponding catalytic performances will be investigated.

3.3. Conclusions

In this chapter, the contribution of organodispersible vTA-CMp containing PS-co-DVB beads which were successfully synthesized via UV light induced suspension polymerization is demonstrated. The effects of cross-linker ratio, solvent presence and agitation were examined in detail. Tunability of the recipe has been demonstrated, and the incorporation of vTA-CMp into polymer network was confirmed by methods such as electron microscopy, UV-Vis and PL. A possibility to employ industrial recipe, thermal initiation, was exhibited briefly. As a model application of the beads, aqueous RhB dye photodegradation experiments were performed. In order to compare a photodegradation activity with the possible physical dye adsorption, same experiments were also simultaneously performed without visible light irradiation and results clearly showed that rather than dye adsorption, photocatalytic dye degradation occurs. Enhanced photoactivity of the beads was noted when vTA-CMp is utilized as a photoactive component. Organophilicity of the so-formed beads was confirmed via organosoluble dye (Sudan red 7B, perylene) adsorption from a biphasic systems. Adsorption-desorption of aqueous and organic dyes were monitored in addition. A first try on the visible light induced surface modification of PS-co-DVB-vTA-CMp beads was demonstrated, and

such approach promises benign surface modifications to be applied from lab to industrial scale.

Bringing g-CN into organic media, which has been quite a challenge until recently, now enables a significant broadening of applications. Herein, we have rendered one of the most commercial polymers, PS-co-DVB beads, with photoactivity via g-CN addition by sticking to the traditional suspension polymerization. In such a way, organodispersible g-CN could be used to decorate the inner pore system, donating photoactivity to such resins, which in turn increases the lifetime and reusability of the photocatalyst by surface heterogenisation and brings it to bead-based reaction columns and automated synthesizers.

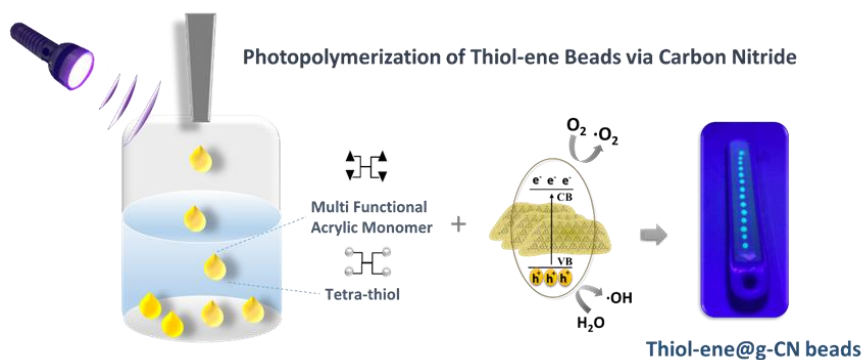
Chapter 4

Thiol-ene Polymer Beads via Liquid-Liquid Printing: Armored Interfaces and Photopolymerization via Graphitic Carbon Nitride*

Carbon Nitride in Organic Media

4.1. Overview

Polymerization of multifunctional thiol-ene molecules are attractive as a proof of concept in photopolymerization, yet formation of bead structure is highly restricted. This chapter will exhibit graphitic carbon nitride based liquid-liquid printing and subsequent photopolymerization to form thiol-ene polymer beads with extreme simplicity and potential scalability.



Scheme 4.1. Fabrication of thiol-ene polymer beads via liquid-liquid printing technique.

Metal-free graphitic carbon nitride (g-CN) is a visible light active semiconductor and has many appealing applications in photocatalysis. Despite it represents a family of carbon and nitrogen based semiconducting structures with repeating units of triazine, heptazine or tri-s-triazine, all structures are dominated by strong π interactions hence they are in heterogeneous nature in photocatalytic reactions. Integration of g-CN into polymer chemistry has been flourishing in the last 4 years and many synthetic examples, from radical polymerization to oxidative polymerization, were shown.

g-CN dispersions hold a great potential for wide range of applications from photovoltaics to bioimaging. Once employed in dispersion, g-CN-polymer hybrids can be prepared as well. While it is possible to encounter aqueous dispersions of g-CN prepared via sonication in literature, stable organic dispersions of g-CN were achieved once g-CN surface modification reaction is conducted. In organic media, the stability arises from electrostatic forces and carbon nitride nanosheets are highly charged.

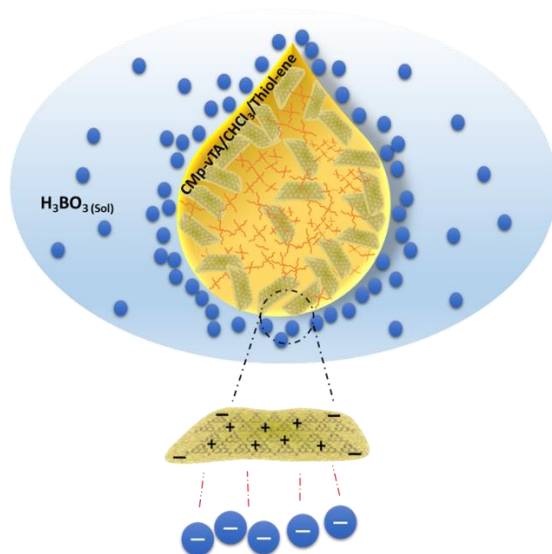
In recent years, liquid-liquid printing has been popularized due to its versatility to form dimensionally stable soft matter based on interfacial strengthening. This innovative approach relies on the utilization of oppositely charged molecules (ideally one has to be long order) in non-miscible phases. Once they are immersed, opposite charges on the interface undergoes 'jamming' effect and complex liquid shape is stabilized, based on solidification of the interface while inner phase is still liquid. Shi and Russell pioneered many possible charged molecules in alternative solvents to produce complex architectures. Our group has investigated the potential of organic g-CN (denoted as CMp-vTA) as interface stabilizer to access liquid-liquid printing. Furthermore, interfacial photoactivity of edible oil-in-water printed soft structure was exhibited in another work. Overall, liquid-liquid printing is a nanoarchitectonic concept as oppositely charged natural molecules can form biological structures in nature.

In this chapter, we will take a step further in g-CN based liquid-liquid printing and photoactivity will be harnessed to form polymer beads (**Scheme 4.1**).

Polymerization of multifunctional thiol and ene molecules are shown as a proof of concept in photopolymerization and 3D printing. While it is possible to form many appealing macroscale thiol-ene geometries via 3D printing, heterophase polymerization of thiol-ene is scarce. It is quite challenging to conduct traditional suspension polymerization on such systems, and micron-sized particle fabrication is only possible via microfluidics. Here we will use interfacial nanoscale interactions to form thiol-ene polymer macroscale beads via liquid-liquid printing.

4.2. Results and discussion

CMp-vTA dispersion in chloroform is prepared and mixed with pentaerythritol tetraacrylate and tetrakis(3-mercaptopropionate) (TT bead, 1:1 eq). We also alternated vinyl monomer library by employing 1,3,5-Triallyl-1,3,5-triazine-2,4,6(1H,3H,5H)-trione (TTA bead) and 2,4,6-Triallyloxy-1,3,5-triazine (TTO bead, **Scheme 4.2**, **Scheme S4.1**). Boat shaped aluminium crucible is filled with boric acid aqueous solution. Organic phase is dropped into aqueous solution and stable liquid bead formation is observed due to interaction of CMp-vTA sheets with boric acid (**Figure 4.1a inlet**). Under UV light, CMp-vTA initiates polymerization and within 2 hours organic macroscale beads solidify. This process can be automated and is highly energy efficient as no heat nor stirring is required. It is optimized to form beads within the range of 1 mm - 1 cm. It is important to underline that the system worked best in aluminum surfaces, and glass or polymer surfaces gave defected structures. After purification, ICP was conducted to ensure that boron is removed from the surface and indeed almost no boron was observed (**Table S4.1**).



Scheme 4.2. Overview of interfacial solidification of thiol-ene bead.

Solid UV-Vis spectra of TT and TT@CMp-vTA exhibit significant absorption difference whilst characteristic broad spectrum of pristine CMp-vTA (600-340nm) is matching with TT@CMp-vTA that of can be attributed to success of CMp-vTA integration (photoactivity is not expected from TT beads (**Figure 4.1a**)). Structural investigation performed via FT-IR analysis simply confirmed varied thiol-ene bead compositions. The ester C=O stretching modes appeared at 1732 cm^{-1} for TT@CMp-vTA sample differentiated in TTA@CMp-vTA sample regarding its isocyanurate based structure; C=O stretching at 1730 cm^{-1} and N-C=O 1677 cm^{-1} , aromatic C-N stretching at 1453 cm^{-1} . TTO@CMp-vTA spectra displayed intense cyanurate absorption bands at 1737 cm^{-1} , 1557 cm^{-1} and roughly until 1330 cm^{-1} corresponding to N=C-O and benzene ring vibrations of C-N and C=N bonds, respectively. Overall differences of all spectra at lower fingerprint region additionally confirms the structural variation of resulting thiol-ene beads (**Figure 4.1b**). Thermogravimetric profiles demonstrated slight difference in regards to thermal resistance for all conducted samples including the ones does not possess CMp-vTA. Regardless of CMp-vTA incorporation, significant mass loss starts around $350\text{ }^{\circ}\text{C}$ and eventuates closely $435\text{ }^{\circ}\text{C}$ for TTA, TTO, TTA@CMp-vTA, TTO@CMp-vTA samples unlike TT and TT@CMp-vTA beads that are more stable up $485\text{ }^{\circ}\text{C}$. Regarding residual mass amounts, which were indicating possible thermal

condensation at high temperature (up to 800 °C) that might lead to carbonization of polymer samples, investigated and discussed further in the following parts. (**Figure 4.1c**, **Figure S4.1**).

Considering that the performed reaction condition includes boric acid in aqueous media, it is confirmed that there is no residual boron after purification steps in our as-prepared beads according to ICP-OES measurement results, hence, neither in furtherly carbonized as-prepared beads. (**Table S4.1**).

Scanning electron microscopy (SEM) image of TT@CMp-vTA exhibited very smooth morphology as well as moderate porosity as result of effective photopolymerization based on integrated CMp-vTA nanosheets. Decent surface formation also confirms good compatibility of organic media in which is where CMp-vTA was kept at the interphase and led to stable bead formation during photopolymerization in aqueous media (**Figure 4.2a**, **Figure S4.3 (a1-2)**). In further, confocal laser scanning microscopy image (cross section of TT@CMp-vTA bead) also simply confirmed the successful incorporation of vTA-CMp, based on intense green luminescence around 540 nm as it is the characteristic emissive property of g-CN (**Figure 4.2b**).

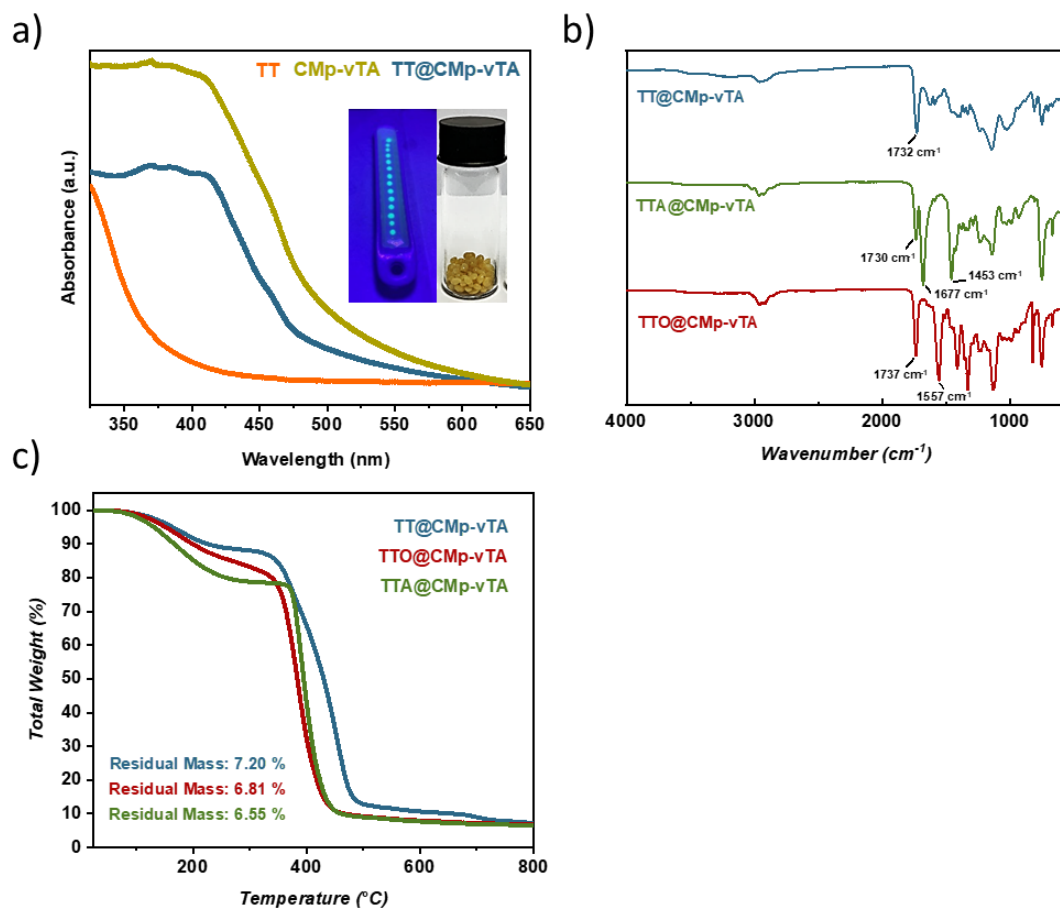


Figure 4.1. Solid UV-Vis spectra of TT, TT@CMP-vTA and pristine CMP-vTA powder along with digital images of TT@CMP-vTA (a), FT-IR spectra of TT@CMP-vTA, TTO@CMP-vTA, TTA@CMP-vTA (b), TGA measurement TT@CMP-vTA, TTO@CMP-vTA, TTA@CMP-vTA.

Furthermore, EDX mapping revealed homogeneous distribution of the atoms with fair amount of abundance without any compartmentalization (**Figure 4.2c**). It is evident that CMP-vTA particles rest on the surface and not inside the bead, thus one can expect no photoactivity. The main reasons are i) CMP is already surface photomodified to obtain dispersible analogue that lowers photoactivity, ii) CMP-vTA forms a covalent thiol-ene polymer hybrid where CMP-vTA can not be removed and iii) g-CN polymer hybrids are photoactive when g-CN is located on the porous interface. As expected, our studies on photocatalytic RhB degradation via TT@CMP-vTA beads showed no remarkable RhB degradation (**Figure 4.2d**), which underlines the restricted photoactivity of TT@CMP-

vTA beads. This observation is in good agreement of a general knowledge that porosity is needed for (photo)catalysis on hybrid structures where the photoactive material should be at the inner porous interface and not on the surface. As the mechanism of liquid-liquid printing solely relies on outer interface interactions, all CMp-vTA particles from organic phase rush towards interface to accommodate stable structure formation.

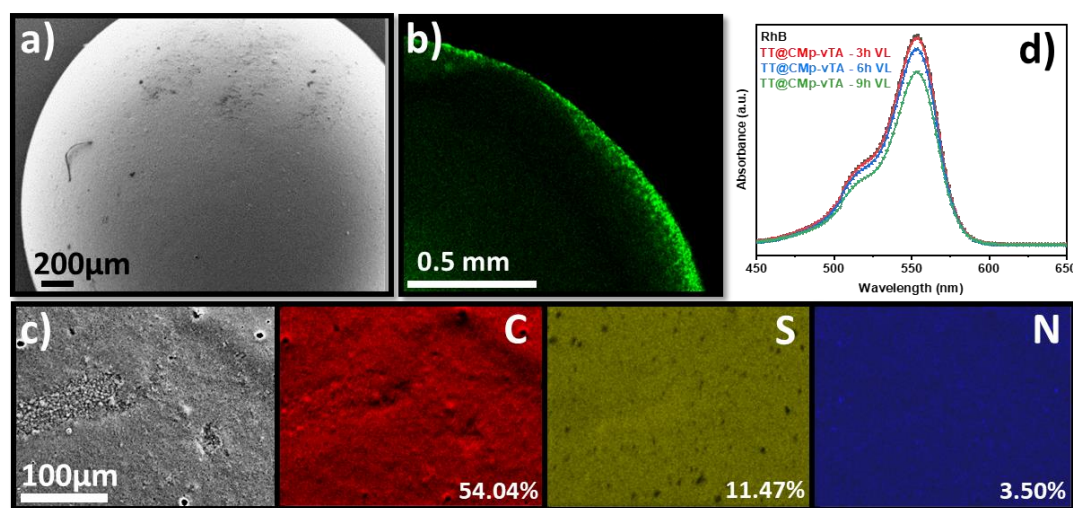


Figure 4.2. Scanning electron microscopy image of TT@CMp-vTA (a), cross sectional confocal laser scanning microscopy image of TT@CMp-vTA (b), Elemental mapping of TT@CMp-vTA via EDX (c), UV-vis spectra of TT@CMp-vTA (RhB dye degradation under visible light irradiation) (d).

In order to investigate solvent uptake performance of TT@CMp-vTA beads, various solvents were tested, and according to results, highest solvent uptake ratio was found in dipolar aprotic acetone (46.8%) and polar aprotic THF (32%) followed by polar protic ethanol (29.5%). Nonpolar solvents such as, toluene (1.1%) and hexane (1.5%), besides to polar protic water (0.7%), did not show diffusion throughout the beads yet resulted in quite low solvent uptake ratios (**Figure S4.2**).

In other words, the beads obtained in this study seem covalently coated with CMp-vTA particles. Possessing thermally stable outer layer is highly interesting for polymer carbonization. In recent years, carbonization of polymeric materials is a growing trend to manufacture doped carbonaceous matter for electrochemical or battery applications. While many polymers reach ceiling temperature, and depolymers yield no carbon,

polymers yielding special carbons require complicated synthesis and are overall very expensive materials to be employed. Additionally, obtaining monolithic doped carbon structures is complicated except for a few exceptional cases. Carbonization of so-formed beads provided S and N codoped carbon materials. To begin with, reduced bead size and enhanced porosity after carbonization of TT@CMp-vTA beads (CTT@CMp-vTA) is clearly seen via scanning electron microscopy images (**Figure 4.3a**, **Figure S6.3 (a-b)**). The preservation of bead shape after carbonization is also quite apparent on digital images (**Figure 4.3b**), and is unique for TT@CMp-vTA beads as the rest of the beads (TTA@CMp-vTA and TTO@CMp-vTA) result in powder form with metallic black color (named CTTA@CMp-vTA and CTTO@CMp-vTA, respectively). EDX mapping results are in good agreement with atomic content and abundance based on increased C and N atoms (wt.%) and significant decrease in S content (wt.%) (**Figure 4.3c**). This is also in accordance with combustive elemental analysis results, which reveal the elemental composition of the analyzed samples. (**Figure 4.3d**, **Table S4.2**). Notable increase of C atom within decrease of S compensated with slight increase of N atom in every sample. In detail, beads that are not consisting of CMp-vTA exhibited varied nitrogen content since isacyanurate and cyanurate based acrylate monomers were the only nitrogen atom possessing monomers. By this reason, TT bead and its derivatives (TT@CMp-vTA, CTT@CMp-vTA) showed lowest nitrogen content unlike the others. On the other hand, the obtained quite high nitrogen contents of TTA and TTO beads before and especially even after carbonization step, allows us to state the hybrid N and S codoped carbonaceous materials in a quite stable and facile way.

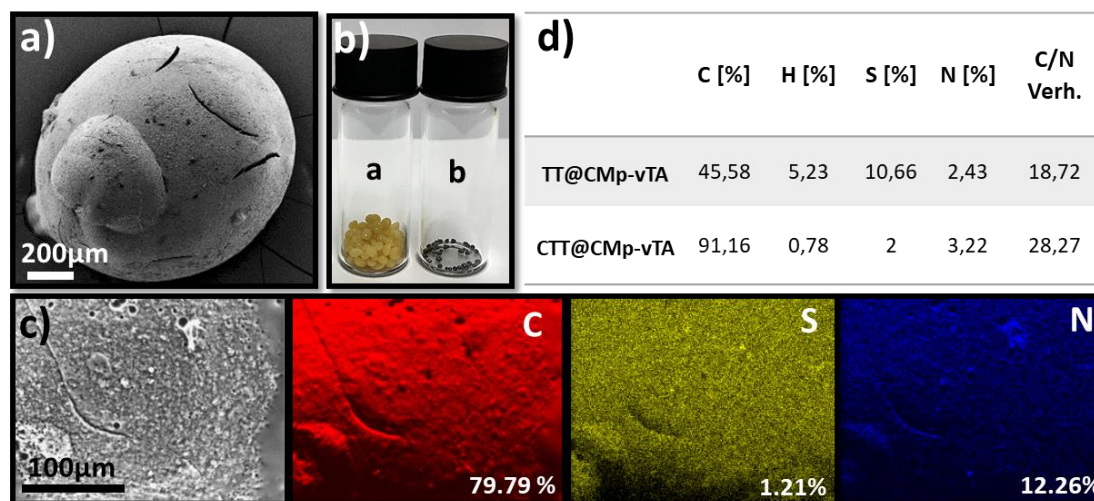


Figure 4.3. Scanning electron microscopy image of CTT@CMp-vTA (a), digital images of TT@CMp-vTA and CTT@CMp-vTA (a-b) (b), Elemental mapping of CTT@CMp-vTA via EDX (c), Combustive elemental analysis results of TT@CMp-vTA and CTT@CMp-vTA (d).

Furthermore, XRD profiles of all carbonized samples exhibited broad diffractions at 25.2° and 43.75° that can be assigned to (002) and (100) planes of the amorphous carbon structure. Moreover, Raman spectra of carbonized CMp-vTA containing samples showed the characteristic defect-induced band (D band, 1358 cm^{-1}) and the crystalline band (G band, 1585 cm^{-1}) with varied ID/IG (intensity ratio of D to G band) values. CTT@CMp-vTA sample which is the only carbon sample preserved prior bead shape as shown previously, exhibited lowest ID/IG value which can be considered as having higher ordering degree than CTTA@CMp-vTA and CTTO@CMp-vTA samples that are obtained in powder form after carbonization. (**Figure S4.5**).

According to N_2 sorption results, CMp-vTA integrated carbonized samples (CTT@CMp-vTA, CTTA@CMp-vTA, CTTO@CMp-vTA) possess very low surface area ($\sim 10\text{ cc/g}$) which can be considered as negligible yet might be also reasonable as neither porogens nor templates were applied during synthesis (**Figure S4.6**).

Overall, a simple synthetic methodology prone to be automated to attain thiol-ene polymer beads, followed by carbonization was presented to obtain scalable S, N-codoped carbon material from very cheap and available monomers that could be highly interesting for electrocatalysis and batteries.

4.3. Conclusions

Liquid-liquid printing is an attractive method to manufacture soft matter structures with high complexity based on interfacial jamming effect of oppositely charged molecules on different side of the interface. Graphitic carbon nitride particles in organic phase can reinforce the interface when injected into aqueous solutions. Once the organic phase contains polymerizable multifunctional thiol and -ene compounds; light irradiation triggers polymerization thanks to the semiconducting property of carbon nitride particles. In this chapter, we formed thiol-ene polymer beads with extreme simplicity and scalability that can potentially be automated. As expected, resulting macroscale beads were not photoactive as the inner porosity is blocked by carbon nitride particles at the interface. However; this innovative, simple and cheap architecture based on nanoarchitectonic principles provided sulfur and nitrogen-codoped carbon materials upon carbonization.

Chapter 5

Photoinduced Post-Modification of Graphitic Carbon Nitride Embedded Hydrogels: Synthesis of 'Hydrophobic Hydrogels' and Pore Substructuring*

Carbon Nitride in Aqueous Media

5.1. Overview

Hydrogels are a special class of crosslinked hydrophilic polymers with a high water content through their porous structures. Postmodifications of hydrogels propose an attractive platform so that a variety of fresh functions, which are not arising from initial monomers, could be accessible on a parental network. Photoinduced post-modification of hydrogels by embedding semiconductor nanosheets would be of high interest and novelty. Here, a metal-free semiconductor graphitic carbon nitride (g-CN) embedded hydrogel as an initial network will be synthesized via redox-couple initiation under dark condition. Post-photomodification of so-formed hydrogel, thanks to the photoactivity of the embedded g-CN nanosheets, will be exemplified in two scenarios. Synthesis of 'hydrophobic hydrogel' will be reported and its application in delayed cation delivery will be investigated. Furthermore, pores of the initial hydrogel will be modified by the formation of a secondary polymer network.

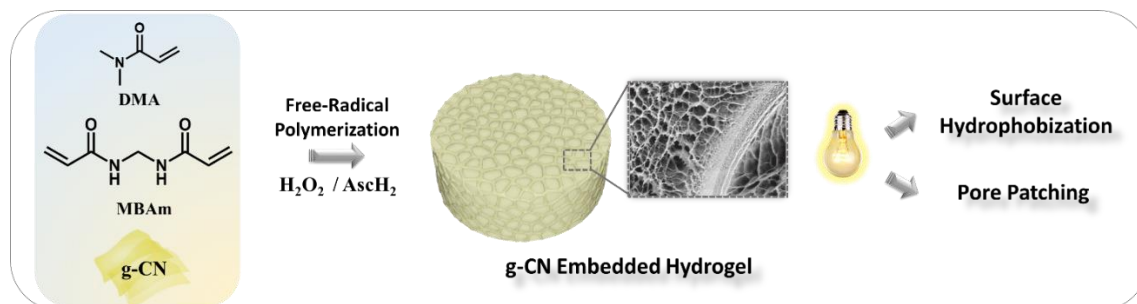
The popularity of hydrogels arises from their structural similarity to natural tissues, meaning that they are stable networks with high water content.¹⁹³ The simplest synthesis of hydrogels can be conducted in an aqueous solution of a water-soluble monomer and crosslinker (bi- or more functional) in the presence of an initiator (generally radical initiation). Since then, many synthetic routes have been developed in order to synthesize artificial matter that mimics the performance of natural tissues. Therefore, many reinforcement methods have been suggested, i.e., host-guest interactions,^{88a, 194} double network formation,¹⁹⁵ reinforcer addition.¹⁹⁶ The potential of hydrogels is beyond biomaterials, currently these soft aqueous materials are prime candidates in agricultural delivery systems as well.¹⁹⁷

In the era of sustainability, utilization of sunlight is of great importance.¹⁹⁸ Metal-containing and mostly toxic and non-sustainable semiconductors are slowly being replaced by a new-generation semiconductor. Graphitic carbon nitride (g-CN) is a metal-free polymeric semiconductor composed mainly carbon and nitrogen elements by tri-s-triazine, triazine imide, or heptazine repeating units.^{19b, 199} g-CN represents a family of materials where the variety of synthetic routes can be applied to form photoactive matter with altered properties, i.e., monomer supramolecular assembly to attain a monomer complex prior to carbonization results in enhanced porosity and photoactivity since ordered structures are formed, and the detailed overview has been reported by Shalom et al.⁴⁴ Facile tunability has rendered g-CN to be applied in visible light induced catalytic reactions such as water splitting,²⁰⁰ pollutant degradation,²⁰¹ CO₂ reduction^{49a, 202}, photonics^{56a, 203} and polymer synthesis.^{50a, 50d, 169b, 204}

Integration of g-CN into hydrogels has been popularized in the last four years, where g-CN nanosheets can be implemented into hydrogels through embedding²⁰⁵ or covalent binding²⁰⁶ for the target application such as reinforced hydrogels¹⁷⁰ and hydrogels for photoredox-based applications.²⁰⁷

Hydrogel post-modification via semiconductors induced by a visible light would be an appealing haven. Herein, we will demonstrate a photoactive g-CN nanosheet addition to

hydrogels through embedding, which will be the anchoring point that grants an access to photoinduced post-modification methods. The effectiveness of this strategy will be demonstrated via a photoinduced transformation of a hydrophilic skeleton to a hydrophobic network. Furthermore, the freeze-dried hydrogel will be subjected to a subsequent photoinduced pore patching (**Scheme 5.1**).



Scheme 5.1. Schematic overview of g-CN embedded hydrogel fabrication and its subsequent photoinduced post-modifications.

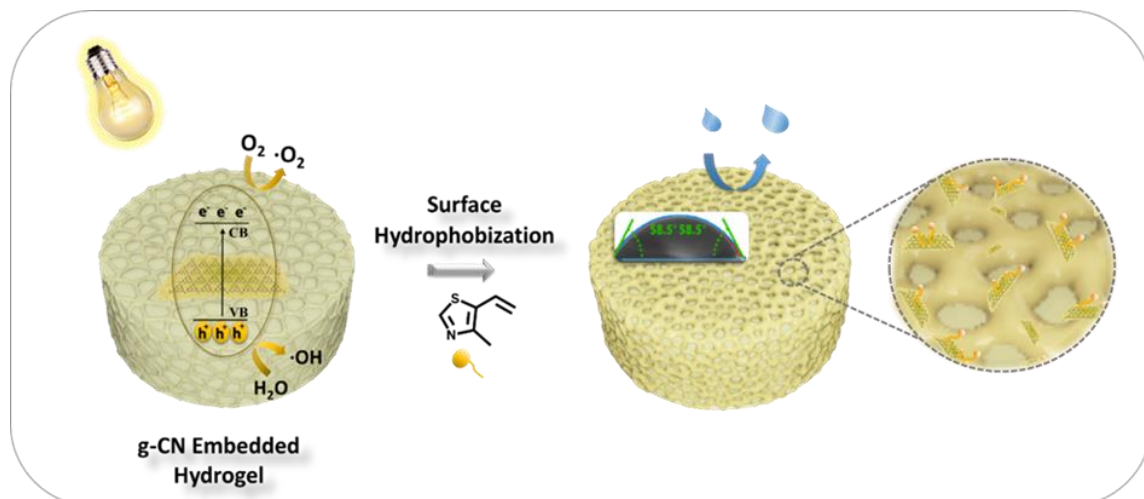
5.2. Results and discussion

Under the scope of this study, which is divided into two parts, the hydrogel denoted as HGCM was utilized as the main substrate for both sections. To prepare HGCM, firstly graphitic carbon nitride was synthesized from the thermal treatment of cyanuric acid-melamine supramolecular complex (CM).²⁰⁸ The resulting yellow powder was ultrasonicated in water to obtain a g-CN aqueous colloidal dispersion. Freshly prepared CM/water colloidal dispersion was mixed with water-soluble monomer (*N,N*-Dimethylacrylamide, DMA) and crosslinker (*N,N'*-methylenebisacrylamide, MBA) followed by the addition of a redox couple, ascorbic acid-hydrogen peroxide, respectively. The mixture was immediately placed in a petri dish to complete the gelation via free radical polymerization under dark conditions. After 3 hours, the resulting hydrogel was purified with water to remove the unreacted species (monomers and redox mediators), then it was freeze-dried overnight (HGCM). Despite the fact that g-CN based hydrogels are appealing as g-CN nanosheets can be employed as photoinitiators to form covalent species, by this chapter's study, external initiators were employed to embed g-

CN nanosheets within hydrogel network.²⁰⁵ In addition, a comparative sample was prepared by the same procedure in the absence of g-CN.

5.2.1. *Hydrophobic Hydrogels Synthesis*

Recently, utilization of hydrogels in nutrient delivery in agricultural science and long-term drug delivery experienced significant interest.²⁰⁹ Most of these methods require aqueous formulations to be delivered over a certain amount of time, yet a hydrophobicity for a long-term open-air application must be possessed in order to prevent the drying and loss of cargo.²¹⁰ Hydrophobic hydrogel is a novel concept that administers the surface properties of the initial network. In this section, we will propose a straightforward photo-based surface modification to introduce hydrophobicity on a hydrophilic network by taking advantage of the photoactive g-CN nanosheets. As explained in the preparation section, the resulting HGCM was immersed in a hydrophobic monomer 4-methyl-5-vinylthiazole, denoted as vTA, then exposed to visible light irradiation to initiate in-situ surface photo modification. Extensive studies over the last years demonstrated photoinduced g-CN surface modification methods through a photoredox system. vTA, a common food additive to donate a nutty taste, has previously shown a significant hydrophobization effect on bulk g-CN,²¹¹ so that a similar strategy is targeted for the present case in hydrogel systems (**Scheme 5.2**). After adequate light irradiation followed by a facile purification step, the resulting sample (HGCM-vTA) and HGCM were investigated via solid-state analysis to evaluate vTA incorporation, and microscopy techniques were employed to examine the impact on their morphology. In terms of applicability, water contact angle measurement, equilibrium swelling ratio analysis, and dye releasing efficiency experiments were also conducted.



Scheme 5.2. Hydrophobic hydrogel via photoinduced surface modification over embedded g-CN nanosheets in hydrogel network.

All hydrogel samples were characterized via FT-IR analysis to elucidate structural footprints of CM embedding and vTA photografting. The broad peak in the range from 3639 cm^{-1} to 3136 cm^{-1} corresponds to the hydrogen bonding between carboxyl and hydroxyl groups with the amide functionality of the hydrogel backbone. Significant stretching at 1620 cm^{-1} is typical for carbonyl groups of amides (**Figure 5.1a**). Thereupon, characteristic hydrogel vibrations explicitly vary according to the applied processes. The major difference between HG and HGCM is the significant peak sharpness around 3274 cm^{-1} , which can be related to $-\text{NH}_2$ functional group stretching relying on buried g-CN structure in the hydrogel network. vTA photografting can be revealed via distinctive signals such as the emergent peak at 3081 cm^{-1} corresponding to C-H aromatic stretchings arising from the thiazole ring, the neck at 1687 cm^{-1} signifies the C=N vibration band, and at last, the intensified peak at 1419 cm^{-1} indicates C-N stretching of the thiazole ring.

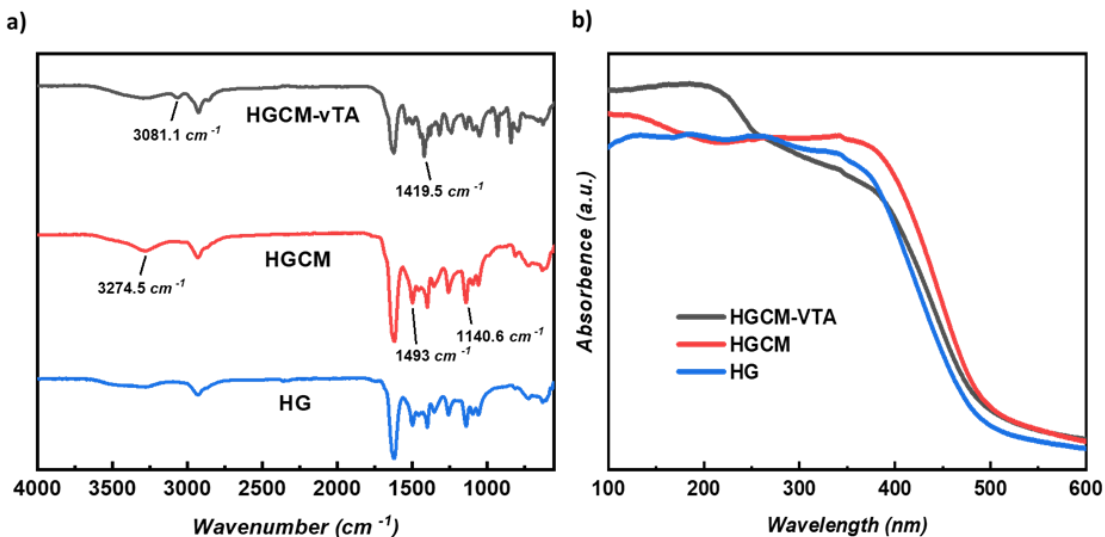


Figure 5.1. a) FT-IR spectra of freeze-dried HGCM-vTA, HGCM and HG. b) UV spectra of freeze-dried HGCM-vTA, HGCM and HG.

Proceeding with the examination by UV-vis spectroscopy, overlaid absorption spectra of the samples revealed the photophysical differences as expected, since HG does not consist of photoactive g-CN particles in contrast to HGCM and HGCM-vTA. Moreover, altered HGCM absorbance after surface modification provides enhanced absorption in deep UV range (**Figure 5.1b**). In addition, digital images of HG, HGCM, HGCM-vTA under UV light irradiation also reveal their emissive properties (**Figure S5.1**).

Scanning electron microscopy is performed to investigate the morphology of freeze-dried HGCM and HGCM-vTA. As shown in **Figure 5.2a**, HGCM exhibits a significantly porous and uniform morphology. The formation of accessible pores for vTA was the key point to activate g-CN nanosheets buried in the hydrogel to perform a photoinduced modification. It must be mentioned that the light transmission is limited since the hydrogel substrate is not fully transparent, and this envisions the importance of porosity as a key factor to diffuse and reflect the incoming light that can reach embedded g-CN nanosheets to enhance the modification.

Surface transformation has drastically changed the parental hydrogel morphology. Closure of pores (**Figure 5.2**) are the supportive evidences for a successful modification

as they are not observed in parental hydrogel (**Figure 5.2a**). Besides, the elemental mapping results of HGCM-vTA exhibit a sulfur content allocation in accordance with the nitrogen atom distribution in a fair amount of abundance (**Figure 5.2b**). Determination of sulfur content is a facile approval for the surface modification as neither monomers nor g-CN from HGCM possesses a sulfur atom (**Figure 5.2a**).

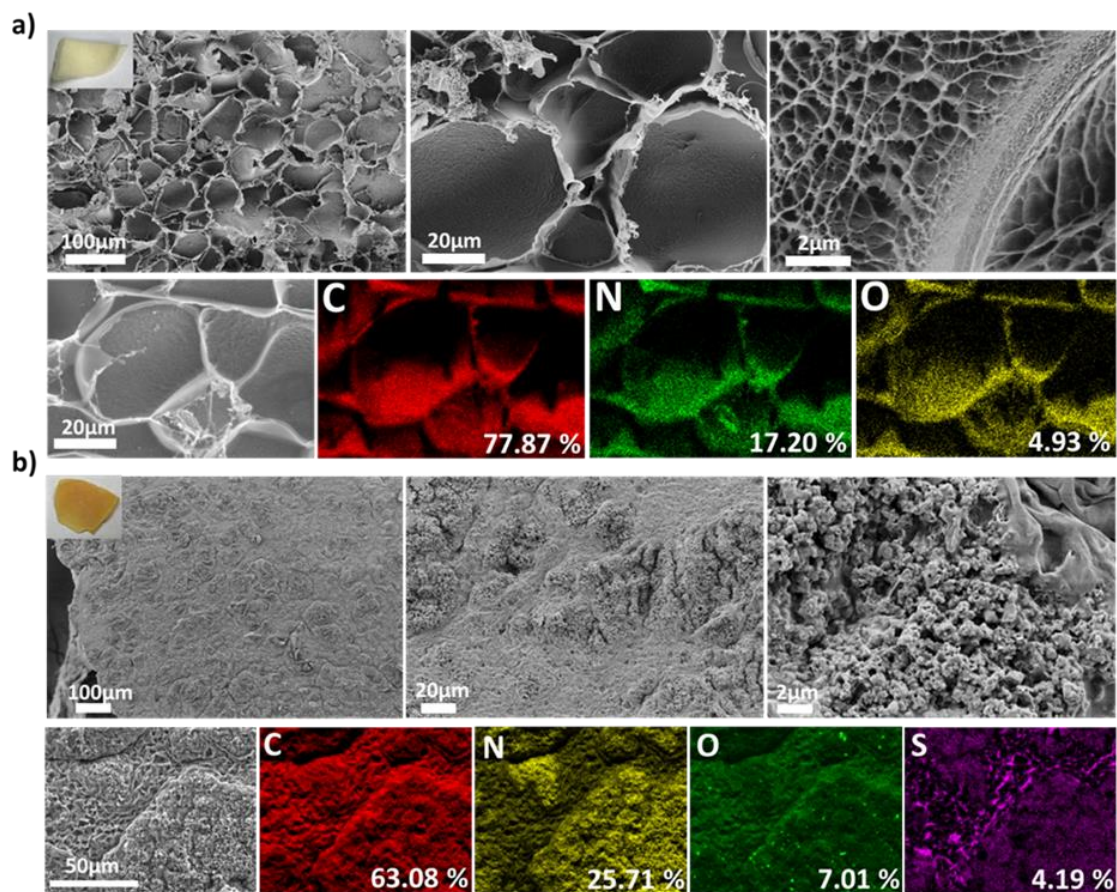


Figure 5.2. Scanning electron microscopy (SEM) images of a) HGCM and b) HGCM-vTA in combination with their elemental mapping results via EDX.

As we attempted to modify HGCM surface from hydrophilic to hydrophobic, the corresponding material surface wettability is expected to be influenced. To investigate this, wet forms of HGCM and HGCM-vTA were subjected to a water contact angle (WCA) measurement by utilizing multiple contact points (**Figure S5.2**). The most stable result regarding the smooth and unwrinkled contact point of HGCM-vTA has resulted in 58.5° over 40 seconds, and the other spots have resulted in 77.8° and 68.3° . On the other

hand, HGCM showed a super hydrophilic character by imbibing the water with high-speed that even imaging was not possible.

It is known that the competition between the hydrophobic and hydrophilic character of hydrogels has a role in affecting water absorption and retention. In this regard, synthesized hydrogels were subjected to a swelling measurement to reveal their overall water affinity, and then TGA measurement was conducted to examine the water retention performances. The swelling ratio results showed that the surface hydrophobization led to a significant decrease, nearly 50 % of the unmodified samples (**Figure 5.3a**). Following that, water retention performances of HGCM and HGCM-vTA were investigated after leaving the samples to dry at room temperature for 2 days before conducting the TGA measurement (**Figure 5.3b**). TGA profiles did not indicate a significant difference in water retention, but the thermal stability of HGCM-vTA within the range of 150 °C to 318 °C has improved. Considering the water retention, the first trials of the hydrophobization process were designed to perform the hydrophobization with the swollen sample instead of using freeze-dried versions to take advantage of entrapped water that might provide the opportunity to control water retention. Unfortunately, during the photomodification, diffusion of vTA molecules has driven the water molecules outside the network. Despite this fact, the wet-modified sample resulted in a fair water contact angle result but, however not enhanced water retention. Another parameter on the water swelling was the effect of g-CN presence. It was observed that the presence of g-CN in hydrogel did not affect the water swelling ratio compared to reference hydrogel, which is reasonable in terms of the physicochemical nature of hydrophilic hydrogels.

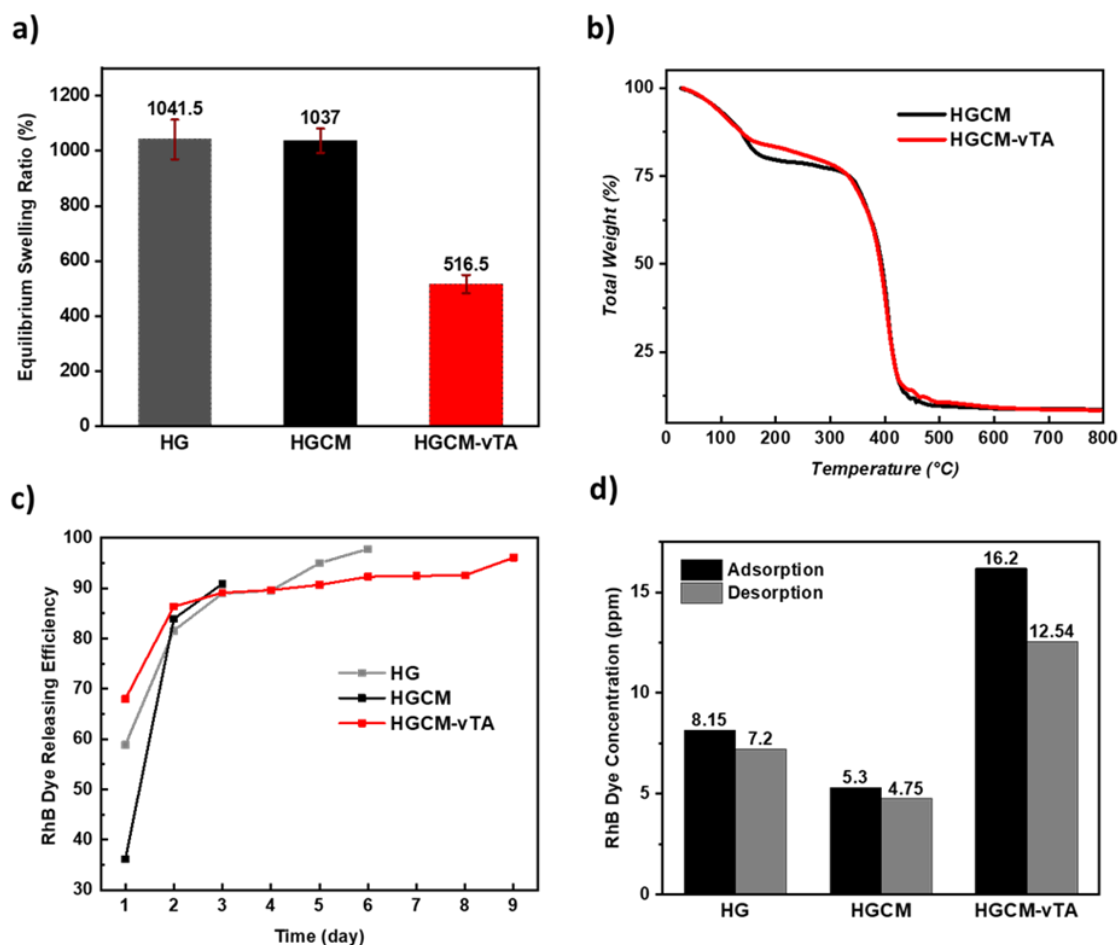


Figure 5.3. a) Equilibrium swelling ratios of HG, HGCM, HGCM-vTA at specified time intervals. b) Thermogravimetric analysis of HGCM and HGCM-vTA. c) RhB dye releasing efficiency versus time plot of HG, HGCM, and HGCM-vTA. d) RhB dye adsorption/desorption concentrations of HG, HGCM, HGCM-vTA.

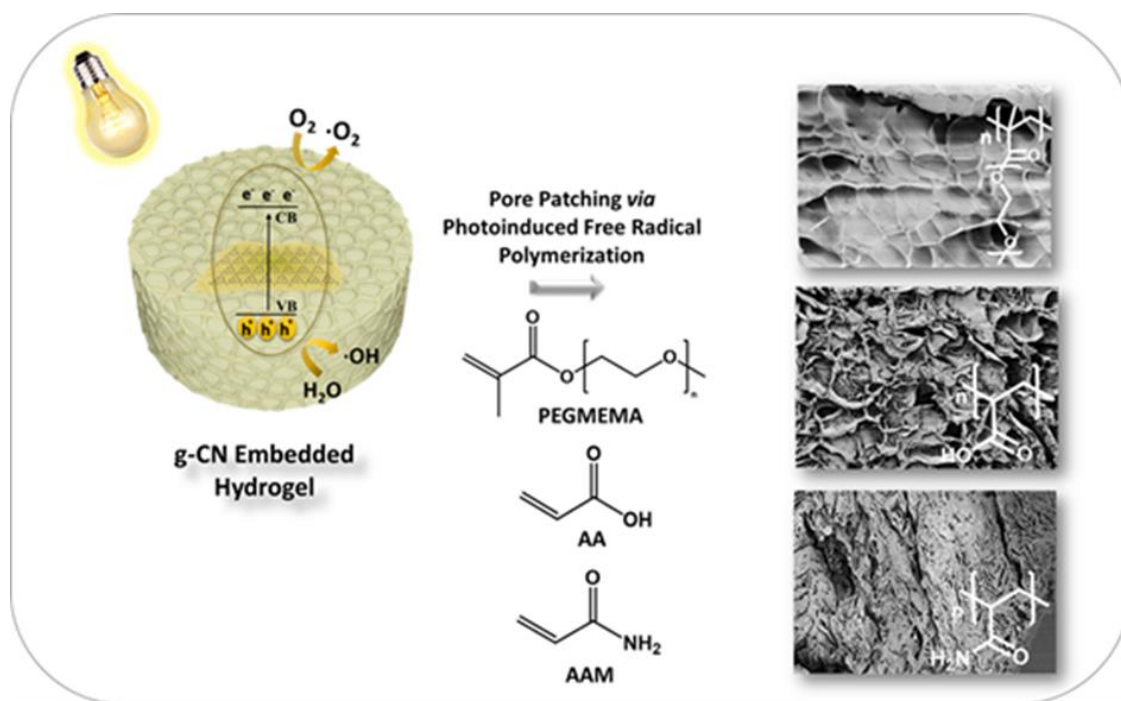
After the swelling experiment, samples were contacted to an aqueous RhB dye solution to investigate their dye releasing efficiency by gradually washing out the samples, in order to mimic a drug or nutrient release. One of the attractive applications of g-CN relies on the adsorption and/or photodegradation of dyes. Generally, these performances are reported on bulk g-CN materials, such as the self-standing ultra-long porous g-CN wires exhibiting outstanding RhB adsorption values by minimized solvent uptakes.²¹² In our case, we focus on the RhB releasing profiles of RhB swollen hydrogels. HG, HGCM, and HGCM-vTA were immersed in RhB solution for 24 hours, then washed with distilled water every 24 hours, and all collected samples were investigated by UV-vis spectroscopy

until reaching the minimum dye absorbance (**Figure 5.3c-d, Figure S5.4**). According to the released RhB dye concentration versus time plots of all samples, HGCM-vTA completed dye releasing with the longest time period of 9 days. It was followed by HG, which resulted in 6 days whereas HGCM was accomplishing the process in 3 days (**Figure 5.3c**). Besides, according to periodically collected RhB dye concentrations summed up and compared with adsorption concentrations for each sample (stock RhB concentration:40ppm), HG released 88% of adsorpt RhB dye in 6 days, HGCM 89% in 3 days, and HGCM-vTA 77% in 9 days (**Figure 5.3d**). In addition to RhB dye, albumin–fluorescein isothiocyanate and fluorescein isothiocyanate-dextran fluorescent probes were subjected to HGCM and HGCM-vTA samples with a comparatively shorter releasing experiment than the one performed for RhB dye (**Figure S5.4a**). Static experiment principally relies on physical adsorption/releasing performance being under the control of intermolecular interactions. Hydrophobization might enhance the hydrophobic interactions between the dye core and the polymer network, thus releasing can be achieved in a longer term. As a last simulative experiment, cation (K^+ , Ca^{2+} , Mg^{2+}) releasing performances of HGCM and HGCM-vTA after an overnight immersion in separately prepared stock solutions were analyzed via ICP-OES (**Figure S5.4b**). HGCM shows higher cation releasing which might be driven by osmosis however, HGCM-vTA retains cations thus offering a slower release which is highly beneficial for agricultural delivery systems.

This grand outcome of embedded g-CN based surface photomodification has significant advantages in terms of its non-toxic process and cost-efficient material resources.

5.2.2. *Pore Substructuring*

In porous materials, the functionality of the pores is responsible for the main catalytic activity, such as in carbonaceous materials.²¹³ When a network with full functionality can not be formed easily, one can form a rigid neutral host and modify the pores subsequently. Herein, the nanoporous system is magnified to macropores in a hydrogel systems as a representative synthetic approach to modulate porous structures of hydrogels with secondary polymers via visible light induced reaction. The photoactivity of g-CN materials are attractive in this sense as covalent modification of the surface of g-CN has offered a versatile post modification platform.²¹⁴ The as-prepared hydrogel network (HGCM) was immersed in various acrylic monomers. Following that, photo-induced free radical polymerization of employed monomers performed under visible light irradiation by taking advantage of embedded g-CN nanosheets in HGCM. According to the literature, g-CN as an organic semiconductor is utilized in polymerization processes as a photoinitiator by generation of reactive radical species ($O_2^{\cdot-}$, HO^{\cdot} , HO_2^{\cdot}) under convenient light illumination. The ability of g-CN to initiate polymerization and act as a polymerization locus for a covalent polymer growth has been investigated in detail in literature.^{206a, 215} Inspired by these, we now attempt to conduct a pore modification on g-CN embedded hydrogels by visible light induced reaction. HGCM was a host network and the variety of monomers were swollen in the network, polymerized, and purified (**Scheme 5.3**). After the polymerization was completed, polymer networks were purified as delineated in the experimental section. Altered pore morphology was investigated by SEM, and functional group analysis was achieved by FT-IR.



Scheme 5.3. Overview of pore substructuring via photoinduced free radical polymerization over embedded g-CN nanosheets in hydrogel network.

Enrichment of hydrogel network with subsequent radical polymerization using various acrylic monomers possessing different functional groups were explicitly confirmed via FT-IR (**Figure 5.4**). Regarding polyacrylic acid-based system (PAA), the broadened signal from 2730 cm^{-1} to 3703 cm^{-1} and sharp signal at 3303 cm^{-1} corresponds to O-H stretching of carboxylic acid group. The peak appearing at 1723 cm^{-1} can be attributed to asymmetric C=O group stretching vibrations of carboxylic acid groups on PAA chains. Polyacrylamide-based (PAAM) pore substructure spectrum is exhibiting the typical -NH stretching vibrations at 3420 cm^{-1} and the band at 1656 cm^{-1} is corresponding to the strong primary amide C=O stretching vibration of amide group. The strong signals at 1558 and 1404 cm^{-1} are originated from amine N-H bending and scissoring -CH₂- vibrations, respectively. At last, poly(ethylene glycol) methyl ether methacrylate -based (PEGMEMMA) network displays O-H stretching from 3106 cm^{-1} to 3710 cm^{-1} relying on pendant hydroxyl groups of PEG structure, the signal at 1719 cm^{-1} is corresponding to C=O group stretching and the more pronounced intensities from 980 cm^{-1} to 1202 cm^{-1}

are attributed to C-H bending and C-O stretching vibrations. Consequently, all FT-IR spectra results confirm the photoinduced polymerization within the hydrogel network.

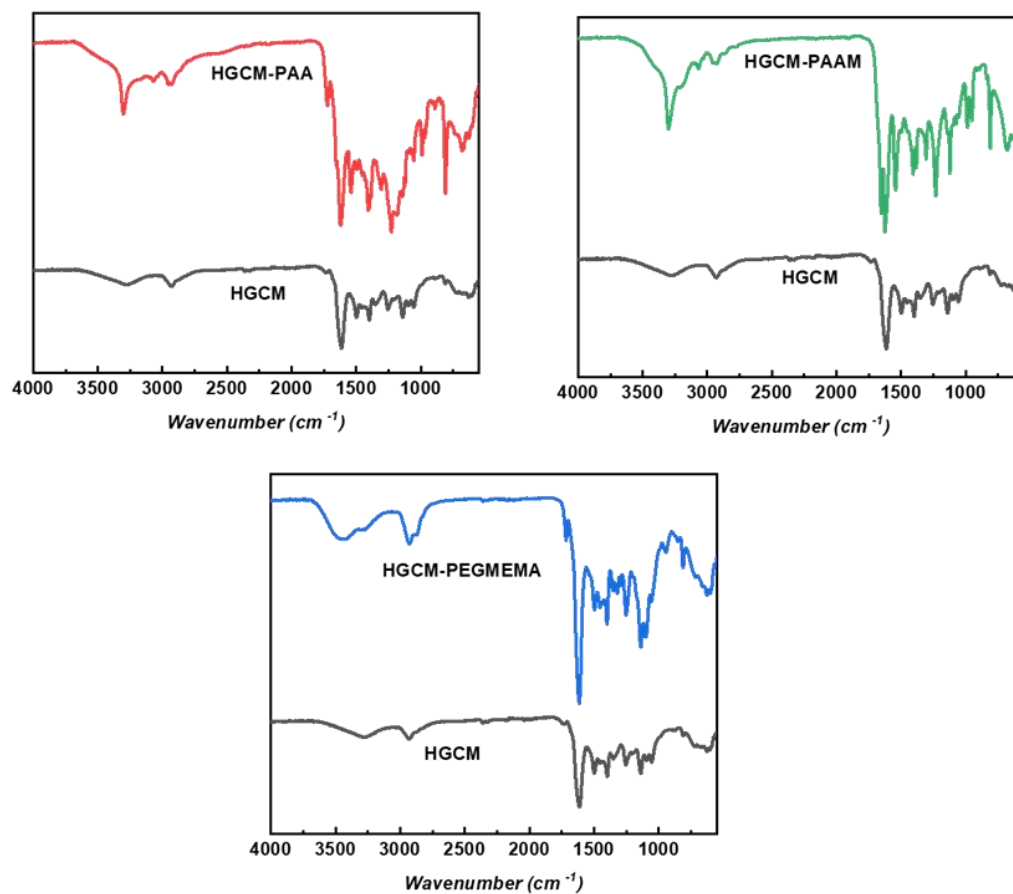


Figure 5.4. FT-IR spectra of freeze-dried HGCM-PAA, HGCM-PAAM, HGCM-PEGMEMA in comparison with HGCM.

Visible light irradiation leads to a polymerization of monomers within a three-dimensional hydrogel network, thus one can expect altered pore morphologies. In that regard, SEM images are useful to explore the pore substructuring for each type of polymer, which are compacted and attached to the hydrogel skeleton (**Figure 5.5**). The morphology of HGCM as a main substructure was already investigated in the previous chapter. Considering HGCM porous structure as a reference point, HGCM derived hydrogels demonstrated altered pore structures based on the type of the interpenetrated

polymer. While PAA and PEGMEMA formations mostly bound intrinsically surface-attached, PAAM exhibited comb-like strands by connecting two junction points on the substrate. The reason of this might be both topological selectivity of polymers and the arbitrary photopolymerization process. In addition, we were not able to identify free polymer chains during the purification process, which indicates a covalent growth of polymers on a hydrogel host.

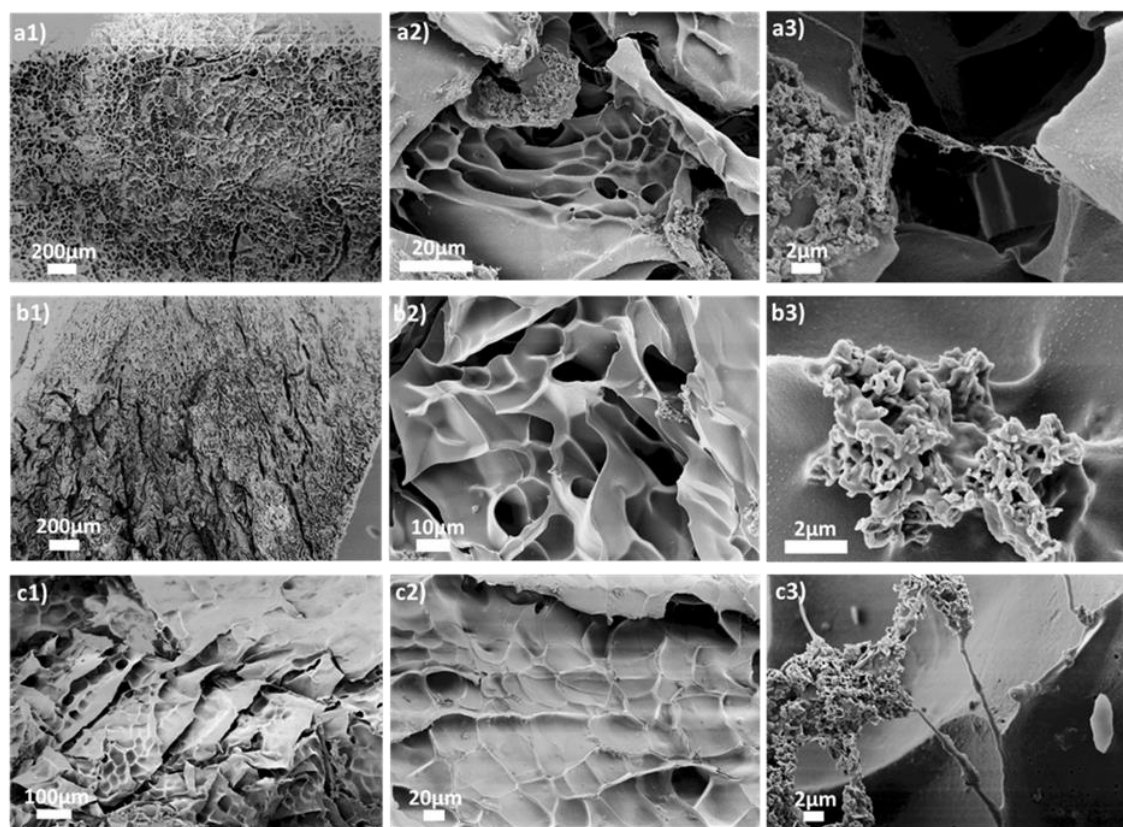


Figure 5.5. Scanning electron microscopy (SEM) images of a) HGCM-PAA, b) HGCM-PAAM, and c) HGCM-PEGMEMA.

It is expected that pore modification on networks will influence the thermal stability of the initial substrate. Regarding this, thermogravimetric analysis results confirmed the enhanced thermal stability for each employed polymer network compared to the initial substrate (**Figure 5.6a**). HGCM curve indicates the evaporation of entrapped water (up to 150 °C) followed by structural decomposition starting from 307 °C and ending with 8.44% total weight at 800 °C, at the first place. HGCM-PAA maintained thermal stability up to

305 °C with 8.4% mass change and resulted in 12.6% total weight whereas HGCM-PAAM was stable up to 250 °C with 7% mass change ending up with 13.4% total weight. At last, HGCM-PEGMEMA exhibited thermal stability up to 307 °C with 13% mass change and resulted in 8.5% total weight. When the temperature range between 160°C and 300°C is subjected for all curves, it can be concluded that the occupied pores by subsequent polymer networks are providing the thermal stability to parental HGCM substrate.

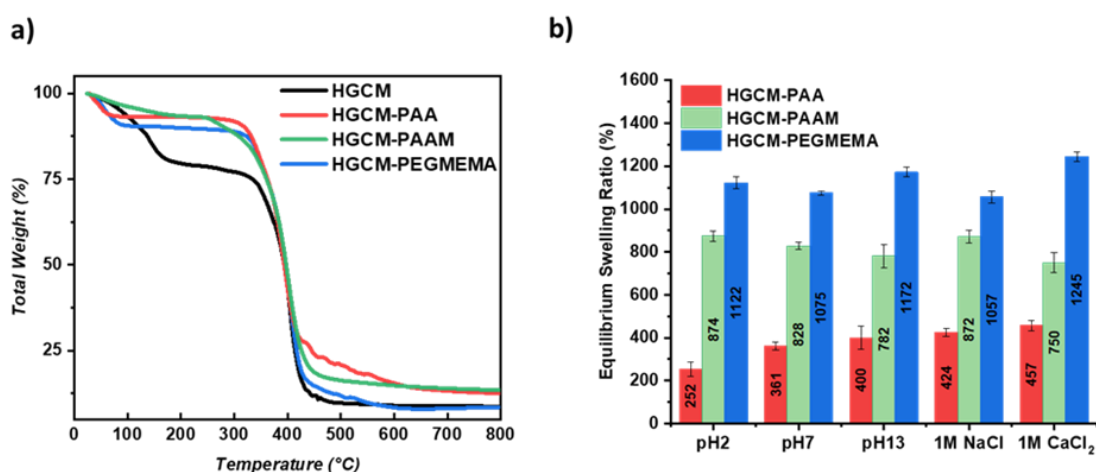


Figure 5.6. a) Thermogravimetric analysis of HGCM, HGCM-PAA, HGCM-PAAM and HGCM-PEGMEMA. b) Equilibrium swelling ratio results of HGCM-PAA, HGCM-PAAM, HGCM-PEGMEMA in various conditions; pH2, pH7, pH13, 1M NaCl, 1M CaCl₂.

Employing a diverse set of monomers to HGCM network can have an influence on the swelling properties as well. Regarding this, swelling performances of so-formed networks were examined via swelling process at an equilibrium state in various conditions (**Figure 5.6b**). The first overall interpretation is that the condition variety did not drastically affect ESR results of each sample. HGCM-PEGMEMA has the highest ESR in every condition that is in good agreement with the nonionic and highly flexible structure of PEG that can resist electrolytes and pH stimuli.

On the other hand, PAAM and PAA depicted significantly decreased ESR results, which are confirming the subsequent network formation by occupying the pores. The gap between the ESR results in each network could be considered as their patching efficiency.

HGCM-PAAM performed a slight decrease from low pH to high pH value due to amine groups' protonation on the polymer backbone via electrostatic attraction, and it responded to monovalent electrolyte with a higher ESR. With the increased pH, HGCM-PAA eventuated with enhanced ESR results arising from the dissociation of carboxylic acid groups. Swelling in saltwater conditions demonstrated similar results, yet significantly lower compared to previous examples.

In addition, the error margins of equilibrium swelling behavior were affected by isotropic accretion of polymer networks over the substrate. It is important to underline that the presented polymerization process relies on a light access in the porous network, so conducting the reaction on thin substrates is favored.

5.3. Conclusions

Embedding photoactive g-CN nanosheets in hydrogels could be an advanced trick to access photoinduced post-modification. The pores of the dried hydrogel can be filled with the precursor of a secondary network, and a visible light illumination forms an extended network with interlocked character. Alternatively, hydrophobization of a hydrogel can be attained by visible light induced photografting of vinyl thiazole groups. In the present chapter, two straightforward synthetic pathways for hydrogel post-modification are presented, and final products could be of great interest from the material science perspective. Visible light induced post modification technology by semiconductors on porous networks could be extended to other porous systems as well, such as carbonaceous networks.

Chapter 6

Oxidative Photopolymerization of 3,4-Ethylenedioxythiophene (EDOT) via Graphitic Carbon Nitride: A Modular Toolbox for Attaining PEDOT*

Carbon Nitride as Heterogeneous Photocatalyst

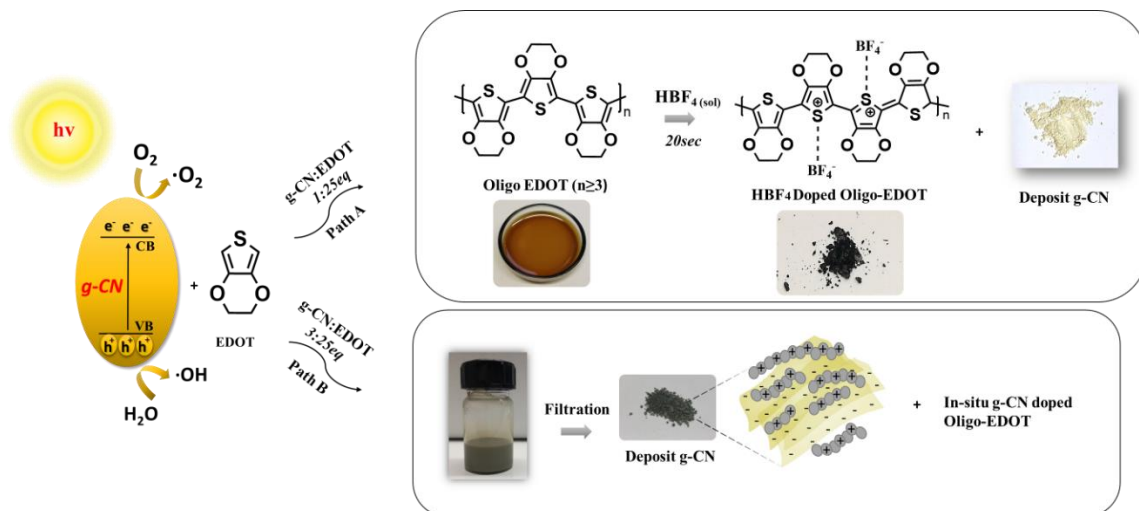
6.1. Overview

Conductive polymers found key applications ranging from optoelectronics and OLEDs to conductive composite materials. The synthesis of conductive polymers from monomers such as thiophene derivatives, pyrroles, and aniline mainly relies on oxidative polymerization, and the processing of so-formed (insoluble) polymers is a major issue that needs to be addressed. In this chapter, oxidative photopolymerization of 3,4-ethylenedioxythiophene (EDOT) by visible light employing the metal-free semiconductor graphitic carbon nitride (g-CN) is presented. Two main reaction pathways based on g-CN content will be described, and the formation of processable oligo-EDOT will be demonstrated.

Conductive polymers have introduced a novel dimension in polymer science, that is the capability to manufacture organic matter that conducts electrons.²¹⁶ Ever since, many conductive polymers have been presented, such as polyacetylene,²¹⁷ polyaniline,²¹⁸ polypyrrole,²¹⁹ and thiophene based polymers.²²⁰ The application range of such conductive materials span from OLED materials, thermoelectrics, photovoltaics, electrochemistry, optoelectronics and biomedical.²²¹ 3,4-ethylenedioxythiophene (EDOT) has withdrawn special attention as even in the doped state it exhibits high conductivity as well as stability.²²² Polymerization of EDOT can be performed via three methods: coupling reaction of halogen substituted EDOT derivatives,²²³ electrochemical polymerization²²⁴, and oxidative polymerization by oxidative agents.²²⁵ The so-formed PEDOT is a black insoluble material with very restricted processability.²²⁶ For example, electrochemical polymerization grants formation of PEDOT only on conductive surfaces.²²⁷ To overcome this problem, researchers have added poly(styrene sulfonic acid) (PSS) during oxidative polymerization of EDOT catalysed via FeCl_3 or $\text{Fe}(\text{Tos})_3$ in water, which provides a water dispersible PSS doped PEDOT material.²²⁸ Despite the processability is gained via PSS addition, the polymer properties are lowered compared to pure PEDOT analogue.²²⁹ Other methodologies that would endorse the synthesis of a processable PEDOT are certainly welcomed.

Graphitic carbon nitride (g-CN, g- C_3N_4) is a semiconductor polymer that is mainly composed of nitrogen and carbon atoms in a conjugated framework, such as tri-s-triazine.²³⁰ g-CN represents a family of materials with facile tunability such as bandgap, work function, surface properties and elemental doping in the framework.^{19b, 166b} Furthermore, its non-toxic and highly stable character, together with the synthesis from low-cost and abundant precursors (i.e., melamine, urea, dicyandiamide), place g-CN as a new generation semiconductor to be investigated in fields such as photocatalytic water splitting, CO_2 reduction, pollutant degradation and light-induced sanitization.^{199a, 203, 231} For instance, Kui Li et.al recently reported a graphitic carbon nitride integrated multicomponent nano-composite via dual ligand adopted hierarchical-MOFs which shows enhanced H_2 generation in water.²³² Furthermore, the integration of g-CN into

polymer systems is expanding.²³³ Embedding a charge transfer mediator consisting of conductive polymer as a heterostructure onto g-CN resulted in a highly efficient dual noble-metal-free cocatalyst designed by Kui Li and co-workers.²³⁴ So far, g-CN has been employed as a heterogeneous photoinitiator for polymer synthesis,^{50b, 50d} alternatively g-CN dispersions were utilized for hydrogel synthesis¹⁷⁰ and for heterophase polymerizations.²¹⁵ Also, the combination of g-CN with conductive polymers is full of opportunities²³⁵ however, this method is restricted by means of processing techniques. Formation of g-CN-PEDOT:PSS composites reported in the literature are obtained through blending method to enhance the photocatalytic efficiencies,²³⁶ however, g-CN assisted PEDOT synthesis was not yet described. This chapter will present the utilization of g-CN as a photoredox type photoinitiator for oxidative photopolymerization of EDOT via visible light. Two different pathways to promote oligo-EDOT processing at different g-CN concentration will be demonstrated, i.e. processable oligomeric liquid oligo-EDOT (Path A) and in-situ g-CN doped oligo-EDOT composites (Path B) (**Scheme 6.1**).



Scheme 6.1. Oxidative photopolymerization of EDOT via g-CN.

6.2. Results and discussion

g-CN photocatalyst was synthesized by thermal condensation of cyanuric acid-melamine supramolecular complex as reported in the literature²⁰⁸ to obtain a yellow powder material. Following that, g-CN in different proportions (100 or 300 mg) are mixed with 2 mL EDOT and stirred under visible light irradiation for 24 hours at room temperature. A simple filtration is sufficient to separate the catalyst from the product thus, both can be independently analyzed. Catalyst amount granted two synthetic pathways, path A (100 mg g-CN) promotes dark-brown oligo-EDOT formation together with unaltered g-CN powder, and path B (300 mg g-CN) exhibits in-situ g-CN oligo-EDOT formation, with oligo-EDOT finally deposited on g-CN powder by electric charge compensation.

The crystal structures of all g-CN powders (pristine catalyst is denoted as g-CN, g-CN isolated from path A is denoted as g-CN R1, and g-CN isolated from path B is denoted as g-CN R2) can be investigated via powder XRD. All three samples demonstrate the two typical peaks corresponding to (100) and (002) planes at 13° and 27° , representing intralayer spacing and interlayer sheet-sheet spacing, respectively (**Figure S6.1a**).²⁰⁸ However, a significant enhancement on the (002) plane intensity was observed for g-CN R2, which can be ascribed to an oligo-EDOT deposition. g-CN possesses a strong light absorbance between 270-450 nm (**Figure S6.1b**) thus rendering it suitable for a visible light-driven photoredox reactions.²³⁷ As depicted in **Figure S6.1b**, the spectrum of pristine g-CN overlays with the one of g-CN R1, thus indicating that the g-CN R1 remained photophysically unchanged after photopolymerization initiation. In the case of g-CN R2, an intensified and broader absorbance was recorded which confirms strong electronic coupling by conjugation of oligo-EDOT on the g-CN surface. In addition to that, oligo-EDOT deposition on g-CN R2 can also be observed from thermogravimetric analysis which shows enhanced thermal stability in comparison with other g-CN samples (**Figure S6.1c**). FT-IR analysis was carried out for all g-CN samples, and similar spectra for all three samples were obtained, C-N conjugated ring vibrations in the range of $1255\text{-}1630\text{ cm}^{-1}$, triazine motif vibration around 810 cm^{-1} and $\text{-NH}_2 + \text{-OH}$ bands around 3250 cm^{-1} (**Figure S6.1d**). Furthermore, elemental compositions of all g-CN samples were

determined via combustive elemental analysis, which confirms the similarity between pristine g-CN and g-CN R1, but an enhanced sulfur content of g-CN R2 arises from oligo-EDOT deposition which also allows the quantification of its content (**Table S6.1**). Following that, homogeneously distributed sulfur and oxygen content linked to a oligo-EDOT deposition on g-CN R2 was also observed by elemental mapping analysis via EDX (**Figure S6.2**). At last, Tauc plots derived from UV absorption of CM, and CM R1 and CM R2 at a specified range are presented in **Figure S6.3** with calculated bandgap values at g-CN absorption maximum. As expected, CM (2.89 eV) and CM R1 (2.84 eV) exhibited quite a similar band gap values, unlike CM R2 (2.76 eV), which was based on shifted absorption spectrum caused by oligo-EDOT deposition.

After the oxidative photopolymerization of colorless EDOT, the resulting liquid oligo-EDOT (after separation of g-CN) undergoes significant darkening compared to EDOT. Generally, the pitch black color of oligo-EDOT arises from its fully oxidized state however, a photoredox synthesis can not donate a full oxidation, so a linear oligo-EDOT with moderate oxidation is obtained in the present case. In order to get more insight about eventual molecular weight, UV-vis spectra were applied as inspired by the literature (**Figure S6.1a**).²³⁸ The significant bathochromic shift on UV-vis spectrum from 450 nm to 650 nm is explicated as a sign of increased molecular weight of EDOT based on extended conjugated units. It should be noted that a reductive pre-treatment is subjected to conduct neutral stated PEDOT in the literature however, as the procedure is compatible for simultaneously assisted PEDOT coupled materials, e.g., PEDOT:PSS or PEDOT-Lignosulfonate but not to our conditions, it was not performed before the measurement and by this reason, an intensified peak at 389.31 nm detected as a sign for oligo-EDOT formation instead of a significant red-shifting. Moreover, when the reaction went under argon atmosphere, the intensity of the peak, which was attained to oligo-EDOT formation, has lowered as a correspond to the lack of oxygen. Following that, photoluminescence spectra of oligo-EDOT showed broad emission with λ_{\max} 417 nm as a sign of π - π^* transition in its as-formed conjugated system (**Figure S6.4b**).

Not only by means of color, but an enhanced viscosity of oligo-EDOT compared to EDOT was measured (**Figure S6.5**), which hints toward oligomer formation. Furthermore, structural investigations of liquid oligo-EDOT were performed via FT-IR analysis (**Figure 6.1**). The C=C and C-C stretching modes of the thiophene ring are found at 1362, 1443, and 1492 cm^{-1} , the peak at 1585 cm^{-1} indicates the conjugation in polymeric structure, and the ether ethylenedioxy stretching modes are displayed at 1180, and 1047 cm^{-1} and finally, the C-S vibration modes appear at 751, 888 and 930 cm^{-1} .²³⁹ All signals and the assignments are in good agreement with the literature, underlining the formation of oligo-EDOT.

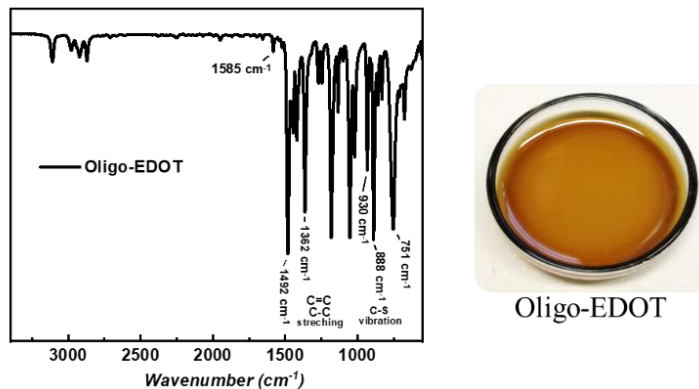


Figure 6.1. FT-IR spectrum of oxidatively photopolymerized oligo-EDOT along with its digital image (after catalyst separation).

It is known that monomers such as EDOT, aniline, and pyrrole are prone to oxidative polymerization and, even further, an in-situ polymerization based upon a redox relay mechanism assisted with non-noble metal can result in a highly efficient catalyst for solar conversion, as reported by Kui Li and colleagues.²⁴⁰ In our case, we have attempted to obtain a possible reaction mechanism. A similar reaction in the absence of air does not yield a polymer product, and the same reaction under oxygen feeding is much more effective, which hints that the oxygen is the species to be reduced to close the photoredox cycle (**Figure S6.6**). Likewise, reaction in the absence of a photocatalyst does not yield any oligomerized product confirmed via unaltered EDOT absorption. The main factor to consider in EDOT photopolymerization is the matching bandgaps, a milestone article which employed perovskite quantum dots for the PEDOT synthesis was only possible

when trimerEDOT was employed as a monomer, and the main mechanism was based on photoformed holes.²⁴¹ Mixture without light irradiation shows no change under the same conditions, which indicates the necessity for the strong oxidation power of the light activated hole in the valence band of carbon nitride to drive the polymerization. From the photoredox chemistry point of view, another question is the fate of the photoformed excited electrons. As EDOT polymerization forms cationic species,²⁴² charge balancing is important for propagation. A similar scenario is observed when PSS is added to EDOT polymerization, on one side, it provides enhanced aqueous processability, and on the other side, it renders a charge balance, thus facilitating the polymerization.²⁴³ It is expected that photoformed holes take a hydrogen from EDOT molecule providing a radical cation in our case. Excited electron activates dissolved oxygen to form $O_2^{\cdot-}$, which balances the positive charge (through ^-OOH) and EDOT molecules undergo radical-radical coupling therefore forming an oligomerization, as depicted in the proposed reaction mechanism (**Figure S6.6**). Advantage of photoredox compared oxidative polymerization is that in the present case, one obtains a PEDOT that is not fully oxidized as no real negative counterions are present. Fabrication of such PEDOT must possess a significant affinity to dissolved negative charges. In order to investigate that, we have performed doping of oligo-EDOT (2 mL) via aqueous HBF_4 solution (0.1 mL). As expected, only in 20 seconds, significant darkening takes place, and a viscous as well as dispersed material is formed.

Regarding FT-IR analysis of post-doped oligo-EDOT, the broadened peak from 3612 to 3153 cm^{-1} along with the reduced signal at 3106 cm^{-1} can be attributed to the integration of the counterion due to doping into the polymeric structure. The bathochromic shift with a broadening from 1550 to 1410 cm^{-1} can be considered as a result of de-doping by reversing the charge carriers through the presence of dopant ion (**Figure 6.2a, Figure S6.7**).²⁴⁴ The structural information of doped oligo-EDOT was investigated via powder XRD that exhibits low-intensity diffraction peaks indicating the amorphous nature of the polymeric material at 12.8° with respect to the two-dimensional arrangement of oligo-

EDOT and dopant ion, whereas the sharp peak at 24.1° represents the ring stacking of the stiff aromatic polymer chains (**Figure 6.2b**).²⁴⁵

The broad UV-vis absorption band of doped oligo-EDOT is typical for organic electron conductors. Furthermore, an intensified peak from 478 nm with λ_{max} 662 nm to 530 nm can be correlated to π - π^* transition of the thiophene ring and the shoulder from 547 nm to 759 nm can be attributed to the oxidized state of oligo-EDOT according to literature (**Figure 6.2c**).²⁴⁶

In order to quantify the thermal stability of post-doped oligo-EDOT, thermogravimetric analysis is performed. The first weight loss occurring from 58°C to 180°C can be attributed to the evaporation of residual water molecules (from HBF_4 solution) in the sample, following that, the step-wise weight losses eventuated in about 40 wt.% residual mass at 800°C (**Figure 6.2d**).

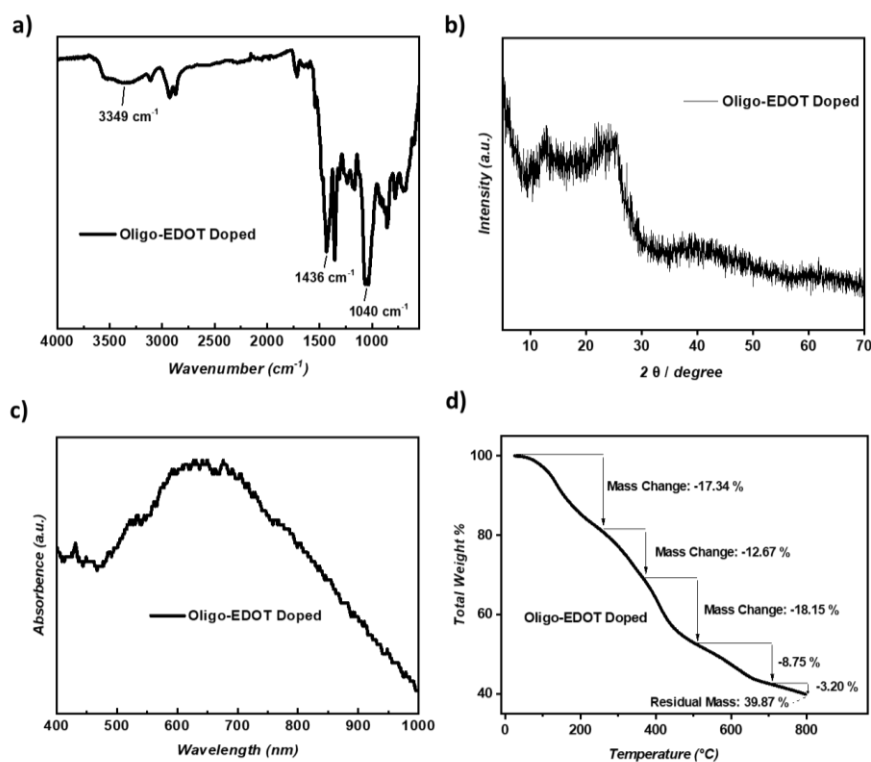


Figure 6.2. a) FT-IR spectrum, b) XRD profile, c) UV-Vis spectrum, d) Thermogravimetric analysis of post-doped oligo-EDOT.

It is known that the thermal decomposition of oligo-EDOT takes place between 300°C and 400°C as reported in publications,²⁴⁷ and employing doped oligo-EDOT as a carbon precursor seems to be very appealing. Therefore, carbonization of doped oligo-EDOT was conducted at 800°C in a nitrogen protected oven. After the carbonization process, doped oligo-EDOT and the resulting carbonaceous material were analyzed via combustive elemental analysis. As expected, carbon content has increased significantly after carbonization, as well as a decrease in hydrogen content was found. The most significant element in this case is sulfur, and a surprisingly high sulfur content (16.5 wt.%) for an 800 °C treated carbon product was observed, which can be of significant interest in catalysis (**Table 6.1**).²⁴⁸

Table 6.1. Combustive elemental analysis results of doped oligo-EDOT and its carbonized product.

<i>Sample</i>	<i>C (%)</i>	<i>N (%)</i>	<i>S (%)</i>	<i>H (%)</i>
Doped Oligo-Edot	47.68	0.54	20.65	3.78
Carbonized Oligo-Edot	71.34	1.1	16.56	0.8

During carbonization, doped oligo-EDOT precursor effortlessly granted access for homogeneous film deposition on the walls of the crucible and on the lid (Figure S5.8), which can be a practically useful observation to decipher the potential of doped oligo-EDOT as a carbon film precursor. SEM characterization and EDX mapping of the carbon powder exhibits the homogeneous distribution of the atoms without any compartmentalization (**Figure S6.9**).

One of the major drawbacks of PEDOT is its processability, especially when applied-scale coating and film formation are required.²⁴⁹ Fabrication of a liquid PEDOT and post-doping brings a significant solution for these issues, and for that, we have performed a coating on glass, metal coin, and ITO-coated glass slide surfaces via dip-coating. SEM images of post-doped oligo-EDOT (a powder obtained from a coating, **Figure 6.3a1**) and its coating on glass (**Figure 6.3a2**) exhibited a perfect planar morphology, and successful coating could be confirmed. Besides its simple processability, the coated film also

possesses an adequate resistance against water over 5 days, and no peeling was observed (**Figure S6.10**). Since the surface coating process is performed effectively, sheet/surface resistivity measurement can be the next step accordingly. Post-doped oligo-EDOT and in-situ g-CN doped oligo-EDOT were applied on ITO coated glass slide via dip coating, and their resistivities were verified via a two-probe multimeter and compared with pristine ITO-coated surface (**Figure S6.11**). The results showed that the sheet resistivity of the post-doped oligo-EDOT film ($20.1 \Omega/\text{sq}$) is lower than ITO surface resistivity ($36.8 \Omega/\text{sq}$), which in reverse means that the conductivity is enhanced with the applied oligo-EDOT film on ITO coated glass surface. This also confirms that the resulting oligo-EDOT and its further post-doping level are eligible to accelerate surface conductivity explicitly. On the other hand, in-situ g-CN doped oligo-EDOT exhibited higher surface resistivity ($1.706 \Omega/\text{sq}$) measured on higher sensitivity scale that indicates a restricted electron movement over the sample compared to post-doped PEDOT (**Figure S6.11c**).

As a final statement for all these promising results that have been reported so far, combining the described procedures with elaborated coating technologies could be of high interest for industrial-scale conductive polymer applications.

Increasing g-CN content for oxidative photopolymerization of EDOT again reveals an unusual composite system. As discussed above, the product from this reaction (g-CN R2) is a g-CN coated with oligo-EDOT, thus presenting a straightforward mechanism to form g-CN oligo-EDOT composite materials. As oligo-EDOT remains on g-CN surface despite long purification processes, we assume direct charge conjugation between a negatively charged g-CN and the positively charged doped oligo-EDOT. This can be related to the ability of g-CN to store and buffer a rather high amount of photogenerated electrons and the coupled negative charges,²⁵⁰ which then- instead of a low molecular weight counterion- compensate the positive charge of oligo-EDOT in the hybrid structure. Such hybrids are very stable, as they cannot be resolved by a simple oxidation or reduction process, as then always the opposite charge is left unbalanced, and only the addition of special ion pairs can destabilize the structure. In addition to stability, the presence of

oxygen might affect the storage stability of as-prepared oligo-EDOT therefore, it is recommended to store freshly synthesized samples with an inert gas purge.

g-CN is well-dispersed in the polymer media and dopes oligo-EDOT in addition. In-situ g-CN doped oligo-EDOT is captured by optical microscopy under normal and polarized light (**Figure 6.3 b1, b2**) which confirms the dispersion of g-CN particles in oligo-EDOT phase. The fact that spontaneous charge transfer at the semiconductor-semiconductor occurs according to their work function is a classic phenomenon of semiconductor physics, but rather rarely used for electronically diverse aromatic semiconductors in solution or dispersion.²⁵¹ One can say that the electronically very diverse oligo-EDOT and g-CN undergo a mutual doping effect, potentially highly accelerated by light irradiation.

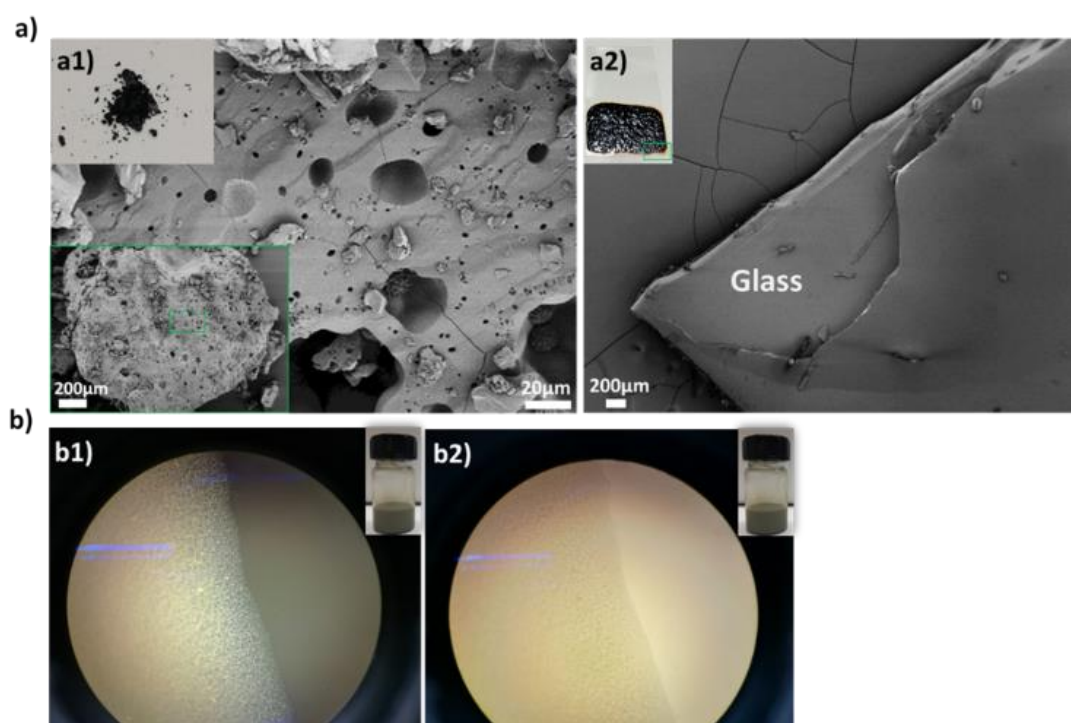


Figure 6.3. a) Scanning electron microscopy images of powder post-doped oligo-EDOT (a1) and coated post-doped oligo-EDOT coating on glass (a2). b) Optical microscopy images of in-situ g-CN doped oligo-EDOT under polarized (b1) and normal light (b2).

6.3. Conclusions

The metal-free semiconductor g-CN can be used for the oxidative photopolymerization of EDOT with visible light. A one-pot synthetic procedure in the presence of oxygen was presented, and the high selectivity of g-CN oxidation allows neutral oligo-EDOT formation but stops before oxidative doping when other ions are absent. Throughout this process, no polymer precipitation is obtained, films can be formed, which then can be post-doped to generate conductive and insoluble films and coatings. On the other hand, utilization of excess g-CN facilitates the formation of a hybrid heterojunction material where oligo-EDOT is deposited on g-CN powder through surface polaron formation. Furthermore, the organic oligo-EDOT phase is in-situ doped with g-CN nanosheets through a negative surface charge, thus offering a novel avenue of semiconductor heterojunctions. Overall, a simple, light-induced procedure to manufacture highly functional materials enabled by g-CN will be highly impacted in polymer chemistry and catalysis fields.

Chapter 7

Conclusions

This thesis elucidated various cases of light-driven integration of graphitic carbon nitride in polymeric networks spanning from resin type cross-linked beads to soft-matter like hydrogels, from a conductive materials (e.g., PEDOT) to synthetic hybrid thiol-ene beads. Simplicity of chemical approaches has been the primary focus, and the use of light to form advanced materials was the central theme.

In the third chapter, organodispersible carbon nitride (CMp-vTA) utilization in PS-DVB bead fabrication via suspension photopolymerization was demonstrated. Adequately dispersed vTA-CMp in 1-octanol, furtherly combined with organic monomer (St) and crosslinker (DVB), mixed with aqueous phase under agitation, succeeded in forming stable droplets which are isolated as solid-beads at the end of photopolymerization initiated under UV light. Photopolymerization has been accomplished either via using vTA-CMp as photoinitiator or with the addition of commercial photoinitiator (DPO). In each case, vTA-CMp nanosheets remained at the interface of as-formed beads and stabilized the spherical shape during photopolymerization, while a porogen was creating porosity all over the bead, and granting access to light and organic molecules. As a result, a remarkable RhB dye

photodegradation rate (89% degradation efficiency in 5 h, R^2 value of 0.971, and photocatalytic recyclability up to 7 cycles with moderate loss of photoactivity, 55.6%) was achieved. Furthermore, photo-induced surface modification was able to introduce acid-base functionalities throughout the surface (employing either vinylsulfonic acid or 4-vinyl pyridine) under visible light illumination. Besides, tailoring bead size by changing reaction conditions such as crosslinking ratio, the presence of porogen and exploring the role of agitation rate was readily possible. Lastly, pH variation over photodegradation resulted in good stability with no host degradation and dye adsorption/desorption properties based on RhB dye as well as Sudan red 7B and perylene in biphasic systems were quite successful. Concludingly, donating photoactivity to a dormant commercial material by simply dressing it with metal-free semiconductor g-CN was able to create novel photoactive hybrid material.

Following that, **with the fourth chapter of the thesis**, an alternative way of synthesizing thiol-ene polymer beads based on photo-induced polymerization via liquid-liquid printing technique was presented. In this subject, a dispersion of CMP-vTA prepared in chloroform was mixed with multifunctional thiol (tetra thiol) and acrylate monomers (tetra acrylate). The prepared organic mixture was injected in aqueous media, and the as-formed beads kept the spherical shape during photopolymerization which is initiated by CMP-vTA under UV light irradiation. CMP-vTA nanosheets were located exclusively on the surface by liquid-liquid printing principles, and variety of multifunctional acrylate monomers with different organic structures spanning from linear to cycloaliphatic and aromatic side chains were polymerized successfully. The relatively porous beads, were not effective in organic dye photodegradation, however, they possessed high thermal stability which in further allowed carbonization resulting in carbon spheres within fair amounts of sulfur and nitrogen. Interestingly, some of the samples retained their bead shape after carbonization, which can be an interesting subject for catalytic applications. Not necessarily for photocatalytic applications; however, based on molecular engineering, one can obtain advanced carbonaceous materials with extreme ease and scalability.

In the fifth chapter, g-CN (CM) was integrated into a highly porous hydrogel network that was synthesized by redox-induced polymerization (redox couple: ascorbic acid-hydrogen peroxide). DMA monomer and MSA cross-linker were employed in the aqueous dispersion of CM. With this technique, CM nanosheets embedded in pristine hydrogel acting like anchoring points led to two photoinduced post-modifications; in-situ photo grafting of vTA (4-methyl-5-vinylthiazole), which allowed fabrication of a 'hydrophobic hydrogel' and 'pore substructuring' of pristine hydrogel after filling the pores with various vinyl monomers (AA, PEGMEA, AAM), followed by photopolymerization. Transformation of the hydrogel to hydrophobic hydrogel via simple light-driven modification provided control over cation release (K^+ , Ca^{2+} and Mg^{2+}) in addition to effective RhB dye removal. Two fluorescent probes (albumin-fluorescein isothiocyanate and fluorescein isothiocyanate-dextran) were also analyzed for their adsorption/releasing performances. Success is followed by the introduced secondary polymer networks possessing different functionalities (acid, base, neutral), which is directly influenced pristine hydrogel morphology by exhibiting high interpenetration with compact character, described as 'pore substructuring'. In summary, embedding photoactive carbon nitride into a porous hydrogel network turned to an advance trick for obtaining 'hydrophobic hydrogel' and secondary network formation via visible light irradiation.

By the sixth chapter, oxidative photopolymerization of EDOT through g-CN (CM) performed under visible light irradiation was demonstrated. Visible light induced photo-oxidative polymerization resulted in liquid, non-doped oligoEDOT formation which is prone to post-doping in the presence of counter ion (negative). By this approach, the advantage taken from photoredox mechanism over oxidative polymerization was revealed by the formation of a not fully oxidized oligoEDOT that remained open to post-doping owing to the absence of real counterions (negative) during photopolymerization. The resulting moderate viscosity enabled facile filtration of CM from reaction (recyclability), whereas oligoEDOT can be solution-processed. Following up the thermal stability of oligoEDOT up to 800 °C with high residual mass ratio, led the way to investigate

carbonization. As a result, the obtained carbon material exhibited quite high sulfur content which can be very promising as sulfur-carbon material for energy storage applications. In alternative, excess of g-CN resulted in success for synthesizing oligoEDOT as well as a hybrid material, which was oligoEDOT coated g-CN powder showing surface polarons. g-CN can pave the way for novel polymerization mechanisms that are superior compared to traditional oxidative polymerization which requires charged oxidizing agents resulting in precipitated doped polymer, which is mostly not further processable.

Merging metal-free semiconductor g-CN with polymer materials turned out to be extremely exciting and rewarding, especially considering facile, scalable and cheap methodologies to forge materials that can harvest light or being synthesized through light. g-CN can introduce major benefits both in colloidal state and as non-dispersed powder. Advanced polymer composites based on g-CN can answer academic and industrial needs in advanced applications. This thesis has shown resins, hydrogels, thiol-ene resins and conducting polymers with g-CN, with being able to cover only a part of the new options.

8. Appendix

8.1. Materials

1,3,5-Triallyl-1,3,5-triazine-2,4,6(1H,3H,5H)-trione (98%, Sigma Aldrich), 2,4,6-Triallyloxy-1,3,5-triazine (97%, Sigma Aldrich), 2,4,6-Trimethylbenzoyl diphenylphosphine oxide (DPO, 98%, Sigma Aldrich), 2,2'-Azobis(2-methylpropionitril) (AIBN, %98 Sigma Aldrich), 2,4-diamino-6-phenyl-1,3,5 triazine (Mp, 97%, Sigma Aldrich), 3,4-Ethylenedioxythiophene (EDOT, 97%, Sigma Aldrich), 4-methyl-5-vinylthiazole (vTA, 97%, Sigma Aldrich), 4-vinylpyridine (VP, 95%, 100ppm hydroquinone as inhibitor, Sigma Aldrich), 1-octanol ($\geq 99\%$, Sigma Aldrich), L-(+)-Ascorbic acid (AsA, 98+%, Alfa Aesar), *N,N*-Dimethylacrylamide (99.0+%, TCI), *N,N'*-Methylenebis(acrylamide) (MBA, 99%, Sigma Aldrich), *N,N*-Dimethylformamide (DMF, ≥ 99 , Sigma Aldrich), acetone (ACS reagent, $\geq 99.5\%$, Sigma Aldrich), acrylic acid (AA, 99%, Sigma Aldrich), acrylamide (AAM, 98.5%, Acros), albumin–fluorescein isothiocyanate conjugate (FITC-Albumin, Sigma Aldrich), basic aluminum oxide, boric acid (ACS reagent, $\geq 99.5\%$, Sigma Aldrich), calcium chloride (CaCl_2 , 97%, Alfa Aesar), chloroform (HPLC, $\geq 99.8\%$, contains 0.5-1.0% ethanol as stabilizer, Sigma Aldrich), cyanuric acid (98%, Sigma Aldrich), dimethyl sulfoxide (DMSO, 99.9% ACS reagent, Sigma), divinylbenzene (DVB, $\geq 99\%$, 4-tert-butylcatechol as stabilizer, Sigma Aldrich), ethanol (HPLC, $\geq 99.8\%$, Sigma Aldrich), fluoresceinisothiocyanat-dextran (FITC–Dextran, 10.000 MW), hydrochloric acid (HCl, 37%, Sigma Aldrich), hydrochloric acid (1M solution, Sigma Aldrich), hydrogen peroxide (30% aqueous solution, Merck), magnesium chloride (MgCl_2 , 99%, Merck), melamine (99%, Sigma Aldrich), indium tin oxide (ITO) coated glass slide (Rectangular, 8-12 Ω/sq , Sigma Aldrich), pentaerythritol tetraacrylate (contains 350 ppm monomethyl ether hydroquinone as inhibitor, Sigma Aldrich), pentaerythritol tetrakis(3-mercaptopropionate) ($>95\%$, Sigma Aldrich), perylene (Sigma Aldrich), poly(ethylene glycol) dimethacrylate average (PEGDMA, Mn 550, Sigma Aldrich), poly(ethylene glycol) methyl ether methacrylate (PEGMEMA, Mn 300, Sigma Aldrich), polyvinyl alcohol (PVA, fully hydrolyzed,

approx. 145000 Da), potassium chloride (KCl, 99%, Merck), rhodamine B (RhB, 95%, Sigma Aldrich), sodium chloride (NaCl, 99%, Sigma Aldrich), styrene (St, $\geq 99\%$, 4-tert-butylcatechol as stabilizer, Sigma Aldrich), sudan red 7B (Sigma Aldrich), tetrafluoroboric acid (HBF₄, 48% in water, Sigma Aldrich), tetrahydrofuran (THF, anhydrous 99.9%, HPLC grade, Sigma Aldrich), toluene (anhydrous 99.8%, Sigma Aldrich), vinylsulfonic acid sodium salt solution (VSA, 25 wt.% in water, Sigma Aldrich).

St, DVB, DMA, PEGDMA and PEGMEMA were passed through basic alumina column prior to use to remove the inhibitor. Ceramic crucibles for bead synthesis (boat shape 97×17×12mm) were obtained from VWR.

Ultraviolet (UV) light irradiation was performed via 30 W UV chip (Fdit 395-400nm UV LED) connected to a self-made circuit and a cooling system. Visible light irradiation was implemented via two 50W LEDs (Chip Bulb Light DIY White 3800LM 6500 K) connected to a self-made circuit and a cooling system.

8.2. Synthetic Procedures

Chapter 3

Synthesis of organodispersible vTA-CMp via vinyl thiazole photografting: vTA-CMp particles were synthesized according to the cited literature.⁵⁴ 100 mg CMp was mixed with 1 mL vTA and sonicated for 5 minutes in a sonic bath. Mixture was degassed with nitrogen flux for 10 minutes and placed between 2 50W LEDs and stirred for 3 hours under continuous visible light irradiation and for purification, the mixture was filtered and washed with ethanol 3 times (20 mL each portion) and dried under vacuum at 60 °C overnight. After cooling to ambient temperature, dark-yellow vTA-CMp powder was obtained and well grinded before usage.

Preparation of vTA-CMp /1-octanol suspension: In order to obtain well dispersed vTA-CMp /1-octanol dispersion, the bulk vTA-CMp was sonicated to exfoliate carbon nitride. 100 mg vTA-CMp and 8 mL of 1-octanol were added to a 10 mL plastic centrifuge tube

then exfoliated in a sonic bath for 3 times / 30 minutes cycles. The dispersion was set to rest for 1 hour prior to use in order to allow a sedimentation of larger particles.

Synthesis of beads via suspension photopolymerization: Various PS-DVB-vTA-CMp beads were termed according to indicated parameters: Crosslinking ratio (numbering), solvent presence (T), agitation speed (m-medium 700 rpm, s-slow 400 rpm), vTA-CMp as photoinitiator (C). For example; a Model bead, BT5m, was prepared by DPO as photoinitiator, 25% DVB to Styrene, a defined amount of toluene added, stirred at a medium speed. A second example: CBT5m beads were prepared in the same way with BT5m except for DPO photoinitiator addition, herein vTA-CMp nanosheets were utilized as a photoinitiator.

The reference beads (PS-DVB) are the same as with BT5m and only differ by the presence of vTA-CMp.

General Procedure using BT5m as an example: 0.025g photo-initiator weighed in a glass vial, dissolved in 0.5 mL toluene, followed by the addition of 1.1 mL styrene, 0.55mL DVB and 0.5 mL vTA-CMp dispersion (monomer phase). On the other side, 15 mL PVA/ water solution (1 wt.%) was prepared in 25 mL round bottom flask. Afterwards, the organic phase was injected into the flask. The flask was capped with a glass cap, placed in front of an Ultraviolet source (10 cm apart from flask) at 700 rpm on a magnetic stirrer for 8 hours to complete a photoinduced suspension polymerization. After 4 hours, liquid monomer droplets began to solidify distinctively. After 8 hours, the solidified beads were filtered and transferred into a glass petri dish, where solvent evaporation at ambient temperature was performed over 2 days in the fume hood in order to avoid any possible cracking via temperature-induced drying. Then after, solid and dried PS-DVB-vTA-CMp were ready for further use.

Bead synthesis by thermal initiator: 0.025g thermal initiator (AIBN) weighed in a glass vial, dissolved in 0.2 mL toluene, followed by the addition of 1.1 mL styrene, 0.35 mL DVB and 0.5 mL 1-octanol. 15 mL water phase consisting 1 wt.% PVA was poured in 25 mL round bottom flask and purged with nitrogen for 15 minutes. After purging, organic

phase was injected into the flask and the mixture was purged with nitrogen for another 15 minutes, then the flask was capped with a glass cap and placed in an oil-bath under stirring at 700 rpm with a magnetic stirrer. The temperature was gradually increased from room temperature to 60°C in one hour and left at 60°C for 1 hour to initiate the polymerization. After 2 hours in total, temperature was gradually increased again every 15 minutes until reaching 70°C in 1 hour and left for 1 hour at 70°C. After 4 hours, solidified beads were filtered, washed 2 times with THF and dried in a vacuum oven overnight, labeled as Reference bead (I-Ref). Alternatively, 0.025g thermal initiator (AIBN) weighed in a glass vial, dissolved in 0.2 mL toluene, followed by the addition of 1.1 mL styrene, 0.35 mL DVB and 0.5 mL vTA-CMp 1-octanol dispersion. 15 mL water phase consisting 1 wt.% PVA was poured in 25 mL round bottom flask and purged with nitrogen for 15 minutes. After purging, organic phase was injected into the flask and the mixture was purged with nitrogen for another 15 minutes, then the flask was capped with a glass cap and placed in an oil-bath under stirring at 700 rpm with a magnetic stirrer. The temperature was gradually increased from room temperature to 60°C in one hour and left at 60°C for 1 hour to initiate the polymerization. After 2 hours in total, temperature was gradually increased again every 15 minutes until reaching 70°C in 1 hour and left for 1 hour at 70°C. After 4 hours, solidified beads were filtered, washed 2 times with THF and dried in a vacuum oven overnight, labeled as Model bead (I-Model)

Surface Photomodification of PSDVB-vTA-CMp Beads via VSA and VP: Photo-induced surface modification via VSA was performed by following this procedure: 0.050g CBT5m beads were weighted in a glass vial and 3 mL VSA:DMF (2:1 vol.%) mixture was injected, thereafter vial was capped and left for 30 minutes to complete adsorption-desorption equilibrium under medium magnetic stirring. Afterwards, visible light irradiation was performed via white 50 W LED (Chip Bulb Light DIY White 3800LM 6500 K) overnight (~12 h). Beads were filtered and washed with 10 mL deionized water:DMF (1:1 v%) 3 times and left overnight in water:DMF (2:1 vol.%) mixture. After purification, they were dried in a vacuum oven overnight.

Photo-induced surface modification via VP was performed by following this **procedure**: 0.050g CBT5m beads were weighted in a glass vial and 3 mL VP was injected thereafter vial was capped and left for 30 minutes to complete adsorption-desorption equilibrium under medium magnetic stirring. Afterwards, visible light irradiation was performed via white 50 W LED (Chip Bulb Light DIY White 3800LM 6500 K) overnight (~12 h). Beads were filtered and washed with 10 mL ethanol 3 times and left overnight in toluene. After purification, they were dried in a vacuum oven overnight.

Photocatalytic RhB degradation: The photocatalytic activity of PS-DVB-vTA-CMp beads were investigated via photocatalytic degradation of aqueous RhB solution (2 ppm in deionized water) under visible light irradiation. As an example procedure of RhB degradation experiment, for each sample: 55 mg beads and 1.5 mL RhB dye solution were mixed in a glass vial in the dark under continuous stirring for 30 minutes in order to complete an adsorption-desorption equilibrium. Afterwards, the irradiation was performed by a white 50 W LED (Chip Bulb Light DIY White 3800LM 6500 K) under continuous stirring for 5 hours. Additionally, the same procedure was applied additionally without visible light irradiation to all samples.

A recycled photocatalytic activity test was carried out by following the above-mentioned process. A certain amount of RhB solution in suspension was withdrawn every 1 hour and RhB absorption was followed by spectrophotometrically. After completing each cycle, employed beads were collected, washed by immersing in deionized water, and dried overnight. Additionally, the same procedure only with one run cycle was applied without visible light irradiation to BT5m and CBT5m samples (dark measurements).

The kinetic experiment of pristine vTA-CMp for RhB degradation was assessed by the following procedure; vTA-CMp/RhB solution ($1\text{g}\cdot\text{L}^{-1}$) was prepared and after 30 minutes of adsorption/desorption equilibrium, set in front of a visible light source. Every 30 minutes, 1mL sample was collected from suspension, centrifuged for 5 minutes at 10000 rpm then investigated via UV-visible spectroscopy to follow RhB degradation.

pH effect on photodegradation of RhB was investigated by conducting RhB stock solution adjusted with 1M HCL and 1M NaOH solutions to pH2, pH7 and pH13 values and one run cycle kinetic measurement procedure (1 hour time interval) was applied as described.

Aqueous RhB dye adsorption & desorption: Model (BT5m) and reference beads were weighted in two glass vials containing aqueous RhB solution (0.055g beads/1.5mL), then the vials were capped and left in the dark for 24 hours in order to investigate the adsorption performance. After 24 hours, RhB dye adsorbed model and reference beads were separately immersed into glass vials containing 1 mL deionized water and left in the dark for an additional 24 hours for the desorption. Afterwards, the desorption performance was measured the same way as adsorption measurement. Adsorption/desorption recycle test was evaluated according to the described procedure. To investigate pH effect on adsorption/desorption activity, above-mentioned procedure was performed by conducting as-prepared RhB solutions at pH2, pH7 and pH13 to model bead and every 24-hour certain amount of RhB solution was withdrawn from suspension to monitor RhB absorption at λ_{\max} (554 nm) via UV-vis spectroscopy.

Oil-soluble dye adsorption in biphasic system & desorption: Model (BT5m) beads were weighted separately in two glass vials containing deionized water (0.050 g beads/4 mL) and shaken for 20 seconds. Following that, 50 μ L Sudan Red 7B and perylene solutions (200 ppm in toluene) were separately injected into the vials and adsorption performance was investigated by taking digital photos in every 5 minutes for 30 minutes. Thereafter, dye soaked beads were immersed into 4 ml toluene and dye releasing performance was followed by taking digital photos after 1 and 3 hours. Following that, as a second releasing round, partially dye desorbed beads were immersed in 4 ml toluene and dye releasing performances were monitored by taking digital photos after 10 minutes, 1 hours and 24 hours.

Chapter 4

Synthesis of phenyl doped g-CN (CMp): Phenyl-modified g-CN (CMp) was synthesized according to literature.⁵⁴ 1.3 g of cyanuric acid and 1.8 g of 2,4-diamino-6-phenyl-1,3,5-triazine were weighed and mixed with 50 mL distilled water and shaken overnight. After centrifugation at 5000 rpm for 5 minutes, the precipitate was dried at 60 °C under vacuum overnight. The dried product is transferred into a capped crucible and put into N₂ protected oven at 450 °C for 2 hours, with a heating rate of 2.3 °C /min. After cooling to ambient temperature, yellow CMp powder was obtained and well grinded prior to use.

Synthesis of CMp-vTA: CMp-vTA particles were synthesized according to the cited literature.⁵⁴ 100 mg CMp was mixed with 1 mL vTA and sonicated for 5 minutes in a sonic bath. Mixture was degassed with nitrogen flux for 10 minutes and placed between 2 50W LEDs and stirred for 3 hours under continuous visible light irradiation and for purification, the mixture was filtered and washed with ethanol 3 times (20 mL each portion) and dried under vacuum at 60 °C overnight. After cooling to ambient temperature, dark-yellow vTA-CMp powder was obtained and well grinded before usage.

Preparation of CMp-vTA/chloroform dispersion: 40 mg vTA-CMp was sonicated in 1 mL of chloroform in a sonic bath for 3 times / 30 minutes cycles to exfoliate carbon nitride. The dispersion was set to rest for 1 hour prior to use in order to allow a sedimentation of larger particles.

Synthesis of CMp-vTA incorporated Thiol-ene polymer beads (TT@CMp-vTA, TTA@CMp-vTA, TTO@CMp-vTA): Pentaerythritol tetraacrylate and tetrakis(3-mercaptopropionate) (1:1 eq) were weighted in glass vial, 1 ml of freshly prepared CMp-vTA/chloroform dispersion was added into vial and all components mixed properly. Meanwhile, boat shape crucibles were fulfilled with aqueous boric acid solution (4wt.%). As-prepared monomer and CMp-vTA containing organic mixture was carefully dropped into boric acid solution as demonstrated in a digital video reported in the ESI. Subsequently, crucibles placed under UV light source at 15 cm distance from top to

crucible level, for 2 hours to complete polymerization. Afterwards, as-prepared polymer beads were washed with adequate amount of THF and water for three times and left in fume hood for drying (depicted as TT@CMp-vTA). In order to vary bead composition, same process performed by conducting 1,3,5-Triallyl-1,3,5-triazine-2,4,6(1H,3H,5H)-trione and 2,4,6-Triallyloxy-1,3,5-triazine with tetrakis(3-mercaptopropionate) (1:1 eq) and resulting samples were depicted as TTA@CMp-vTA, TTO@CMp-vTA, respectively.

Given the fact that CMp-vTA is the photoinitiator for photopolymerization, reference materials with the absence of CMp-vTA were synthesized by addition of DPO (1wt.%) and obtained materials named as TT, TTA, TTO in accordance with CMp-vTA containing analogues.

Carbonization of CMp-vTA incorporated Thiol-ene beads: after the purification & drying step, beads were separately placed in capped crucibles and put into N₂ protected chamber furnace at 800°C for 30 minutes with a heating rate of 5°C /min. Resulting materials named according to source beads e.g. CTT@CMp-vTA derived from TT@CMp-vTA (CTTA@CMp-vTA made by TTA@CMp-vTA, CTTO@CMp-vTA made by TTO@CMp-vTA).

Photocatalytic RhB degradation: The photocatalytic activity of TT@CMp-vTA beads was investigated via photocatalytic degradation of aqueous RhB solution (50mg bead : 2 mL of 2 ppm RhB in deionized water) under visible light irradiation. Beads were mixed with RhB dye solution in a glass vial under dark at continuous stirring for 30 minutes in order to complete an adsorption-desorption equilibrium. Afterwards, the irradiation was performed by a white 50 W LED (Chip Bulb Light DIY White 3800LM 6500 K) under continuous stirring for 9 hours. Degradation performance followed via by UV-VIS spectroscopy by conduction samples taken every 3 hours.

Chapter 5

Synthesis of g-CN: g-CN was synthesized from cyanuric acid-melamine supramolecular complex as reported in literature.⁴² Cyanuric acid (1.29 g) and melamine (1.26 g, 1:1

molar ratio) were mixed in 50 mL distilled water overnight to form cyanuric acid-melamine complex, then the solid was filtered and dried in vacuum overnight. The dried product was transferred into a capped crucible and put into N₂ protected oven at 550 °C for 4 hours, with a heating rate of 2.3 °C /min. The resulting yellow powder is labeled as g-CN (CM).

Synthesis of g-CN nanosheets embedded hydrogel (HGCM): 150 mg as-prepared CM was dispersed in 30 mL distilled water and sonicated 3 times for 30 minutes to exfoliate g-CN nanosheets (CM-W). 9 g freshly prepared CM-W, 0.8 g DMA, 0.150 g MBA and 0.150 g AsA were weighted into a flask, mixed for 5 minutes, then sonicated for 20 seconds. Following that, 1.5 mL hydrogen peroxide solution was injected into the mixture and placed in a petri dish after mixed thoroughly. Petri dish was capped and left for 3 hours to obtain a gelation via redox-induced free radical polymerization. Afterwards, it was washed with distilled water to remove the unreacted species and freeze dried for 24 hours. The resulting light and brittle g-CN nanosheets embedded hydrogel was ready for further usage. In addition, comparative sample was prepared with the same procedure in the absence of CM, then the final hydrogel is denoted as (HG).

Synthesis of hydrophobic hydrogels (HGCM-vTA): 100 mg as-prepared HGCM and 5mL vTA were put in a glass vial and left for 30 minutes to complete adsorption-desorption equilibrium. Afterwards, it was placed between two visible light sources (10 cm distance each) for 5 hours to perform in-situ photomodification based on the photoactivity of embedded g-CN nanosheets within hydrogel network. After 5 hours, hydrophobized HD-CM was placed in a petri dish and washed with 20 mL acetone to remove the remaining vTA, then left in a fume hood for drying overnight.

Pore substructuring of HGCM by photoinitiation: 100 mg as-prepared HGCM and certain amounts of patching monomer (consisting 10 mol. % crosslinker) were added into a capped glass vial containing 2 g distilled water and left for 2 hours to complete adsorption-desorption equilibrium. After 2 hours, monomer swollen hydrogel was replaced into another capped glass vial and set between two visible light sources (10 cm

Chapter 8

distance each) overnight to accomplish photopolymerization. Afterward, it was purified by immersing in 20 mL distilled water refreshed repeatedly every 2 hours for 3 times and then left in fume hood for drying overnight. This procedure was repeated for each substructuring monomer categorized as acidic AA (10 mol. % MBA), cationic AAM (10 mol. % MBA), and neutral PEGMEMA (10 mol. % PEGDMA).

Rhodamine B dye releasing experiment: 40 mg HD, HGCM and HGCM-vTA were weighted separately in a capped glass vial containing 4 mL RhB dye solution (4×10^{-2} M) and left for 24 hours. Afterward, all samples were replaced in another glass vial containing 4 mL distilled water to follow the dye releasing progress spectroscopically every 24h. The RhB dye releasing efficiency was calculated by using the following formula for each sample:

$$\text{Releasing efficiency (\%)} = (C_t - C_o)/C_o \times 100$$

C_o : Initial RhB dye concentration, C_t : RhB dye concentration at specified time.

FTIC-Albumin & FTIC-Dextran releasing experiment: 40 mg HGCM and HGCM-vTA were weighted separately in a capped glass vial containing 4 mL FTIC-Albumin (2000 ppm) and FTIC-Dextran (2000 ppm) solutions and left overnight. Afterwards, all samples were placed in another glass vial containing 4 mL distilled water to spectroscopically monitor the labeled molecule release process after 24h.

Cation releasing experiment: 100 mg HGCM and HGCM-vTA were separately immersed in freshly prepared KCl, CaCl₂ and MgCl₂ stock solutions (corresponding concentration for each cation, K⁺, Ca²⁺ and Mg²⁺ = 1000 ppm) overnight. Afterwards, samples were placed in capped glass vial containing 10 mL distilled water and left overnight. Released contents of each cations were analyzed via ICP-OES.

Chapter 6

Synthesis of g-CN: 5.0 g of cyanuric acid and 5.0 g of melamine were mixed with 100 mL distilled water and shaken overnight to form cyanuric acid-melamine supramolecular precursor.⁴² After centrifugation at 6000 rpm for 15 minutes, a precipitate was collected.

A precipitate was dried overnight at 60°C under vacuum. The dried product was transferred into a capped crucible and put into N₂ protected oven at 550°C for 4 hours, with a heating rate of 2.3°C /min. The resulting yellow powder is denoted as g-CN and it is well grinded prior to use.

Photopolymerization of EDOT: 100 mg g-CN and 2 mL EDOT are mixed in a vial and sonicated in a sonic bath for 10 minutes. Following that, the vial is placed in front of a 50W visible light source with a continuous stirring for 24 hours at room temperature (29°C was measured after 24 hours of irradiation). oligo-EDOT can be obtained by filtering the photocatalyst (Yield: 75%). Filtered photocatalyst is extensively washed with DMSO and ethanol and dried in an oven. Reused catalyst is denoted as g-CN R1.

Control Reaction-Photopolymerization of EDOT in the absence of air: 100 mg g-CN and 2 mL EDOT are mixed in a vial, nitrogen or argon flux was applied for 30 minutes, the mixture is then sonicated in a sonic bath for 10 minutes. Following that, the vial is placed in front of a 50W visible light source with a continuous stirring for 24 hours at room temperature.

Control Reaction-Photopolymerization of EDOT in the absence of light: 100 mg g-CN and 2 mL EDOT are mixed in a vial, nitrogen flux was applied for 30 minutes, the mixture is then sonicated in a sonic bath for 10 minutes. Following that, continuous stirring for 24 hours at room temperature in the dark was applied.

Doping oligo-EDOT: 0.1 mL HBF₄ solution is poured over 2 mL liquid oligo-EDOT in a petri dish, and significant darkening as well as spontaneous dispersion formation are observed in 20 seconds upon mixing. Resulting dark material is dried in an oven at 60°C for 4 hours to obtain doped oligo-EDOT solid material.

Photopolymerization of EDOT via excess g-CN: 300 mg g-CN and 2 mL EDOT are mixed in a vial and sonicated in a sonic bath for 10 minutes. Following that, the vial is placed in front of a 50W visible light source with a continuous stirring for 24 hours at room temperature (30°C was measured after 24 hours of irradiation). Resulting composite

was characterized further by the means of both solid and liquid phase. Filtered photocatalyst is extensively washed with DMSO and ethanol and dried in an oven. Reused catalyst is denoted as g-CN R2.

Doped oligo-EDOT coating processes: Indium tin oxide (ITO) coated glass slide was treated to a wet chemical etching/cleaning process; firstly washed with aqueous HCl then immersed in isopropanol and sintered at 250 °C for 2 hours. After the cleaning process, post-doped-oligo-EDOT and in-situ g-CN doped oligo-EDOT were manually coated on ITO surfaces and placed in an oven at 70°C overnight. A coin and a glass surface were immersed in a liquid doped oligo-EDOT, and coated surfaces are placed in an oven at 60°C for 2 hours.

Carbonization of Post-doped oligo-EDOT: 460 mg HBF₄ doped oligo-EDOT was placed in a capped crucible and put into N₂ protected chamber furnace at 800°C for 30 minutes with a heating rate of 5°C /min. The resulting material is a solid black powder.

8.3. Characterization Methods

Raman spectra were recorded using a confocal Raman microscope alpha300 (WITec, Germany) coupled with a laser excitation at wavelength of 532 nm.

N₂ sorption measurements were accomplished with N₂ at -196° C, after degassing the sample at 150°C for 20 hours under vacuum, using a Quantachrome Quadrasorb SI porosimeter. The specific surface area was calculated by applying the Brunauer-Emmet-Teller model in the relative pressure region of (0-0.05) for the adsorption branch (ABET).

X-ray diffraction (XRD) patterns of powders were obtained using Bruker D8 Advance X-ray diffractometer via Cu-K α radiation and a scintillation counter. XRD provides information about crystallinity and order of the material. Bragg law describes the diffraction of a wavelength $n\lambda=2d\sin\theta$ where θ is the angle from diffraction, d is distance between planes and n represents the order of diffraction. The resulting pattern is characteristic for a sample which labels the crystalline orientation accordingly.

Scanning electron microscopy (SEM) images were obtained using SM-7500F (JEOL) equipped with an Oxford Instruments X-MAX 80 mm² detector. SEM records scattered electrons from sample after electron beam interaction and SEM images are used to observe the structures of samples.

Energy Dispersive X-Ray Analysis (EDX) is attached to SEM instrument. This technique presents the interaction of electron beam with inner electrons of the sample creating hole on the upper shell of sample, which emits X-ray and is specific for each atom.

Combustive elemental analysis (EA) was performed utilizing Vario Micro device. The sample is combusted in oxygen atmosphere and decomposition products are detected to elaborate elemental ratios of C, H, N and S.

Fourier transform infrared (FT-IR) spectra were taken on Nicolet iS 5 FT-IR spectrometer. FT-IR is non-destructive and facile method to distinguish functional groups in samples.

Solid state ultraviolet-visible (UV-Vis) spectroscopy was recorded via a Cary 500 Scan spectrophotometer equipped with an integrating sphere. It is predominantly used for determination of photo and electrical properties of materials due to light absorption. From absorption spectra band gaps can be deduced via Tauc plots.

Size exclusion chromatography (SEC) was conducted in N-methyl pyrrolidone (NMP, Sigma Aldrich, GC grade) with 0.05 mol·L⁻¹ LiBr and BSME as internal standard using a column system by PSS GRAM 100/1000 column (8 × 300 mm, 7 μm particle size) with a PSS GRAM precolumn (8 × 50 mm) and a Shodex RI-71 detector and a calibration with PS standards from PSS. The method is utilized to determine molecular weight and molecular dispersity of polymer samples.

Freeze drying of hydrogel and organohydrogel samples are applied for solid state hydrogel analysis. After standing in distilled water for 2 days; the hydrogels were cut into smaller pieces, transferred into a flask and dried by pump thaw cycles until the moisture

droplets on the flask were not visible anymore. In this frozen form, they were immediately put into Lyotech GT 2E freeze dryer overnight. Resulting products are brittle samples which retain their pores on the microscopic level.

Thermogravimetric analysis (TGA) was recorded via TG 209 Libra from Netzsch in nitrogen atmosphere with a heating rate 10 K min⁻¹ using aluminum crucible for samples. The sample is heated with a certain rate in defined atmosphere and mass loss with increasing temperature is measured.

Water contact angle measurement was investigated using Krüss contact angle measuring system G10 and recorded via Krüss official software. Sample with ideally flat surface is placed in front of camera which records the water drop on surface and estimates the angle between water droplet and surface. This method is useful to determine surface properties, such as hydrophilicity and hydrophobicity.

Ultrasonication was performed via an ultrasonicator at 50% amplitude (Branson D450) which facilitates dispersion preparation.

Photoluminescent (PL) emission spectra were recorded on Jasco FP-8300 instrument with the excitation wavelength at 360 nm or at changing excitation wavelength between 300-420 nm. It is an effective method to probe electronic structure of semiconductors. Light triggers photoexcitation of sample which material is excited to higher electronic state and relaxes back to lower energy level. The emission is known as PL. Facile and non-destructive method can be employed to determine excitonic properties, evaluation of surfaces and recombination rates. Time resolved PL measures the luminescence lifetime of exciton.

pH values was measured via SI analytics Titro7000 and average values were taken after 3 measurements. pH is a logarithmic scale which shows the power of hydrogen in solution, therefore helps to measure acidity or basicity of aqueous solution.

Fluorescence images and **Optical microscopy images** were obtained by confocal laser scanning microscopy (CLSM, TCS SP5, Leica, Germany) and by Olympus BX41, respectively.

8.4. Supplementary Figures and Tables

Chapter 3

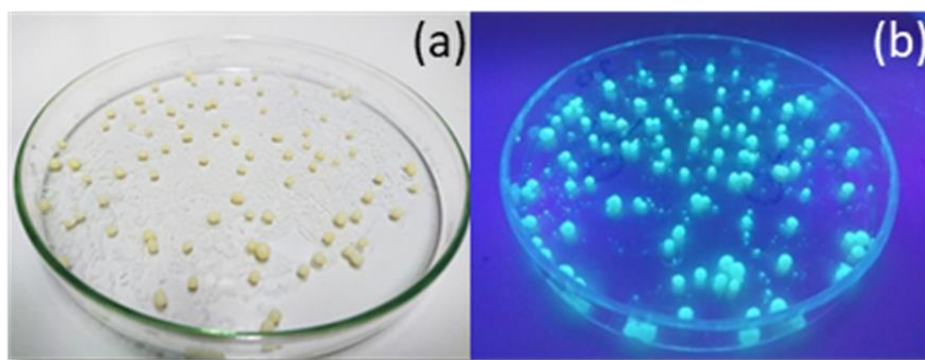


Figure S3.1. a) Digital image of vTA-CMp incorporated model PS-co-DVB beads and b) vTA-CMp incorporated model PS-co-DVB beads under UV illumination

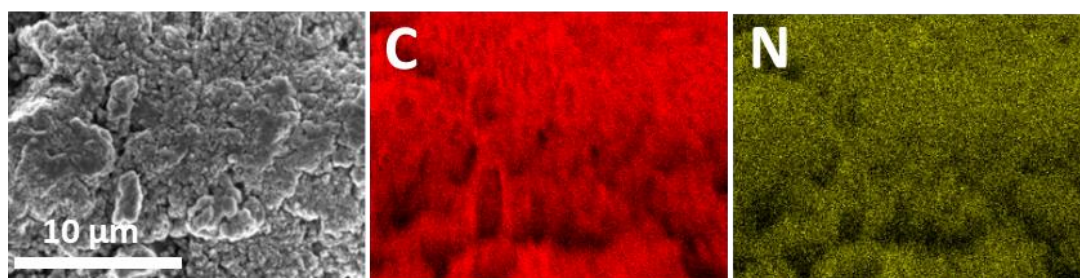


Figure S3.2. Elemental mapping of Model-I bead via EDX.

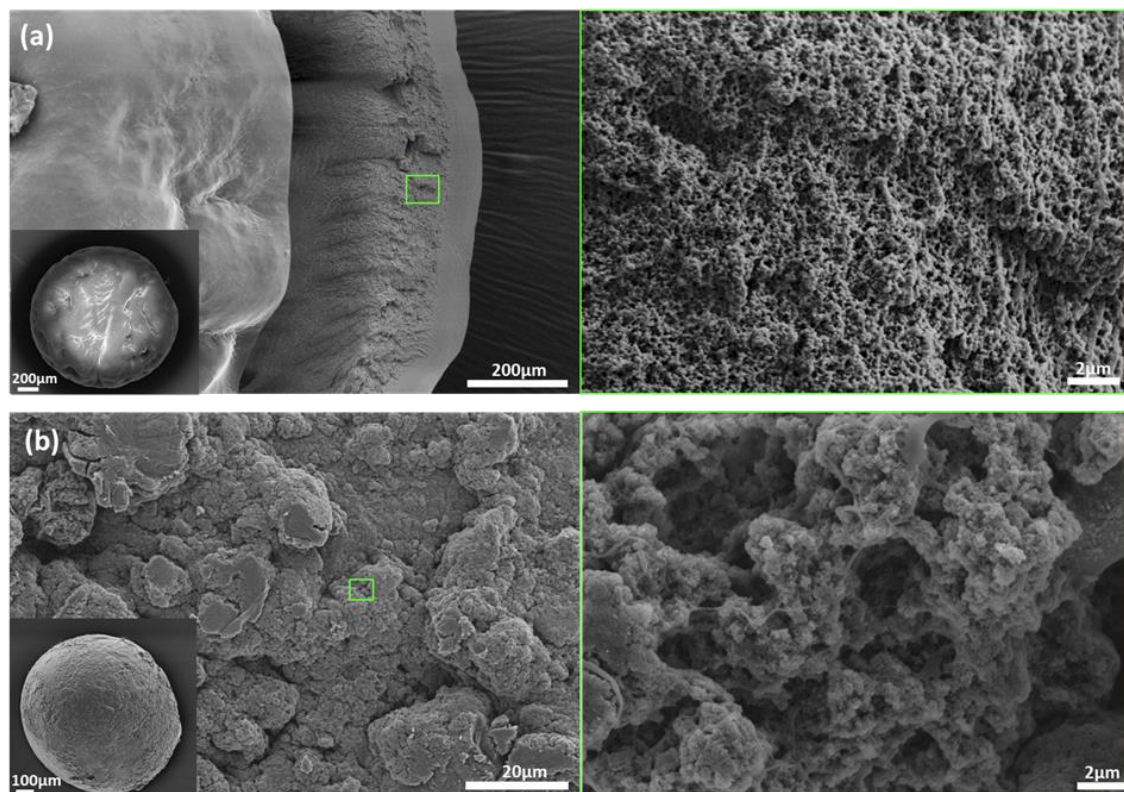


Figure S3.3. Scanning electron microscopy (SEM) images of a) Reference-I and b) Model-I beads fabricated by thermal initiation.

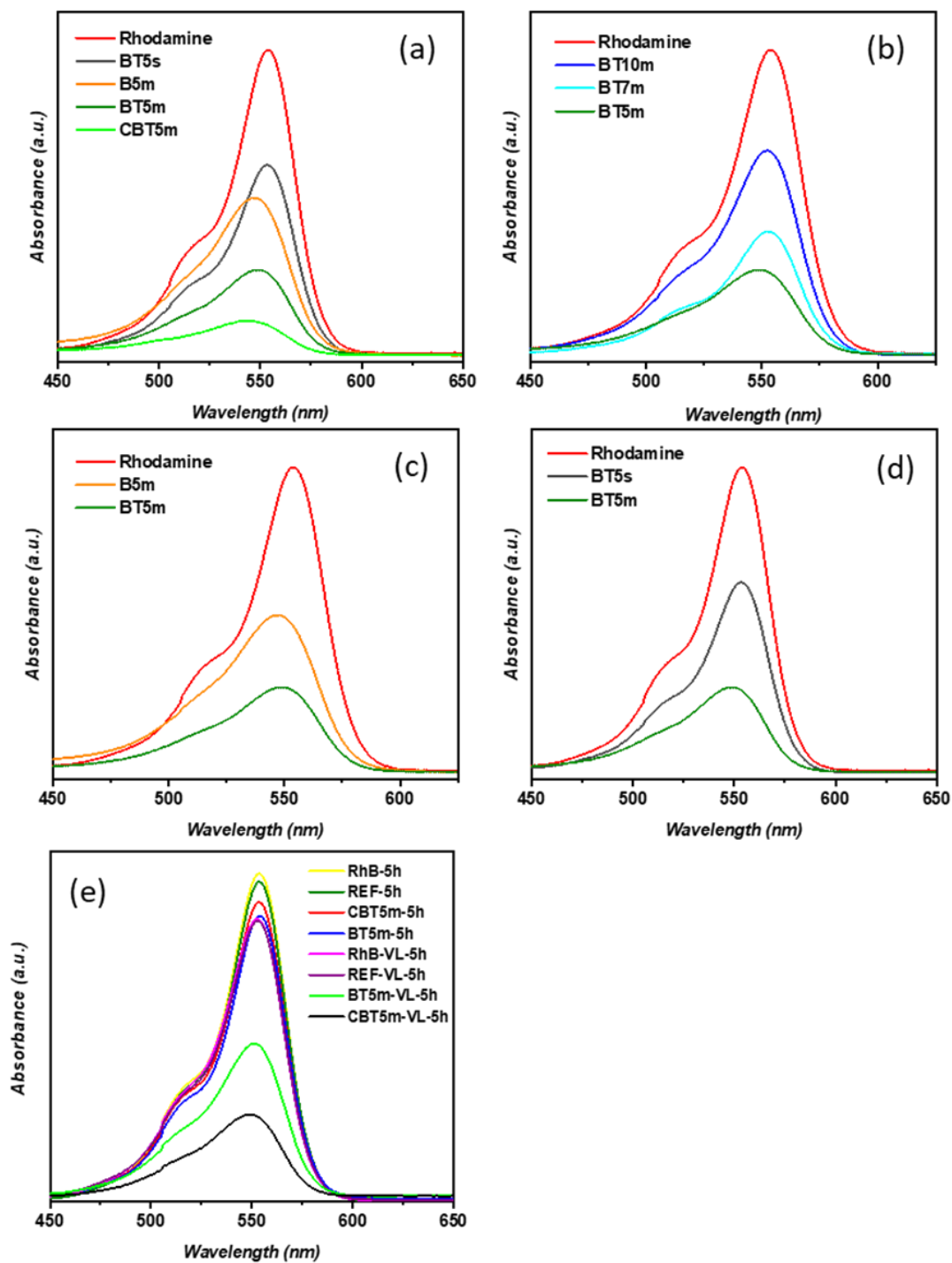


Figure S3.4. *a-d*) UV-vis spectra of BT5m, B5m, BT5s, CBT5m, BT7m, B7m, BT10m and RhB dye solution after 5 hours visible light irradiation. *a*) Model bead (BT5m) analogues according to reaction preparation, *b*) Model bead with increasing crosslinker amount, *c*) Solvent effect comparison *d*) Agitation effect comparison *e*) UV-vis spectra of Reference, BT5m, CBT5m beads under dark conditions for 5 hours (VL samples are the results from visible light irradiation)

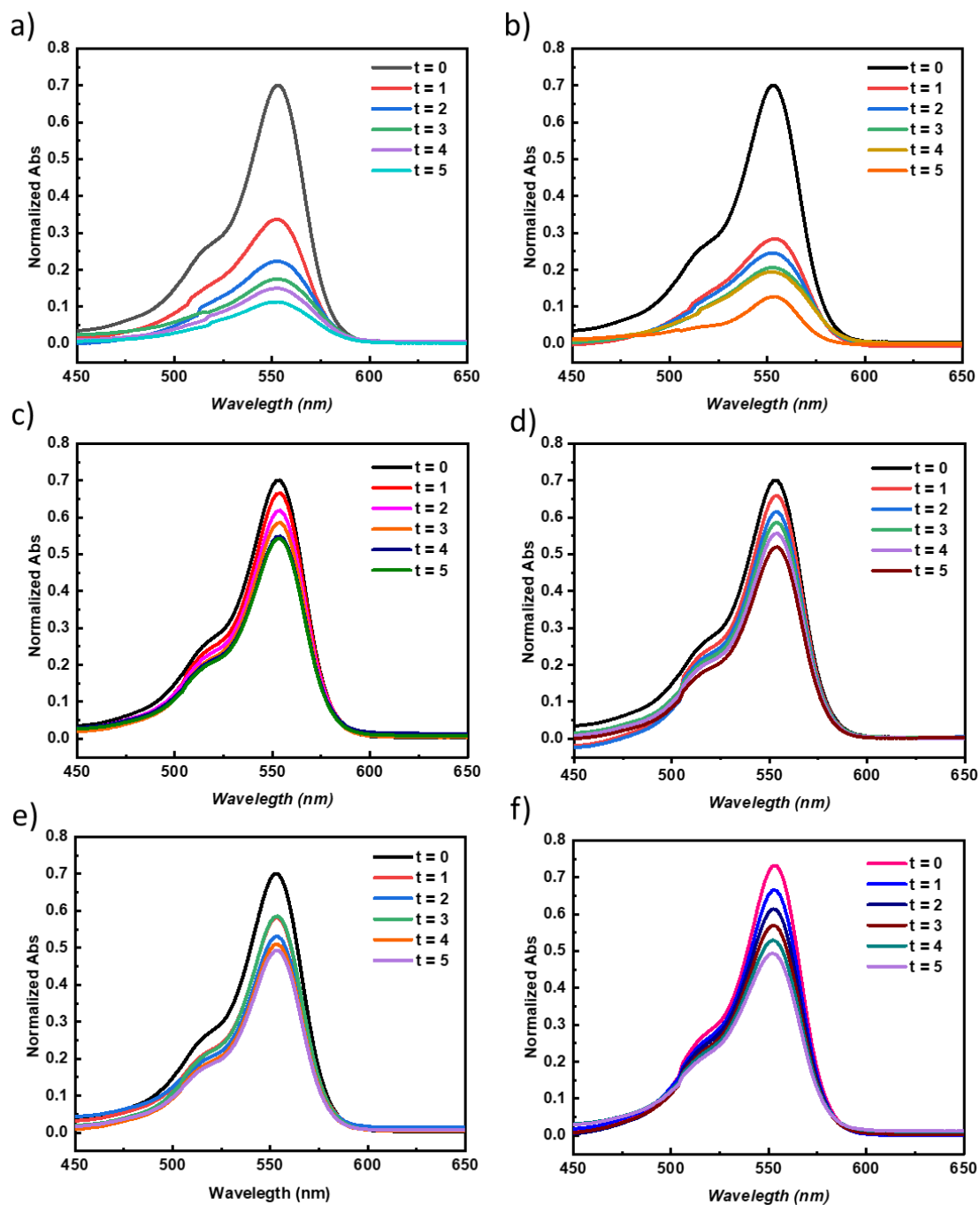


Figure S3.5. a) UV-vis absorption spectra of RhB dye degradation in the presence of a) CBT5m under visible light irradiation b) BT5m under visible light irradiation c) CBT5m without visible light exposure (dark measurement) d) BT5m without visible light exposure (dark measurement) e) reference beads under visible light irradiation, f) RhB dye solution in the absence of photocatalyst.

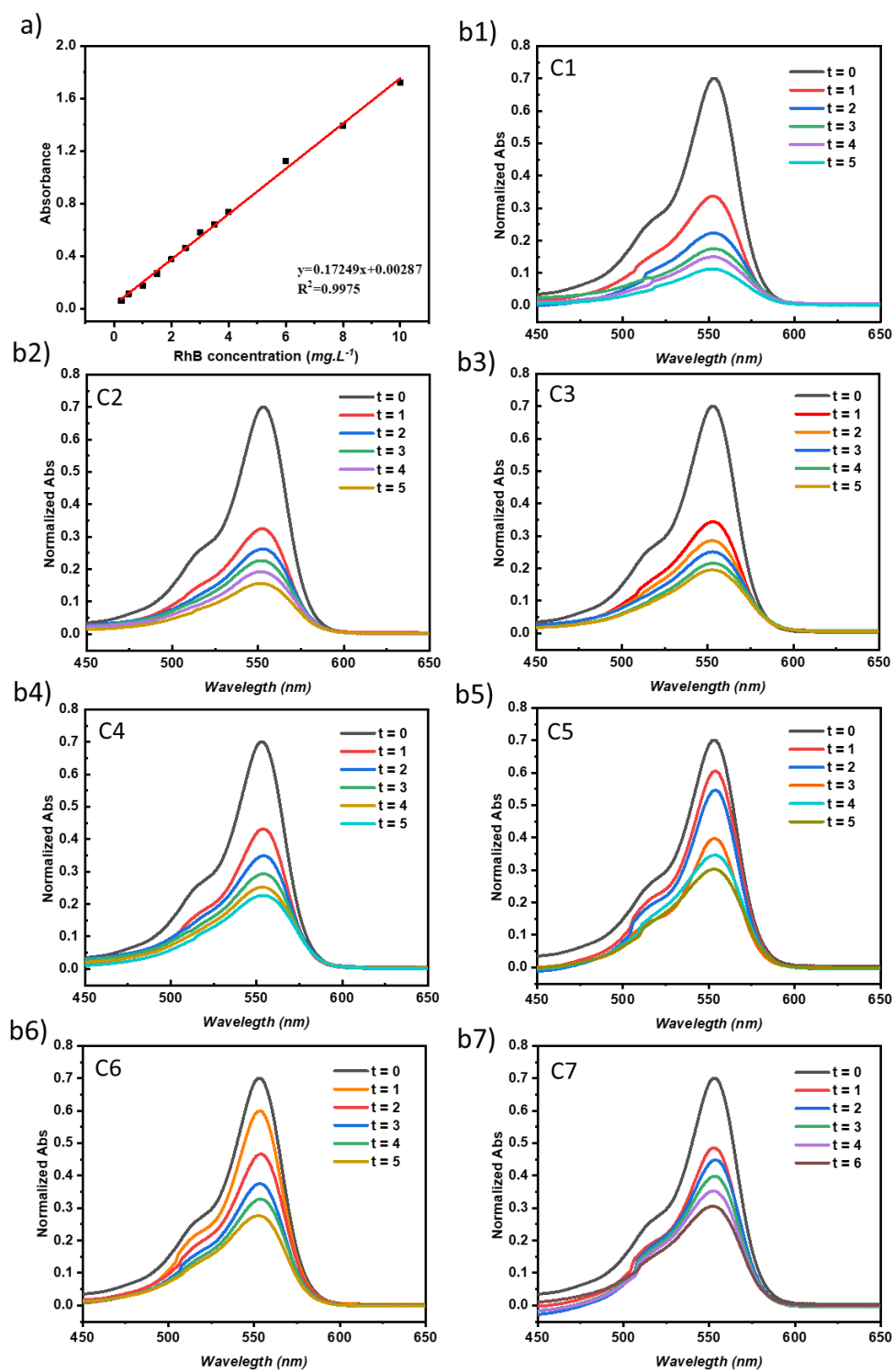


Figure S3.6. a) RhB dye calibration curve. b1-7) UV-vis absorption spectra of RhB dye photodegradation catalytic cycles (1h interval) in the presence of CBT5m under visible light irradiation.

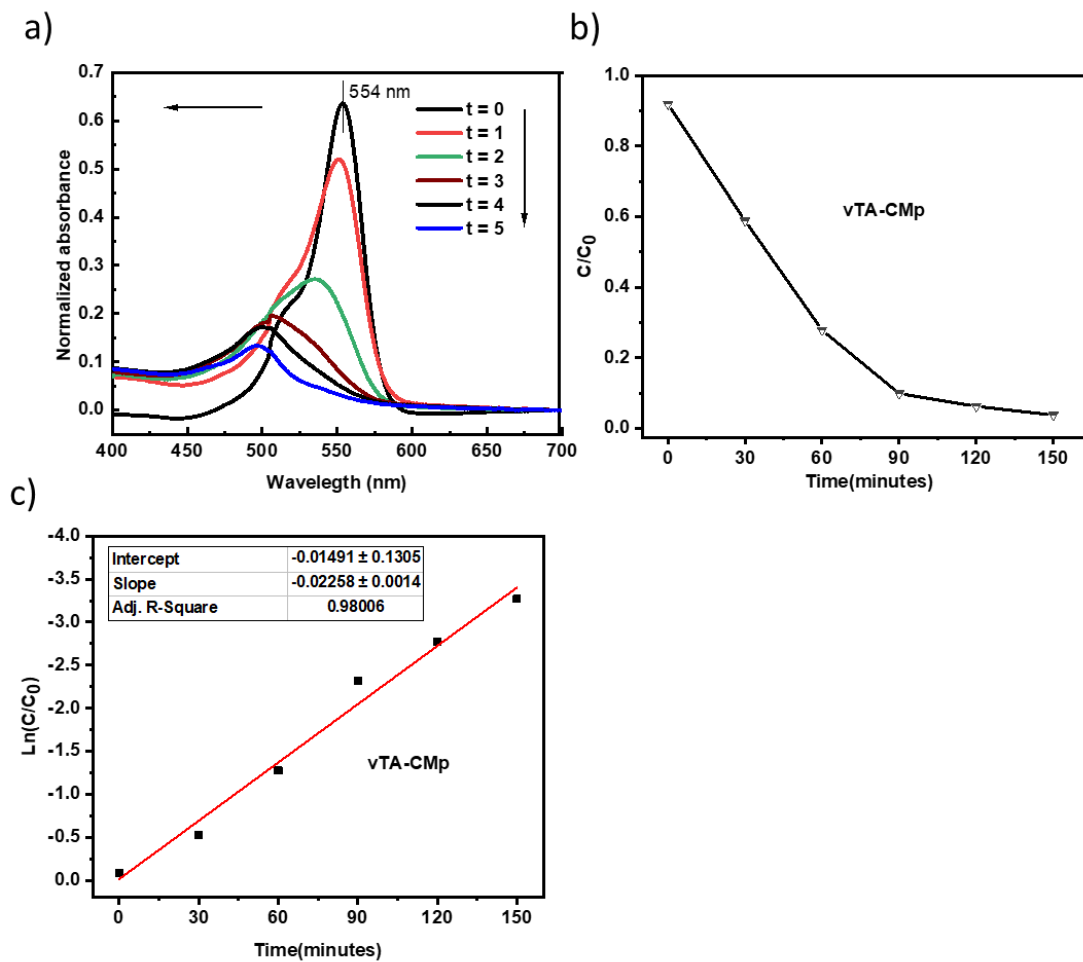


Figure S3.7. a) UV-vis absorption spectra of RhB photodegradation in the presence of vTA-CMp (10mg/10mL) under visible light irradiation (30 minutes interval). b) RhB photodegradation of vTA-CMp. c) Pseudo-first order kinetic fitting data of RhB photodegradation in the presence of vTA-CMp.

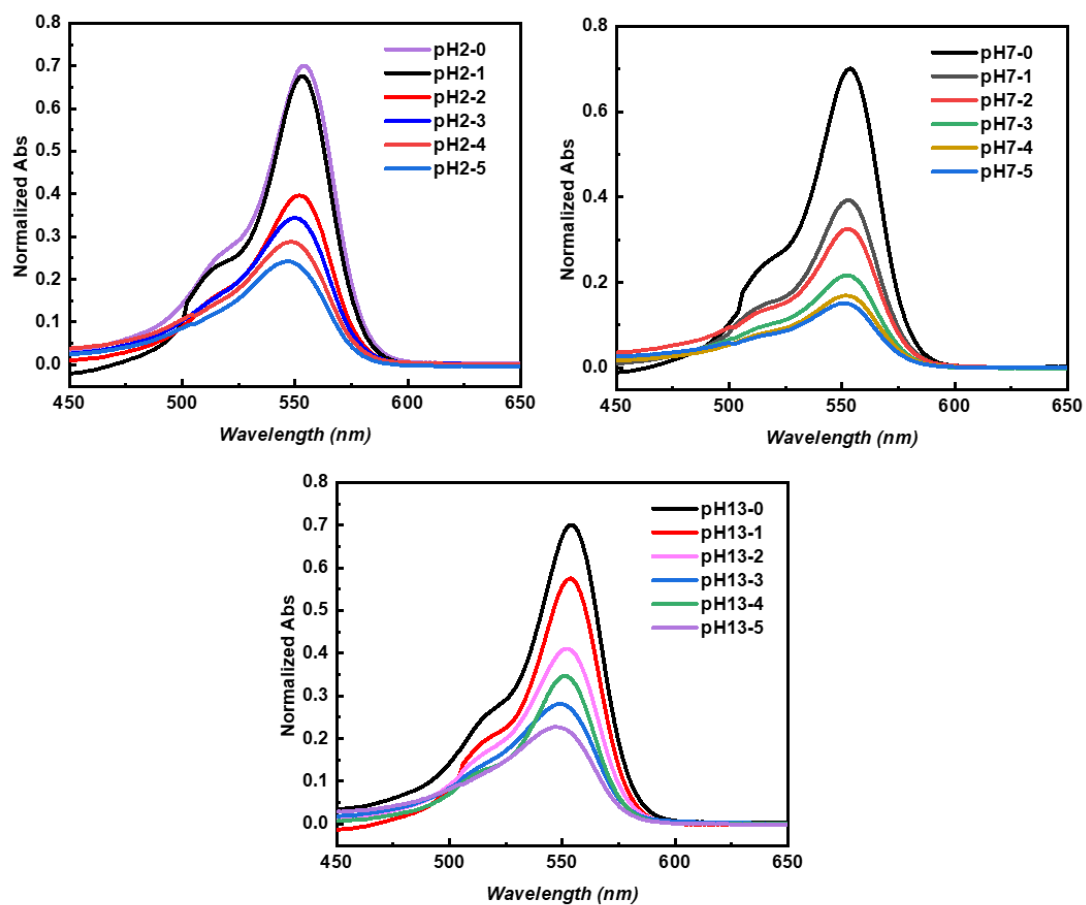


Figure S3.8. a) UV-vis absorption spectra of RhB photodegradation at different pH values in the presence of CBT5m (1 hour interval) under visible light irradiation.

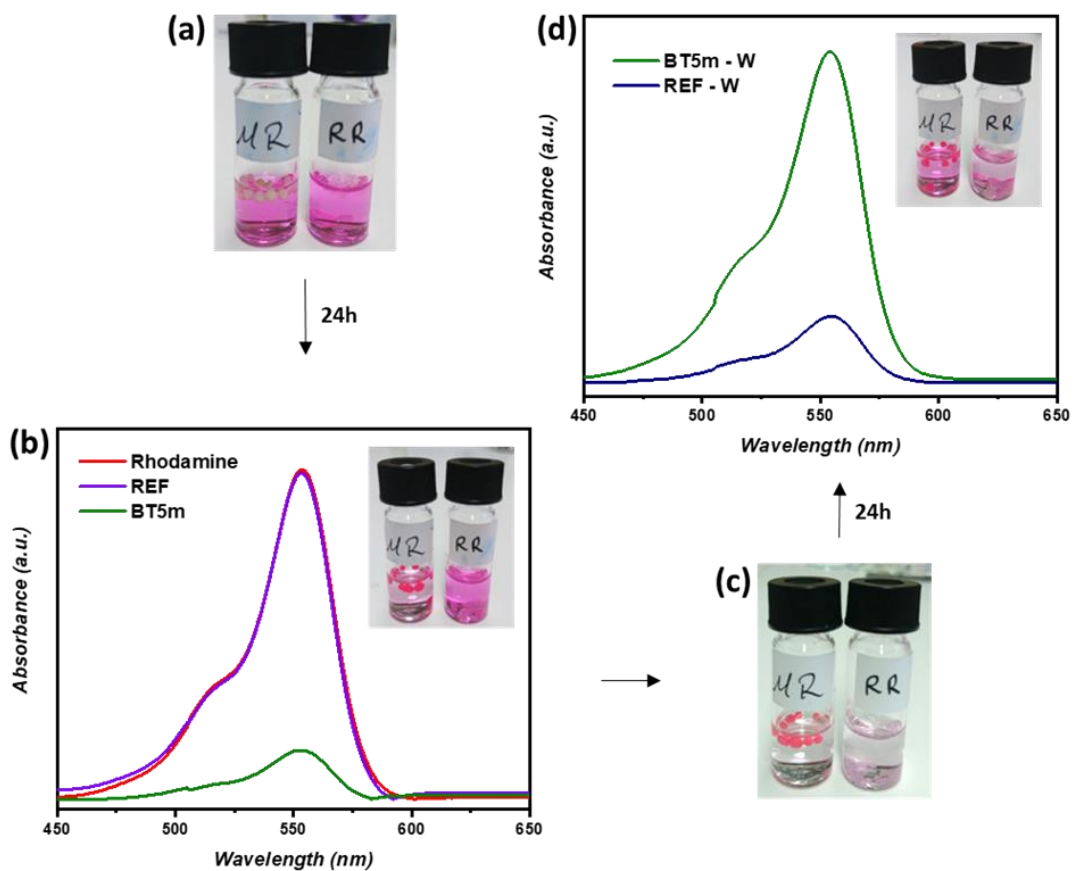


Figure S3.9. a) Digital image of Model and Reference beads in aqueous RhB dye solution at initial moment. b) UV-vis spectra of Model and reference beads after 24 hours at room temperature. c) Digital image of dye adsorbed Model and reference beads in water. d) UV-vis spectra of dye adsorbed Model and reference beads in water after 24 hours at room temperature.

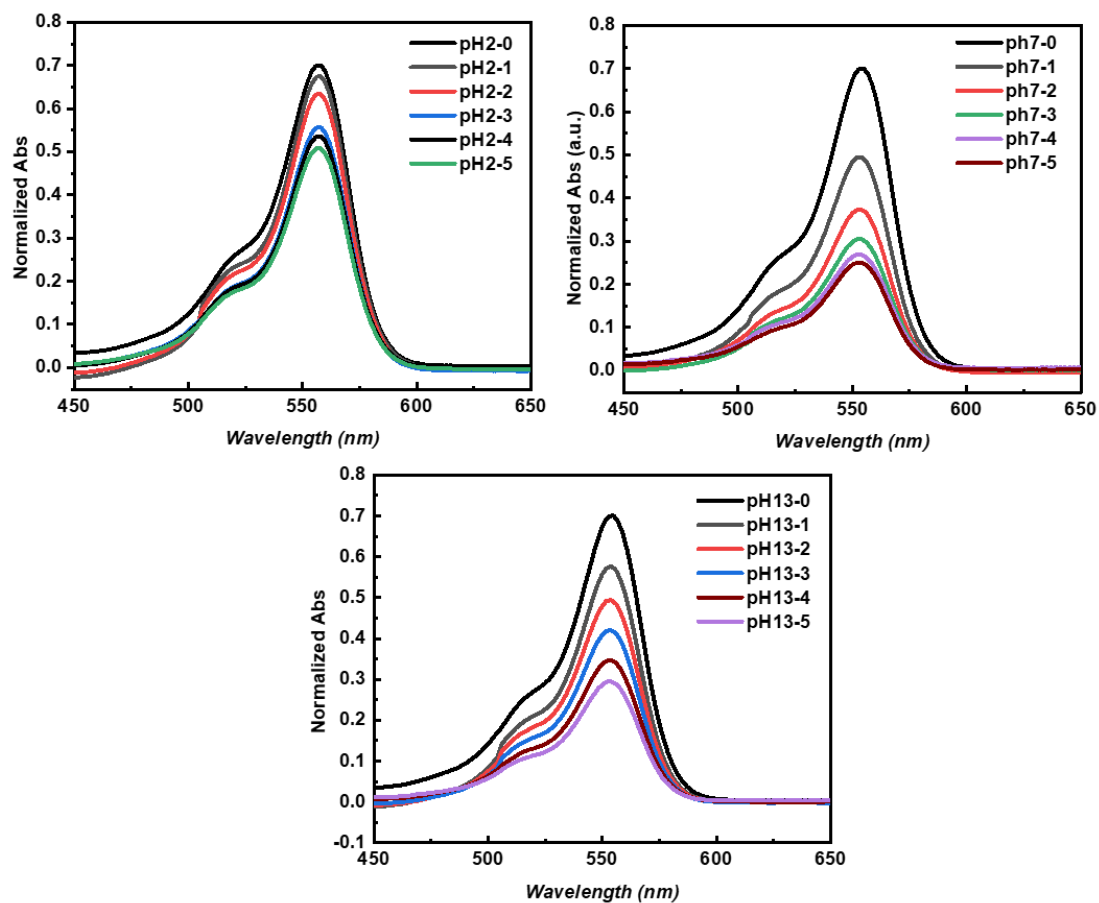


Figure S3.10. a) UV-vis absorption spectra of RhB dye adsorption at different pH values in the presence of model bead (1 hour interval).

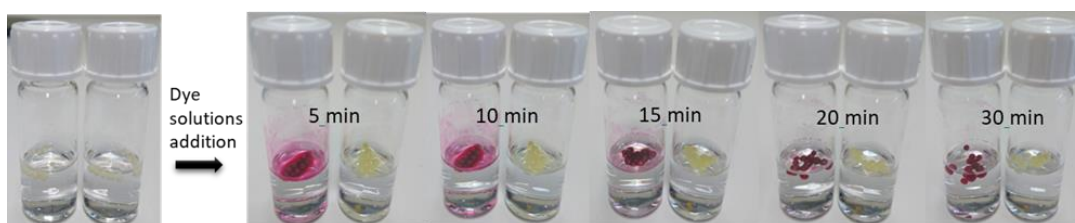


Figure S3.11. Digital images of organic dye (Red dye: Sudan Red 7B, yellow dye: Perylene in Toluene - 50 μ L of each dye solution is injected in a vial that contains 4 mL water and model beads) adsorption process via Model beads in biphasic system.

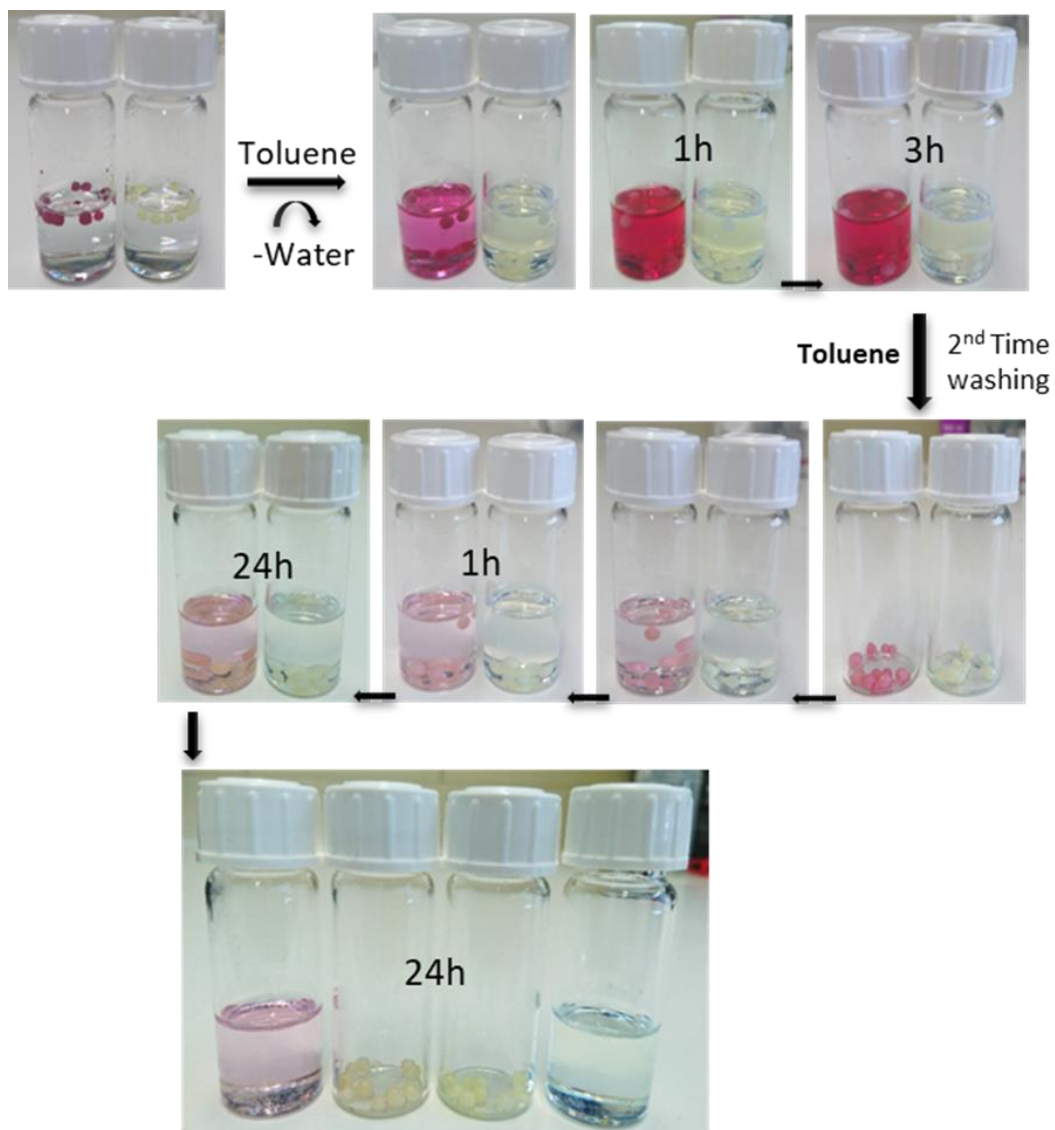


Figure S3.12. Digital images of organic dye (Red dye: Sudan red 7B, yellow dye: Perylene in Toluene) desorption into toluene via Model beads.

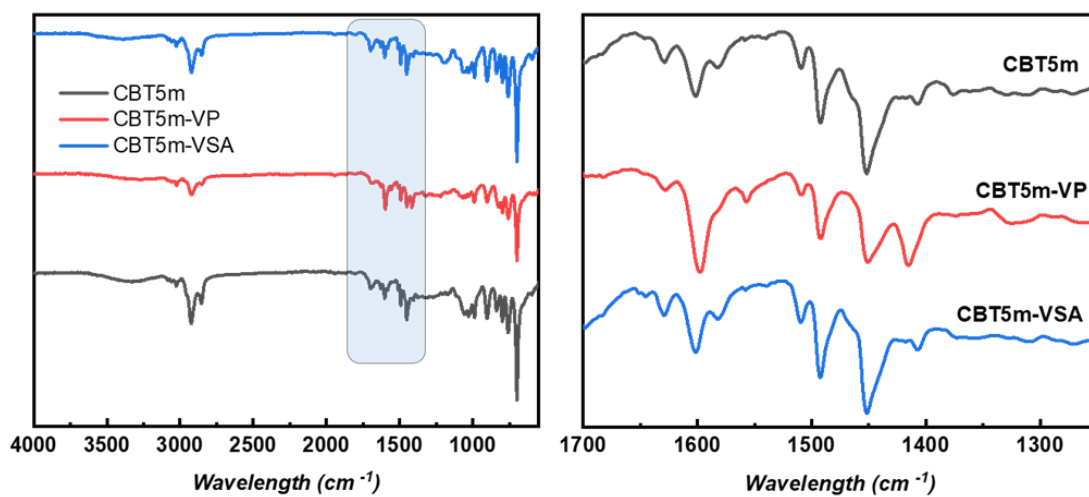


Figure S13. FT-IR spectra of CBT5m, CBT5m-VP and CBT5m-VSA.

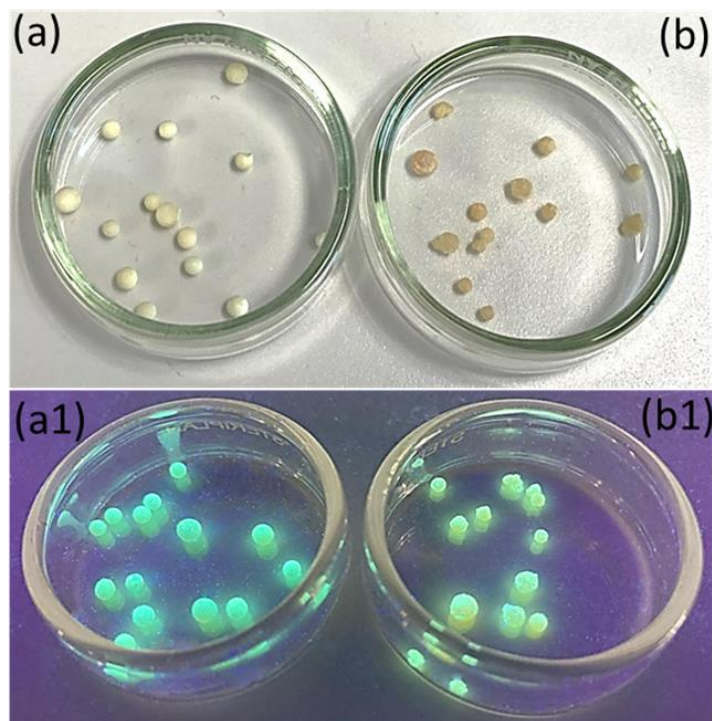
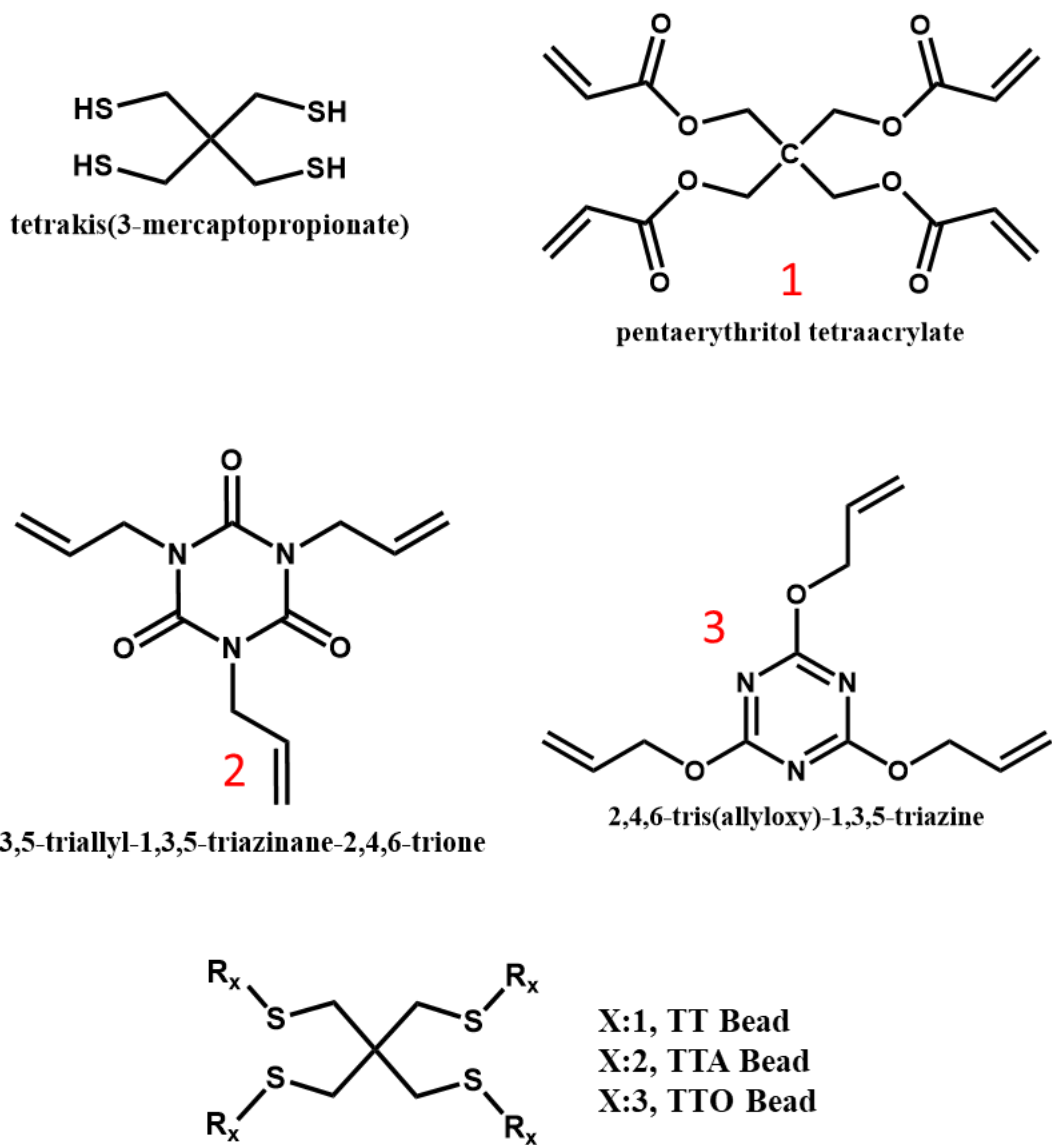


Figure S3.14. Digital images of CBT5m (left petri dish, a) and CBT5m-VP (right petri dish, b) beads at normal light (above) and under UV illumination (below, a1-b1).

Chapter 4



Scheme S4.1. Chemical structures of utilized monomers in synthesis of thiol-ene polymer beads.

<i>Samples</i>	<i>Boron (wt%)</i>
TT@CMp-vTA	0,541 mg/g
CTT@CMp-vTA	0,181 mg/g

*Calib Conc. Units 0.1-1-10 mg/L

Table S4.1. ICP-OES results of TT@CMp-vTA and CTT@CMp-vTA in regard to residual boron amount.

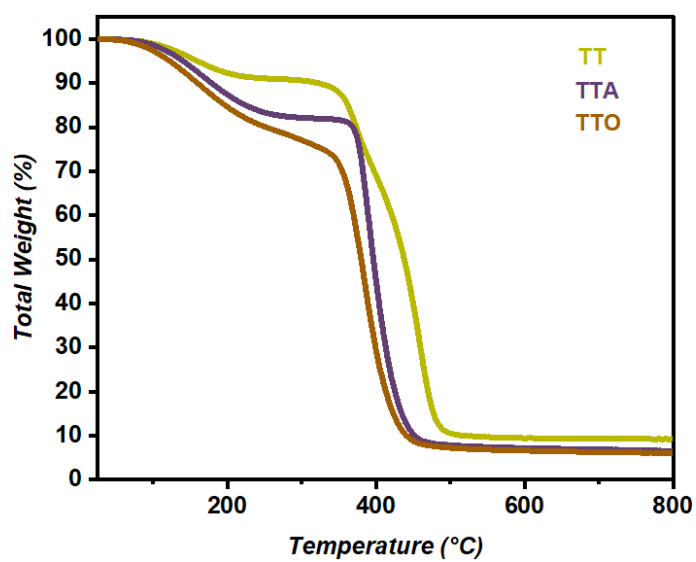


Figure S4.1. Thermogravimetric analysis of TT, TTA, TTO, TT@CMp-vTA, TTO@CMp-vTA and TTA@CMp-vTA.

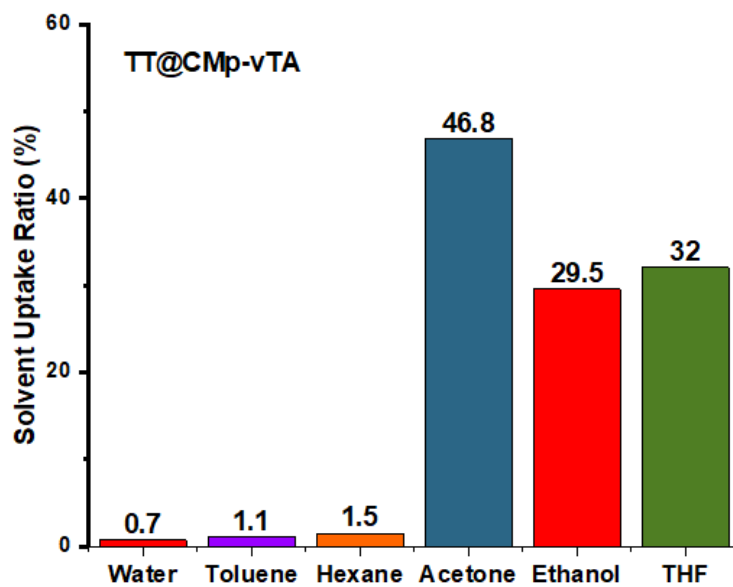


Figure S4.2. Solvent uptake results of TT@CMp-vTA.

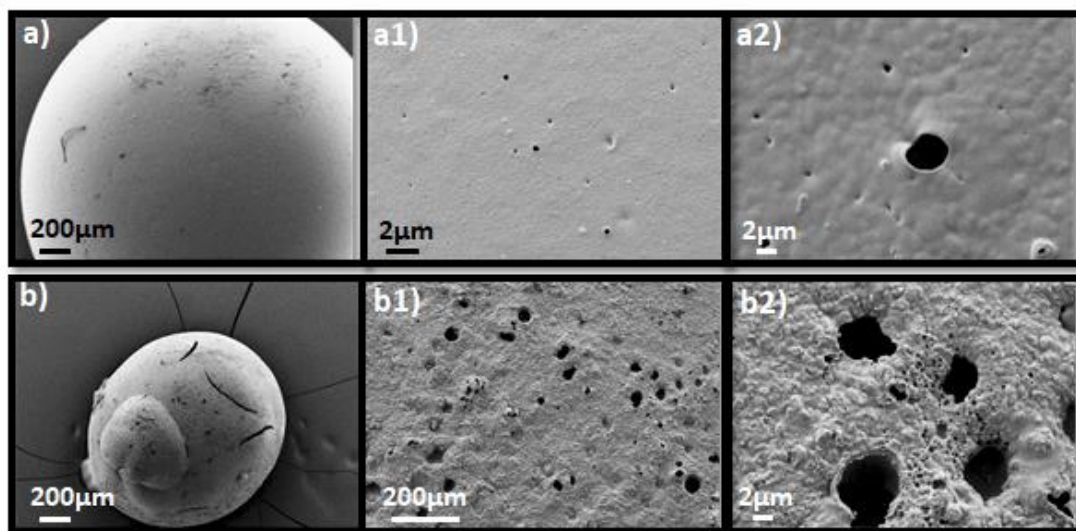


Figure S4.3. SEM images of TT@CMp-vTA (a1-2) and CTT@CMp-vTA (b1-2).

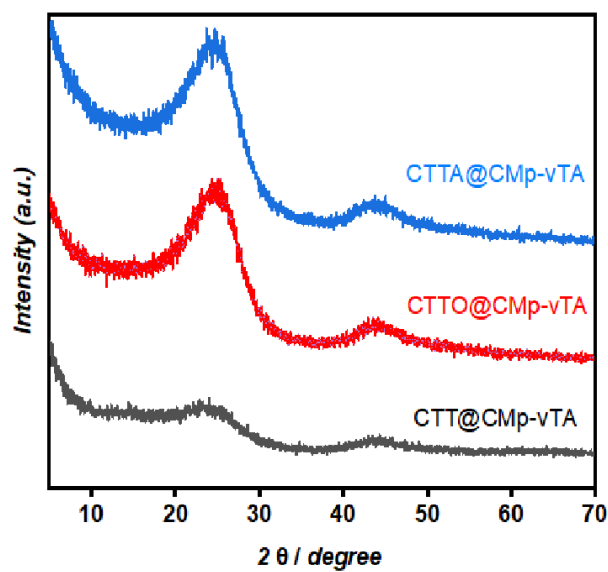


Figure S4.4. XRD profiles of CTT, CTTA, CTTO, CTT@CMp-vTA, CTTO@CMp-vTA and CTTA@CMp-vTA.

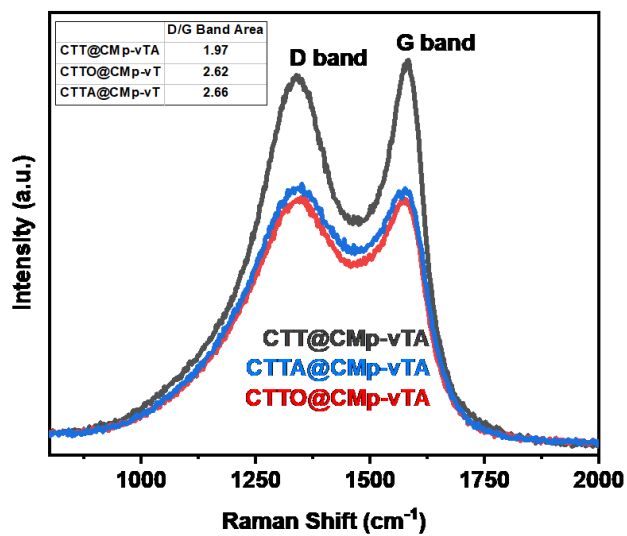


Figure S4.5. Raman spectra of CTT@CMp-vTA, CTTA@CMp-vTA and CTTO@CMp-vTA.

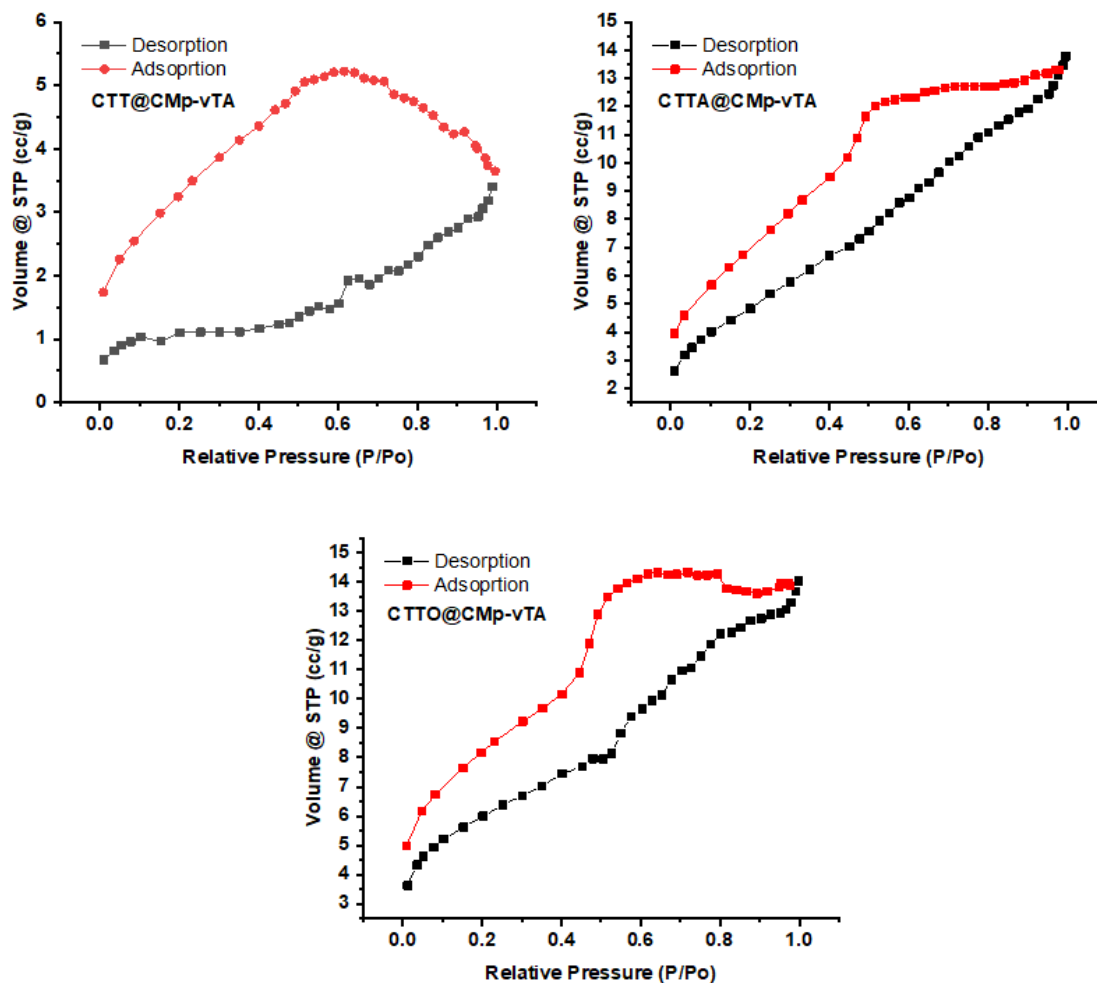


Figure S4.6. N_2 sorption isotherms of CTT@CMp-vTA, CTTA@CMp-vTA and CTTO@CMp-vTA, respectively.

<i>Samples</i>	<i>N [%]</i>	<i>C [%]</i>	<i>H [%]</i>	<i>S [%]</i>
TT	0,04	47,2	5,53	11,91
TT@CMp-vTA	2,43	45,58	5,23	10,66
CTT@CMp-vTA	3,22	91,16	0,78	2
TTA	6,37	43,77	5,06	11,3
TTA@CMp-vTA	7,38	42,95	5,07	11,6
CTTA@CMp-vTA	8,68	85,98	0,9	1,45
TTO	6,25	41,14	4,75	11,04
TTO@CMp-vTA	7,62	44,4	5,18	12,16
CTTO@CMp-vTA	8,68	85,98	0,9	1,45

Table S4.2. Chemical composition of TT, TTA, TTO, TT@CMp-vTA, TTA@CMp-vTA, TTO@CMp-vTA, CTT@CMp-vTA, CTTA@CMp-vTA and CTTO@CMp-vTA obtained by combustive elemental analysis.

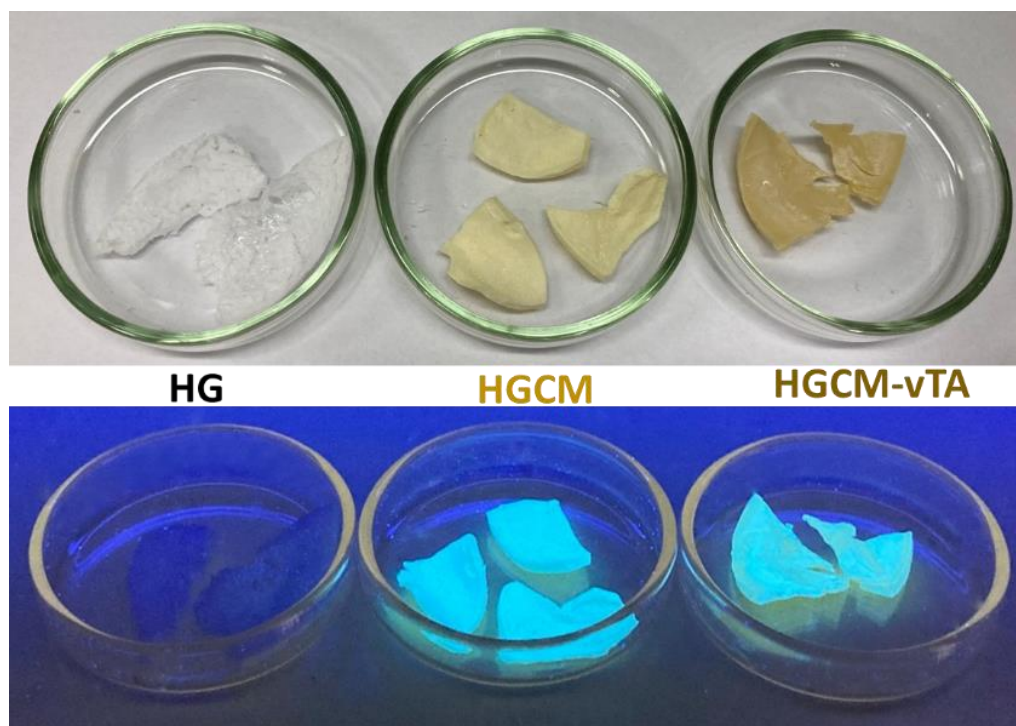


Figure S5.1. Digital images of HG, HGCM and HGCM-vTA under daylight and UV light illumination.

HGC-vTA

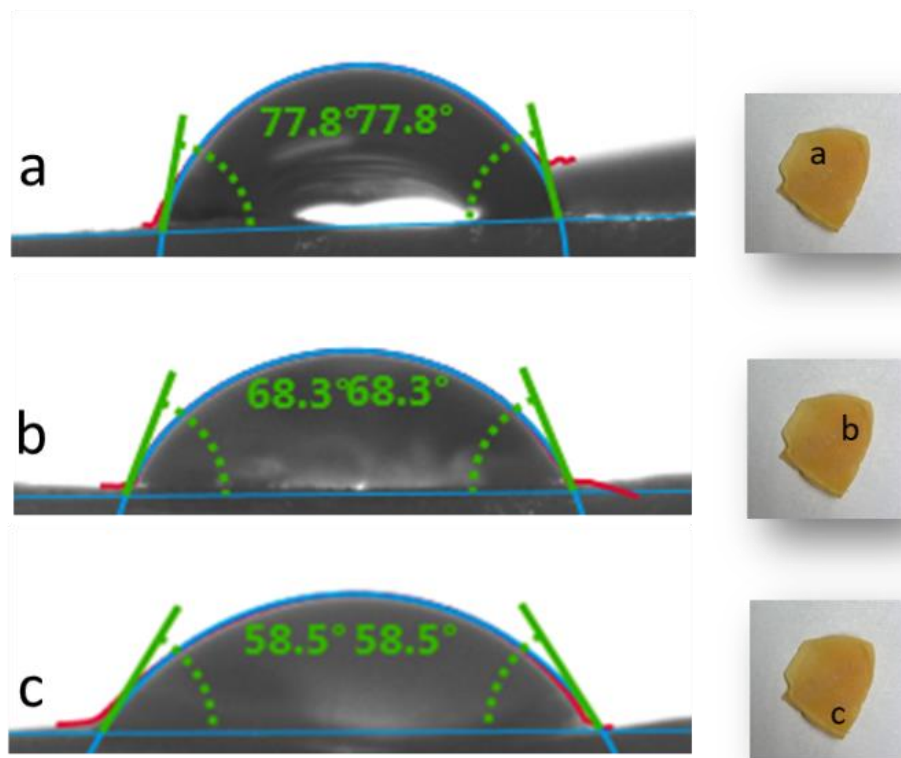


Figure S5.2. Water contact angle results of HGCM-vTA on multiple contact points (obtained after 15 seconds of equilibrium).

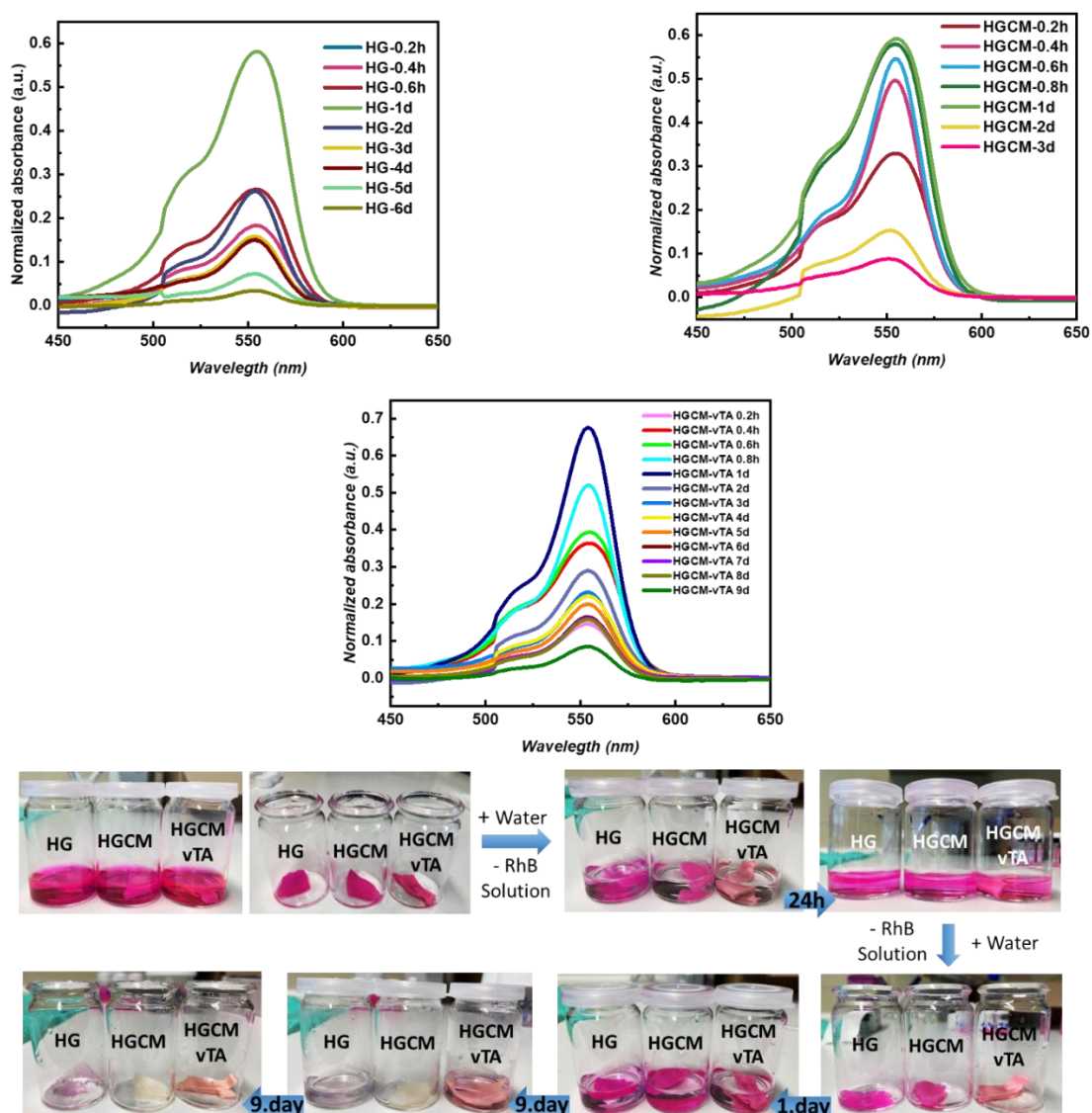


Figure S5.3. RhB dye releasing progress of HG, HGCM and HGCM-vTA at specified time intervals followed by UV-vis spectroscopy.

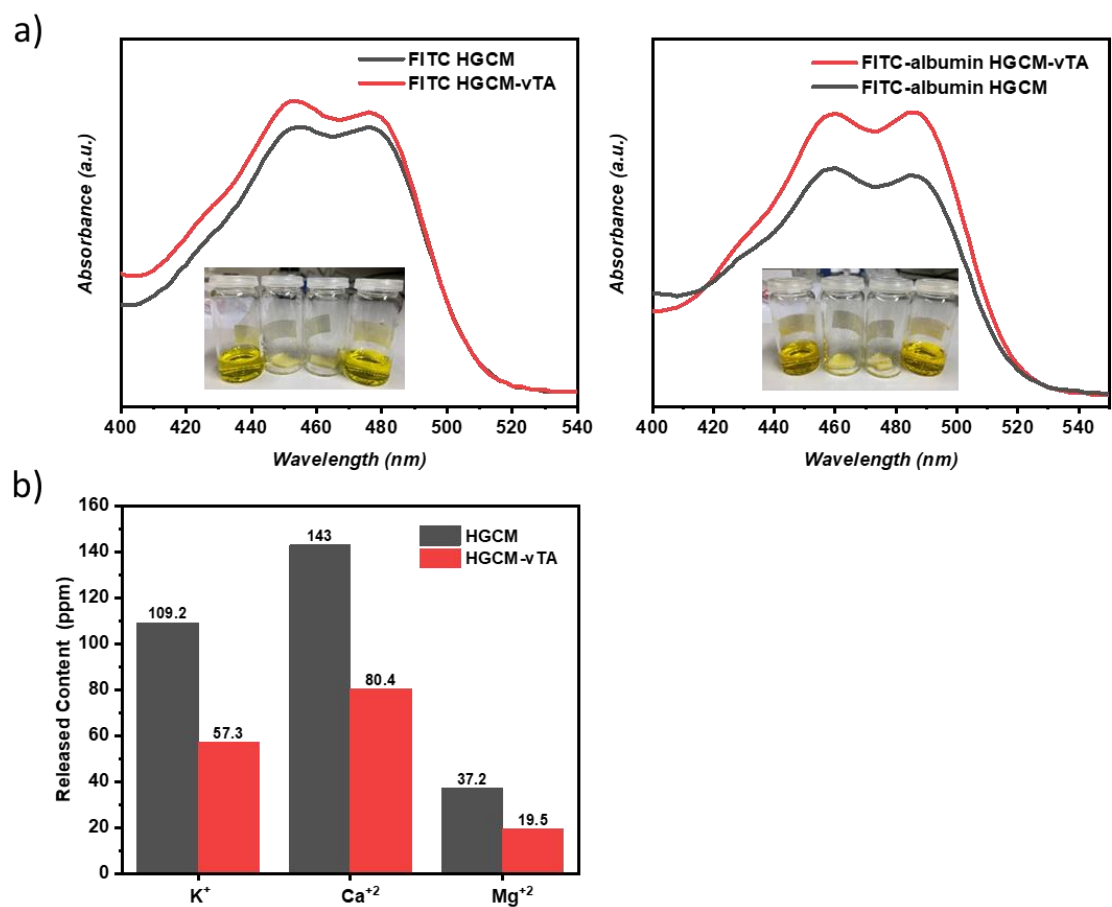


Figure S5.4. a) FITC-dextran and FITC-albumin releasing progress (after 24 hours) of HGCM and HGCM-vTA monitored by UV-vis spectroscopy. b) Inductively coupled plasma optical emission spectroscopy (ICP-OES) results of released K^+ , Ca^{2+} and Mg^{2+} content for HGCM and HGCM-vTA.

Chapter 6

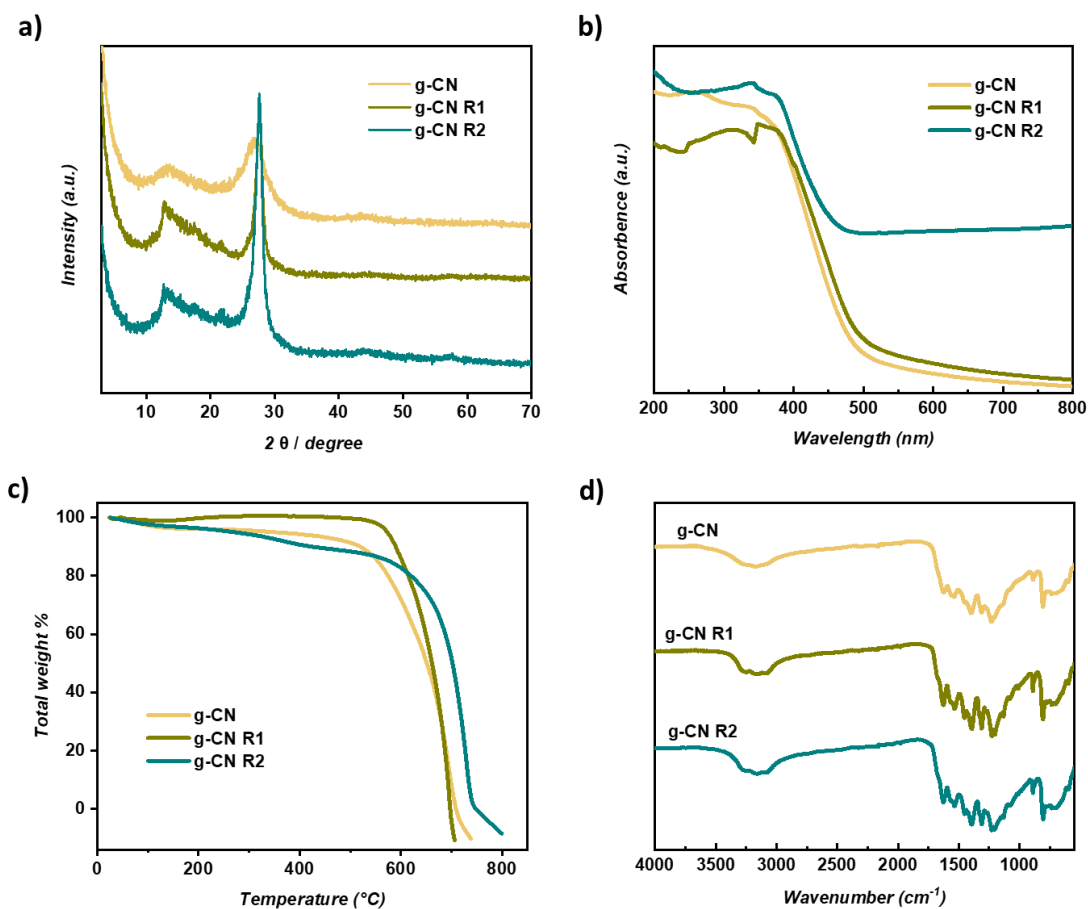


Figure S6.1. a) XRD profiles of freshly synthesized g-CN, isolated g-CN from path A (g-CN R1) and path B (g-CN R2), b) UV-Vis spectra of freshly synthesized g-CN, isolated g-CN from path A (R1) and path B (R2), c) TGA measurement of freshly synthesized g-CN, isolated g-CN from path A (g-CN R1) and path B (g-CN R2), d) FT-IR spectra of freshly synthesized g-CN and isolated g-CN from path A (g-CN R1) and path B (g-CN R2).

<i>Name</i>	<i>N(%)</i>	<i>C(%)</i>	<i>H(%)</i>	<i>S(%)</i>	<i>C/N</i>
CM	52,38	34,42	1,6	0,05	0,66
CM-R1	53,46	35,13	1,64	0,03	0,66
CM-R2	46,88	35,45	1,97	2,64	0,76

Table 6.1. Combustive elemental analysis results (in wt. %) of pristine g-CN, recovered g-CN R1 and oligo-EDOT deposited g-CN R2.

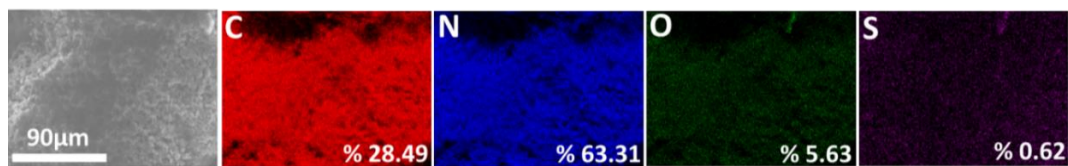


Figure S6.2. Elemental mapping via EDX results of oligo-EDOT deposited on g-CN R2.

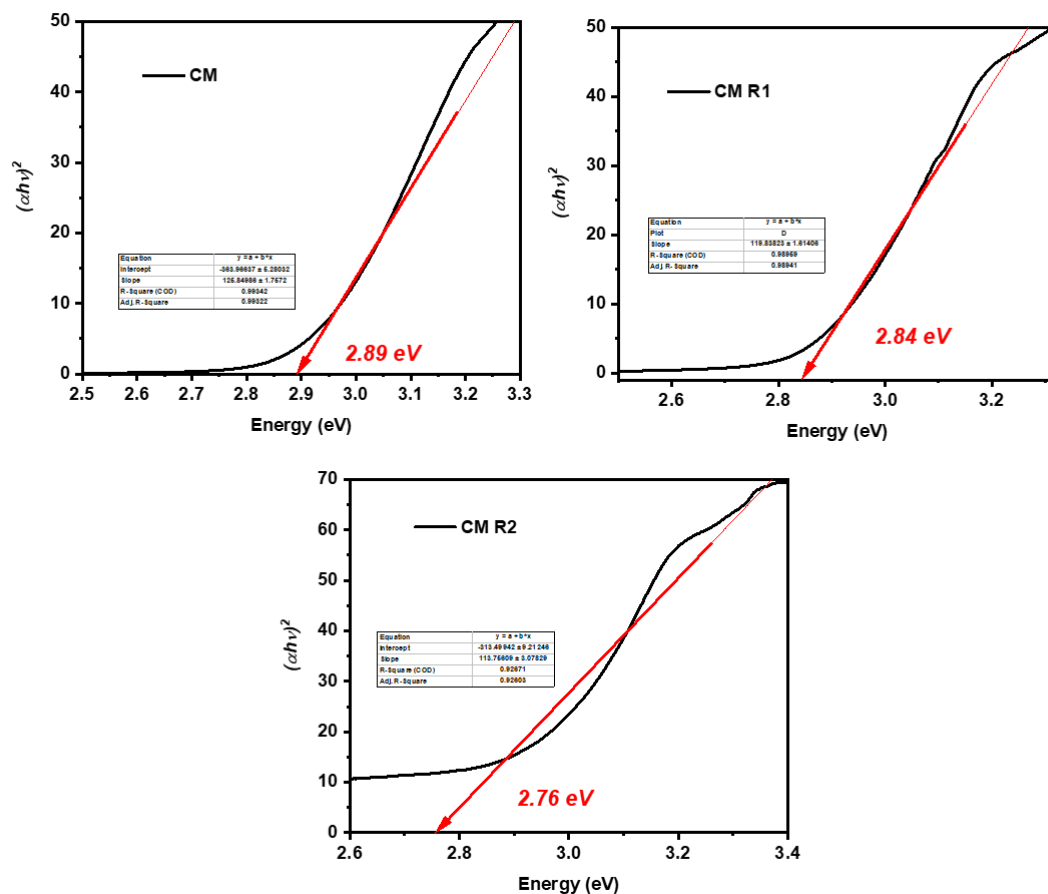


Figure S6.3. Tauc plots and estimated optical bandgaps of CM, CM R1 and CM R2 (calculated at the maximum absorption of CM for each sample).

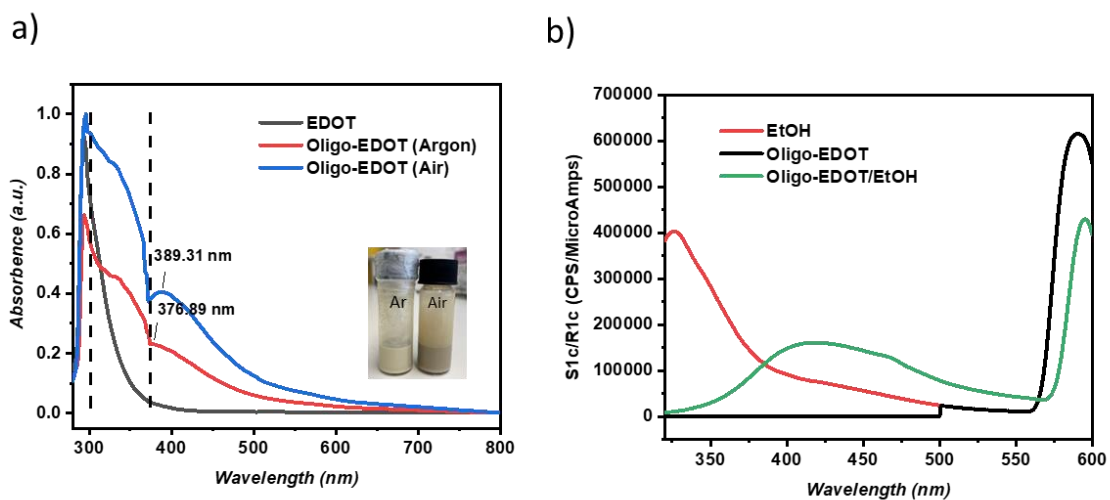


Figure S6.4. UV-vis spectra of EDOT, oligo-EDOT (Argon) and oligo-EDOT (Air) (after the depicted purification step, samples were prepared at 10^{-5} M in THF). b) Photoluminescence spectra of pure ethanol, oligo-EDOT and oligo-EDOT (10^{-5} M) in EtOH.

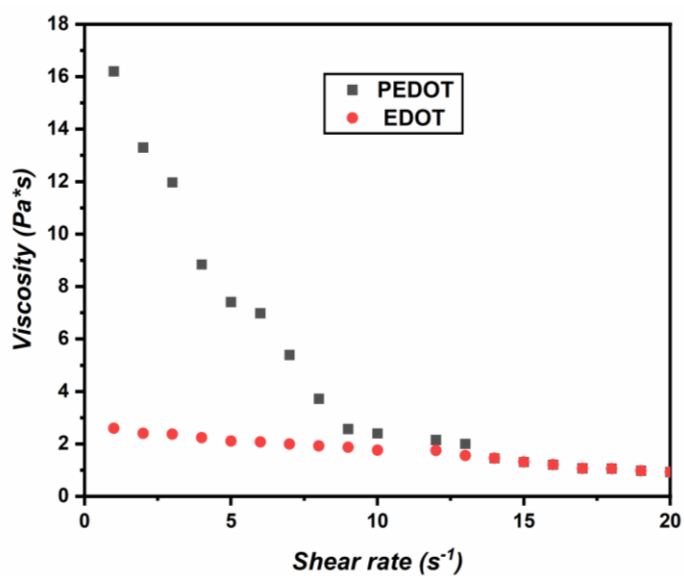


Figure 6.5. Viscosimetry results of EDOT and oligo-EDOT in varied shear rate.

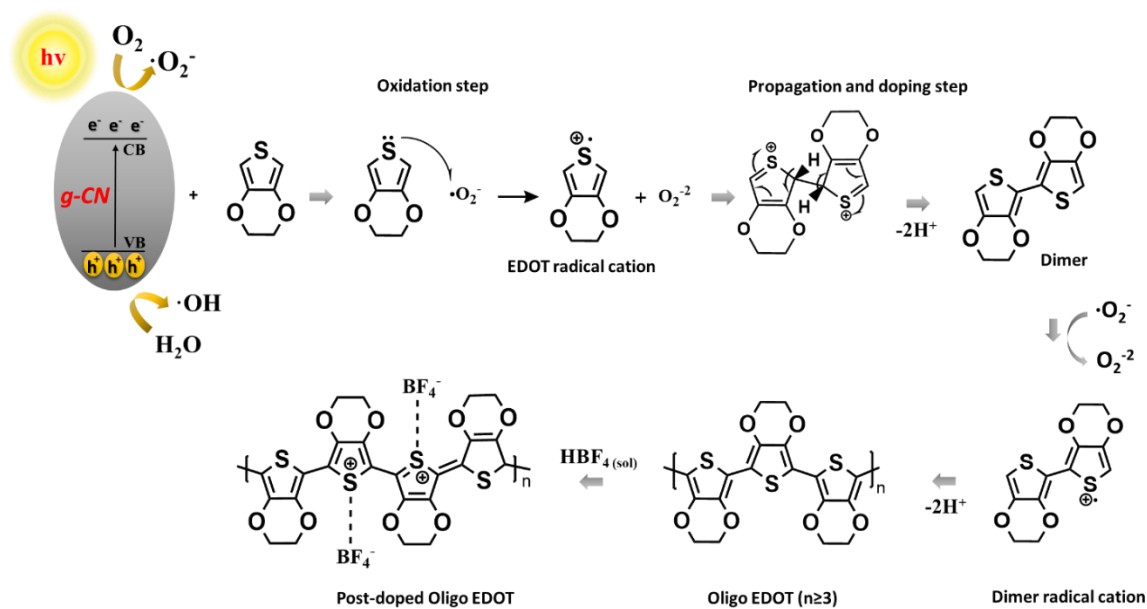


Figure S6.6. Proposed photoredox induced reaction mechanism of EDOT oligomerization in the presence of g-CN under visible light irradiation.

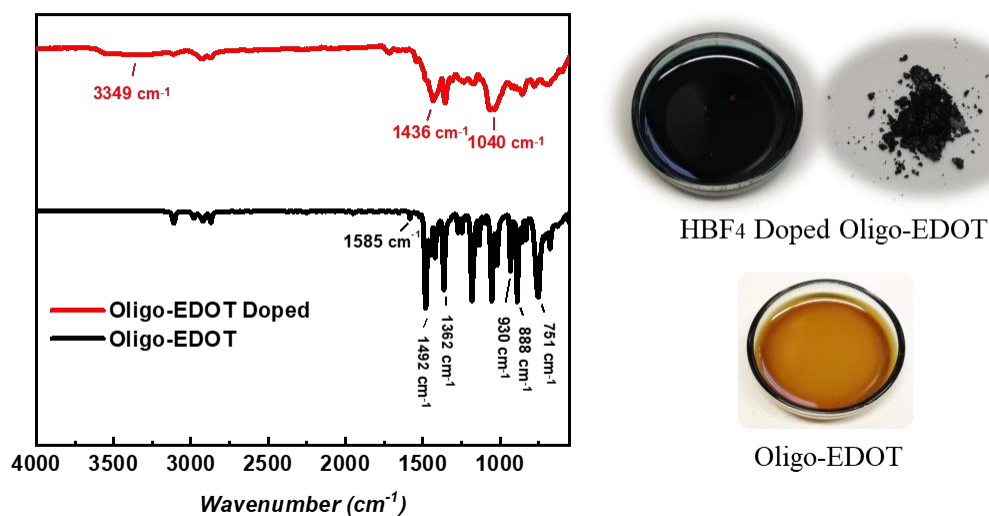


Figure S6.7. FT-IR spectra of oligo-EDOT and post doped oligo-EDOT in combination with their digital images.

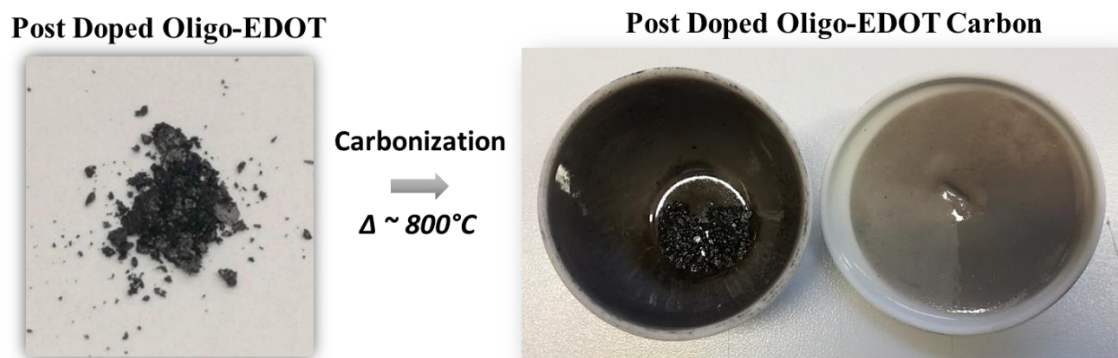


Figure S6.8. Post doped oligo-EDOT digital images before and after carbonization process.

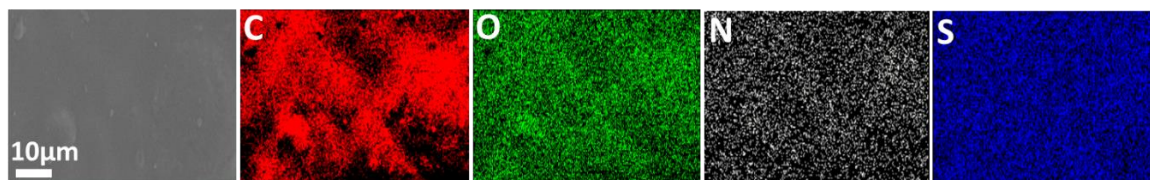


Figure S6.9. Elemental mapping via EDX results of a carbonaceous material derived from doped oligo-EDOT as a precursor.

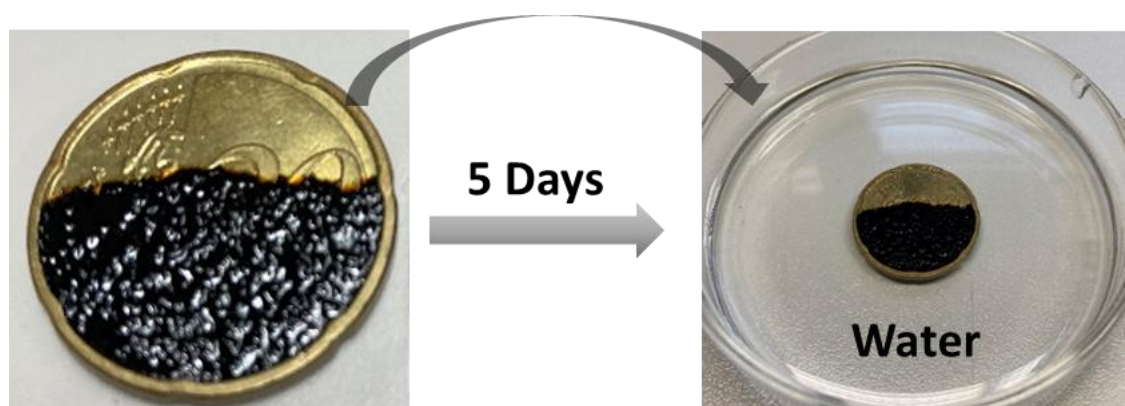


Figure S6.10. Post doped oligo-EDOT dried on a coin surface at 60°C in oven and immersed in water for 5 days.

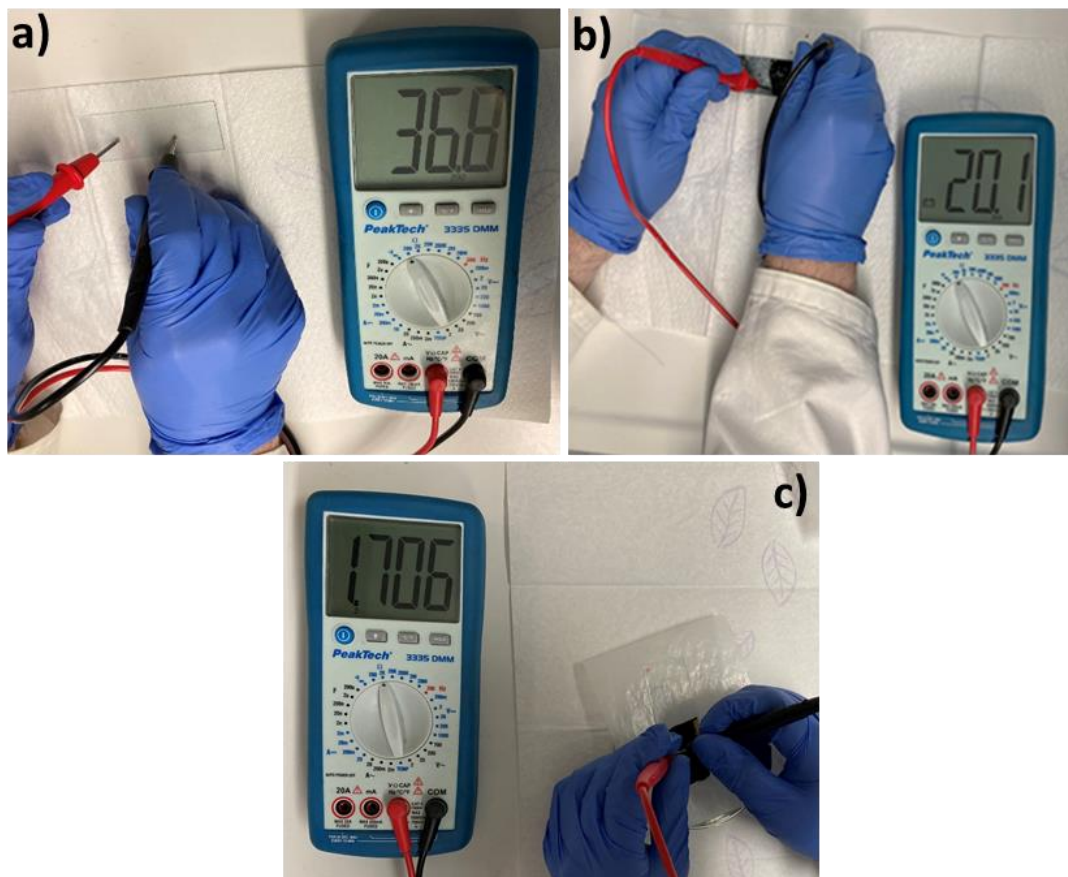


Figure S6.11. Resistivity measurement of a) ITO coated glass slide and b) post doped oligo-EDOT film on ITO coated glass slide (dial scale at: 200 Ω). c) in-situ g-CN doped oligo-EDOT coated glass slide (dial scale at: 2k Ω).

8.5. List of Figures

Chapter 2

Figure 2.1.	Triazine (a) and tri-s-triazine (heptazine) units of g-C ₃ N ₄	6
Figure 2.2.	Schematic overview of g-CN synthesis via nitrogen-rich precursors.	8
Figure 2.3.	Tunable properties of g-CN.	9
Figure 2.4.	Representative scheme of supramolecular structure formation via supramolecular complexation.	12
Figure 2.5.	Utilization of g-CN in various photo-based applications.	15
Figure 2.6.	Franck-Condon energy diagram (a) ⁶⁴ , extended Jablonski diagram with transient absorption displays the time-independent energies for the electronic states of a molecule (b). ⁶⁵	17
Figure 2.7.	Radical photopolymerization mechanism.	20
	21
Figure 2.8.	Overview of intermolecular photochemical and photoredox mechanisms through photo-radical polymerization.....	21
Figure 2.9.	a) Photocatalytic hydrogen production from water using TiO ₂ containing hydrogels with varied TiO ₂ amounts (TiO ₂ amount doubled on right curve) and the digital image of photoactive hydrogel before and after photocatalytic reaction, ¹²¹ b) Digital images of photoactive hydrogel cylinder against 500 g load (top) and tubular photoactive hydrogel against compression and its recovery (bottom), ¹²² c) SEM images of photoactive porous hydrogel beads (with varied g-CN content and crosslinker amount) obtained via inverse suspension polymerization. ⁵³	29
Figure 2.10.	a) Digital images and SEM images of g-CN based photoactive CO ₂ -induced porous hydrogels synthesized via tunable parameters and their influence on photocatalytic RhB degradation, ¹²⁵ b) Digital images of photoactive hydrogel beads in the column for RhB photodegradation as well as recyclability data, ¹²⁹ c) Photoactive hydrogel composite in dye removal and the influence of light intensity and direction on photocatalytic reaction inspired by natural seagrass. ¹³⁶	30

- Figure 2.11.** a) Schematic description and digital images of g-CN based aerogel synthesis,¹³⁸ b) Digital images and SEM images of 3D-printed photocatalytic aerogels.¹⁴¹ 37
- Figure 2.12.** a) Visible light induced self-cleaning activity of g-CN based PDMS sponge visualized via photocatalytic RhB degradation,¹⁵¹ b) Formation of rose Bengal grafted photocatalytic PDMS sponge,¹⁵² c) Schematic description for fabrication of g-CN based photoactive melamine sponge, as well as digital images of various samples and a preliminary compression strength demonstration.¹⁵⁴ 42
- Figure 3.1.** a) XRD profiles and b) FT-IR spectra of the CBT5m, BT5m (model), and reference beads. c) Solid UV-Vis spectra of BT5m (model), reference beads and pure vTA-CMp powder. d) TGA measurement of the CBT5m, BT5m (model), and reference beads. e) Photoluminescence spectra of CBT5m, BT5m and reference beads at 380 nm excitation wavelength. 53
- Figure 3.2.** Scanning electron microscopy (SEM) images of a1-a3) Model bead and a4-a6) its cross-section. b) Elemental mapping of Model bead via EDX, c) Confocal laser scanning microscopy images of toluene immersed Model bead from the right and left side, d) optical microscope image of Model bead taken after immersing in toluene. 55
- Figure 3.3** a) Average bead size of PS-co-DVB derived beads along with the size range (measured manually) and corresponding digital images of the tunable bead sizes, b) solvent uptake ratio measurements performed by 0.020g beads in 1 mL solvent for 24 hours. 57
- Figure 3.4.** Digital images of PS-co-DVB derived beads in RhB solution, from left to right: RhB Dye, REF, B5m, BT5m, CBT5m, BT5s, B7m, BT7m, BT10m a) before visible light irradiation, b) after 5 hours visible light irradiation. 58
- Figure 3.5.** a) RhB dye degradation of BT5M, CBT5m, reference and RhB dye solution (no catalyst) under visible light irradiation (BT5m-dark and CBT5m-dark were not exposed to visible light). b) Cyclic photocatalytic RhB dye degradation with several run cycles in the presence of CBT5m under visible light irradiation. c) Pseudo-first order kinetic fitting data of cycle 1 (pH:6.3, T=25° C, bead/RhB:0.055/0.0015 g.L⁻¹ d) pH effect on photodegradation of CBT5m under visible light irradiation. 62

- Figure 3.6.** a) Adsorption/desorption rate versus number cycles plot of model bead (24h time interval). b) pH effect on adsorption rate of model bead. 64
- Figure 3.7.** Elemental mapping results of CBT5m-VSA via EDX. 66
- Figure 4.1.** Solid UV-Vis spectra of TT, TT@CMp-vTA and pristine CMp-vTA powder along with digital images of TT@CMp-vTA (a), FT-IR spectra of TT@CMp-vTA, TTO@CMp-vTA, TTA@CMp-vTA (b), TGA measurement TT@CMp-vTA, TTO@CMp-vTA, TTA@CMp-vTA. 74
- Figure 4.2.** Scanning electron microscopy image of TT@CMp-vTA (a), cross sectional confocal laser scanning microscopy image of TT@CMp-vTA (b), Elemental mapping of TT@CMp-vTA via EDX (c), UV-vis spectra of TT@CMp-vTA (RhB dye degradation under visible light irradiation) (d). 75
- Figure 4.3.** Scanning electron microscopy image of CTT@CMp-vTA (a), digital images of TT@CMp-vTA and CTT@CMp-vTA (a-b) (b), Elemental mapping of CTT@CMp-vTA via EDX (c), Combustive elemental analysis results of TT@CMp-vTA and CTT@CMp-vTA (d). 77
- Figure 5.1.** a) FT-IR spectra of freeze-dried HGCM-vTA, HGCM and HG. b) UV spectra of freeze-dried HGCM-vTA, HGCM and HG. 84
- Figure 5.2.** Scanning electron microscopy (SEM) images of a) HGCM and b) HGCM-vTA in combination with their elemental mapping results via EDX. 85
- Figure 5.3.** a) Equilibrium swelling ratios of HG, HGCM, HGCM-vTA at specified time intervals. b) Thermogravimetric analysis of HGCM and HGCM-vTA. c) RhB dye releasing efficiency versus time plot of HG, HGCM, and HGCM-vTA. d) RhB dye adsorption/desorption concentrations of HG, HGCM, HGCM-vTA. 87
- Figure 5.4.** FT-IR spectra of freeze-dried HGCM-PAA, HGCM-PAAM, HGCM-PEGMEMA in comparison with HGCM. 91
- Figure 5.5.** Scanning electron microscopy (SEM) images of a) HGCM-PAA, b) HGCM-PAAM, and c) HGCM-PEGMEMA. 92
- Figure 5.6.** a) Thermogravimetric analysis of HGCM, HGCM-PAA, HGCM-PAAM and HGCM-PEGMEMA. b) Equilibrium swelling ratio results of HGCM-PAA, HGCM-

PAAM, HGCM-PEGMEMA in various conditions; pH2, pH7, pH13, 1M NaCl, 1M CaCl ₂	93
Figure 6.1. FT-IR spectrum of oxidatively photopolymerized oligo-EDOT along with its digital image (after catalyst separation).	100
Figure 6.2. a) FT-IR spectrum, b) XRD profile, c) UV-Vis spectrum, d) Thermogravimetric analysis of post-doped oligo-EDOT.	102
Figure 6.3. a) Scanning electron microscopy images of powder post-doped oligo-EDOT (a1) and coated post-doped oligo-EDOT coating on glass (a2). b) Optical microscopy images of in-situ g-CN doped oligo-EDOT under polarized (b1) and normal light (b2).	105

8.6.List of Tables

Chapter 3

Table 3.1. Preparation parameters of PS-co-DVB beads with vTA-CMp.	51
Table 3.2. Combustive elemental analysis results before and after surface modification of CBT5m via VSA and VP.	67
Table 6.1. Combustive elemental analysis results of doped oligo-EDOT and its carbonized product.	103

8.7.List of Schemes

Scheme 1.1 Versatility of g-CN into various polymer materials that are presented in this thesis.	4
Scheme 2.1. A sketch of crosslinked polymer network and subjects under the scope of the thesis.	26
Scheme 3.1. Schematic overview of organomodified g-CN (vTA-CMp) incorporation into PS-DVB beads via suspension photopolymerization	50
Scheme 3.2. The application spectra of vTA-CMp incorporated PS-co-DVB beads.	58

Scheme 3.3. Schematic overview of photo-induced surface modification of PS-co-DVB-vTA-CMp beads via visible light irradiation.	65
Scheme 4.1. Fabrication of thiol-ene polymer beads via liquid-liquid printing technique.	69
Scheme 4.2. Overview of interfacial solidification of thiol-ene bead.	72
Scheme 5.1. Schematic overview of g-CN embedded hydrogel fabrication and its subsequent photoinduced post-modifications.	81
Scheme 5.2. Hydrophobic hydrogel via photoinduced surface modification over embedded g-CN nanosheets in hydrogel network.	83
Scheme 5.3. Overview of pore substructuring via photoinduced free radical polymerization over embedded g-CN nanosheets in hydrogel network.	90
Scheme 6.1. Oxidative photopolymerization of EDOT via g-CN.....	97

Chapter 9

9. References

- [1] a) A. Molina-Garcia, A. D. Hansen, E. Muljadi, V. Gevorgian, J. Fortmann, E. Gomez-Lazaro, in *Large Scale Grid Integration of Renewable Energy Sources*, Institution of Engineering and Technology, **2017**, pp. 29-57; b) J. B. Dunn, E. Newes, H. Cai, Y. Zhang, A. Brooker, L. Ou, N. Mundt, A. Bhatt, S. Peterson, M. Bidy, *Energy Environ. Sci.* **2020**, *13*, 2262-2274.
- [2] a) E. E. Agency, IEA, *Population trends 1950 – 2100: globally and within Europe*, **2021**.
- [3] a) H. J. Cleaves, *Evol.: Educ. Outreach.* **2012**, *5*, 342-360; b) T. L. Davis, *J. Chem. Educ.* **1935**, *12*, 3.
- [4] Y. N. a. Harari, *Sapiens : a brief history of humankind*, First U.S. edition. New York : Harper, [2015], **2015**.
- [5] V. Balzani, G. Pacchioni, M. Prato, A. Zecchina, *Rend. Lincei Sci. Fis. Nat.* **2019**, *30*, 443-452.
- [6] R. W. J. Lim, A. C. Fahrenbach, *Pure Appl. Chem.* **2020**, *92*, 1971-1986.
- [7] G. Busch, *Eur. J. Phys.* **1989**, *10*, 254-264.
- [8] a) T. Jenkins, *Phys. Educ.* **2005**, *40*, 430-439; b) L. Łukasiak, A. Jakubowski, *J. Telecommun. Inf. Technol.* **2010**, 3-9.
- [9] A. Fujishima, K. Honda, *Nature* **1972**, *238*, 37-38.
- [10] a) J. W. Fan, X. H. Liu, J. Zhang, *Environ. Technol.* **2011**, *32*, 427-437; b) M. R. Espino-Estévez, C. Fernández-Rodríguez, O. M. González-Díaz, J. Araña, J. P. Espinós, J. A. Ortega-Méndez, J. M. Doña-Rodríguez, *Chem. Eng. J.* **2016**, *298*, 82-95; c) E. M. Rockafellow, L. K. Stewart, W. S. Jenks, *Appl. Catal., B* **2009**, *91*, 554-562; d) P. Chowdhury, J. Moreira, H. Gomaa, A. K. Ray, *Ind. Eng. Chem. Res.* **2012**, *51*, 4523-4532.
- [11] a) X. Zhou, Q. Xu, W. Lei, T. Zhang, X. Qi, G. Liu, K. Deng, J. Yu, *Small* **2014**, *10*, 674-679; b) L. Shang, B. Tong, H. Yu, G. I. N. Waterhouse, C. Zhou, Y. Zhao, M. Tahir, L.-Z. Wu, C.-H. Tung, T. Zhang, *Adv. Energy Mater.* **2016**, *6*, 1501241; c) F. Xu, Y. Shen, L. Sun, H. Zeng, Y. Lu, *Nanoscale* **2011**, *3*, 5020-5025; d) G. Mamba, A. K. Mishra, *Applied Catal., B:* **2016**, *198*, 347-377; e) J. C. Murillo-Sierra, A. Hernández-Ramírez, L. Hinojosa-Reyes, J. L. Guzmán-Mar, *Chem. Eng. J. Adv.* **2021**, *5*, 100070; f) K. Vinodgopal, I. Bedja, P. V. Kamat, *Chem. Mater.* **1996**, *8*, 2180-2187; g) W. D. Kim, J.-H. Kim, S. Lee, S. Lee, J. Y. Woo, K. Lee, W.-S. Chae, S. Jeong, W. K. Bae, J. A. McGuire, J. H. Moon, M. S. Jeong, D. C. Lee, *Chem. Mater.* **2016**, *28*, 962-968; h) J. Lin, C. Yao, L. Wu, K. Jiang, Z. Hu, L. Li, N. Xu, J. Sun, J. Wu, *J. Phys. Chem. C.* **2021**, *125*, 9119-9128; i) F. A. Harraz, A. A. Ismail, S. A. Al-Sayari, A. Al-Hajry, *J. Photochem. Photobiol., A* **2015**, *299*, 18-24; j) L. Gu, J. Wang, R. Qi, X. Wang, P. Xu, X. Han, *J. Mol. Catal. A: Chem.* **2012**, *357*, 19-25; k) S. Ghosh, A. K. Mallik, R. N. Basu, *Solar Energy* **2018**, *159*, 548-560.
- [12] a) X. Wang, K. Maeda, A. Thomas, K. Takanabe, G. Xin, J. M. Carlsson, K. Domen, M. Antonietti, *Nat. Mater.* **2009**, *8*, 76-80; b) S. C. Yan, Z. S. Li, Z. G.

- Zou, *Langmuir* **2009**, *25*, 10397-10401; c) W.-J. Ong, L.-L. Tan, Y. H. Ng, S.-T. Yong, S.-P. Chai, *Chem. Rev.* **2016**, *116*, 7159-7329.
- [13] a) M. Antonietti, K. Tauer, *Macromol. Chem. Phys.* **2003**, *204*, 207-219; b) A. S. Abd-El-Aziz, M. Antonietti, C. Barner-Kowollik, W. H. Binder, A. Böker, C. Boyer, M. R. Buchmeiser, S. Z. D. Cheng, F. D'Agosto, G. Floudas, H. Frey, G. Galli, J. Genzer, L. Hartmann, R. Hoogenboom, T. Ishizone, D. L. Kaplan, M. Leclerc, A. Lendlein, B. Liu, T. E. Long, S. Ludwigs, J.-F. Lutz, K. Matyjaszewski, M. A. R. Meier, K. Müllen, M. Müllner, B. Rieger, T. P. Russell, D. A. Savin, A. D. Schlüter, U. S. Schubert, S. Seiffert, K. Severing, J. B. P. Soares, M. Staffilani, B. S. Sumerlin, Y. Sun, B. Z. Tang, C. Tang, P. Théato, N. Tirelli, O. K. C. Tsui, M. M. Unterlass, P. Vana, B. Voit, S. Vyazovkin, C. Weder, U. Wiesner, W.-Y. Wong, C. Wu, Y. Yagci, J. Yuan, G. Zhang, *Mater. Chem. Phys.* **2020**, *221*, 2000216.
- [14] a) J. V. Liebig, *Ann. Pharm.* **1834**, *10*, 1-47; b) J. Liebig, *Liebigs Ann.* **1845**, *53*, 330-348; c) A. Thomas, A. Fischer, F. Goettmann, M. Antonietti, J.-O. Müller, R. Schlögl, J. M. Carlsson, *J. Mater. Chem.* **2008**, *18*, 4893-4908.
- [15] V. W.-h. Lau, B. V. Lotsch, *Adv. Energy Mater.* **2022**, *12*, 2101078.
- [16] R. S. Hosmane, M. A. Rossman, N. J. Leonard, *J. Am. Chem. Soc.* **1982**, *104*, 5497-5499.
- [17] A. Y. Liu, M. L. Cohen, *Science* **1989**, *245*, 841-842.
- [18] E. G. Gillan, *Chem. Mater.* **2000**, *12*, 3906-3912.
- [19] a) B. Kumru, in *Concepts and Design of Materials Nanoarchitectonics*, The Royal Society of Chemistry, **2022**, pp. 193-209; b) B. Kumru, M. Antonietti, *Adv. Colloid Interface Sci.* **2020**, *283*, 102229.
- [20] Y. Wang, X. Wang, M. Antonietti, Y. Zhang, *ChemSusChem* **2010**, *3*, 435-439.
- [21] a) X. Zhang, X. Xie, H. Wang, J. Zhang, B. Pan, Y. Xie, *J. Am. Chem. Soc.* **2013**, *135*, 18-21; b) Q. Gu, Z. Gao, H. Zhao, Z. Lou, Y. Liao, C. Xue, *Rsc Advances* **2015**, *5*, 49317-49325; c) L. Chen, R. Yan, M. Oschatz, L. Jiang, M. Antonietti, K. Xiao, *Angew. Chem. Int. Ed. Engl.* **2020**, *59*, 9067-9073; d) X. H. Li, J. S. Zhang, X. F. Chen, A. Fischer, A. Thomas, M. Antonietti, X. C. Wang, *Chem. Mater.* **2011**, *23*, 4344-4348; e) S. Wang, C. Li, T. Wang, P. Zhang, A. Li, J. Gong, *J. Mater. Chem. A* **2014**; f) J. H. Sun, J. S. Zhang, M. W. Zhang, M. Antonietti, X. Z. Fu, X. C. Wang, *Nat. Commun.* **2012**, *3*, 1-7; g) Q. Cui, J. Xu, X. Wang, L. Li, M. Antonietti, M. Shalom, *Angew. Chem. Int. Ed. Engl.* **2016**, *55*, 3672-3676.
- [22] Y. Zhang, J. Liu, G. Wu, W. Chen, *Nanoscale* **2012**, *4*, 5300-5303.
- [23] X. Wang, K. Maeda, X. Chen, K. Takanabe, K. Domen, Y. Hou, X. Fu, M. Antonietti, *J. Am. Chem. Soc.* **2009**, *131*, 1680-1681.
- [24] X. Bai, S. Yan, J. Wang, L. Wang, W. Jiang, S. Wu, C. Sun, Y. Zhu, *J. Mater. Chem. A* **2014**, *2*, 17521-17529.
- [25] F. Dong, Y. J. Sun, L. W. Wu, M. Fu, Z. B. Wu, *Catal. Sci. Technol.* **2012**, *2*, 1332-1335.
- [26] B. H. Long, J. L. Lin, X. C. Wang, *J. Mater. Chem. A* **2014**, *2*, 2942-2951.
- [27] Y. Zheng, Z. S. Zhang, C. H. Li, *J. Photochem. Photobiol., A* **2017**, *332*, 32-44.
- [28] H. Liu, X. Wang, H. Wang, R. Nie, *J. Mater. Chem. B* **2019**, *7*, 5432-5448.

- [29] B. V. Lotsch, M. Doblinger, J. Sehnert, L. Seyfarth, J. Senker, O. Oeckler, W. Schnick, *Chem. Eur. J.* **2007**, *13*, 4969-4980.
- [30] W.-J. Ong, L.-L. Tan, Y. H. Ng, S.-T. Yong, S.-P. Chai, *Chem. Rev.* **2016**, *116*, 7159-7329.
- [31] M. Shalom, M. Guttentag, C. Fettkenhauer, S. Inal, D. Neher, A. Llobet, M. Antonietti, *Chem. Mater.* **2014**, *26*, 5812-5818.
- [32] F. K. Kessler, Y. Zheng, D. Schwarz, C. Merschjann, W. Schnick, X. C. Wang, M. J. Bojdys, *Nat. Rev. Mater.* **2017**, *2*, 17030.
- [33] Z. Yang, Y. J. Zhang, Z. Schnepf, *J. Mater. Chem. A* **2015**, *3*, 14081-14092.
- [34] H. Li, L. Z. Wang, Y. D. Liu, J. Y. Lei, J. L. Zhang, *Res. Chem. Intermed.* **2016**, *42*, 3979-3998.
- [35] Z. Mo, X. She, Y. Li, L. Liu, L. Huang, Z. Chen, Q. Zhang, H. Xu, H. Li, *RSC Adv.* **2015**, *5*, 101552-101562.
- [36] D. J. Martin, K. Qiu, S. A. Shevlin, A. D. Handoko, X. Chen, Z. Guo, J. Tang, *Angew. Chem. Int. Ed.* **2014**, *53*, 9240-9245.
- [37] a) H. Schlomberg, J. Kröger, G. k. Savasci, M. W. Terban, S. Bette, I. Moudrakovski, V. Duppel, F. Podjaski, R. e. Siegel, J. r. Senker, R. E. Dinnebier, C. Ochsenfeld, B. V. Lotsch, *Chem. Mater.* **2019**, *31*, 7478-7486; b) S. Y. Chong, J. T. A. Jones, Y. Z. Khimiyak, A. I. Cooper, A. Thomas, M. Antonietti, M. J. Bojdys, *J. Mater. Chem. A* **2013**, *1*, 1102-1107.
- [38] a) E. Wirnhier, M. Doblinger, D. Gunzelmann, J. Senker, B. V. Lotsch, W. Schnick, *Chemistry-a European Journal* **2011**, *17*, 3213-3221; b) L. Tian, J. Y. Li, F. Liang, J. K. Wang, S. S. Li, H. J. Zhang, S. W. Zhang, *Appl. Catal., B* **2018**, *225*, 307-313; c) G. Zhang, G. Li, T. Heil, S. Zafeirotos, F. Lai, A. Savateev, M. Antonietti, X. Wang, *Angew. Chem. Int. Ed. Engl.* **2019**, *58*, 3433-3437.
- [39] H. L. Gao, S. C. Yan, J. J. Wang, Z. G. Zou, *Dalton Trans.* **2014**, *43*, 8178-8183.
- [40] a) J. S. Zhang, J. H. Sun, K. Maeda, K. Domen, P. Liu, M. Antonietti, X. Z. Fu, X. C. Wang, *Energy Environ. Sci.* **2011**, *4*, 675-678; b) F. He, G. Chen, Y. Yu, Y. Zhou, Y. Zheng, S. Hao, *Chem. Commun.* **2014**, *51*, 425-427; c) Z. F. Huang, J. J. Song, L. Pan, Z. M. Wang, X. Q. Zhang, J. J. Zou, W. B. Mi, X. W. Zhang, L. Wang, *Nano Energy* **2015**, *12*, 646-656; d) Y. Zhou, L. Zhang, W. Huang, Q. Kong, X. Fan, M. Wang, J. Shi, *Carbon* **2016**, *99*, 111-117; e) J. R. Ran, T. Y. Ma, G. P. Gao, X. W. Du, S. Z. Qiao, *Energy Environ. Sci.* **2015**, *8*, 3708-3717; f) S. C. Yan, Z. S. Li, Z. G. Zou, *Langmuir* **2010**, *26*, 3894-3901.
- [41] a) H. Yan, Y. Chen, S. Xu, *Int. J. Hydrogen Energy* **2012**, *37*, 125-133; b) X. S. Zhang, J. Y. Hu, H. Jiang, *Chem. Eng. J.* **2014**, *256*, 230-237; c) J. Gao, Y. Zhou, Z. Li, S. Yan, N. Wang, Z. Zou, *Nanoscale* **2012**, *4*, 3687-3692.
- [42] M. Shalom, S. Inal, C. Fettkenhauer, D. Neher, M. Antonietti, *J. Am. Chem. Soc.* **2013**, *135*, 7118-7121.
- [43] J. Xia, G. Mark, M. Volokh, Y. Fang, H. Chen, X. Wang, M. Shalom, *Nanoscale* **2021**, *13*, 19511-19517.
- [44] J. Barrio, M. Shalom, *ChemCatChem* **2018**, *10*, 5573-5586.
- [45] Y.-S. Jun, E. Z. Lee, X. Wang, W. H. Hong, G. D. Stucky, A. Thomas, *Adv. Funct. Mater.* **2013**, *23*, 3661-3667.

- [46] G. Algara-Siller, N. Severin, S. Y. Chong, T. Bjorkman, R. G. Palgrave, A. Laybourn, M. Antonietti, Y. Z. Khimyak, A. V. Krasheninnikov, J. P. Rabe, U. Kaiser, A. I. Cooper, A. Thomas, M. J. Bojdys, *Angew. Chem. Int. Ed. Engl.* **2014**, *53*, 7450-7455.
- [47] L. M. Peter, in *Photocatalysis*, The Royal Society of Chemistry, **2016**, pp. 1-28.
- [48] a) X. Liu, R. Ma, L. Zhuang, B. Hu, J. Chen, X. Liu, X. Wang, *Crit. Rev. Env. Sci. Tec.* **2020**; b) H. H. Xiao, W. Y. Wang, G. G. Liu, Z. M. Chen, K. L. Lv, J. J. Zhu, *Appl. Surf. Sci.* **2015**, *358*, 313-318.
- [49] a) J. Qin, S. Wang, H. Ren, Y. Hou, X. Wang, *Appl. Catal., B* **2015**, *179*, 1-8; b) P. Niu, L. L. Zhang, G. Liu, H. M. Cheng, *Adv. Funct. Mater.* **2012**, *22*, 4763-4770.
- [50] a) B. Kiskan, J. Zhang, X. Wang, M. Antonietti, Y. Yagci, *ACS Macro Lett.* **2012**, *1*, 546-549; b) S. Dadashi-Silab, M. A. Tasdelen, B. Kiskan, X. Wang, M. Antonietti, Y. Yagci, *Macromol. Chem. Phys.* **2014**, *215*, 675-681; c) S. Dadashi-Silab, B. Kiskan, M. Antonietti, Y. Yagci, *RSC Adv.* **2014**, *4*, 52170-52173; d) Q. Fu, Q. Ruan, T. G. McKenzie, A. Reyhani, J. Tang, G. G. Qiao, *Macromolecules* **2017**, *50*, 7509-7516.
- [51] K. Kaya, B. Kiskan, B. Kumru, B. V. K. J. Schmidt, Y. Yagci, *Eur. Polym. J.* **2020**, *122*, 109410.
- [52] Q. Cao, B. Kumru, M. Antonietti, B. V. K. J. Schmidt, *Mater. Horiz.* **2020**, *7*, 762-786.
- [53] Q. Cao, J. Barrio, M. Antonietti, B. Kumru, M. Shalom, B. V. K. J. Schmidt, *ACS Appl. Polym. Mater.* **2020**, *2*, 3346-3354.
- [54] B. Kumru, D. Cruz, T. Heil, B. V. K. J. Schmidt, M. Antonietti, *J. Am. Chem. Soc.* **2018**, *140*, 17532-17537.
- [55] Q. Cao, B. Kumru, *Polymers* **2020**, *12*.
- [56] a) P. Giusto, D. Cruz, T. Heil, H. Arazoe, P. Lova, T. Aida, D. Comoretto, M. Patrini, M. Antonietti, *Adv. Mater.* **2020**, *32*, 1908140; b) S. Mazzanti, G. Manfredi, A. J. Barker, M. Antonietti, A. Savateev, P. Giusto, *Acs Catalysis* **2021**, *11*, 11109-11116; c) P. Giusto, B. Kumru, J. Zhang, R. Rothe, M. Antonietti, *Chem. Mater.* **2020**.
- [57] a) K. Xiao, P. Giusto, L. P. Wen, L. Jiang, M. Antonietti, *Angew. Chem. Int. Ed.* **2018**, *57*, 10123-10126; b) K. Tkacz-Śmiech, K. Koper, A. Mikula, B. Sahraoui, J. Jaglarz, *Thin Solid Films* **2018**, *646*, 28-35.
- [58] a) G. W. Zou, W. Wu, C. B. Cong, X. Y. Meng, K. Zhao, Q. Zhou, *Rsc Advances* **2016**, *6*, 106237-106247; b) J. S. Xu, T. J. K. Brenner, L. Chabanne, D. Neher, M. Antonietti, M. Shalom, *J. Am. Chem. Soc.* **2014**, *136*, 13486-13489; c) J. Xu, M. Shalom, F. Piersimoni, M. Antonietti, D. Neher, T. J. K. Brenner, *Adv. Opt. Mater.* **2015**, *3*, 913-917.
- [59] a) M. Ismael, *J. Alloys Compd.* **2020**, *846*, 156446; b) N. Rono, J. K. Kibet, B. S. Martincigh, V. O. Nyamori, *Crit. Rev. Solid State Mater. Sci.* **2020**, *46*, 189-217.
- [60] a) J. C. Scaiano, *Photochemistry Essentials*, ACS, **2021**; b) J. Franck, E. Rabinowitsch, *Trans. Faraday Soc.* **1934**, *30*, 120-130.
- [61] a) C. N. Bowman, C. J. Kloxin, *AIChE J.* **2008**, *54*, 2775-2795; b) A. Albin, *Photochem. Photobiol. Sci.* **2016**, *15*, 319-324; c) T. Liu, J. P. Sullivan, K. Asai,

- C. Klein, Y. Egami, in *Pressure and Temperature Sensitive Paints* (Eds.: T. Liu, J. P. Sullivan, K. Asai, C. Klein, Y. Egami), Springer International Publishing, Cham, **2021**, pp. 13-30.
- [62] G. Casasanta, F. Falcini, R. Garra, *J. Photochem. Photobiol., A* **2022**, *432*, 114086.
- [63] U. E. Steiner, in *Photodynamic Therapy: From Theory to Application* (Ed.: M. H. Abdel-Kader), Springer Berlin Heidelberg, Berlin, Heidelberg, **2014**, pp. 25-58.
- [64] A. Nano, **2015**.
- [65] J. Zhao, W. Wu, J. Sun, S. Guo, *Chem. Soc. Rev.* **2013**, *42*, 5323-5351.
- [66] K. Stranius, K. Börjesson, *Sci. Rep.* **2017**, *7*, 41145.
- [67] B. S. I. P. Dinda, **2017**.
- [68] a) G. Moad, E. Rizzardo, S. H. Thang, *Aust. J. Chem.* **2005**, *58*, 379-410; b) N. V. Tsarevsky, K. Matyjaszewski, *Chem Rev* **2007**, *107*, 2270-2299; c) E. Harth, A. Bosman, C. Hawker, *Chem. Rev* **2001**, *101*, 3661-3688; d) B. M. Rosen, V. Percec, *Chem. Rev.* **2009**, *109*, 5069-5119; e) K. Hayashi, *Polym. J.* **1980**, *12*, 583-596; f) J. F. Quinn, L. Barner, C. Barner-Kowollik, E. Rizzardo, T. P. Davis, *Macromolecules* **2002**, *35*, 7620-7627; g) S. Yamago, *Chem. Rev.* **2009**, *109*, 5051-5068; h) M. Ouchi, T. Terashima, M. Sawamoto, *Chem Rev* **2009**, *109*, 4963-5050.
- [69] T. M. Lovestead, A. K. O'Brien, C. N. Bowman, *J. Photochem. Photobiol., A* **2003**, *159*, 135-143.
- [70] a) J.-P. Fouassier, J. Lalevée, *Photoinitiators for polymer synthesis: scope, reactivity, and efficiency, Vol. 52*, John Wiley & Sons, **2012**; b) M.-A. Tehfe, F. Dumur, B. Graff, F. Morlet-Savary, D. Gimes, J.-P. Fouassier, J. Lalevée, *Polym. Chem.* **2013**, *4*, 2313-2324.
- [71] a) M. Kaur, A. K. Srivastava, *J. Macromol. Sci., Polym. Rev.* **2002**, *42*, 481-512; b) J. Kabatc, Z. Kucybała, M. Pietrzak, F. Ścigalski, J. Pączkowski, *Polymer* **1999**, *40*, 735-745.
- [72] M. Chen, M. Zhong, J. A. Johnson, *Chem. Rev.* **2016**, *116*, 10167-10211.
- [73] B. L. Buss, G. M. Miyake, *Chem. Mater.* **2018**, *30*, 3931-3942.
- [74] a) F. Nzulu, S. Telitel, F. Stoffelbach, B. Graff, F. Morlet-Savary, J. Lalevée, L. Fensterbank, J.-P. Goddard, C. Ollivier, *Polym. Chem.* **2015**, *6*, 4605-4611; b) M. A. Tasdelen, M. Ciftci, Y. Yagci, *Macromol. Chem. Phys.* **2012**, *213*, 1391-1396; c) Y. Kwak, K. Matyjaszewski, *Macromolecules* **2010**, *43*, 5180-5183; d) M. A. Tasdelen, M. Uygun, Y. Yagci, *Macromol. Rapid Commun.* **2011**, *32*, 58-62.
- [75] a) S. Mazzanti, A. Savateev, *Chempluschem* **2020**, *85*, 2499-2517; b) A. J. Rieth, Y. Qin, B. C. M. Martindale, D. G. Nocera, *J. Am. Chem. Soc.* **2021**, *143*, 4646-4652; c) G. Chen, Z. Zhang, W. Zhang, L. Xia, X. Nie, W. Huang, X. Wang, L. Wang, C. Hong, Z. Zhang, Y. You, *Mater Horiz* **2021**, *8*, 2018-2024.
- [76] a) K. Ikemura, T. Endo, *Dent. Mater. J.* **2010**, *29*, 481-501; b) M. D. Goodner, C. N. Bowman, C. N. Bowman, *Chem. Eng. Sci.* **2002**, *57*, 887-900; c) J. E. Krause, N. D. Brault, Y. Li, H. Xue, Y. Zhou, S. Jiang, *Macromolecules* **2011**, *44*, 9213-9220; d) R. J. Vonk, S. Wouters, A. Barcaru, G. Vivó-Truyols, S. Eeltink, L. J. de Koning, P. J. Schoenmakers, *Anal. Bioanal. Chem.* **2015**, *407*, 3817-3829; e) J. B. Tan, G. Y. Zhao, Y. J. Lu, Z. H. Zeng, M. A. Winnik, *Macromolecules* **2014**, *47*, 6856-6866; f) J. Guo, M. R. Gleeson, J. T. Sheridan, *Phys. Res. Int.* **2012**, *2012*,

- 803439; g) Z. Huang, G. C.-P. Tsui, Y. Deng, C.-Y. Tang, *Nanotechnol. Rev.* **2020**, *9*, 1118-1136.
- [77] T. F. Scott, A. D. Schneider, W. D. Cook, C. N. Bowman, *Science* **2005**, *308*, 1615-1617.
- [78] a) Y. Yanagisawa, Y. Nan, K. Okuro, T. Aida, *Science* **2018**, *359*, 72-76; b) S. Yu, R. Zhang, Q. Wu, T. Chen, P. Sun, *Adv. Mater.* **2013**, *25*, 4912-4917.
- [79] a) D. J. Fortman, J. P. Brutman, G. X. De Hoe, R. L. Snyder, W. R. Dichtel, M. A. Hillmyer, *ACS Sustainable Chem. Eng.* **2018**, *6*, 11145-11159; b) C. J. Kloxin, T. F. Scott, B. J. Adzima, C. N. Bowman, *Macromolecules* **2010**, *43*, 2643-2653.
- [80] J. F. Chen, E. S. Garcia, S. C. Zimmerman, *Acc. Chem. Res.* **2020**, *53*, 1244-1256.
- [81] a) B. Kumru, V. Molinari, M. Hilgart, F. Rummel, M. Schaffler, B. V. K. J. Schmidt, *Polym. Chem.* **2019**, *10*, 3647-3656; b) O. Ozer, A. Ince, B. Karagoz, N. Bicak, *Desalination* **2013**, *309*, 141-147; c) M. Liu, Y. Ishida, Y. Ebina, T. Sasaki, T. Hikima, M. Takata, T. Aida, *Nature* **2015**, *517*, 68-72.
- [82] a) K. D. Q. Nguyen, M. Crespo-Ribadeneyra, O. Picot, B. Colak, J. E. Gautrot, *Acs Applied Polymer Materials* **2021**, *3*, 5373-5385; b) X. Fernández-Francos, X. Ramis, *Eur. Polym. J.* **2015**, *70*, 286-305; c) N. S. A. Rahman, N. A. Ahmad, M. F. Yhaya, B. Azahari, W. R. Ismail, *J. Appl. Polym. Sci.* **2016**, *133*, 43576.
- [83] Y. Wang, Q. B. Chen, M. Chen, Y. Guan, Y. Zhang, *Polym. Chem.* **2019**, *10*, 4844-4851.
- [84] P. Mondal, S. K. Saha, P. Chowdhury, *J. Appl. Polym. Sci.* **2012**, *127*, 5045-5050.
- [85] Y. J. Wang, X. N. Zhang, Y. H. Song, Y. P. Zhao, L. Chen, F. M. Su, L. B. Li, Z. L. Wu, Q. Zheng, *Chem. Mater.* **2019**, *31*, 1430-1440.
- [86] X. T. Le, S. L. Turgeon, *Soft Matter* **2013**, *9*, 3063-3073.
- [87] T. Chen, M. Li, J. Liu, *Cryst. Growth Des.* **2018**, *18*, 2765-2783.
- [88] a) T. Li, B. Kumru, N. Al Nakeeb, J. Willersinn, B. Schmidt, *Polymers (Basel)* **2018**, *10*, 576; b) E. A. Appel, F. Biedermann, U. Rauwald, S. T. Jones, J. M. Zayed, O. A. Scherman, *J. Am. Chem. Soc.* **2010**, *132*, 14251-14260.
- [89] a) B. Kumru, V. Molinari, R. Dunnebacke, K. G. Blank, B. Schmidt, *Macromol. Rapid Commun.* **2019**, *40*, e1800712; b) R. Parhi, *Adv Pharm Bull* **2017**, *7*, 515-530.
- [90] Q. Z. Liu, K. Yan, J. H. Chen, M. Xia, M. F. Li, K. Liu, D. Wang, C. Z. Wu, Y. Xie, *Aggregate* **2021**, *2*, e30.
- [91] B. Kumru, B. Gure, N. Bicak, *J. Polym. Sci., Part A: Polym. Chem.* **2013**, *51*, 3892-3900.
- [92] L. P. Zeng, X. X. Lin, P. Li, F. Q. Liu, H. Guo, W. H. Li, *Prog. Org. Coat.* **2021**, *159*, 106417.
- [93] D. Y. Zhu, S. Handschuh-Wang, X. C. Zhou, *J. Mater. Chem. A* **2017**, *5*, 16467-16497.
- [94] C. D. Spicer, *Polymer Chemistry* **2020**, *11*, 184-219.
- [95] Y. P. Liang, J. H. He, B. L. Guo, *Acs Nano* **2021**, *15*, 12687-12722.
- [96] P. L. Tsai, T. Y. Sung, C. Y. Chong, S. Y. Huang, S. F. Chen, *Anal. Methods* **2018**, *10*, 4756-4764.
- [97] J. Suriboot, H. S. Bazzi, D. E. Bergbreiter, *Polymers (Basel)* **2016**, *8*, 140.

- [98] a) Y. Y. Xiao, L. J. Li, S. Z. Zhang, J. Z. Feng, Y. G. Jiang, J. Feng, *Macromol. Mater. Eng.* **2019**, *304*, 1900137; b) H. W. Lim, S. J. Lee, *Desalination* **2022**, *526*, 115540.
- [99] J. Z. Zhang, E. Reisner, *Nat. Rev. Chem.* **2020**, *4*, 6-21.
- [100] M. D. Kärkäs, O. Verho, E. V. Johnston, B. Åkermark, *Chem. Rev.* **2014**, *114*, 11863-12001.
- [101] B. Zhang, L. Sun, *Chem. Soc. Rev.* **2019**, *48*, 2216-2264.
- [102] M. Chhowalla, D. Jena, H. Zhang, *Nat. Rev. Mater.* **2016**, *1*, 16052.
- [103] C. Wang, H. Dong, L. Jiang, W. Hu, *Chem. Soc. Rev.* **2018**, *47*, 422-500.
- [104] a) T. Teranishi, M. Sakamoto, *J. Phys. Chem. Lett.* **2013**, *4*, 2867-2873; b) F. Chen, T. Ma, T. Zhang, Y. Zhang, H. Huang, *Adv. Mater.* **2021**, *33*, e2005256.
- [105] E. Sundin, M. Abrahamsson, *Chem. Commun. (Camb)* **2018**, *54*, 5289-5298.
- [106] a) N. Karjule, R. Phatake, M. Volokh, I. Hod, M. Shalom, *Small Methods* **2019**, *3*, 1900401; b) J. Zhang, M. Antonietti, B. Kumru, *J. Chem. Educ.* **2021**, *98*, 1347-1351.
- [107] a) L. Jin, H. G. Zhao, Z. M. M. Wang, F. Rosei, *Adv. Energy Mater.* **2021**, *11*, 2003233; b) K. Villa, J. R. Galan-Mascaros, N. Lopez, E. Palomares, *Sustainable Energy & Fuels* **2021**, *5*, 4560-4569; c) H. Bian, D. Li, J. Q. Yan, S. Z. Liu, *J. Energy Chem.* **2021**, *57*, 325-340.
- [108] a) M. H. Shaw, J. Twilton, D. W. MacMillan, *J. Org. Chem.* **2016**, *81*, 6898-6926; b) N. A. Romero, D. A. Nicewicz, *Chem. Rev.* **2016**, *116*, 10075-10166.
- [109] a) A. K. Jena, A. Kulkarni, T. Miyasaka, *Chem. Rev.* **2019**, *119*, 3036-3103; b) V. Avrutin, N. Izyumskaya, H. Morkoc, *Superlattices Microstruct.* **2011**, *49*, 337-364.
- [110] C. Byrne, G. Subramanian, S. C. Pillai, *J. Environ. Chem. Eng.* **2018**, *6*, 3531-3555.
- [111] M. Marszewski, S. W. Cao, J. G. Yu, M. Jaroniec, *Mater. Horiz.* **2015**, *2*, 261-278.
- [112] a) B. Kumru, D. Cruz, T. Heil, M. Antonietti, *Chem. Mater.* **2020**, *32*, 9435-9443; b) E. Buz, F. Morlet-Savary, J. Lalevée, H. Y. Acar, *Macromol. Chem. Phys.* **2017**, *219*, 1700356.
- [113] a) J. H. Kim, S. Seo, J. H. Lee, H. Choi, S. Kim, G. Piao, Y. R. Kim, B. Park, J. Lee, Y. Jung, H. Park, S. Lee, K. Lee, *Adv. Funct. Mater.* **2021**, *31*, 2008277; b) A. Tashakory, N. Karjule, L. Abisdri, M. Volokh, M. Shalom, *Adv. Sustainable Syst.* **2021**, *5*, 2100005.
- [114] C. Coperet, M. Chabanas, R. P. Saint-Arroman, J. M. Basset, *Angew. Chem. Int. Ed.* **2003**, *42*, 156-181.
- [115] a) H. Q. N. Gunaratne, C. J. Pestana, N. Skillen, J. N. Hui, S. Saravanan, C. Edwards, J. T. S. Irvine, P. K. J. Robertson, L. A. Lawton, *Environ. Sci.-Water Research & Technology* **2020**, *6*, 945-950; b) S. Q. Zhang, J. Zhang, J. Sun, Z. Y. Tang, *Chem. Eng. Process. Process Intensif.* **2020**, *147*, 107746; c) K. Bell, S. Freeburne, M. Fromel, H. J. Oh, C. W. Pester, *J. Polym. Sci.* **2021**, *59*, 2844-2853.
- [116] a) P. Bansal, A. Verma, *J. Photochem. Photobiol., A* **2017**, *342*, 131-142; b) I. D. Dallabona, A. L. Mathias, R. M. M. Jorge, *Colloids Surf., A* **2021**, *627*, 127159.

- [117] D. W. Li, Q. Zhu, C. J. Han, Y. N. Yang, W. Z. Jiang, Z. Y. Zhang, *J. Hazard. Mater.* **2015**, 285, 398-408.
- [118] W. Lei, N. Suzuki, C. Terashima, A. Fujishima, *Front. Energy* **2021**, 15, 577-595.
- [119] Y. Ma, J. Wang, S. Xu, Z. Zheng, J. Du, S. Feng, J. Wang, *RSC Adv.* **2017**, 7, 15077-15083.
- [120] N. X. D. Mai, J. Bae, I. T. Kim, S. H. Park, G.-W. Lee, J. H. Kim, D. Lee, H. B. Son, Y.-C. Lee, J. Hur, *Environ. Sci. Nano* **2017**, 4, 955-966.
- [121] X. You, H. Huang, R. Zhang, Z. Yang, M. Xu, X. Wang, Y. Yao, *Catalysts* **2021**, 11, 613.
- [122] J. Sun, B. V. K. J. Schmidt, X. Wang, M. Shalom, *ACS Appl. Mater. Interfaces* **2017**, 9, 2029-2034.
- [123] B. Kumru, V. Molinari, M. Hilgart, F. Rummel, M. Schäffler, B. V. K. J. Schmidt, *Poly. Chem.* **2019**, 10, 3647-3656.
- [124] C. Esen, B. Kumru, *Beilstein J. Org. Chem.* **2021**, 17, 1323-1334.
- [125] G.-B. Fu, R. Xie, J.-W. Qin, X.-B. Deng, X.-J. Ju, W. Wang, Z. Liu, L.-Y. Chu, *Ind. Eng. Chem. Res.* **2021**, 60, 8762-8775.
- [126] H. Heidarpour, M. Golizadeh, M. Padervand, A. Karimi, M. Vossoughi, M. H. Tavakoli, *J. Photochem. Photobiol., A* **2020**, 398, 112559.
- [127] J. Yang, Z. Li, H. Zhu, *Applied Catal., B:* **2017**, 217, 603-614.
- [128] H. Zhu, Z. Li, J. Yang, *Chem. Eng. J.* **2018**, 334, 1679-1690.
- [129] J. Byun, K. Landfester, K. A. I. Zhang, *Chem. Mater.* **2019**, 31, 3381-3387.
- [130] H. Sai, A. Erbas, A. Dannenhoffer, D. Huang, A. Weingarten, E. Siismets, K. Jang, K. Qu, L. C. Palmer, M. Olvera de la Cruz, S. I. Stupp, *J. Mater. Chem. A.* **2020**, 8, 158-168.
- [131] T. Kuckhoff, K. Landfester, K. A. I. Zhang, C. T. J. Ferguson, *Chem. Mater.* **2021**, 33, 9131-9138.
- [132] Y. Gao, S. Gu, L. Duan, Y. Wang, G. Gao, *Soft Matter* **2019**, 15, 3897-3905.
- [133] A. Katzenberg, A. Raman, N. L. Schnabel, A. L. Quispe, A. I. Silverman, M. A. Modestino, *React. Chem. Eng.* **2020**, 5, 377-386.
- [134] J. Liu, H. Chen, X. Shi, S. Nawar, J. G. Werner, G. Huang, M. Ye, D. A. Weitz, A. A. Solovev, Y. Mei, *Environ. Sci. Nano* **2020**, 7, 656-664.
- [135] C. Ma, W. C. Seo, J. Lee, Y. Kim, H. Jung, W. Yang, *Chemosphere* **2021**, 275, 130052.
- [136] Z. Yong, L. W. Yap, R. Fu, Q. Shi, Z. Guo, W. Cheng, *Mater. Horiz.* **2021**, 8, 2533-2540.
- [137] H. Zhang, L. Zhou, J. Li, S. Rong, J. Jiang, S. Liu, *Front. Chem.* **2021**, 8.
- [138] W. Wan, R. Zhang, M. Ma, Y. Zhou, *J. Mater. Chem. A.* **2018**, 6, 754-775.
- [139] H. Ou, P. Yang, L. Lin, M. Anpo, X. Wang, *Angew. Chem. Int. Ed.* **2017**, 56, 10905-10910.
- [140] C. T. Mehmood, Z. Zhong, H. Zhou, C. Zhang, Y. Xiao, *RSC Adv.* **2020**, 10, 36349-36362.
- [141] M. Schreck, N. Kleger, F. Matter, J. Kwon, E. Tervoort, K. Masania, A. R. Studart, M. Niederberger, *Small* **2021**, 17, 2104089.
- [142] C. Rizzo, S. Marullo, F. Billeci, F. D'Anna, *Eur. J. Org. Chem.* **2021**, 2021, 3148-3169.

- [143] S. Chatterjee, B. Kuppan, U. Maitra, *Dalton Trans.* **2018**, 47, 2522-2530.
- [144] I. M. Sosnin, S. Vlassov, L. M. Dorogin, *React. Funct. Polym.* **2021**, 158, 104781.
- [145] Z.-Y. Deng, W. Wang, L.-H. Mao, C.-F. Wang, S. Chen, *J. Mater. Chem. A* **2014**, 2, 4178-4184.
- [146] D. H. Kim, M. C. Jung, S.-H. Cho, S. H. Kim, H.-Y. Kim, H. J. Lee, K. H. Oh, M.-W. Moon, *Sci. Rep.* **2015**, 5, 12908.
- [147] R. Hickman, E. Walker, S. Chowdhury, *J. Water Process Eng.* **2018**, 24, 74-82.
- [148] S. Y. Lee, D. Kang, S. Jeong, H. T. Do, J. H. Kim, *ACS Omega* **2020**, 5, 4233-4241.
- [149] Z. Lian, C. Wei, B. Gao, X. Yang, Y. Chan, J. Wang, G. Z. Chen, K. S. Koh, Y. Shi, Y. Yan, Y. Ren, J. He, F. Liu, *RSC Adv.* **2020**, 10, 9210-9225.
- [150] S. Hossain, D.-M. Chun, *Mater. Chem. Phys.* **2020**, 255, 123589.
- [151] I. A. Abdelhafeez, X. Zhou, Q. Yao, Z. Yu, Y. Gong, J. Chen, *ACS Omega* **2020**, 5, 4181-4190.
- [152] X. Li, Y. Li, Y. Huang, T. Zhang, Y. Liu, B. Yang, C. He, X. Zhou, J. Zhang, *Green Chem.* **2017**, 19, 2925-2930.
- [153] T. Zhang, W. Liang, Y. Huang, X. Li, Y. Liu, B. Yang, C. He, X. Zhou, J. Zhang, *Chem. Commun.* **2017**, 53, 12536-12539.
- [154] Y. Yang, Q. Zhang, R. Zhang, T. Ran, W. Wan, Y. Zhou, *Front. Chem.* **2018**, 6.
- [155] G. Cao, Z. Liu, *Mater. Lett.* **2017**, 202, 32-35.
- [156] F. Li, X. Lan, J. Shi, L. Wang, *J. Water Process Eng.* **2021**, 40, 101965.
- [157] S. Guo, X. Li, J. Li, B. Wei, *Nat. Commun.* **2021**, 12, 1343.
- [158] G. Zhang, W. Choi, *Chem. Commun.* **2012**, 48, 10621-10623.
- [159] D. Olivo-Alanís, M. M. Atilano-Camino, A. García-González, L. Humberto-Álvarez, R. B. García-Reyes, *J. Sol-Gel Sci. Technol.* **2021**, 100, 538-554.
- [160] J. M. Tobin, T. J. D. McCabe, A. W. Prentice, S. Holzer, G. O. Lloyd, M. J. Paterson, V. Arrighi, P. A. G. Cormack, F. Vilela, *ACS Catal.* **2017**, 7, 4602-4612.
- [161] L. Wang, X. Chen, Y. Duan, Q. Luo, D. Wang, *Catal. Sci. Technol.* **2020**, 10, 4191-4200.
- [162] C. Esen, M. Antonietti, B. Kumru, *J. Appl. Polym. Sci.* **2021**, 138, 50879.
- [163] C. Esen, B. Kumru, *Nanoscale Adv.* **2022**.
- [164] a) G. Liao, F. He, Q. Li, L. Zhong, R. Zhao, H. Che, H. Gao, B. Fang, *Prog. Mater. Sci.* **2020**, 112, 100666; b) N. Rono, J. K. Kibet, B. S. Martincigh, V. O. Nyamori, *Crit. Rev. Solid State Mater. Sci.* **2020**, 1-29; c) S. Cao, J. Low, J. Yu, M. Jaroniec, *Adv. Mater.* **2015**, 27, 2150-2176; d) K. Xiao, P. Giusto, L. Wen, L. Jiang, M. Antonietti, *Angew. Chem. Int. Ed.* **2018**, 57, 10123-10126; e) Z. Sun, W. Wang, Q. Chen, Y. Pu, H. He, W. Zhuang, J. He, L. Huang, *J. Mater. Chem. A* **2020**, 8, 3160-3167; f) W. Xiong, F. Huang, R.-Q. Zhang, *Sustain. Energy Fuels* **2020**, 4, 485-503.
- [165] a) A. Naseri, M. Samadi, A. Pourjavadi, A. Z. Moshfegh, S. Ramakrishna, *J. Mater. Chem. A* **2017**, 5, 23406-23433; b) J. Liu, H. Wang, Z. P. Chen, H. Moehwald, S. Fiechter, R. van de Krol, L. Wen, L. Jiang, M. Antonietti, *Adv. Mater.* **2015**, 27, 712-718; c) Y. Xia, D. K. Xiao, B. Cheng, J. Yu, L. Jiang, M. Antonietti, S. Cao, *ChemSusChem* **2020**, 13, 1730-1734.

- [166] a) Z. Zhao, Y. Sun, F. Dong, *Nanoscale* **2015**, *7*, 15-37; b) M. Majdoub, Z. Anfar, A. Amedlous, *ACS Nano* **2020**, *14*, 12390-12469.
- [167] H. Yang, Z. Wang, S. Liu, Y. Shen, Y. Zhang, *Chinese Chem. Lett.* **2020**, *31*, 3047-3054.
- [168] D. Han, D. Ni, Q. Zhou, J. Ji, Y. Lv, Y. Shen, S. Liu, Y. Zhang, *Adv. Funct. Mater.* **2019**, *29*, 1905576.
- [169] a) L. Zhang, G. Ye, X. Huo, S. Xu, J. Chen, K. Matyjaszewski, *ACS Omega* **2019**, *4*, 16247-16255; b) B. Kumru, D. Cruz, T. Heil, M. Antonietti, *Chem. Mater.* **2020**, *32*, 9435-9443.
- [170] B. Kumru, V. Molinari, M. Hilgart, F. Rummel, M. Schaeffler, B. V. K. J. Schmidt, *Polym. Chem.* **2019**, *10*, 3647-3656.
- [171] Q. Cao, T. Heil, B. Kumru, M. Antonietti, B. V. K. J. Schmidt, *Polym. Chem.* **2019**, *10*, 5315-5323.
- [172] Q. Cao, J. Barrio, M. Antonietti, B. Kumru, M. Shalom, B. V. K. J. Schmidt, *ACS Appl. Polym. Mater.* **2020**, *2*, 3346-3354.
- [173] Y. Zhang, Z. Zhou, Y. Shen, Q. Zhou, J. Wang, A. Liu, S. Liu, Y. Zhang, *ACS Nano* **2016**, *10*, 9036-9043.
- [174] a) N. Yandrapalli, T. Robinson, M. Antonietti, B. Kumru, *Small* **2020**, *16*, 2001180; b) D. Cruz, J. G. Cerrillo, B. Kumru, N. Li, J. D. Perea, B. V. K. J. Schmidt, I. Laueremann, C. J. Brabec, M. Antonietti, *J. Am. Chem. Soc.* **2019**, *141*, 12322-12328.
- [175] V. Chaudhary, S. Sharma, *J. Polym. Res.* **2019**, *26*, 102.
- [176] a) M. Grochowicz, B. Gawdzik, *J. Porous Mater.* **2013**, *20*, 339-349; b) C. A. McNamara, M. J. Dixon, M. Bradley, *Chem. Rev.* **2002**, *102*, 3275-3300.
- [177] Google Patents, **1944**.
- [178] a) M. A. Harmer, Q. Sun, *Appl. Catal., A General* **2001**, *221*, 45-62; b) P. Gupta, S. Paul, *Catal. Today* **2014**, *236*, 153-170; c) B. Wang, W. Ran, *Chem. Eng. Commun.* **2012**, *199*, 1236-1250; d) D. C. Sherrington, *Chem. Commun.* **1998**, 2275-2286.
- [179] a) M. P. Tsyurupa, V. A. Davankov, *React. Funct. Polym.* **2006**, *66*, 768-779; b) M. Albuszis, P. J. Roth, W. Pauer, H.-U. Moritz, *Polym. Chem.* **2014**, *5*, 5689-5699.
- [180] a) M. Lavén, T. Alsberg, Y. Yu, M. Adolfsson-Erici, H. Sun, *J. Chromatogr. A* **2009**, *1216*, 49-62; b) S. Weigel, R. Kallenborn, H. Hühnerfuss, *J. Chromatogr. A* **2004**, *1023*, 183-195; c) M. Moeder, S. Schrader, M. Winkler, P. Popp, *J. Chromatogr. A* **2000**, *873*, 95-106; d) J. D. Cahill, E. T. Furlong, M. R. Burkhardt, D. Kolpin, L. G. Anderson, *J. Chromatogr. A* **2004**, *1041*, 171-180; e) M. W. F. Nielen, R. W. Frei, U. A. T. Brinkman, in *J. Chromatogr. Library, Vol. 39* (Eds.: R. W. Frei, K. Zech), Elsevier, **1988**, pp. 5-80; f) M. M. Hassan, C. M. Carr, *Chemosphere* **2018**, *209*, 201-219.
- [181] a) K. Hong, X. Ni, Z. Shen, *Rubber Chem. Technol.* **2016**, *89*, 700-711; b) J. Lu, P. H. Toy, *Chem. Rev.* **2009**, *109*, 815-838; c) M. Benaglia, A. Puglisi, F. Cozzi, *Chem. Rev.* **2003**, *103*, 3401-3430; d) H. P. Hentze, M. Antonietti, *Rev. Mol. Biotechnol.* **2002**, *90*, 27-53.

- [182] B. Karagoz, G. Bayramoglu, B. Altintas, N. Bicak, M. Y. Arica, *Ind. Eng. Chem. Prod. Res.* **2010**, *49*, 9655-9665.
- [183] a) Q. Li, S. Jin, B. Tan, *Sci. Rep.* **2016**, *6*, 31359; b) D. F. Liu, Y. J. Xiang, X. C. Wu, Z. X. Zhang, L. F. Liu, L. Song, X. W. Zhao, S. D. Luo, W. J. Ma, J. Shen, W. Y. Zhou, G. Wang, C. Y. Wang, S. S. Xie, *Nano Lett.* **2006**, *6*, 2375-2378.
- [184] P. Cyganowski, A. Dzimitrowicz, *Polymers* **2020**, *12*, 784.
- [185] P. A. G. Cormack, A. Davies, N. Fontanals, *React. Funct. Polym.* **2012**, *72*, 939-946.
- [186] P. Veverka, K. Jeřábek, *React. Funct. Polym.* **1999**, *41*, 21-25.
- [187] a) A. Unciti-Broceta, E. M. V. Johansson, R. M. Yusop, R. M. Sánchez-Martín, M. Bradley, *Nature Protocols* **2012**, *7*, 1207-1218; b) W. Bauman, J. Eichhorn, *J. Am. Chem. Soc.* **1947**, *69*, 2830-2836.
- [188] C. W. Huck, G. K. Bonn, *Chem. Eng. Technol.* **2005**, *28*, 1457-1472.
- [189] S. Moulay, *Polymer-Plastics Technology and Engineering* **2018**, *57*, 1045-1092.
- [190] C. Chen, N. Janoszka, C. K. Wong, C. Gramse, R. Weberskirch, A. H. Gröschel, *Angew. Chem. Int. Ed.*, *n/a*.
- [191] P. Giusto, B. Kumru, J. Zhang, R. Rothe, M. Antonietti, *Chem. Mater.* **2020**, *32*, 7284-7291.
- [192] a) M. Yin, Z. Li, J. Kou, Z. Zou, *Environ. Sci. Technol.* **2009**, *43*, 8361-8366; b) Y. Jiang, Z. Jin, C. Chen, W. Duan, B. Liu, X. Chen, F. Yang, J. Guo, *RSC Advances* **2017**, *7*, 12856-12870; c) D. Tu, H. Liao, Q. Deng, X. Liu, R. Shang, X. Zhang, *RSC Advances* **2018**, *8*, 21905-21914; d) Q. Cao, B. Kumru, M. Antonietti, B. V. K. J. Schmidt, *Mater. Horiz.* **2020**, *7*, 762-786.
- [193] a) E. Caló, V. V. Khutoryanskiy, *Eur. Polym. J.* **2015**, *65*, 252-267; b) L. Li, B. Yan, J. Yang, W. Huang, L. Chen, H. Zeng, *ACS Appl. Mater. Interfaces* **2017**, *9*, 9221-9225; c) H. Yuk, S. Lin, C. Ma, M. Takaffoli, N. X. Fang, X. Zhao, *Nat. Commun.* **2017**, *8*, 14230.
- [194] T. Murakami, B. V. K. J. Schmidt, H. R. Brown, C. J. Hawker, *Macromolecules* **2015**, *48*, 7774-7781.
- [195] a) Q. Chen, H. Chen, L. Zhu, J. Zheng, *J. Mater. Chem. B* **2015**, *3*, 3654-3676; b) Z. Li, Y. Su, B. Xie, X. Liu, X. Gao, D. Wang, *J. Mater. Chem. B* **2015**, *3*, 1769-1778; c) M. A. Haque, T. Kurokawa, J. P. Gong, *Polymer* **2012**, *53*, 1805-1822.
- [196] a) G. Gao, G. Du, Y. Cheng, J. Fu, *J. Mater. Chem. B* **2014**, *2*; b) Q. Wang, R. X. Hou, Y. J. Cheng, J. Fu, *Soft Matter* **2012**, *8*, 6048-6056; c) J. Djonlagic, A. Lancuski, M. S. Nikolic, J. Rogan, S. Ostojic, Z. Petrovic, *J. Appl. Polym. Sci.* **2017**, *134*; d) L. Liu, L. Li, Y. Qing, N. Yan, Y. Wu, X. Li, C. Tian, *Polym. Chem.* **2016**, *7*, 7142-7151.
- [197] a) M. Klein, E. Poverenov, *J. Sci. Food Agric.* **2020**, *100*, 2337-2347; b) K. Sampathkumar, K. X. Tan, S. C. J. Loo, *iScience* **2020**, *23*, 101055.
- [198] P. K. Nayak, S. Mahesh, H. J. Snaith, D. Cahen, *Nat. Rev. Mater.* **2019**, *4*, 269-285.
- [199] a) G. Liao, F. He, Q. Li, L. Zhong, R. Zhao, H. Che, H. Gao, B. Fang, *Prog. Mater. Sci.* **2020**, *112*, 100666; b) S. K. Gaddam, R. Pothu, R. Boddula, *Polym. Compos.* **2020**, *41*, 430-442.

- [200] a) Q. Liu, X. Wang, Q. Yang, Z. Zhang, X. Fang, *Appl. Surf. Sci.* **2018**, *450*, 46-56; b) B. Luo, R. Song, J. Geng, D. Jing, Y. Zhang, *Appl. Catal., B* **2018**, 238, 294-301; c) Q. Han, B. Wang, Y. Zhao, C. Hu, L. Qu, *Angew. Chem., Int. Ed.* **2015**, *54*, 11433-11437.
- [201] a) Y. Yang, G. Zeng, D. Huang, C. Zhang, D. He, C. Zhou, W. Wang, W. Xiong, B. Song, H. Yi, S. Ye, X. Ren, *Small* **2020**, *16*, 2001634; b) G. Xu, Y. Xu, Z. Zhou, Y. Bai, *Diam. Relat. Mater.* **2019**, *97*, 107461; c) J. Sun, J. Xu, A. Grafmueller, X. Huang, C. Liedel, G. Algara-Sillere, M. Willinger, C. Yang, Y. Fu, X. Wang, M. Shalom, *Appl. Catal., B* **2017**, *205*, 1-10; d) Q. Cao, S. Amini, B. Kumru, B. V. K. J. Schmidt, *ACS Appl. Mater. Interfaces* **2021**, *13*, 4643-4651.
- [202] a) J. Lin, Z. Pan, X. Wang, *ACS Sustain. Chem. Eng.* **2014**, *2*, 353-358; b) X. Gong, S. Yu, M. Guan, X. Zhu, C. Xue, *J. Mater. Chem. A* **2019**, *7*, 7373-7379.
- [203] P. Giusto, B. Kumru, J. Zhang, R. Rothe, M. Antonietti, *Chem. Mater.* **2020**, *32*, 7284-7291.
- [204] B. Kumru, J. M. Mesa, M. Antonietti, M. Al-Naji, *ACS Sustain. Chem. Eng.* **2019**, *7*, 17574-17579.
- [205] J. Sun, B. V. K. J. Schmidt, X. Wang, M. Shalom, *ACS Appl. Mater. Interfaces* **2017**, *9*, 2029-2034.
- [206] a) J. Liu, T. An, Z. Chen, Z. Wang, H. Zhou, T. Fan, D. Zhang, M. Antonietti, *J. Mater. Chem. A* **2017**, *5*, 8933-8938; b) B. Ye, C. Yao, M. Yan, H. Zhang, F. Xi, J. Liu, B. Li, X. Dong, *Macromol. Mater. Eng.* **2019**, *304*.
- [207] a) J. H. Thurston, A. J. Clifford, B. S. Henderson, T. R. Smith, D. Quintana, K. F. Cudworth, T. J. Lujan, K. A. Cornell, *ACS Appl Bio Mater* **2020**, *3*, 1681-1689; b) C. Hu, Y. R. Lin, H. C. Yang, *ChemSusChem* **2018**, *12*, 1794-1806.
- [208] M. Shalom, S. Inal, C. Fettkenhauer, D. Neher, M. Antonietti, *J. Am. Chem. Soc.* **2013**, *135*, 7118-7121.
- [209] X. Zhou, P. Zhang, F. Zhao, G. Yu, *ACS Materials Lett.* **2020**, *2*, 1419-1422.
- [210] A. Sikder, A. K. Pearce, S. J. Parkinson, R. Napier, R. K. O'Reilly, *ACS Appl. Polym. Mater.* **2021**, *3*, 1203-1217.
- [211] B. Kumru, D. Cruz, T. Heil, B. V. K. J. Schmidt, M. Antonietti, *J. Am. Chem. Soc.* **2018**, *140*, 17532-17537.
- [212] J. Barrio, M. Shalom, *ACS Appl Mater Interfaces* **2018**, *10*, 39688-39694.
- [213] a) M. E. d. O. Ferreira, B. G. Vaz, C. E. Borba, C. G. Alonso, I. C. Ostroski, *Micropor. Mesopor. Mat.* **2019**, *277*, 208-216; b) Y. Yu, J. Miyawaki, *Carbon* **2020**, *170*, 380-383.
- [214] J. Barrio, M. Volokh, M. Shalom, *J. Mater. Chem. A.* **2020**, *8*, 11075-11116.
- [215] N. Yandrapalli, T. Robinson, M. Antonietti, B. Kumru, *Small* **2020**, *16*, e2001180.
- [216] Y. Shi, L. Peng, Y. Ding, Y. Zhao, G. Yu, *Chem. Soc. Rev.* **2015**, *44*, 6684-6696.
- [217] P. Bujak, I. Kulszewicz-Bajer, M. Zagorska, V. Maurel, I. Wielgus, A. Pron, *Chem. Soc. Rev.* **2013**, *42*, 8895-8999.
- [218] B. Kumru, N. Bıcak, *Macromol. Symp.* **2015**, *352*, 42-45.
- [219] A. L. Pang, A. Arşad, M. Ahmadipour, *Polym. Adv. Technol.* **2020**.
- [220] M. E. Cinar, T. Ozturk, *Chem. Rev.* **2015**, *115*, 3036-3140.
- [221] T. Nezakati, A. Seifalian, A. Tan, A. M. Seifalian, *Chem. Rev.* **2018**, *118*, 6766-6843.

- [222] L. Groenendaal, F. Jonas, D. Freitag, H. Pielartzik, J. R. Reynolds, *Adv. Mater.* **2000**, *12*, 481-494.
- [223] L. G. Mercier, M. Leclerc, *Acc. Chem. Res.* **2013**, *46*, 1597-1605.
- [224] T. Lindfors, Z. A. Boeva, R.-M. Latonen, *RSC Adv.* **2014**, *4*, 25279-25286.
- [225] C. Jiang, G. Chen, X. Wang, *Synth. Met.* **2012**, *162*, 1968-1971.
- [226] M. N. Gueye, A. Carella, J. Faure-Vincent, R. Demadrille, J.-P. Simonato, *Prog. Mater. Sci.* **2020**, *108*, 100616.
- [227] V. Castagnola, C. Bayon, E. Descamps, C. Bergaud, *Synth. Met.* **2014**, *189*, 7-16.
- [228] X. Fan, W. Nie, H. Tsai, N. Wang, H. Huang, Y. Cheng, R. Wen, L. Ma, F. Yan, Y. Xia, *Adv. Sci.* **2019**, *6*, 1900813.
- [229] J. Ouyang, *Displays* **2013**, *34*, 423-436.
- [230] G. Zhang, Z.-A. Lan, X. Wang, *Chem. Sci.* **2017**, *8*, 5261-5274.
- [231] a) P. Xia, B. Zhu, J. Yu, S. Cao, M. Jaroniec, *J. Mater. Chem. A* **2017**, *5*, 3230-3238; b) S. Cao, J. Yu, *J. Phys. Chem. Lett.* **2014**, *5*, 2101-2107; c) Z. Zhou, Y. Zhang, Y. Shen, S. Liu, Y. Zhang, *Chem. Soc. Rev.* **2018**, *47*, 2298-2321; d) J. Ji, J. Wen, Y. Shen, Y. Lv, Y. Chen, S. Liu, H. Ma, Y. Zhang, *J. Am. Chem. Soc.* **2017**, *139*, 11698-11701.
- [232] M.-L. Xu, L.-W. Liu, K. Wang, Y.-C. Dou, K. Li, X. Cheng, F.-M. Zhang, *J. Mater. Chem. A* **2020**, *8*, 22124-22133.
- [233] Q. Cao, B. Kumru, M. Antonietti, B. V. K. J. Schmidt, *Macromolecules* **2019**, *52*, 4989-4996.
- [234] K. Li, Y.-Z. Lin, K. Wang, Y. Wang, Y. Zhang, Y. Zhang, F.-T. Liu, *Appl. Catal., B* **2020**, *268*, 118402.
- [235] Y. Xu, W. Lei, J. Su, J. Hu, X. Yu, T. Zhou, Y. Yang, D. Mandler, Q. Hao, *Electrochim. Acta* **2018**, *259*, 994-1003.
- [236] a) Z. Xing, Z. Chen, X. Zong, L. Wang, *Chem. Commun.* **2014**, *50*, 6762-6764; b) W. Wu, A. Ali, R. Jamal, M. Abdulla, T. Bakri, T. Abdiryim, *RSC Adv.* **2019**, *9*, 34691-34698.
- [237] G. Dong, Y. Zhang, Q. Pan, J. Qiu, *J. Photochem. Photobiol. C* **2014**, *20*, 33-50.
- [238] a) C. D. Spicer, M. A. Booth, D. Mawad, A. Armgarth, C. B. Nielsen, M. M. Stevens, *Chem* **2017**, *2*, 125-138; b) Q. Fu, Y. Li, X. Wang, Q. Li, F. Wang, R. Yang, *J. Mater. Chem. C* **2020**, *8*, 17185-17193; c) Y. Li, H. Lou, F. Wang, Y. Pang, X. Qiu, *ChemistrySelect* **2019**, *4*, 11406-11412.
- [239] S. V. Selvaganesh, J. Mathiyarasu, K. L. N. Phani, V. Yegnaraman, *Nanoscale Res. Lett.* **2007**, *2*, 546.
- [240] T. Li, J.-D. Cui, L.-M. Gao, Y.-Z. Lin, R. Li, H. Xie, Y. Zhang, K. Li, *ACS Sustainable Chem. Eng.* **2020**, *8*, 13352-13361.
- [241] K. Chen, X. Deng, G. Dodekatos, H. Tüysüz, *J. Am. Chem. Soc.* **2017**, *139*, 12267-12273.
- [242] D. Mantione, I. D. agua, A. Sanchez-Sanchez, D. Mecerreyes, *Polymers* **2017**, *9*, 354.
- [243] M. Mueller, M. Fabretto, D. Evans, P. Hojati-Talemi, C. Gruber, P. Murphy, *Polymer* **2012**, *53*, 2146-2151.
- [244] Y. Wang, K. Cai, X. Yao, *ACS Appl. Mater. Interfaces* **2011**, *3*, 1163-1166.

- [245] Q. Zhao, R. Jamal, L. Zhang, M. Wang, T. Abdiryim, *Nanoscale Res. Lett.* **2014**, *9*, 557.
- [246] Y. Osman, R. Jamal, A. Rahman, F. Xu, A. Ali, T. Abdiryim, *Synth. Met.* **2013**, *179*, 54-59.
- [247] S. Bontapalle, S. Varughese, *Polym. Degrad. Stab.* **2020**, *171*, 109025.
- [248] J. P. Paraknowitsch, A. Thomas, J. Schmidt, *Chem. Commun.* **2011**, *47*, 8283-8285.
- [249] Y. Wen, J. Xu, *J. Polym. Sci., Part A: Polym. Chem.* **2017**, *55*, 1121-1150.
- [250] A. Savateev, Y. Markushyna, C. M. Schuesslbauer, T. Ullrich, D. M. Guldi, M. Antonietti, *Angew. Chem. Int. Ed.* **2021**.
- [251] K. Xu, H. Sun, T.-P. Ruoko, G. Wang, R. Kroon, N. B. Kolhe, Y. Puttisong, X. Liu, D. Fazzi, K. Shibata, C.-Y. Yang, N. Sun, G. Persson, A. B. Yankovich, E. Olsson, H. Yoshida, W. M. Chen, M. Fahlman, M. Kemerink, S. A. Jenekhe, C. Müller, M. Berggren, S. Fabiano, *Nat. Mater.* **2020**, *19*, 738-744.

10. List of Publications

✚ Ind. Eng. Chem. Res. **2022**, 61, 30, 10616–10630.

C Esen, B Kumru

Photocatalyst Incorporated Crosslinked Porous Polymer Networks.

DOI: 10.1021/acs.iecr.2c01658

✚ Nanoscale Adv. **2022**, 2022, 4, 3136-3141.

C Esen, B Kumru

Thiol-ene Polymer Beads via Liquid-Liquid Printing: Armored Interfaces and Photopolymerization via Graphitic Carbon Nitride. DOI: 10.1039/D2NA00254J

✚ Polym. Chem., **2022**, 13, 139-146.

C Esen, M Antonietti, B Kumru

On the Photopolymerization of Mevalonic Lactone Methacrylate: Exposing the Potential of an Overlooked Monomer. DOI: 10.1039/D1PY01497H

✚ ChemPhotoChem. **2021**, 5, 857–862.

C Esen, M Antonietti, B Kumru

Oxidative Photopolymerization of 3,4-Ethylenedioxythiophene (EDOT) via Graphitic Carbon Nitride: A Modular Toolbox for Attaining PEDOT. DOI:10.1002/cptc.202100046

✚ Beilstein J. Org. Chem. **2021**, 17, 1323–1334.

C Esen, B Kumru

Photoinduced Post-Modification of Graphitic Carbon Nitride Embedded Hydrogels: Synthesis of 'Hydrophobic Hydrogels' and Pore Substructuring. DOI: 10.3762/bjoc.17.92

✚ J. Appl. Polym. Sci. **2021**, 138, 50879.

C Esen, M Antonietti, B Kumru

Upgrading poly(styrene-co-divinylbenzene) Beads: Incorporation of Organomodified Metal-Free Semiconductor Graphitic Carbon Nitride Through Suspension Photopolymerization to Generate Photoactive Resins. DOI: 10.1002/app.50879

✚ Polym. Chem. **2016**, 7, 7094-7100.

M Cetin, **C Esen**, O Daglar, S Luleburgaz, G Hizal, H Durmaz, U Tunca.

1,3-Dipolar and Diels–Alder cycloaddition reactions on polyester backbones possessing internal electron-deficient alkyne moieties. DOI: 10.1039/C6PY01827K

Conference Presentations & Awards

 **C Esen, B Kumru**

Materials Proceedings, 2021

“Light-driven Integration of Graphitic Carbon Nitride into Porous Polymer Networks”

Best Paper Award Published: 05 November 2021 by MDPI in The 2nd International Online Conference on Polymer Science-Polymers and Nanotechnology for Industry 4.0 session Smart polymeric Synthesis and Modification for Industry 4.0

doi.org/10.3390/IOCPS2021-11590

 **C Esen, B Kumru**

The European Young Chemists' Meeting 2022 and Swiss Academy of Sciences January 19–21.2022 (virtual)

Special Sponsor Awards (Innomedica) to the poster presentation entitled:

“Integration of Graphitic Carbon Nitride into Porous Polymer Networks”

 **C Esen, M Antonietti, B Kumru**

Bordeaux Polymer Conference 2022, Bordeaux June 13–16.2022

Poster presentation entitled:

“Lights up for an Overlooked Monomer: Photopolymerization of Mevalonic Lactone Methacrylate”

 **C Esen, B Kumru**

European Polymer Conference 2022 (EPF), Prague June 26– July 1.2022

Oral presentation entitled:

“Examples on Graphitic Carbon Nitride in Synthetic Polymer Chemistry”

11. Declaration

Die vorliegende Dissertation entstand in dem Zeitraum zwischen Februar 2020 und April 2022 am Max-Planck-Institut für Kolloid- und Grenzflächenforschung unter Betreuung von Prof. Dr. Dr. h.c. Markus Antonietti.

Hiermit erkläre ich, dass die vorliegende Arbeit selbstständig angefertigt wurde und keine anderen als die angegebenen Hilfsmittel und Quelle verwendet wurden.

Die Arbeit wurde bisher weder im Inland noch im Ausland in gleicher oder ähnlicher Form einer anderen Prüfungsbehörde vorgelegt. Es habe bisher keine früheren erfolglosen Promotionsverfahren stattgefunden.

The present work was carried during the period between February 2020 and April 2022 at the Max Planck Institute of Colloids and Interfaces under the supervision of Prof. Dr. Dr. h.c. Markus Antonietti.

I declare that I have written this work on my own and used no other than the named aids and references. This thesis was not submitted to another examination board in this or other countries. There were no unsuccessful examination processes.

Cansu Esen

POTSDAM, den 17.08.2022